Neutron Scattering:
Theory, Instrumentation, and Simulation

Kim Lefmann
Niels Bohr Institute, University of Copenhagen
with contributions from:
Jacob Kirkensgaard, Lise Arleth, Bente Lebech, and Maria Thomsen, Niels Bohr Institute, Univ. Copenhagen,
Markus Strobl, European Spallation Source,
and Andrew Wildes, Institut Laue-Langevin

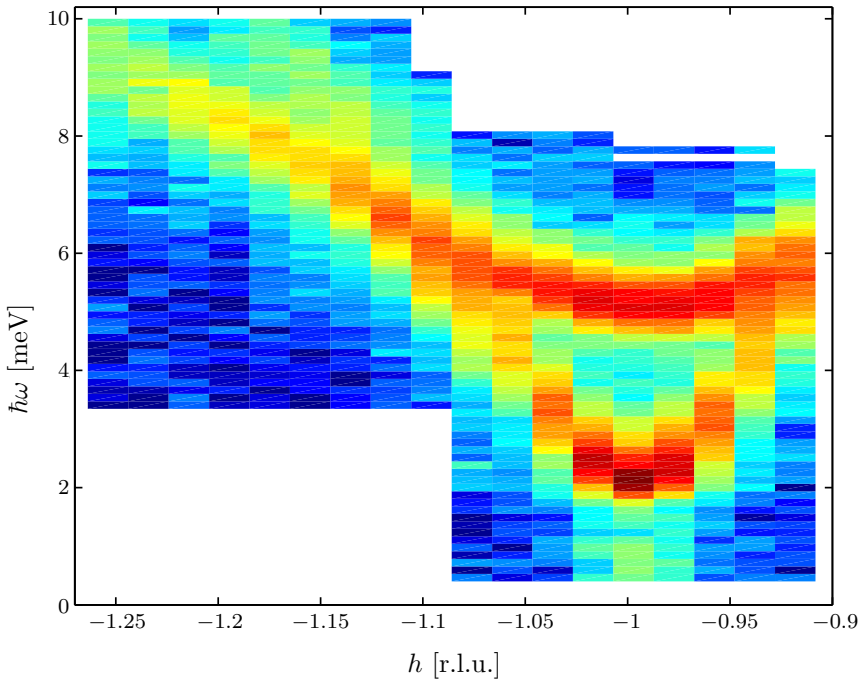

Image on front page: Inelastic neutron scattering data on a single crystal of the multiferroic $YMnO_3$, taken by Sonja Holm and the students at the Copenhagen neutron scattering course, November 2012.

Foreword and acknowledgements

This text is written as lecture notes for a University course in Neutron Scattering, University of Copenhagen, autumn 2014. In contrast to most textbooks on this topic, these notes cover both theoretical and experimental aspects, as well as an introduction to ray-tracing simulations of neutron instruments.

The theoretical parts of these notes are largely inspired by the classical textbooks by Marshall and Lovesey[1], and Squires[2], but the material has been simplified to make it appropriate for beginners in this field and re-organised in (for me) a more streamlined way. Further, this text contains more recent topics: small-angle scattering, reflectivity, and tomography. It is intended to make the notation consistent with Squires[2]. One major difference, though, is the use of q in stead of κ for the scattering vector, in order to make the notation compatible with current practice.

The reader of these notes is supposed to have an interest in learning the fundamentals of the neutron scattering technique and have a mathematical foundation corresponding to a typical 1st year university curriculum of *e.g.* Physics, Chemistry, or Enigineering. In particular, I assume knowledge of complex numbers for description of waves.

I am strongly indepted to Kurt N. Clausen for introducing me to the secrets of neutron scattering and for support far beyond the duties and timespan of a Ph.D. supervisor. Without him this work would have been utterly impossible.

A wholehearted thank you goes to Robert McGreevy for providing me the "five reasons" for neutron scattering and for leading the EU projects SCANS, NMI3, and ISIS-TS2, which inspired and funded much of the work related to computer simulations.

In the present EU projects (named NMI3 and NMI3-2), led by Helmut Schober and Mark Johnson (both from ILL), Pia Jensen, Jesper Bruun, Linda Udby, and I develop simulation tools for the notes to create a virtual EU course for the teaching of neutron scattering and instrumentation. In this respect, the students at the Copenhagen course have acted as "guinea pigs", helping us to find scores of mistakes and imprecisions. Thanks to all $\sim$ 160 participants for good spirit and much discussion. Thanks in particular to Sara Eisenhardt, Jacob Larsen, Elisabeth Ulrikkeholm, Maria Thomsen, Pia Jensen, Johan Jacobsen, Henrik Jacobsen, and Andreas Nørgård Larsen for spotting many errors and for useful suggestions.

I would at this point like to thank all persons who joined me in developing the McStas simulation package (in chronological order): Kristian Nielsen, Henrik M. Rønnow, Emmanuel Farhi, Per-Olof Åstrand, Peter K. Willendrup, Klaus Lieutenant, Peter Christiansen, Erik Knudsen, Linda Udby, and Uwe Filges.

I thank Jonas Okkels Birk, Bente Lebech, Ursula Hansen, Monika Kovacic, and Pia Jensen for drawing most of the illustrations. The remaining figures were provided by Peter K. Willendrup, Peter Christiansen, Linda Udby, and Robert McGreevy.

Finally, thanks once again to Linda Udby and Pia Jensen for helping me with the editing and for making the material available interactively on the internet.

Contents

Part I

Basics of neutron scattering

Chapter 1

Introduction to neutron scattering

Neutron scattering is one of the most powerful and versatile experimental methods to study the structure and dynamics of materials on the atomic and nanometer scale. Quoting the Nobel committee, when awarding the prize to C. Shull and B. Brockhouse in 1994, these pioneers have "helped answer the question of where atoms are and ... what atoms do" [3].

Neutron scattering is presently used by more than 8000 researchers worldwide, and the scope of the method is continuously broadening. In the 1950'ies and 1960'ies, neutron scattering was an exotic tool in Solid State Physics and Chemical Crystallography, but today it serves communities as diverse as Biology, Earth Sciences, Planetary Science, Engineering, Polymer Science, and Cultural Heritage. In brief, neutrons are used in all scientific fields that deal with hard, soft, or biological materials.

It is, however, appropriate to issue a warning already here. Although neutron scattering is a great technique, it is also time-consuming, expensive, and rare. Neutron scattering experiments last from hours to days and are performed only at a few handfuls of large international facilities. Here, access to measurement time is difficult, and the running costs correspond to several thousand Euros per instrument day. Hence, neutron scattering should be used only where other methods are inadequate.

For the study of atomic and nanometer-scale structure in materials, X-ray scattering is the technique of choice. X-ray sources are by far more abundant and are, especially for synchrotron X-ray sources, much stronger than neutron sources. Hence, the rule of thumb goes: "If an experiment can be performed with X-rays, use X-rays". For an introduction to X-ray scattering, see, *e.g.*, the excellent textbook by D. F. McMorrow and J. Als-Nielsen [4].

However, neutrons have a number of properties that make them extremely useful for purposes where X-rays are not sufficient. This chapter is devoted to presenting the properties of the neutron and describing the essential differences

between neutron and X-ray scattering.

1.1 Basic properties of the neutron

The neutron is a nuclear particle with a mass, m_{n}, rather close to that of the proton [5]

$$m_{\mathrm{n}} = 1.675 \cdot 10^{-27}\,\mathrm{kg}. \tag{1.1}$$

The neutron does not exist naturally in free form, but decays into a proton, an electron, and an anti-neutrino. The neutron lifetime, $\tau = 886$ s [6], is much longer than the time a neutron spends within a scattering experiment, which is merely a fraction of a second. Hence, neutron decay can typically be neglected in experiments.

The neutron is electrically neutral but still possesses a magnetic moment

$$\mu = \gamma\mu_{\mathrm{N}}, \tag{1.2}$$

where $\gamma = -1.913$ is the neutron magnetogyric ratio and the nuclear magneton is given by $\mu_{\mathrm{N}} = e\hbar/(2m_{\mathrm{p}}) = 5.051 \cdot 10^{-27}$ J/T. The neutron magnetic moment is coupled antiparallel to its spin, which has the value $s = 1/2$.

The neutron interacts with nuclei via the strong nuclear force and with magnetic moments via the electromagnetic force. Most of this text deals with the consequences of these interactions; *i.e.* the scattering and absorption of neutrons by atoms and nuclei inside materials, as well as reflection from surfaces and interfaces.

1.2 Particle-wave duality

One of the remarkable consequences of quantum mechanics is that matter has both particle- and wave-like nature [7]. The neutron is no exception from this. In neutron scattering experiments, neutrons behave predominantly as particles when they are created in a nuclear process, as interfering waves when they are scattered, and again as particles when they are detected by another nuclear process.

To be more specific on the wave nature of matter, a particle moving with constant velocity, v, can be ascribed a corresponding (de-Broglie) wavelength, given by

$$\lambda = \frac{2\pi\hbar}{mv}. \tag{1.3}$$

In neutron scattering, the wave nature is often referred to in terms of the neutron *wave number*,

$$\boxed{k = \frac{2\pi}{\lambda}}, \tag{1.4}$$

or the *wave vector* of length k and with same direction as the velocity:

$$\mathbf{k} = \frac{m_{\mathrm{n}}\mathbf{v}}{\hbar}. \tag{1.5}$$

	v [ms^{-1}]	λ^{-1} [Å^{-1}]	k [Å^{-1}]	$\sqrt{E}$ [meV$^{1/2}$]
v [ms^{-1}]	1	2.528×10^{-4}	1.588×10^{-3}	2.286×10^{-3}
λ^{-1} [Å^{-1}]	3956	1	6.283	9.045
k [Å^{-1}]	629.6	0.1592	1	1.440
$\sqrt{E}$ [meV$^{1/2}$]	437.4	0.1106	0.6947	1

Table 1.1: Conversion table between different neutron parameters in the most commonly used units. Examples of use: $v\,[\mathrm{ms}^{-1}] = 629.6\,k\,[\mathrm{Å}^{-1}]$ and $(\lambda[\mathrm{Å}])^{-1} = 0.1106\sqrt{E[\mathrm{meV}]}$. Adapted from Ref. [2].

Energy interval	λ interval	Common name	Usual origin
less than 0.05 meV	> 40 Å	ultra cold	special sources below 4 K
0.05 meV - 14 meV	2.4 - 40 Å	cold	H_2 moderators at 25 K
14 meV - 200 meV	0.6 - 2.4 Å	thermal	H_2O moderators at 300 K
200 meV - 1 eV	0.3 - 0.6 Å	hot	graphite moderators at 2000 K
1 eV - 10 keV	< 0.3 Å	epithermal	background from moderators

Table 1.2: Common naming of neutron energy ranges, and typical origin of neutrons with these energies. The "standard" thermal energy is 25 meV, corresponding to $\lambda_{\mathrm{th}} = 1.798$ Å, or $v_{\mathrm{th}} = 2200$ m/s.

By tradition, wavelengths are measured in Å (10^{-10} m), and wave numbers in Å^{-1}, while the neutron velocity is measured in SI units: m/s. For our purpose we consider the neutrons as non-relativistic, and the neutron kinetic energy is given by

$$\boxed{E = \frac{\hbar^2 k^2}{2m_{\mathrm{n}}}}, \tag{1.6}$$

which is measured in eV or meV, where 1 eV$= 1.602 \cdot 10^{-19}$ J. A useful conversion table between velocity, wave number, wavelength, and energy, is shown in Table 1.1.

1.3 Neutron scattering facilities

Neutron sources with flux densities adequate for neutron scattering investigations of materials are based on one of two principles, also illustrated in Fig. 1.1:

- **Fission.** A high continuous flux of neutrons is produced in the core of a conventional fission reactor.
- **Spallation.** A pulsed production of neutrons is obtained by bombarding a target of heavy elements with high-energy particles, typically accelerated protons.

Common to both types of sources is that neutrons are moderated to "thermal" or "cold" velocities close to the source and then transported to the neutron

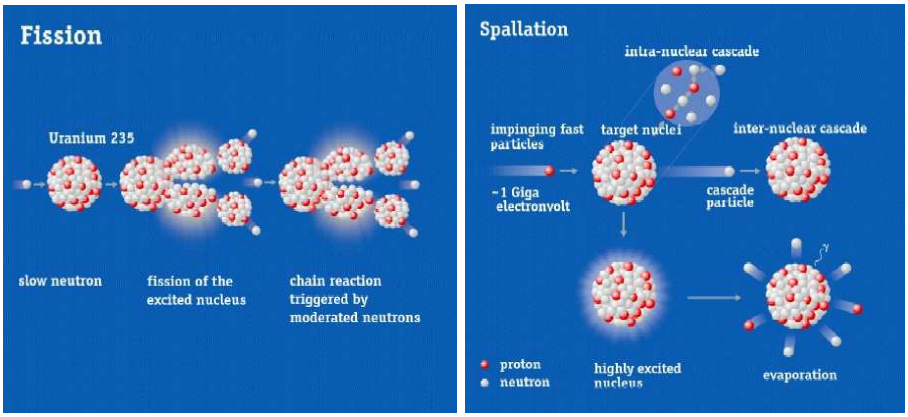

Figure 1.1: The two main methods of neutron production. Left: Traditional nuclear reactors make use of production of neutrons for maintaining the chain reaction; surplus of neutrons can be used for neutron scattering. Right: Protons accelerated into the GeV regime can split heavy nuclei with a large neutron surplus, creating free neutrons among the reaction products.

scattering instruments in neutron guide systems. For the naming of neutron energy intervals, see Table 1.2.

Both types of neutron sources are built as dedicated facilities, each hosting tens of instruments. All major sources are user facilities, meaning that they serve a research community much larger than the staff affiliated with the facilities. Typically, user experiments are selected through a competitive proposal system.

At the time of writing, more than twenty neutron facilities are in operation worldwide, the most important being the reactor source ILL, Grenoble, France, and the spallation source ISIS, Oxfordshire, UK. However, the European dominance is challenged by the powerful, recently commissioned spallation sources: Spallation Neutron Source (SNS), Oak Ridge, USA, and Japan Proton Accelerator Research Complex (J-PARC), Tokai, Japan [8]. For this and other reasons, it was has long been proposed to build a European Spallation Source (ESS). In 2009, it was decided to place this source in Lund, Sweden. After some years of preparation work, the actual construction was initiated in the summer of 2014[9].

A list of the most significant neutron sources worldwide is given in Chapter 3.

1.4 Five reasons for using neutrons

We will now present some of the assets of neutron scattering. We will focus on cases where neutrons can be preferred to X-rays or where neutrons are needed to complement X-rays. It is commonly agreed in the neutron scattering community that this can be formulated in five general points:

1. **Energy and wavelength.** Thermal neutrons have a wavelength (around 1.8 Å) similar to inter-atomic distances, and an energy (around 25 meV) similar to elementary excitations in solids. One can thus obtain simultaneous information on the structure and dynamics of materials and *e.g.* measure dispersion relations (energy-wavelength dependence) of excitations in crystalline solids.

2. **Isotopes and light elements.** The neutron scattering cross section varies in a seemingly random fashion between elements and even between different isotopes of the same element. One can thus use neutrons to study light isotopes. In particular, this is important for hydrogen, which is almost invisible to X-rays. With neutrons, the large difference in scattering between usual hydrogen (^{1}H) and deuterium, (^{2}D) can be used in biological and soft matter sciences to change the contrast in the scattering and also "highlight" selected groups within large molecules or aggregates.

3. **Quantitative experiments.** The interaction between neutrons and (most) matter is rather weak, implying that neutrons can probe the bulk of the sample, and not only its surface. The weak interaction also diminishes higher order effects. Hence, quantitative comparisons between neutron scattering data and theoretical models can be performed to a high precision.

4. **Transparency.** Since neutrons penetrate matter easily, neutron scattering can be performed with samples stored in all sorts of sample environment: Cryostats, magnets, furnaces, pressure cells, *etc.* Furthermore, very bulky samples can be studied, up to tens of cm thickness, depending on their elemental composition. The sample is left relatively unharmed by the neutron experiment, although beam experiments should certainly not be performed on living organisms.

5. **Magnetism.** The neutron magnetic moment makes neutrons scatter from magnetic structures or magnetic field gradients. Unpolarized neutrons are used to learn about the periodicity and magnitude of the magnetic order, while scattering of spin-polarized neutrons can reveal the direction of the atomic magnetic moments.

In most cases, neutron scattering is performed in combination with other experimental techniques; often with neutron scattering as one of the final techniques to be applied before conclusions can be drawn.

1.5 On these notes

After this brief introduction, we will continue the introductory part by presenting the formalism of the neutron scattering process (chapter 2). In part II, we go into details with neutron sources, moderators, and guide systems (chapter 3), components for neutron optics and instruments (chapter 4).

In the later parts, we will describe the actual applications of neutron scattering. For each case, we give the necessary theoretical background, a description of the experimental set-up, and a number of corresponding problems.

- Part III describes the study of material structure by elastic neutron scattering. Small angle neutron scattering (SANS) is presented in chapter 5, reflectometry in chapter 6, diffraction from crystals in chapter 7, and tomography in chapter 8.
- Part IV deals with the study of dynamics in materials by inelastic neutron scattering, in particular the study of coherent lattice vibrations (phonons) in chapter 10.
- Part V describes elastic and inelastic scattering from magnetic materials in chapters 11 and 13.

The final part VI contains an introduction to neutron ray-tracing simulations, often used for instrument design and for simulating the effect of the combined geometry of neutron scattering instruments. Here, however, they are also used to form the basis for a number of working problems shaped as "virtual experiments", where the student investigate a problem in neutron science or instrumentation by means of simulations [11].

1.5.1 Reading the text

The text is intended so that after the introduction in part I and part II, each part can in principle be studied independently. However, parts IV and V relies to a minor extent on basic results from part III. Part VI forms the basis for the simulation problems, but requires only knowledge of part II.

The reader is assumed to have a general knowledge of classical physics and complex numbers for the description of waves, and a general knowledge of mathematics, corresponding to first year curriculum on most university educations in Physics, Chemistry, and Engineering. The first four parts of the text assumes very little knowledge of quantum mechanics. At places where a deeper quantum mechanical presentation could be elucidating for some students, there will be alternative sections containing the formal derivation of the results. These sections can be omitted without essential loss of contents; they are marked by an asterisk (*).

1.5.2 Future extensions

In later versions of this note, we aim to include a number of other utilizations of neutron scattering, like single crystal diffraction, quasielastic scattering from diffusion, and scattering from liquids.

More advanced topics, like scattering with polarized neutrons, analytical calculations of instrumental resolution, or ultracold neutrons will be written in a second part of the notes.

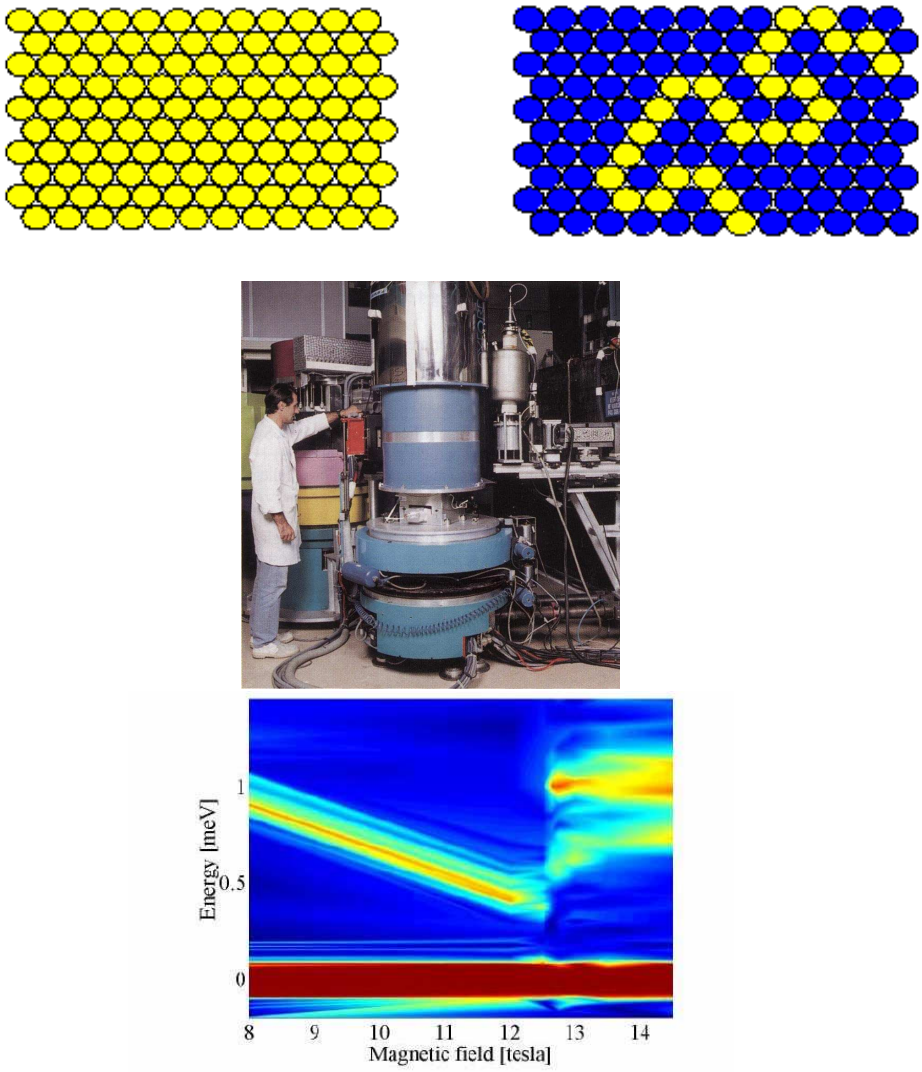

Figure 1.2: Illustration of two of the "five reasons" for neutron scattering. Top row shows schematically the neutron visibility of one polymer chain in two different solutions (left) hydrogenous solvent, (right) deuterated solvent. The enhanced contrast from the deuterated solvent gives a significant effect in a small-angle scattering experiment. Bottom row shows the measurement of magnetic excitations in an applied magnetic field. To perform the measurements, the neutron beam must penetrate the Al walls of a large cryomagnet (left). The data from the $CuGeO_3$ sample is shown with neutron counts presented as a colour scale as a function of neutron energy transfer and magnetic field value (right). Adapted from [10].

Chapter 2

Basics of neutron scattering theory

This chapter contains the basics of scattering theory. The present description is specialised to neutron scattering, but is in general valid also for scattering of other types of radiation, like electrons or X-rays.

In the process we describe in this chapter, neutrons are scattered by the nuclei by the strong nuclear forces. The range of these forces are femtometers (fm), much smaller than the neutron wavelength (measured in Å). Thus, the neutron cannot probe the internal structure of the nucleus, and the scattering from a single nucleus is isotropic [12].

The process of neutron scattering is unavoidably of quantum mechanical nature. However, most of this chapter is kept less rigorous, since for many applications a full formal treatment is unnecessary. In particular, this is the case for section 2.2, for which an alternative quantum-based section is given as 2.3*. Although vastly different, these two approaches lead to identical results.

The contents of this chapter form the basis for the understanding of the later parts of these notes, in particular elastic and inelastic neutron scattering from particles, surfaces, powders, and crystals.

2.1 The neutron cross sections

We fist introduce the terms by which we describe the scattering of a neutron beam. In particular, we describe the interaction of a neutron beam with materials by introducing the central concept of cross sections.

2.1.1 Neutron flux

We define the flux of a neutron beam as the neutron rate per area

$$\boxed{\Psi = \frac{\text{number of neutrons impinging on a surface per second}}{\text{surface area perpendicular to the neutron beam direction}}}, \tag{2.1}$$

usually given in the unit $\mathrm{n/(cm^2 s)}$.

Experimental consideration. At most neutron scattering experiments, the incoming flux at the sample position lies in the range 10^5 to 10^9 $\mathrm{n/(cm^2 s)}$.

2.1.2 The scattering cross section

The *neutron scattering cross section*, σ, of a system is defined by its ability to scatter neutrons:

$$\boxed{\sigma = \frac{1}{\Psi} \cdot \text{ number of neutrons scattered per second}}, \tag{2.2}$$

which has units of area. The scattering intensity is divided by the neutron flux to ensure that σ is an intrinsic property, independent on the neutron flux at the particular experimental set-up.

For a single nucleus, σ can now be seen as the effective area of the nucleus perpendicular to the neutron beam, as will be elaborated in problem 2.6.1. The scattering cross section used here is the total cross section, which depends on the system (sample) volume, V. For thin samples, σ can be described by the volume specific cross section, Σ, through

$$\sigma = V\Sigma. \tag{2.3}$$

For thicker samples, beam attenuation must be taken into account; see section 2.1.5.

2.1.3 The differential scattering cross section

The angular dependence of the scattered neutrons is a most important aspect of all neutron scattering. To describe this dependence, we define the *differential scattering cross section*:

$$\boxed{\frac{d\sigma}{d\Omega} = \frac{1}{\Psi} \frac{\text{number of neutrons scattered into solid angle } d\Omega \text{ per second}}{d\Omega}}. \tag{2.4}$$

The total number of scattered neutrons is of course the sum of neutrons in all of the 4π solid angle, hence

$$\sigma = \int \frac{d\sigma}{d\Omega} d\Omega. \tag{2.5}$$

2.1.4 The partial differential scattering cross section

In some scattering processes, the neutron delivers energy to or absorbs energy from the scattering system. This type of scattering we denote *inelastic scattering*. We define the neutron energy transfer by

$$\boxed{\hbar\omega = E_\mathrm{i} - E_\mathrm{f} = \frac{\hbar^2(k_\mathrm{i}^2 - k_\mathrm{f}^2)}{2m_\mathrm{n}}}, \tag{2.6}$$

where the indices "i" and "f" denote *initial* and *final*, respectively. Note that the energy change is defined with the opposite sign of most definitions of changing properties, so that neutron energy loss gives a positive value of $\hbar\omega$.

In inelastic scattering processes, energy is transfered to - or taken from - the sample. Energy conservation gives that the energy change, ΔE, of the sample is given by

$$\Delta E = \hbar\omega. \tag{2.7}$$

For describing inelastic scattering, one needs to take into account the energy dependence of the scattered neutrons. This is described by the *partial differential scattering cross section*:

$$\boxed{\frac{d^2\sigma}{d\Omega dE_\mathrm{f}} = \frac{1}{\Psi}\frac{\begin{array}{c}\text{no. of neutrons scattered per sec. into } d\Omega \\ \text{with energies } [E_\mathrm{f}; E_\mathrm{f} + dE_\mathrm{f}]\end{array}}{d\Omega dE_\mathrm{f}}}. \tag{2.8}$$

Integrating over all final energies, E_f, we reach the differential cross section described earlier:

$$\frac{d\sigma}{d\Omega} = \int \frac{d^2\sigma}{d\Omega dE_\mathrm{f}} dE_\mathrm{f}. \tag{2.9}$$

Following (2.5), the total cross section is found by a double integration:

$$\sigma = \iint \frac{d^2\sigma}{d\Omega dE_\mathrm{f}} d\Omega dE_\mathrm{f}. \tag{2.10}$$

For a closer description of inelastic scattering, a quantum mechanical treatment of the scattering process is required, as initiated in section 2.3 and described in detail in part IV.

2.1.5 Beam attenuation due to scattering

Since the number of neutrons scattered is necessarily limited by the number of incoming neutrons, the total cross section cannot be truly proportional to volume, at least not for large, strongly scattering systems. Hence, (2.3) should be understood only as what is called the *thin sample approximation* or the *Born approximation*. This equation is valid only when the total scattering cross section of a given sample is much smaller than its area perpendicular to the beam.

For a thick sample, we must consider successive thin slices of thickness dz, each attenuating the incident beam (which we take to travel in the positive z direction):

$$\text{no. of neutrons scattered per sec. from } dz = \Psi(z)\Sigma A dz, \tag{2.11}$$

where A is the area of a sample slice perpendicular to the beam. We assume that A and Σ are constants and that the scattering cross section is uniform within the sample. The flux of the incident beam in the neutron flight direction is then attenuated inside the sample according to

$$\boxed{\Psi(z) = \Psi(0)\exp(-\mu z)}, \tag{2.12}$$

where we have defined the attenuation coefficient

$$\mu = \mu_{\rm s} = \Sigma. \tag{2.13}$$

The derivation is simple and is left as an exercise to the reader, see problem 2.6.2.

When the attenuation coefficient varies along the neutron path, (2.12) is generalized to

$$\boxed{\Psi(z) = \Psi(0)\exp\left(-\int_0^z \mu(z')dz'\right)}. \tag{2.14}$$

This equation is essential in the use of neutrons transmission for real-space *imaging* of samples, in analogy to medical X-ray images. This application of neutrons will be elaborated more in chapter 8.

2.1.6 The absorption cross section

Neutron absorption takes place as a result of neutron-induced nuclear processes, which destroy the neutrons, emitting secondary radiation (α, β, or γ) as a result. In most cases, the absorption cross section, $\sigma_{\rm a}$, of thermal neutrons is inversely proportional to the neutron velocity. In other words, the absorption is proportional to the neutron wavelength: $\sigma_{\rm a} \propto \lambda$.

The neutron absorption cross sections are measured and tabelized for all but the rarest isotopes, see *e.g.* the Neutron Data Booklet [13], or the NIST home page [14]. Traditionally, the absorption cross section of isotope i is given as $\sigma_{\rm a,i,\,th}$ per nucleus in units of "barns" (1 barn = 10^{-28} m^2) and is listed at the standard "thermal" velocity $v_{\rm th} = 2200$ ms^{-1} ($\lambda_{\rm th} = 1.798$ Å, see also table 1.1). The actual absorption cross section is then given by

$$\sigma_{\rm a,i} = \sigma_{\rm a,i,\,th}\frac{v_{\rm th}}{v} = \sigma_{\rm a,i,\,th}\frac{\lambda}{\lambda_{\rm th}}. \tag{2.15}$$

In a solid, many nuclei contribute to the total absorption. As in (2.12), the resulting attenuation coefficient is

$$\mu_{\rm a} = \sum_i \frac{N_i\sigma_{{\rm a},i}}{V} = \sum_i n_i\sigma_{{\rm a},i}. \tag{2.16}$$

In this sum, N_i represents the number of nuclei of isotope i in the sample volume V, and $n_i = N_i/V$ is the corresponding atomic density. The attenuation coefficients for scattering and absorption are additive due to the rule of addition of probabilities (see problem 2.6.2):

$$\mu_{\mathrm{t}} = \mu_{\mathrm{s}} + \mu_{\mathrm{a}}. \tag{2.17}$$

An abbreviated list of absorption and scattering cross sections for selected isotopes/elements is given in table 2.1.

Experimental consideration. For a single neutron, the probabilty of scattering or absorption will typically be much smaller than unity. However, real experiments deal with thousands to billions of neutrons onto the sample per second, so here the many small probabilities will give rise to a total neutron count, N, which can often be considerable.

The actual counting number is a stocastic variable that follows a Poisson distribution with mean $\bar{N}$ and standard deviation $\sigma = \sqrt{\bar{N}}$. For $\bar{N} > 10$, it can be approximated with a normal distribution with the same average and standard deviation, meaning that 68% of the times the count value will lie in the interval $\bar{N} \pm \sqrt{\bar{N}}$ - and 95% in the interval $\bar{N} \pm 2\sqrt{\bar{N}}$.

Most often, one replaces the (unknown) true mean value with the actual count number in the expression for the standard deviation, reaching $\sigma = \sqrt{N}$. Although neither this approximation nor the assumption of Gaussian statistics hold for small count numbers, they are in practice often used down to $N = 1$. For $N = 0$, a zero value of standard deviation will lead to divergences during model fitting, and a standard deviation value of $\sigma = 1$ is often used instead.

2.2 Wave description of nuclear scattering

In this section, we discuss the basics of scattering of waves from a semi-classical point of view. For an equivalent, fully quantum mechanical treatment of this topic, see section 2.3*.

2.2.1 The neutron wave

The incoming (or initial) neutron can be described as a (complex) plane wave

$$\boxed{\psi_{\mathrm{i}}(\mathbf{r}) = \frac{1}{\sqrt{Y}} \exp(i\mathbf{k}_{\mathrm{i}} \cdot \mathbf{r})}, \tag{2.18}$$

where Y is a normalization constant, implying that the density of the incoming neutron wave is $|\psi_{\mathrm{i}}|^2 = 1/Y$. This has no implication on the final results, since Y will eventually cancel in the final equations, but we keep the normalization for completeness. We have in (2.18) omitted an explicit time dependence, $\exp(-i\omega t)$, which plays no role until we discuss inelastic scattering.

Z	Nucleus	b (10^{-15} m)	σ_{inc} (10^{-28} m^2)	$\sigma_{\mathrm{a,th}}$ (10^{-28} m^2)
1	H	-3.741	80.26 *	0.3326
1	^{1}H	-3.742	80.27 *	0.3326
1	^{2}D	6.674	2.05	0.000519
2	^{3}He	5.74	1.532	5333
2	^{4}He	3.26	0	0
3	Li	-1.90	0.92	70.5
3	^{6}Li	2.0	0.46	940
3	^{7}Li	-2.22	0.78	0.0454
4	Be	7.79	0.0018	0.0076
5	B	5.30	1.70	767
5	^{10}B	-0.2	3.0	3835
5	^{11}B	6.65	0.21	0.0055
6	C	6.6484	0.001	0.00350
7	N	9.36	0.50	1.90
8	O	5.805	0	0.00019
9	F	5.654	0.0008	0.0096
10	Ne	4.566	0.008	0.039
11	Na	3.63	1.62	0.530
12	Mg	5.375	0.08	0.063
13	Al	3.449	0.0082	0.231
14	Si	4.1507	0.004	0.171
15	P	5.13	0.005	0.172
16	S	2.847	0.007	0.53
17	Cl	9.5792	5.3	33.5
18	Ar	1.909	0.225	0.675
19	K	3.67	0.27	2.1
20	Ca	4.70	0.05	0.43
21	Sc	12.1	4.5	27.5
22	Ti	-3.37	2.87	6.09
23	V	-0.443	5.08	5.08
24	Cr	3.635	1.83	3.05
25	Mn	-3.750	0.40	13.3
26	Fe	9.45	0.40	2.56
27	Co	2.49	4.8	37.18
28	Ni	10.3	5.2	4.49
29	Cu	7.718	0.55	3.78
30	Zn	5.68	0.077	1.11
31	Ga	7.288	0.16	2.75
32	Ge	8.185	0.18	2.20
48	Cd	4.83	3.46	2520
51	Sb	5.57	0	4.91
58	Ce	4.84	0	0.63
60	Nd	7.69	9.2	50.5
64	Gd	9.5	151	49700
65	Tb	7.34	0.004	23.4
82	Pb	9.401	0.0030	0.171

Table 2.1: Neutron cross sections and scattering lengths for the first 32 elements (isotopic average using the natural abundancies). In addition, data for selected isotopes and for some heavier elements are presented. Data taken from [13].
* It should be noted that the important incoherent cross section for H varies with neutron wavelength. The value listed is valid for $\lambda > 1.798$ Å [15, 16].

From (1.5), the velocity of a neutron described by a plane wave is

$$v = \frac{\hbar k_{\mathrm{i}}}{m_{\mathrm{n}}}. \tag{2.19}$$

Similarly, the corresponding incoming neutron flux is

$$\Psi_{\mathrm{i}} = |\psi_{\mathrm{i}}|^2 v = \frac{1}{Y}\frac{\hbar k_{\mathrm{i}}}{m_{\mathrm{n}}}. \tag{2.20}$$

We will use this result as a stepping stone in the following calculations.

2.2.2 Elastic neutron scattering from a single nucleus

We consider the idealized situation where a neutron with a well defined velocity is scattered by a single nucleus, labeled j, which is (somehow) fixed in position. The scattered neutron can be described as a spherical wave leaving the nucleus, which is centered at $\mathbf{r}_j$, as shown in Fig. 2.1. The scattered, or final, wave function reads:

$$\boxed{\psi_{\mathrm{f}}(\mathbf{r}) = \psi_{\mathrm{i}}(\mathbf{r}_j)\frac{-b_j}{|\mathbf{r}-\mathbf{r}_j|}\exp(ik_{\mathrm{f}}|\mathbf{r}-\mathbf{r}_j|)}, \tag{2.21}$$

where b_j is a quantity characteristic for the particular isotope. Since b_j has the unit of length, it is usually denoted *scattering length* and is of the order fm. This above equation is valid only "far" from the nucleus, *i.e.* for $|\mathbf{r}-\mathbf{r}_j| \gg b$, The minus sign in (2.21) is a convention chosen so that most nuclei will have a positive value of b_j.

In experiments, r is typically of the order 1 m. In addition, we will position Origo close to the centre of the "relevant" part of the sample. Hence, the nuclear coordinate, r_j, is typically of the order 1 mm or less, and the density of outgoing neutrons can be approximated by $|\psi_{\mathrm{f}}|^2 \approx b_j^2/(Yr^2)$, omitting $\mathbf{r}_j$ in the denominator of (2.21). The number of neutrons per second intersecting a small surface, dA, is $v|\psi_{\mathrm{f}}|^2 dA = vb_j^2/(Yr^2)dA$. Using (2.19) and the expression for solid angle $d\Omega = dA/r^2$, we reach

$$\text{number of neutrons per second in } d\Omega = \frac{1}{Y}\frac{b_j^2\hbar k_{\mathrm{f}}}{m_{\mathrm{n}}}d\Omega. \tag{2.22}$$

Since the scattering nucleus is fixed, energy conservation requires that the energy of the neutron is unchanged. In this so-called *elastic scattering*, we therefore have $k_{\mathrm{i}} = k_{\mathrm{f}}$. Using (2.4) and (2.20), this leads to the simple expression for the differential cross section for one nucleus:

$$\boxed{\frac{d\sigma}{d\Omega} = b_j^2}, \tag{2.23}$$

giving the total scattering cross section of

$$\boxed{\sigma = 4\pi b_j^2}. \tag{2.24}$$

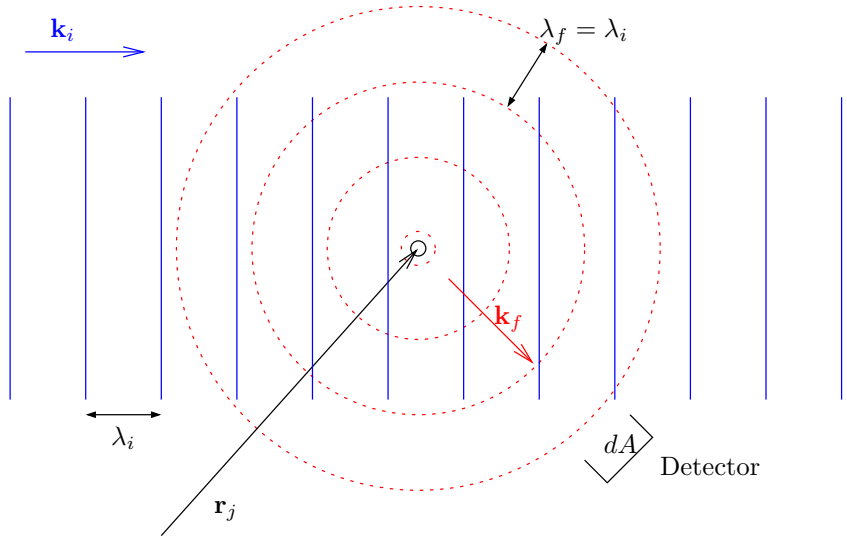

Figure 2.1: An illustration of the initial wave, ψ_i, of wavelength λ_i, and the final wave, ψ_f, of wavelength λ_f, describing a neutron scattering off a single nucleus with positive scattering length (meaning a phase shift of π). The area, dA, for measuring the flux of the outgoing neutrons is the detector area as sketched.

2.2.3 Scattering from two nuclei – interference

In the field of neutron scattering from materials, we are concerned with the effect of scattering from a system of particles. We begin by considering the scattering from two nuclei, labeled j and j', again placed at fixed positions. This simple system will reveal some very important features, which we will utilize later.

The neutron wave that is scattered from the two nuclei is in fact describing just one single neutron. Nevertheless, this neutron "senses" the presence of both nuclei, meaning that the wave scattered from one nucleus will add to the wave scattered from another nucleus. This *interference* is a central aspect in most scattering techniques.

Let us describe this in more precise terms. We assume elastic scattering, $k_\mathrm{i} = k_\mathrm{f} \equiv k$ and identical nuclei, $b_j = b_{j'} \equiv b$. Generalizing (2.21), the outgoing (final) wave can be described as

$$\psi_\mathrm{f}(\mathbf{r}) = -b\left(\frac{\psi_\mathrm{i}(\mathbf{r}_j)}{|\mathbf{r}-\mathbf{r}_j|}\exp(ik_f|\mathbf{r}-\mathbf{r}_j|) + \frac{\psi_\mathrm{i}(\mathbf{r}_{j'})}{|\mathbf{r}-\mathbf{r}_{j'}|}\exp(ik_f|\mathbf{r}-\mathbf{r}_{j'}|)\right), \quad (2.25)$$

where $\psi_\mathrm{i}(\mathbf{r})$ is the plane wave given by (2.18). The two nuclei are assumed to be closely spaced compared with the distance to the observer: $|\mathbf{r}_j - \mathbf{r}_{j'}| \ll r$. Choosing the origin to lie close to the two particles, the denominators can be

considered equal, giving

$$\psi_{\mathrm{f}}(\mathbf{r}) = -\frac{1}{\sqrt{Y}}\frac{b}{r}\big[\exp(i\mathbf{k}_{\mathrm{i}}\cdot\mathbf{r}_j)\exp(ik_f|\mathbf{r}-\mathbf{r}_j|) + \exp(i\mathbf{k}_{\mathrm{i}}\cdot\mathbf{r}_{j'})\exp(ik_f|\mathbf{r}-\mathbf{r}_{j'}|)\big] \tag{2.26}$$

We now want to calculate the length $|\mathbf{r}-\mathbf{r}_j|$, since it enters in the phase of the complex wave function. It is convenient to write the nuclear coordinate, $\mathbf{r}_j$, as the sum of a component parallel to and a component perpendicular to $\mathbf{r}$:

$$|\mathbf{r}-\mathbf{r}_j| = |\mathbf{r}-\mathbf{r}_{j,||}-\mathbf{r}_{j,\perp}| = \sqrt{\big|\mathbf{r}-\mathbf{r}_{j,||}\big|^2 + |\mathbf{r}_{j,\perp}|^2}, \tag{2.27}$$

where the last step is due to Pythagoras. The last term in the square root is by far the smallest and vanishes to first order. To check the order of magnitude, we take a "large" distance between nuclei of $|r_j| \approx 1\,\mu$m and $|\mathbf{r}-\mathbf{r}_{j,||}| \approx 1$ m. This gives an error in the approximation of ≈ 0.005 Å; much smaller than the typical neutron wavelength we consider. This means that effectively only one nuclear coordinate, $\mathbf{r}_{j,||}$, contributes and that the square root can be lifted to give $|\mathbf{r}-\mathbf{r}_j| = |\mathbf{r}-\mathbf{r}_{j,||}|$. Now, we can write

$$k_f|\mathbf{r}-\mathbf{r}_{j,||}| = \mathbf{k}_{\mathrm{f}}\cdot(\mathbf{r}-\mathbf{r}_{j,||}), \tag{2.28}$$

where $\mathbf{k}_{\mathrm{f}}$ is a wave vector with length k_{f} (which here equals k), oriented parallel to $\mathbf{r}$. Since $\mathbf{k}_{\mathrm{f}}\cdot\mathbf{r}_{j,\perp} = 0$, we are free to add this term to the right side of (2.28), reaching

$$\exp(ik_f|\mathbf{r}-\mathbf{r}_j|) = \exp(i\mathbf{k}_{\mathrm{f}}\cdot(\mathbf{r}-\mathbf{r}_j)). \tag{2.29}$$

Rearranging terms, the final wave can be written as

$$\psi_{\mathrm{f}}(\mathbf{r}) = -\frac{1}{\sqrt{Y}}\frac{b}{r}\exp(i\mathbf{k}_{\mathrm{f}}\cdot\mathbf{r})\left[\exp(i(\mathbf{k}_{\mathrm{i}}-\mathbf{k}_{\mathrm{f}})\cdot\mathbf{r}_j) + \exp(i(\mathbf{k}_{\mathrm{i}}-\mathbf{k}_{\mathrm{f}})\cdot\mathbf{r}_{j'})\right]. \tag{2.30}$$

This shows that the observer at position $\mathbf{r}$ will experience a scattered neutron wave that locally seems like a plane wave with wavevector that is parallel to $\mathbf{r}$.

The intensity of neutrons impinging on a small area is again given as $v|\psi_{\mathrm{f}}(\mathbf{r})|^2 dA$. Hereby we can write the scattering intensity as

$$\text{number of neutrons per second in } d\Omega = \frac{1}{Y}\frac{b^2\hbar k_{\mathrm{f}}}{m_{\mathrm{n}}}d\Omega\left|\exp(i\mathbf{q}\cdot\mathbf{r}_j) + \exp(i\mathbf{q}\cdot\mathbf{r}_{j'})\right|^2, \tag{2.31}$$

where we have defined the very central concept of neutron scattering, the *scattering vector*, as

$$\boxed{\mathbf{q} = \mathbf{k}_{\mathrm{i}} - \mathbf{k}_{\mathrm{f}}}. \tag{2.32}$$

The final expression for the differential scattering cross section for elastic scattering from nuclei now becomes:

$$\frac{d\sigma}{d\Omega} = b^2\big|\exp(i\mathbf{q}\cdot\mathbf{r}_j) + \exp(i\mathbf{q}\cdot\mathbf{r}_{j'})\big|^2 = 2b^2\big(1+\cos[\mathbf{q}\cdot(\mathbf{r}_j-\mathbf{r}_{j'})]\big). \tag{2.33}$$

At some values of $\mathbf{q}$, we have $\cos[\mathbf{q} \cdot (\mathbf{r}_j - \mathbf{r}_{j'})] = -1$, meaning that the waves from the two nuclei are in counter phase and that the cross section thus vanishes. At others values of $\mathbf{q}$, the scattering is in phase, $\cos[\mathbf{q} \cdot (\mathbf{r}_j - \mathbf{r}_{j'})] = 1$, giving a value of the cross section of 4 times that of a single nucleus. This is the essence of interference.

2.3 * Quantum mechanics of scattering

We will now go through the principles of neutron scattering from nuclei in a way, which is more strictly quantum mechanical than that of section 2.2. This section does not contain new results, but may be more satisfactory for readers with a physics background. Further, the formalism developed here carries on to the detailed treatment of inelastic scattering of phonons and magnetic scattering in subsequent chapters.

This section is strongly inspired by the treatments in the textbooks by Marshall and Lovesey [1] and Squires [2].

2.3.1 * The initial and final states

We define the state of the incoming wave as

$$\boxed{|\psi_\mathrm{i}\rangle = \frac{1}{\sqrt{Y}} \exp(i\mathbf{k}_\mathrm{i} \cdot \mathbf{r})}, \tag{2.34}$$

where $Y = L^3$ can be identified as the (large) normalization volume for the state which is assumed enclosed in a cubic box with a side length L. The incoming neutron flux is given as (2.20)

$$\Psi_\mathrm{i} = |\psi_\mathrm{i}|^2 v = \frac{1}{Y} \frac{\hbar k_\mathrm{i}}{m_\mathrm{n}}. \tag{2.35}$$

In contrast to the spherical outgoing wave from section 2.2, we express the final state as a (superposition of) plane wave(s)

$$\boxed{|\psi_\mathrm{f}\rangle = \frac{1}{\sqrt{Y}} \exp(i\mathbf{k}_\mathrm{f} \cdot \mathbf{r})}. \tag{2.36}$$

We here ignore the spin state of the neutron, which will be discussed in the later chapter on neutron polarization.

2.3.2 * Density of states

For the spinless states, we calculate the number density in $\mathbf{k}$-space:

$$\frac{dn}{dV_k} = \left(\frac{2\pi}{L}\right)^{-3} = \frac{Y}{(2\pi)^3}. \tag{2.37}$$

We now consider a spherical shell in **k**-space to calculate the (energy) density of states,

$$\frac{dn}{dE_\mathrm{f}} = \frac{dn}{dV_k}\frac{dV_k}{dk_\mathrm{f}}\left(\frac{dE_\mathrm{f}}{dk_\mathrm{f}}\right)^{-1} = \frac{Y}{(2\pi)^3}4\pi k_\mathrm{f}^2\frac{m_\mathrm{n}}{k_\mathrm{f}\hbar^2} = \frac{Yk_\mathrm{f}m_\mathrm{n}}{2\pi^2\hbar^2}. \tag{2.38}$$

In order to describe the differential scattering cross sections, we would like to describe the fraction of the wavefunction which is emitted into directions of $\mathbf{k}_\mathrm{f}$, corresponding to a solid angle $d\Omega$. Here, the densities are given by

$$\left.\frac{dn}{dV_k}\right|_{d\Omega} = \frac{dn}{dV_k}\frac{d\Omega}{4\pi} = \frac{Y}{(2\pi)^3}\frac{d\Omega}{4\pi}. \tag{2.39}$$

Following the calculations leading to (2.38), we can now calculate the density of states within the scattering direction $d\Omega$:

$$\left.\frac{dn}{dE}\right|_{d\Omega} = \frac{Yk_\mathrm{f}m_\mathrm{n}}{(2\pi)^3\hbar^2}d\Omega. \tag{2.40}$$

We will need this expression in the further calculations.

2.3.3 * The master equation for scattering

We describe the interaction responsible for the scattering by an operator denoted $\hat{V}$. The scattering process itself is described by the *Fermi Golden Rule* [17]. This gives the rate of change between the neutron in the single incoming state, $|\psi_\mathrm{i}\rangle$ and a final state, $|\psi_\mathrm{f}\rangle$, where $|\psi_\mathrm{f}\rangle$ resides in a continuum of possible states.

$$W_{\mathrm{i}\to\mathrm{f}} = \frac{2\pi}{\hbar}\frac{dn}{dE_\mathrm{f}}\left|\langle\psi_\mathrm{i}|\hat{V}|\psi_\mathrm{f}\rangle\right|^2. \tag{2.41}$$

We wish to consider only neutrons scattered into the solid angle $d\Omega$. Using (2.40) and (2.41), we reach

$$W_{\mathrm{i}\to\mathrm{f},d\Omega} = \frac{Yk_\mathrm{f}m_\mathrm{n}}{(2\pi)^2\hbar^3}d\Omega\left|\langle\psi_\mathrm{i}|\hat{V}|\psi_\mathrm{f}\rangle\right|^2. \tag{2.42}$$

$W_{\mathrm{i}\to\mathrm{f},d\Omega}$ is the number of neutrons scattered into $d\Omega$ per second. We now only need the expression for the incoming flux (2.20) to reach the result for the differential scattering cross section (2.4)

$$\begin{aligned}\frac{d\sigma}{d\Omega} &= \frac{1}{\Psi}\frac{W_{\mathrm{i}\to\mathrm{f},d\Omega}}{d\Omega} \\ &= Y^2\frac{k_\mathrm{f}}{k_\mathrm{i}}\left(\frac{m_\mathrm{n}}{2\pi\hbar^2}\right)^2\left|\langle\psi_\mathrm{i}|\hat{V}|\psi_\mathrm{f}\rangle\right|^2.\end{aligned} \tag{2.43}$$

In this expression, the normalization volume, Y, will eventually vanish due to the factor $1/\sqrt{Y}$ in the states $|k_\mathrm{i}\rangle$ and $|k_\mathrm{f}\rangle$, since the interaction, $\hat{V}$, is independent of Y. We will thus from now on neglect the Y dependence in the states and in the cross sections.

The factor $k_\mathrm{f}/k_\mathrm{i}$ in (2.43) is of importance only for inelastic neutron scattering, where it always appears in the final expressions. For elastic scattering, $k_\mathrm{f}/k_\mathrm{i} = 1$ and is thus removed from the expression.

2.3.4 * Elastic scattering from one and two nuclei

The interaction between the neutron and the nuclei is expressed by the *Fermi pseudopotential*

$$\boxed{\hat{V}_j(\mathbf{r}) = \frac{2\pi\hbar^2}{m_\mathrm{n}} b_j \delta(\mathbf{r} - \mathbf{r}_j)}. \tag{2.44}$$

Here, b_j has the unit of length and is of the order fm. It is usually denoted the *scattering length*. The spatial delta function represents the short range of the strong nuclear forces and is a sufficient description for the scattering of thermal neutrons.

It should here be noted that a strongly absorbing nucleus will have a significant imaginary contribution to the scattering length. We will, however, not deal with this complication here.

For a single nucleus, we can now calculate the scattering cross section. We start by calculating the matrix element

$$\begin{aligned}\langle \psi_\mathrm{f} | \hat{V}_j | \psi_\mathrm{i} \rangle &= \frac{2\pi\hbar^2}{m_\mathrm{n}} b_j \int \exp(-i\mathbf{k}_\mathrm{f} \cdot \mathbf{r}) \delta(\mathbf{r} - \mathbf{r}_j) \exp(i\mathbf{k}_\mathrm{i} \cdot \mathbf{r}) d^3\mathbf{r} \\ &= \frac{2\pi\hbar^2}{m_\mathrm{n}} b_j \exp(i\mathbf{q} \cdot \mathbf{r}_j),\end{aligned} \tag{2.45}$$

where we have defined the very central concept of neutron scattering, the *scattering vector*, as

$$\boxed{\boxed{\mathbf{q} = \mathbf{k}_\mathrm{i} - \mathbf{k}_\mathrm{f}}}. \tag{2.46}$$

Inserting (2.45) into (2.43), we reassuringly reach the same result as found from the semi-classical calculation (2.23):

$$\boxed{\frac{d\sigma}{d\Omega} = b_j^2}. \tag{2.47}$$

For a system of two nuclei, we obtain interference between the scattered waves. We can write the scattering potential as a sum $\hat{V} = \hat{V}_j + \hat{V}_{j'}$. In this case, the matrix element becomes

$$\langle \psi_\mathrm{f} | \hat{V} | \psi_\mathrm{i} \rangle = \frac{1}{Y} \frac{2\pi\hbar^2}{m_\mathrm{n}} \big(b_j \exp(i\mathbf{q} \cdot \mathbf{r}_j) + b_{j'} \exp(i\mathbf{q} \cdot \mathbf{r}_{j'}) \big). \tag{2.48}$$

Inserting into (2.43), we reach the same result (2.33) as found by the simpler approach in section 2.2.

2.3.5 * Formalism for inelastic scattering

When describing the quantum mechanics of the inelastic scattering process, it is important to keep track of the quantum state of the scattering system (the sample), since it changes during the scattering process (for $\hbar\omega \neq 0$). The

initial and final sample states are denoted $|\lambda_\mathrm{i}\rangle$ and $|\lambda_\mathrm{f}\rangle$, respectively. The partial differential cross section for scattering from $|\lambda_\mathrm{i}, \mathbf{k}_\mathrm{i}\rangle$ to $|\lambda_\mathrm{f}, \mathbf{k}_\mathrm{f}\rangle$ is given in analogy with (2.43) by

$$\boxed{\left.\frac{d^2\sigma}{d\Omega dE_\mathrm{f}}\right|_{\lambda_\mathrm{i}\to\lambda_\mathrm{f}} = \frac{k_\mathrm{f}}{k_\mathrm{i}}\left(\frac{m_\mathrm{n}}{2\pi\hbar^2}\right)^2 \left|\left\langle\lambda_\mathrm{i}\psi_\mathrm{i}\middle|\hat{V}\middle|\psi_\mathrm{f}\lambda_\mathrm{f}\right\rangle\right|^2 \delta(E_{\lambda_\mathrm{i}} - E_{\lambda_\mathrm{f}} + \hbar\omega)}, \quad (2.49)$$

where the δ-function expresses explicit energy conservation and the normalization factor Y^2 is omitted.

This expression will be our starting point in the chapters on inelastic scattering from lattice vibrations and magnetic excitations.

2.4 Coherent and incoherent scattering

Very often, the neutron scattering length varies randomly from nucleus to nucleus in a sample. This can be caused by the variation of the nuclear spin direction with time, or by variations between isotopes of the same element - or between different elements. We here describe how this affects the scattering cross sections.

2.4.1 The coherent and incoherent cross sections

Variation in scattering length due to element or isotope disorder is a static effect, while nuclear spin variations are dynamic. However, for a macroscopic sample the calculations can be treated in the same way, since we can assume that 1) the sample is large enough to essentially represent an ensemble average and 2) we observe the system over times much longer than nuclear fluctuation times, meaning that the time average equals an ensemble average.

Let us for simplicity assume that the scattering length at site j has the stochastic value

$$b_j = \langle b_j\rangle + \delta b_j, \quad (2.50)$$

where $\langle b_j\rangle$ is shorthand for the average of b_j and δb_j is the local deviation from the average, $\langle\delta b_j\rangle = 0$. The deviations are assumed to be independent between sites, $\langle\delta b_j\, \delta b_{j'}\rangle = 0$. The mean differential scattering cross section is found from interference terms of the type seen in the two-atom problem.

$$\left\langle\frac{d\sigma}{d\Omega}\right\rangle = \left\langle\left|b_j \exp(i\mathbf{q}\cdot\mathbf{r}_j) + b_{j'}\exp(i\mathbf{q}\cdot\mathbf{r}_{j'})\right|^2\right\rangle, \quad (2.51)$$

where the average here means both time and ensemble average. Using (2.50), we now see that the "square terms" in (2.51) give $\langle b_j^2\rangle = \langle b_j\rangle^2 + \langle\delta b_j^2\rangle$, while the "interference terms" give $\langle b_j b_{j'}\rangle = \langle b_j\rangle\langle b_{j'}\rangle$. Identifying $\sigma_{\mathrm{inc},j}$ with $4\pi\langle(\delta b_j)^2\rangle$, we rewrite (2.51) to give

$$\left\langle\frac{d\sigma}{d\Omega}\right\rangle = \frac{\sigma_{\mathrm{inc},j} + \sigma_{\mathrm{inc},j'}}{4\pi} + \left|\langle b_j\rangle\exp(i\mathbf{q}\cdot\mathbf{r}_j) + \langle b_{j'}\rangle\exp(i\mathbf{q}\cdot\mathbf{r}_{j'})\right|^2. \quad (2.52)$$

Here we notice that σ_{inc} represents a constant scattering of neutrons, *i.e.* in all directions, without interference. Hence, σ_{inc} is called the *incoherent scattering cross section*. The average value $\langle b_j \rangle$ represents the strength of the interferent scattering and is denoted the *coherent scattering length*. In general, the coherent scattering depends on the scattering vector $\mathbf{q}$, and hence on the scattering angle. One defines *coherent scattering cross section* for a single nucleus j as $\sigma_{\text{coh,j}} = 4\pi\langle b_j \rangle^2$.

Usually, the explicit average notation $\langle b \rangle$ is dropped, and the symbol b almost exclusively means the average scattering length of a certain isotope or element. This is also the notation used in Table 2.1.

2.4.2 Incoherent nuclear scattering from randomness

There are several sources of the incoherent scattering, described in general terms above. One source is the spin-dependent term, which is described in detail in [1], and which is the one given by the isotope tables. Below, we will deal with incoherent scattering caused by variations in the scattering length due to isotopic mixture or chemical randomness. From the point of view of unpolarized neutron scattering, all these mechanisms are very similar, as described above. The values of the incoherent scattering cross sections for the elements, found in Table 2.1, deal with the combined effect from spin and isotopic mixture.

For a simple example of site randomness, assume that a material consists of two isotopes with the abundances $a_c = a$, and $a_d = 1 - a$, the scattering lengths b_c and b_d, respectively, and no nuclear spin. The average scattering length is

$$\langle b \rangle = ab_c + (1-a)b_d, \tag{2.53}$$

and the average incoherent cross section can be calculated by an average over the isotope abundances:

$$\begin{aligned} \frac{\sigma_{\text{inc}}}{4\pi} &= \langle (\delta b)^2 \rangle \\ &= a(b_c - \langle b \rangle)^2 + (1-a)(b_d - \langle b \rangle)^2 \\ &= a(1-a)(b_c - b_d)^2. \end{aligned} \tag{2.54}$$

This means that we see an incoherent scattering due to the isotope mixture, strongest at 50%-50% mixing ratio.

With a little effort, (2.54) can be generalized to more than two isotopes.

2.5 The total cross section for a system of particles

We have seen above that the total cross section can be written as a sum of the coherent and incoherent cross sections. In general, each of these cross sections can have an elastic and an inelastic part, giving rise to four terms:

$$\frac{d^2\sigma}{d\Omega dE_{\text{f}}} = \sum_j \left.\frac{d\sigma_j}{d\Omega}\right|_{\text{inc}} \delta(\hbar\omega) + \left.\frac{d\sigma}{d\Omega}\right|_{\text{coh}} \delta(\hbar\omega) + \sum_j \left.\frac{d^2\sigma_j}{d\Omega dE_{\text{f}}}\right|_{\text{inc}} + \left.\frac{d^2\sigma}{d\Omega dE_{\text{f}}}\right|_{\text{coh}}. \tag{2.55}$$

We will in the remainder of these notes concentrate upon the two coherent scattering processes, unless explicitly noticed.

Experimental considerations. The distinction between coherent and incoherent scattering is very important. In most types of experiment you will aim to minimize the incoherent cross section, which creates a uniform background, and maximize the coherent cross section, which generates the features you intend to study. A typical strong source of incoherent scattering is hydrogen, ^{1}H, where the incoherence is due to a strong spin dependence of the interaction between the neutron and the proton.

Inelastic incoherent scattering can, however, be used to study dynamic processes; mostly the motion of hydrogen. This type of scattering is not discussed further in this version of the notes.

2.5.1 Coherent elastic scattering from a system of nuclei

In chapters 5 and 7, we will discuss neutron diffraction from macromolecules and crystals, respectively. These topics essentially deal with interference between waves scattered from a large number of nuclei in the same way as we have seen for two nuclei above. For this purpose, equation (2.33) is easily generalized to several particles

$$\boxed{\left.\frac{d\sigma}{d\Omega}\right|_{\rm coh} = \left|\sum_j b_j \exp(i\mathbf{q}\cdot\mathbf{r}_j)\right|^2}. \tag{2.56}$$

This is a very important result, which is used in most types of neutron scattering.

Experimental considerations. In a scattering experiment, one will always measure the *scattering angle* with respect to the incoming beam, as illustrated in Fig. 2.2. The scattering angle is known as 2θ. In elastic scattering, $k_{\rm i} = k_{\rm f} \equiv k$, and we can see from the figure that

$$\boxed{q = 2k\sin(\theta)} \tag{2.57}$$

or the often presented alternative

$$\boxed{q = 4\pi\sin(\theta)/\lambda}. \tag{2.58}$$

2.5.2 * Quantum description of the cross section

We can also derive (2.56) from the quantum mechanical point of view, starting with (2.43).

$$\frac{d\sigma}{d\Omega} = \frac{k_{\rm f}}{k_{\rm i}}\left(\frac{m_{\rm n}}{2\pi\hbar^2}\right)^2 \left|\langle\psi_{\rm i}|\hat{V}|\psi_{\rm f}\rangle\right|^2. \tag{2.59}$$

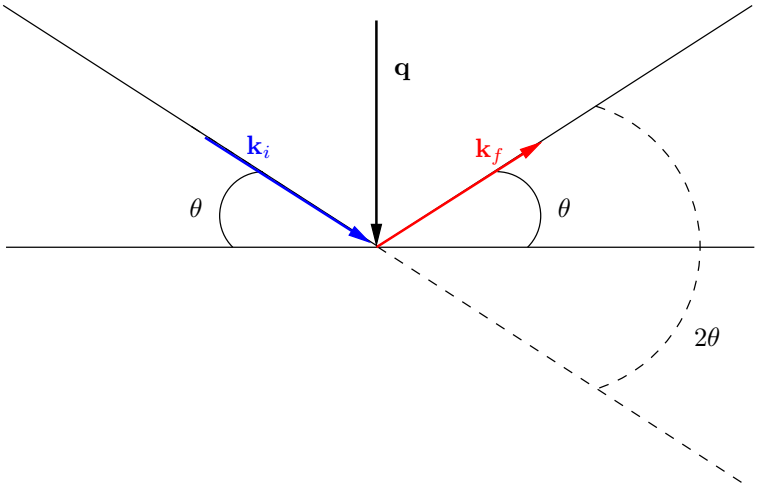

Figure 2.2: An illustration of the scattering process with the incoming and outgoing beam, the wave vectors, $\mathbf{k}_\mathrm{i}$ and $\mathbf{k}_\mathrm{f}$, and the scattering vector $\mathbf{q}$.

In analogy with (2.48), the scattering potential can be considered as the sum of the single nuclear potentials,

$$\hat{V} = \frac{2\pi\hbar^2}{m_\mathrm{n}} \sum_j b_j \delta(\mathbf{r} - \mathbf{r}_{j'}). \tag{2.60}$$

By insertion into (2.43), we arrive directly at (2.56).

2.6 Problems

2.6.1 The cross section

Imagine a beam of neutrons arriving randomly over a surface of area A perpendicular to the beam, with an arrival rate of N neutrons per second. In a semi-classical approximation, you can consider each neutron to be point shaped. Now, on the surface we place one nucleus with an effective radius of $2b$. Assume that each neutron hitting the nucleus is scattered and all other neutrons are left unscattered.

1. Calculate the neutron flux

2. Calculate the probability for one neutron to hit the nucleus

3. Show that the scattering cross section of the nucleus is $\sigma = 4\pi b^2$

2.6.2 Attenuation of the neutron beam

Consider a neutron beam penetrating a sample. For simplicity we can assume the sample to be shaped like a slab with the large area perpendicular to the neutron beam.

1. Derive the exponential decay of the beam inside the sample, (2.12).
2. Prove that when there is both absorption and scattering, the total attenuation coefficient is the sum of the individual coefficients.

2.6.3 Selection of materials for neutron scattering experiments

Most nuclei scatter neutrons incoherently, *i.e.* in random directions. Further, some nuclear isotopes are able to absorb neutrons by nuclear processes. We will now take a closer look at these properties for various materials.

1. Consider the incoherent scattering cross section σ_{inc} for the typical elements occuring in organic materials: H, C, N, O and P. Suggest a method to reduce the incoherent background from organic samples?
2. Some transition metals (Sc $\rightarrow$ Zn) display a strong incoherent scattering, and one of them is used as a standard incoherent scatterer (for calibration purposes). Suggest which one it is.
3. Sometimes other, more easily accessible, materials are used as incoherent scatterers instead. Suggest one.
4. Which metals may be used for neutron shielding? Calculate the penetration depth $1/\mu$ in these materials for neutron energies of 5 meV. Assume that the number density of atoms in the metals is $1/(16\ \text{Å}^3)$.
5. Also boron nitride, BN, ($V_0 = 11.81\ \text{Å}^3$) is used for shielding purposes. This material is used *e.g.* to make adjustable diaphragms (*slits*) to control the size of the neutron beam.

   Calculate the thickness of BN needed to reach an attenuation factor of 10^{-6} (that is, only a fraction of 10^{-6} of the neutrons in the beam are left in the beam at this thickness) for 5 meV neutrons. What will the attenuation then be for neutrons of 20 meV and 180 meV?
6. In a neutron scattering experiment, the sample surroundings must be "clean" in the sense of absorption and (incoherent) scattering. Which metal would you suggest for constructing cryostats for neutron experiments?

Part II

Neutron instrumentation

Chapter 3

Neutron sources and moderators

This chapter deals with the production and moderation of research-purpose neutrons. The instrumentation that extracts and utilizes neutrons from these sources are discussed in chap. 4.

3.1 Neutron sources

We here describe how neutrons are produced, and where large-scale neutron scattering facilities are located around the world.

3.1.1 Producing neutrons

Neutrons can be produced in a number of ways, e.g. as by-products of cosmic radiation or radioactive decay of heavy nuclei. One often used laboratory neutron source is Californium, ^{252}Cf, wich emits neutrons by spontaneous fission (on average around 3-4 neutrons per fission [18]). However, the ^{252}Cf half life time of only 2 years makes frequent source changes necessary. A more long lived laboratory source is the radium-beryllium source. Here, the radium decays spontaneously with a half life of 1600 years according to

$$^{226}\mathrm{Ra} \rightarrow {}^{222}\mathrm{Rn} + {}^{4}\alpha + Q, \tag{3.1}$$

with the heat release $Q = 4.871$ MeV. In the presence of berylium, a neutron is released according to

$$^{4}\alpha + {}^{9}\mathrm{Be} \rightarrow n + {}^{12}\mathrm{C}. \tag{3.2}$$

More recently, neutrons have been produced in a laboratory experiment, using a pyroelectric crystal [19] or a high electrical field [20] to accelerate ions of deuterium (the heavy hydrogen isotope ^{2}D) to high energies. This will produce

neutrons through the reaction

$$^2\mathrm{D} + {}^2\mathrm{D} \rightarrow {}^3\mathrm{He} + n + Q, \tag{3.3}$$

where Q is an excess energy of 3.27 MeV, of which around 2.5 MeV goes to the neutron.

As mentioned in chapter 1, and illustrated in figure 1.1, neutron sources created for the purpose of materials investigation by scattering are either based upon chain reaction in a nuclear reactor or upon accelerator-driven spallation processes.

In nuclear reactors, neutrons are produced in the fission process

$$^{235}\mathrm{U} + n \rightarrow \mathrm{D}_1 + \mathrm{D}_2 + 2\text{-}3\, n + Q, \tag{3.4}$$

where D represent a range of daughter nuclei and the released energy Q is of the order 200 MeV. ^{235}U fission typically yields 1.4 excess neutrons per nuclear process [21]. Research reactors with compact cores are used for neutron scattering purposes, rather than the more abundant nuclear power plants that have much larger cores. Reactor sources usually emits a continuous stream of neutrons, except for the remarkable pulsed reactor source in Dubna (RUS), where two large wheels drive the neutron reflectors in a way, so that criticality is reached only in short bursts.

A spallation source is driven by a proton accelerator, which emits protons with energies in the range 1-3 GeV. The protons collide with heavy, neutron-rich nuclei, which are destroyed in the process to many smaller fragments, releasing of the order 10-20 neutrons per proton. Spallation sources are typically pulsed, but can also be pseudo-continuous, as is the case at SINQ at the Paul Scherrer Institute, PSI (CH).

3.1.2 Neutron scattering facilities

A few dozens of research neutron sources exist over the world, most of these in Europe, North America, and Asia. During the last decade, the leading sources have been those of ILL (F) and ISIS (UK). Many reactor sources built in the 1960'ies have exceeded their lifetime and are now closed. Notable close-downs of research reactors have been seen (in chronological order) at Brookhaven (US), Risø (DK), Studsvik (S), Jülich (D), and Geestacht (D). Also the spallation source IPNS (US) was recently closed down, and the reactor in Berlin is schduled to close by 2020.

To compensate for this loss, and to bring progress to neutron scattering science, new advanced neutron sources are being built and commisioned. I will here mention the new reactors FRM-2 at Technical University of Munich (D), OPAL at ANSTO in Sydney (AUS), and CARR at CIAE (China). In addition, major upgrades are being performed at ILL.

Most important for the future are, however, the spallation sources. The second target station at the ISIS spallation source has almost doubled the number of instruments at this facility. Even more impressive are, however, the new

Figure 3.1: Aerial photo of the new American "Spallation Neutron Source", SNS. This is presently the world's most intense pulsed neutron facility.

powerful spallation sources SNS, Oak Ridge, Tennessee [22] (first neutrons April 2006; Figure 3.1) and J-PARC, Tokai, Japan [23] (first neutrons May 2008; re-opened December 2011 after earthquake/tsunami damage).

An even more ambitious project, the European Spallation Source (ESS) has been promoted over the last 20 years. In May 2009 it was decided to locate this source in Lund (S), and in July 2014 the construction work was initiated. An sketch of the ESS on the local site in Lund is given in Fig. 3.2.

The ESS project is backed up by 17 European countries, including Germany, UK, and France. According to the present plans, the first neutrons will be produced in late 2019 [9].

In Table 3.1, we list the most important present neutron sources. European sources not listed include the smaller reactors in Delft (NL), Budapest (H), Rez (CZ), and Kjeller (N). A continuously updated list of neutron sources worldwide is found at collaborative home pages [24, 25].

3.1.3 Access to neutron sources

Research centers for neutron scattering are typically nationally funded facilities; except ILL and ESS that are European. The most common way of utilizing these facilities are when research groups propose scientific projects to be performed at particular instruments on the facility. These proposals are then considered by an independent expert panel, which will advice the facility directors on the

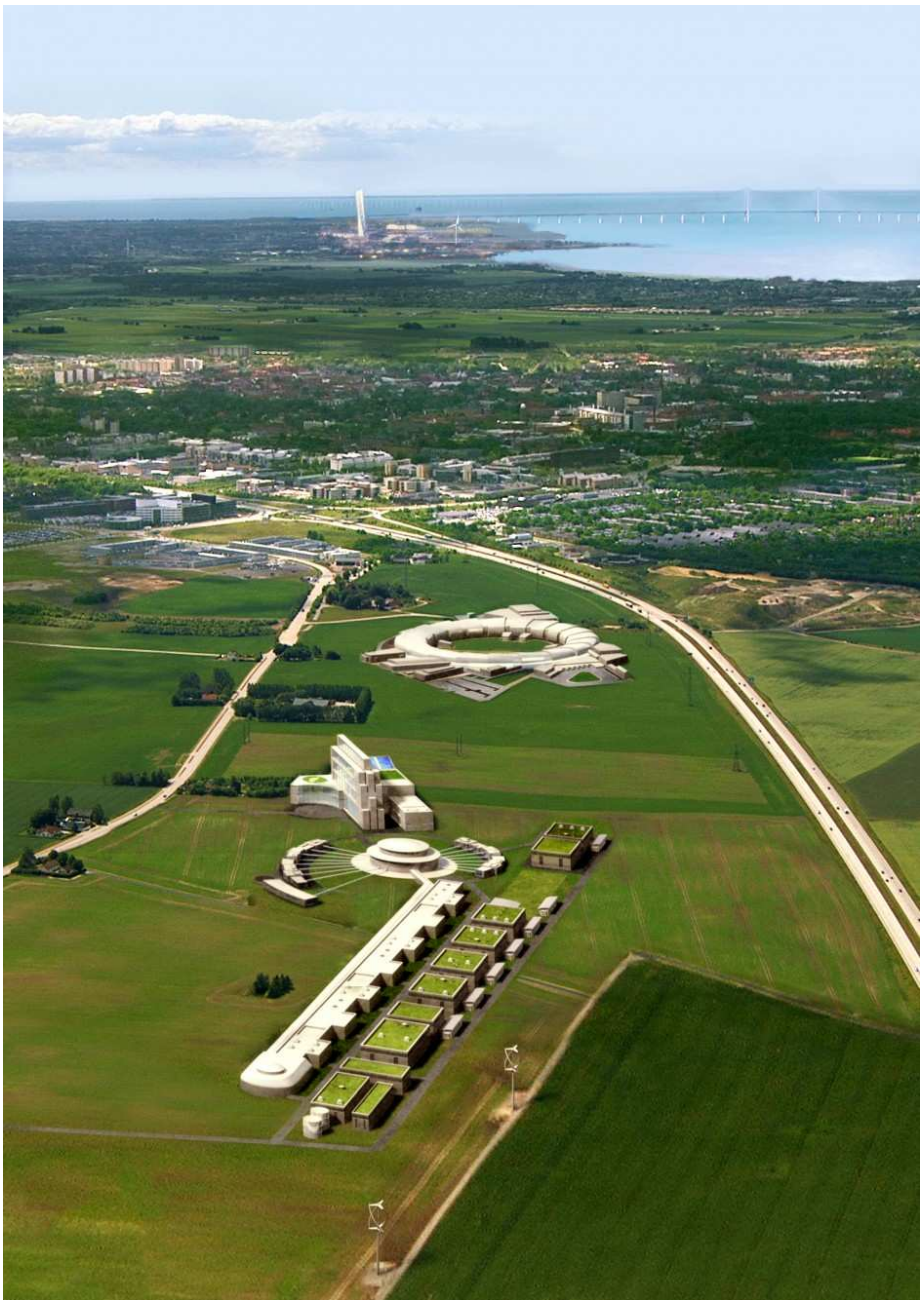

Figure 3.2: Aerial photo of the town of Lund, looking towards Malmö and the Öresund Bridge, superimposed with a sketch of the X-ray synchrotron ring MAX-4 (under construction; first beam in 2016) and the neutron source ESS (foreground), which is designed to become the world leading neutron facility.

Name	Location	Source type	Power	Start year	Instruments in user operation
ILL	Grenoble, France	R	58 MW	1971	45
ORPHEE, LLB	Paris, France	R	14 MW	1982	21
BER-II, HZB	Berlin, Germany	R	10 MW	1992	16
FRM-2, TUM	Munich, Germany	R	20 MW	2004	29
IBR-2	Dubna, Russia	PR			
SINQ, PSI	Villigen, Switzerland	CS	800 kW	1996	14
ISIS, RAL	Oxfordshire, UK	S	160 kW	1985	36
ESS	Lund, Sweden	S	5 MW	2019	$0 \rightarrow 16 \rightarrow 22$
NCNR, NIST	Gaithersburg, MD	R	20 MW	~ 1970	23
HFIR, ORNL	Oak Ridge, TN	R	85 MW	1966	11
NRU, AECL	Chalk River, Canada	R	125 MW	1957	7
LANSCE, LANL	Los Alamos, NM	S	160 kW	19??	11
SNS, ORNL	Oak Ridge, TN	S	1.4 MW	2006	$19 \rightarrow 22$
OPAL, ANSTO	Sydney, Australia	R	20 MW	2007	$11 \rightarrow 14$
JRR-3M, JAERI	Tokai, Japan	R	20 MW	1990	30(?)
Hanaru	South Corea	R	??	201?	?
MLF, J-PARC	Tokai, Japan	S	1 MW	2008	$18 \rightarrow 22$

Table 3.1: Characteristics of significant neutron sources worldwide, in operation or under construction. Reactor sources are marked by "R" and spallation sources by "S". The continuous spallation source at PSI is denoted "CS", and the pulsed reactor source in Dubna is denoted "PR". Data updated August 2012.

quality and scientific urgency of proposals, leading to a selection of successful proposals.

Most facilities have deadline for proposals twice per year, and access (or *beam time*) is often allocated 3-4 months after the deadline for the a half-year period starting 2-3 months later. Hence, the actual experiment is typically performed 6-12 months after the proposal submission. However, most facilities have other ways of allocating beam time for particularly urgent experiments.

3.2 Moderators

Neutrons produced in nuclear reactions typically have energies in the MeV regime. To be useful in materials research, the neutrons must have their energies reduced by many orders of magnitude. We here describe the basics of this problem.

For more information, a good introduction to neutron moderator physics is found in Ref. [26].

3.2.1 The moderation process

The neutron moderation is performed by a large number of successive collisions with a material that scatters strongly, but absorbs weakly. Here, hydrogen (H)

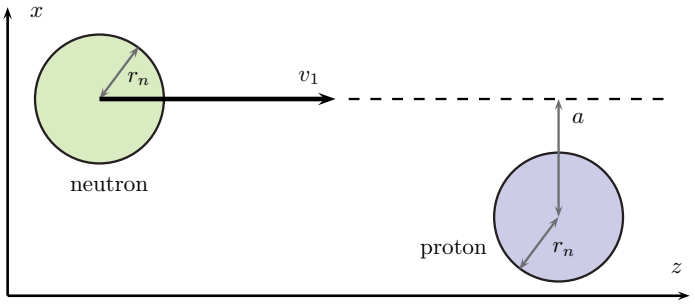

Figure 3.3: Sketch of the neutron-proton moderation process in a classical picture. A neutron moving with the velocity v_1 is about to collide with a proton at rest with an impact parameter (smallest distance from neutron trajectory to proton center) of a. Both particles have a radius of r_n.

is an almost perfect choice, also since its nuclear mass is similar to that of the neutron. This enables the H nucleus to absorb a large fraction of the neutron energy in each collision.

To show this, in a classical mechanics description, let us for simplicity consider the neutron and the protons as spherical particles with identical mass, m_n, and with identical radii, r_n. In the collision, we consider the proton to be at rest, and the neutron to move with the velocity v_1 along the z-axis, and hence with a kinetic energy of $E_1 = m_\mathrm{n} v_1^2/2$. The closest distance from the neutron trajectory to the proton center is denoted the *impact parameter*, a, as seen in Fig. 3.3. We consider the neutron to have a random trajectory, hence the probability for having a particular impact parameter, a, is proportional to a. If $a < 2r_\mathrm{n}$, a collision takes place.

We now define the (x, z) plane to contain both the proton position and the neutron trajectory. After a scattering, the proton will remain in the plane, moving with the velocity $\mathbf{v}_{2,p}$. The proton trajectory makes an angle to the z-axis of

$$\sin\phi = \frac{a}{2r_\mathrm{n}}. \tag{3.5}$$

We denote the neutron velocity after the scattering by $\mathbf{v}_{2,n}$.

Now, energy conservation and momentum conservation in the (x, z) plane gives three equations

$$m_\mathrm{n} v_1^2 = m_\mathrm{n}(v_{2,p}^2 + v_{2,n}^2) \tag{3.6}$$

$$m_\mathrm{n} v_1 = m_\mathrm{n}(v_{2,p}^z + v_{2,n}^z) \tag{3.7}$$

$$0 = m_\mathrm{n}(v_{2,p}^x + v_{2,n}^x) \tag{3.8}$$

and (3.5) give the fourth equation to determine the four unknowns parameters of $\mathbf{v}_{2,n}$ and $\mathbf{v}_{2,p}$. The solution for the velocity of the proton after the collision is

$$v_{2,p} = v_1 \cos\phi. \tag{3.9}$$

Considering that the probability of reaching an impact parameter of a is proportional to a up to a value of $2r_{\mathrm{n}}$, one can calculate the average energy taken up by the proton in the collision. The result is

$$E_{2,p} = \frac{E_1}{2}. \tag{3.10}$$

The proof of this is left to the reader, and is posed as problem 3.3.1.

A more detailed model will also provide the result that the neutron loses on average half of its energy per collision. Slowing the neutron energy by (a typical value) 8 orders of magnitude, thus takes "only" 25-30 collisions. This is clearly within practical limits, since the typical mean free path in a hydrogen-rich material is of the order a few mm.

When the neutron energy becomes comparable to the (thermal) energy of the protons, the approximation of zero proton velocity breaks down, and a much more complex description is necessary, including the thermal motion of the proton and its surroundings. The effect is, nevertheless, that the neutrons quickly reach thermal equilibrium with the surrounding material.

3.2.2 Energy distribution of moderated neutrons

Most moderators consist of a tank with liquid water (H_2O; 300 K), which will slow down neutrons to roughly thermal equilibrium. When neutrons of lower energies are required, moderators of liquid hydrogen (H_2; 30 K) or solid methane (CH_4; 100 K) are used in connection with water pre-moderators. At ILL, there is even a hot moderator consisting of graphite at 2000 K. We will here discuss the implications of the moderator temperature.

Neutrons moderated at a temperature, T, will ideally have a distribution of velocities, v, given by the Maxwellian distribution of velocities, which is proportional to v^2 times the Boltzmann factor $\exp(-E_{\mathrm{kin}}/k_{\mathrm{B}}T)$. Since neutron emission through a (imaginary) hole at the moderator surface is essentially an effusion process, the flux of neutrons from a beam port can be written as:

$$I(v) = I_0 v^3 \exp\left(-\frac{m_{\mathrm{n}} v^2}{2k_{\mathrm{B}}T}\right), \tag{3.11}$$

where I_0 is a constant proportional to the source power, k_{B} is Bolzmann's constant, and the extra power of v comes from the effusion (faster particles have higher probability per time of leaving through the hole). The velocity distribution (3.11) peaks at $v_{\max} = \sqrt{3k_{\mathrm{B}}T/m_{\mathrm{n}}}$, corresponding to an energy of $3k_{\mathrm{B}}T/2$.

It is customary to define the *equivalent temperature* of neutrons with a certain energy. The relation is given by

$$E = \frac{m_{\mathrm{n}} v^2}{2} = k_{\mathrm{B}} T_{\mathrm{equiv}}. \tag{3.12}$$

Describing the Maxwellian distribution (3.11) in terms of wavelength requires some care. Since $v = 2\pi\hbar/(m_{\mathrm{n}}\lambda)$, we have $dv = -2\pi\hbar d\lambda/(m_{\mathrm{n}}\lambda^2)$. Hence, the

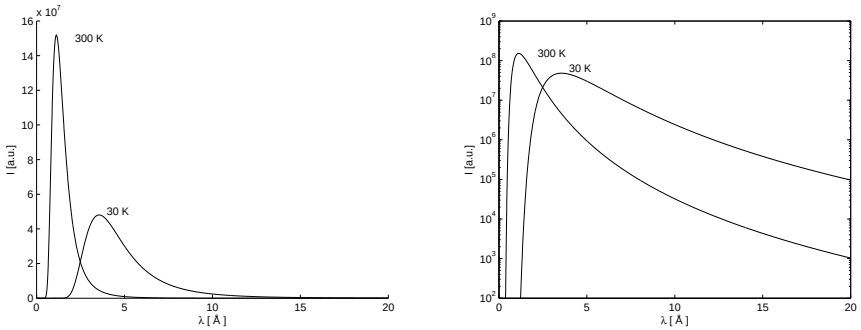

Figure 3.4: Maxwellian wavelength distributions corresponding to typical cold (30 K) and thermal (300 K) sources. Left figure shows a plot with linear axis and right panel shows the intensities on a logarithmic scale to emphasize the behaviour at long wavelengths.

wavelength and velocity axes do not scale linearly, and a transformation of the distribution must be applied:

$$I(\lambda) \equiv \frac{dN}{d\lambda} = \frac{dN}{dv}\left|\frac{dv}{d\lambda}\right| = I_0'\lambda^{-5}\exp\left(-\frac{2\pi^2\hbar^2}{\lambda^2 m_\mathrm{n} k_\mathrm{B} T}\right), \tag{3.13}$$

where $I_0' \propto I_0$ and N is the total number of neutrons. This distribution peaks at $\lambda = 2\pi\hbar\sqrt{3/(5m_\mathrm{n}k_\mathrm{B}T)}$, corresponding to $E = 5k_\mathrm{B}T/3$. The energy equivalent of the peak value is thus changed by 10% between the two representations of the Maxwellian distribution due to the non-linear transformation, even though the two equations describe the same neutrons. Neutron moderator spectra are typically expressed in terms of the wavelength distribution, as illustrated in Fig. 3.4.

3.2.3 Moderator brilliance and the Liouville theorem

Since neutron scattering is mostly an intensity limited technique, an important quantity for a neutron source (a moderator) is the produced number of neutrons per unit of time. However, an even more useful number is the moderator *brilliance*, B, which describes the produced number of neutrons per unit of time, per moderator area, per solid angle of flight direction, per wavelength interval. For example, a compact reactor core will have a higher brilliance than a less dense one, even though the total neutron production may be equal. In reality, the brilliance (or peak brilliance for pulsed sources) is almost the only relevant value for a neutron source. Brilliance is useful also at other positions in the neutron instrument, typically at the sample position, and has the same definition as above. B in general depends upon the position of the moderator, the time (for pulsed sources), and the direction and wavelength of the emitted neutrons

$$B = B(t, \mathbf{r}, \hat{\mathbf{v}}, \lambda). \tag{3.14}$$

In terms of statistical mechanics, the brilliance is closely connected with *phase space density*, $\phi(\mathbf{r}, \mathbf{v})$. This can be seen from the observation that λ can be written in terms of v, and the position perpendicular to the main beam direction is given as $z = vt$.

For an ensemble of particles undergoing only passive processes, the very powerful *Liouville theorem* is valid. It states that the phase space density cannot increase [27]. In the context of a neutron scattering instrument, this means that the brilliance at the neutron beam can under no circumstances be larger than that of the (brightest spot at the) moderator [28]. As a relevant example of this, focusing mirrors or lenses are somtimes used to bring more neutrons on to a small sample. According to the Liouville theorem, however, the increase in number of neutrons will come from an increase in the spread of their velocity directions (their *divergence*).

3.2.4 Real moderators

To improve transmission, real moderators have a limited thickness and hence do not moderate the neutrons completely. Their velocity distribution should rather be described by the sum of two or more Maxwellians, possibly with the addition of a tail towards high energies/low wavelengths, describing neutrons that are scattered only few times in the moderator. This is illustrated for the SINQ source at PSI in Fig. 3.5. To avoid completely unmoderated neutrons from the source, the moderator geometry is chosen so that there is no line-of-sight between the place of neutron production and the *beam port* that opens out to the neutron scattering instruments.

Recent developments have shown that inhomogeneities in the moderator geometry, like holes and grooves, can locally enhance the neutron brilliance by up to a factor two, since these will generate a direct view to the moderator center, where the neutron density is larger [29]. However, design and detailed understanding of moderator systems is complex and is performed with the use of heavy nuclear physics simulations using codes like MCNPX and GEANT-4 [30, 31]. A description of this is beyond the scope of these notes. In the following, we will be satisfied with the existence of thermal and cold neutrons sources, and we will concentrate on the utilization of moderated neutrons.

3.3 Problems in sources and moderators

3.3.1 Hydrogen as a moderator

Show that the energy of a neutron is on average halved by collision with a proton; *c.f.* (3.10).

3.3.2 The moderator temperature

In typical sources for neutron scattering purposes, the neutrons are moderated by water. These “thermal” neutrons will (almost) reach thermal equilibrium

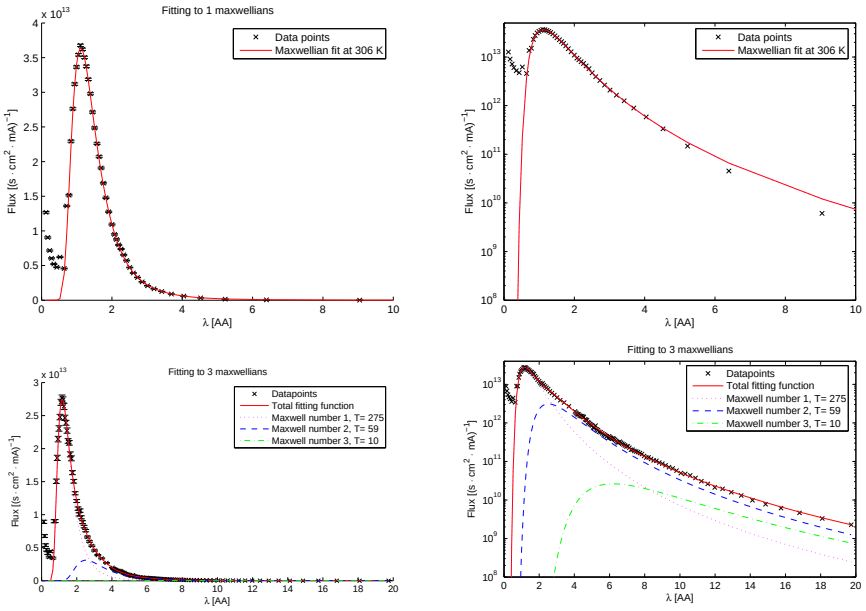

Figure 3.5: Wavelength distributions for SINQ, PSI. Top row shows the measured thermal spectrum (crosses) with a fit to a single Maxwellian at 306 K (red solid line). Bottom row shows similar plots for the cold spectrum, with a fit to the sum of three Maxwellians. Both fits have problems for wavelengths below 0.8 Å, where undermoderated (hot and epithermal) neutrons are observed. Left column shows the data on a linear scale, while the right row uses a logarithmic intensity scale.

with the moderator.

1. Calculate the equivalent energy, E, and velocity, v, of a thermal neutron, moderated by water at $T_{\mathrm{H_2O}} = 300$ K. Calculate the corresponding de Broglie wavelength, λ, and wavenumber, k.

2. Perform the same calculations for neutrons thermalised by liquid H_2 at $T_H = 30$ K.

3. For each of the two types of moderators above, calculate the ratio of intensities: $I(4\ \text{Å})/I(20\ \text{Å})$.

4. Many neutron instruments utilize a band of incident wavelength, $\Delta\lambda$. For many instruments, $\Delta\lambda/\lambda$ is almost constant and is of the order 0.1%-10%, depending on instrument type. For instruments with these bandwidths, calculate the ratio of the neutron fluxes at the sample: $\Psi(4\ \text{Å})/\Psi(20\ \text{Å})$.

3.3.3 The beam port

Consider a moderator of a typical useful size of 150×150 mm^2. The moderator emits neutrons isotropically and uniformly over its surface. A beam port of size

50×50 mm^2 is placed 4 m from the moderator face.

Consider a small area dA centered at the moderator-beam port axis; downstream from the beam port. Calculate how the neutron flux through dA varies with distance, L, from the moderator.

The divergence, η, of a neutron is defined as the angular deviation of the neutron velocity to the "main" axis. Calculate the maximal divergence as a function of L for the case described above.

Hints: The variation in distance between any point of the moderator and any point of the beam port can safely be ignored. Gravity can be neglected.

Chapter 4

Instrumentation

Neutron scattering instruments are built in many different designs, reflecting that they are specialized for vastly different research purposes. Some instruments deal with the study of the crystal structure of materials, others with excitations in materials, others again with the structure of biomolecular aggregates, with properties of thin films, and so forth.

In this chapter, we will describe the neutron-optical hardware and tricks needed to transport the "useful" part of the produced neutron phase space from the moderator to the sample of material we like to investigate. In addition, we will describe the assembly of this hardware to form a selection of neutron instruments, each of which is connected to one or more scientific chapters in the later parts of this text.

Many of these devices utilize the principles of neutron reflection and refraction, which are close to the concepts of classical optics. The theory behind is sketched where needed and explained more carefully in chapter 6.

Instruments using neutron polarization will not be described here, but will appear in a separate chapter in a forthcoming chapter of these notes. Monte Carlo ray-tracing simulations of neutrons and neutron instrumentation is discussed at the end of these notes, in chap. 14.

4.1 Neutron guide systems

The earliest neutron scattering instruments used a beam of neutrons, extracted from the moderator through holes (or tunnels) in the shielding; also called a *beam port*. The neutron intensity from this type of beam port falls off in general as $1/r^2$; for details: see problem 3.3.3. This square law dependence dictates that neutron instruments of this type are placed close to the neutron source. Therefore they will suffer from a relatively high background from the source, *e.g.* from gamma-radiation, and from epithermal and fast neutrons.

In the early 1960'ies, a new concept was invented: The neutron guide. This is a neutron conducting channel, in principle equivalent to an optical fiber. The

guide can extract a beam of neutrons from the moderator and deliver it at another point, further away from the neutron source [32]. Guides are being used on most cold-neutron and many thermal-neutron instruments. Typical guide lengths are 10-100 m.

We will here take a closer look into neutron guide systems.

4.1.1 Guide reflectivity

The neutron guide builds on the principle that surfaces of materials with positive values of b show total reflection of thermal and cold neutrons under sufficiently small angles. At larger angles, the reflectivity falls off to zero very fast.

We define the *critical angle*, $\theta_c(\lambda)$, as the largest angle between the neutron path and the surface that still gives rise to total reflection. For a given material, the critical angle is proportional to the neutron wavelength. Following (2.57) and Fig. 2.2, the critical scattering vector is now given by

$$Q_c = 2k\sin(\theta_c(\lambda)) \approx 4\pi\frac{\theta_c(\lambda)}{\lambda}, \tag{4.1}$$

when θ_c is given in radians. In general, Q_c is independent of λ. For the standard guide material, Ni, the critical scattering vector is

$$Q_{c,Ni} = 0.0217\text{Å}^{-1}. \tag{4.2}$$

For neutrons of 1 Å and 10 Å wavelengths, the critical angles from Ni become $\theta_c = 0.10°$ and $1.00°$, respectively. This should be compared with the divergence requirements from present instruments, which is often in the same range: $0.1°$ to $1.0°$. Hence, neutron optics for 10 Å neutrons is a fairly easy task, while shorter wavelengths present increasingly larger challenges.

Modern guides are made from multilayer material, usually with Ni as the outmost layer. This ensures total reflectivity up to $Q_{c,Ni}$. In addition, the reflectivity is non-zero up to a much higher scattering vector [33]

$$Q_c = mQ_{c,Ni}. \tag{4.3}$$

One therefore often speaks about the m-value of a multilayer, *e.g.* an $m = 3$ guide. An example of a reflectivity profile for an $m = 3.6$ guide is shown in Fig. 4.1 (right). Typical values of m are 2-4, although mirrors with up to $m = 7$ can now be obtained. Multilayer guides can be purchased commercially, typically in pieces of 0.5 m length and cross sections of up to 300×300 mm^2.[34]

4.1.2 Straight guides

The "classical" and most often used guide system is the straight guide, where the guide cross section is constant along the full length of the guide. Typical sizes of cross sections from 20×20 mm^2 to 120×30 mm^2. Assuming the guide

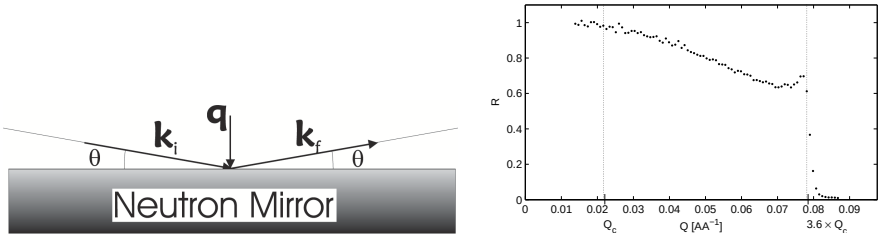

Figure 4.1: Left: The geometry of a neutron reflecting off the surface of a guide, also known as a *neutron mirror*. Right: Measured reflectivity profile for a $m = 3.6$ multilayer guide.

to be sufficiently long, the maximum divergence being transported through the guide is

$$\eta_x = 0.1^\circ \frac{m\lambda}{[\text{Å}]}, \tag{4.4}$$

and the same for the y-direction. However, the effect of the supermirror decreases for large divergences (larger than θ_c), since neutrons will typically experience many reflections, and thus be attenuated by the reflectivity value to a high power.

In addition, we notice that the maximal volume of the available phase space in the guide is proportional to $m^2\lambda^2$. This explains why, until recently, guides were primarily used for cold neutrons and thermal instruments were most often placed at a beam port close to the moderator.

4.1.3 Curved guides

In practice, many constant-cross-section guides have sections which are slightly curved horizontally, with radii of the order $R \approx 0.5 - 3$ km, while keeping the guide cross section constant. This is done in order to avoid direct line-of-sight from the moderator to the experiment, strongly reducing the number of hot and epithermal neutrons passing down the guide, which in turn minimizes the experimental background.

For an example of this *guide cut-off*, imagine a neutron which bounces alternatingly off the left and right walls of a guide with width w. The guide curves to the left with the radius of curvature R_c. We consider the limiting case, where the neutron just glances off the left wall, $2\theta = 0$. Due to the curvature, the neutron will hit the right wall at an angle $\theta = \sqrt{2w/R}$, corresponding to a scattering vector of $q = (4\pi/\lambda)\sqrt{2w/R}$. To scatter the neutron, we need $q \leq mQ_{c,\text{Ni}}$. This leads to a condition for the scattered neutrons

$$\lambda \geq \frac{4\pi}{mQ_{c,\text{Ni}}}\sqrt{\frac{2w}{R}}. \tag{4.5}$$

Using the typical values for a cold-neutron guide: $m = 2$, $w = 30$ mm, and

$R = 2400$ m, we reach a lower cut-off for the transmitted neutrons: $\lambda \geq 1.435$ Å. However, this is not the whole truth. Neutron paths exist, where the neutrons repeatedly scatter off the outer (in this case the right) wall only. The phase space of these so-called *garland reflection* trajectories is, however, much smaller than of the regular left-right trajectories [35].

One way to overcome the garland reflections is to bend the guide first in one direction, then in the opposite. In this so-called S-shaped guide, the shortest wavelengths are completely eliminated.

4.1.4 Tapering guides

To increase the intensity of neutrons onto small samples, some more recently built guide systems have been equipped with focusing "noses", which are often a linear (or curving) tapering piece of high-m supermirror guide that narrows the beam just before the sample [**?**]. A well-designed nose will increase the number of neutrons hitting the sample, but according to the Liouville theorem, this comes at the expense of an increased beam divergence. In addition, the divergence profile from a tapering nose is often non-uniform, due to the difference in divergence between neutrons hitting the nose piece zero, one, or more times, respectively.

A full guide set-up using tapering guides is often known as a *ballistic guide* system. The guide starts with a linearly expanding section, followed by a straight (possibly curved) section, to end with a tapering converging nose. This guide system has the advantage that the expanding section decreases the divergence of the transmitted beam (at the cost of a decreased spatial density, according to Liouville). The lower divergence decreases the number of reflections and hence improves the guide transmission. At the nose piece, the neutron density again increases, with a corresponding increase of divergence [36].

4.1.5 Parabolic and elliptical guides

The parabolic guide system is an improved version of the ballistic guide. It consists of a parabolic expanding start, which ideally (for a point source) would make the beam completely parallel. Then follows a straight (possibly curved) section, and ends with a parabolic nose, which compresses the beam onto the sample [37, 38]. For practical reasons, the guide is often parabolic in the x and y directions separately, so that the cross section of the guide is at any place rectangular.

The elliptical guide system consists of one fully elliptical piece with the moderator close to one focal point and the sample close to the other focal point. Ideally (for a point source), each neutron would then be reflected only once between moderator and sample, although recent work has shown that a finite size of the source would result in more than one reflection [39]. How simple it may sound, elliptical guides are only just being installed at the first instruments, with very good results, *e.g.* at the cold-neutron diffractometer WISH at ISIS

[40]. In practice, also here, the guide cross section is rectangular, so that a general neutron would need a reflection both in the x and the y-direction.

Recent simulation work has shown that parabolic and elliptical guides have almost equal neutron transport properties over large distances (50 m and above), and that they outperform any other guide systems with transmissions of the phase space density close to the Liouville limit. However, there is yet no detailed experimental evidence for this result [36].

4.1.6 Shielding and shutters

To avoid neutron background outside the guide, a neutron absorbing material is being used to shield its outside. In addition, the gamma radiation produced by the neutron capture is shielded, using (typically) lead, steel, or concrete.

For safety reasons, the neutron beam can be blocked close to the guide entry by a *primary beam shutter*, which will be closed during long-term maintanance. The *secondary beam shutter* is placed at the guide end, close before the sample, and will be used for minor experimental interruptions, like change of sample. These shutters are made by a combination of materials that absorb both neutrons and gamma radiation.

4.2 Beam optical components

We here present components that shape the neutron beam, typically between the moderator and the sample, but sometimes also between sample and detector.

4.2.1 Slits

A slit, also known as a *diaphragm*, consists of a neutron-absorbing plate with a hole (rectangular or circular) for passage, as seen in Fig. 4.2. The slit limits the spatial size of the beam and is in particular used just before the sample, to eliminate neutrons that would not hit the sample. These unuseful neutrons would in practice scatter off the sample environment to generate both overall background and false signals, sometimes known as *spurions*.

4.2.2 Collimators

A horizontal *Soller collimator* consists of a number of thin, parallel, equidistant sheets (like every n'th page in a book) of a neutron absorbing material; see Fig. 4.2. Hence, neutrons with "wrong" divergence are eliminated. The degree of collimation is presented as the FWHM of the transmission curve, understood as a plot of neutron intensity vs. angle between the collimator axis and the direction of a very well collimated beam. Usually, the collimation is in the range 10' to 120', where 60' (arc minutes) equals 1°. The degree of collimation is fixed, so a different collimator piece must be inserted in the beam to change the degree of collimation. The geometry of a Soller collimator is calculated in problem 4.10.2.

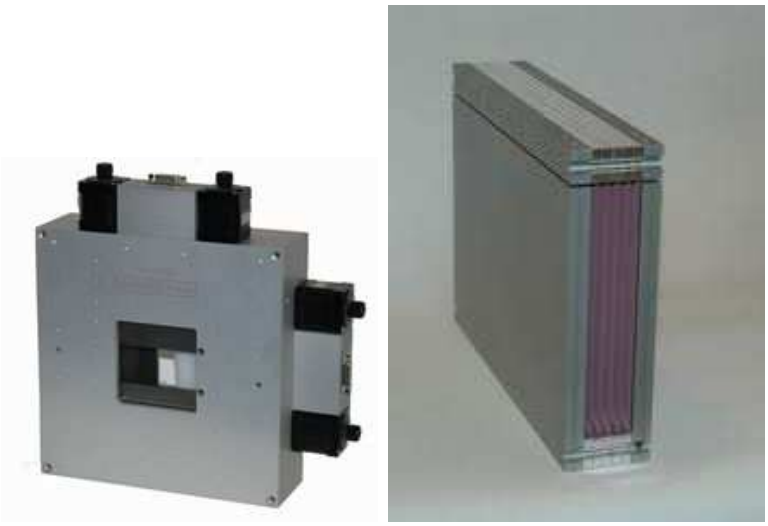

Figure 4.2: (left) Photograph of a typical square neutron slit. (right) Photograph of a narrow Soller collimator. Both pictures are from the vendor JJ-Xray ApS [41].

The divergence of the neutron beam can also be reduced by two slits, placed a distance apart. Often, this will be a pair of pinholes, hence you speak about *pinhole collimation*. Alternatively, collimation can be performed in one direction only by a pair of rectangular slits, which are narrow in one direction. Often, one can control the pinhole diameter and distance, known as the *collimation length*, L_c, by inserting different pinholes at a number of fixed positions. The smallest practical collimation length is typically 1 m, while the longest can be up to 20 m, depending on the particular instrument.

4.2.3 Choppers

A chopper is a spinning device that alternately allows or blocks passage of neutrons.

The most simple chopper design is the *disk chopper*, which is basically a wheel covered by neutron absorbing materials, with slits cut to allow neutron passage at selected times. Disk choppers are being used for slow and medium time-scale events, down to 10-20 μs opening times. The fastest opening times, however, will require very narrow slits, and probably a combination of two closely spaced counter-rotating choppers. A typical disk chopper is shown in Fig. 4.3.

Another type of chopper is the *Fermi chopper*, also shown in Fig. 4.3. Here, a rotating collimator-like system ensures that neutrons are passing in short bursts only. Fermi choppers are typically used when very short opening times are required over a wide beam path.

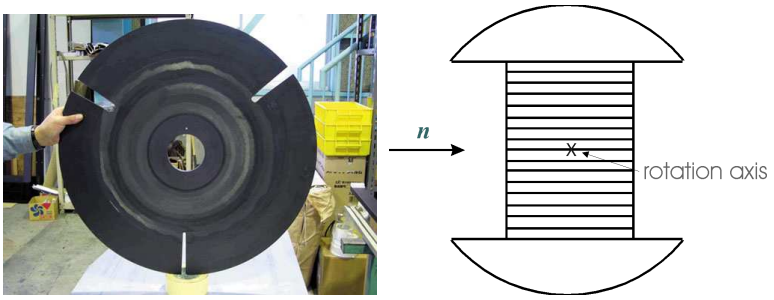

Figure 4.3: (left) Photograph of a disk chopper from the cold-neutron spectrometer at J-PARC, Tokai. The chopper has a radius of $r = 0.35$ m and spins up to $f_{\max} = 350$ Hz. The neutrons are imagined to travel directly from the point of the viewer. (right) sketch of a Fermi chopper, seen from above.

4.3 Neutron detectors

We will here briefly touch upon the way neutrons are detected. The field of neutron detectors is vast and for more information we refer the reader to specialized literature, see *e.g.* ref. [42].

4.3.1 Detection processes

Neutrons are typically detected by use of one of a handful of nuclear reactions, each destroying the neutron as a result. Most used and most efficient is neutron capture of helium-3:

$$^3\mathrm{He} + n \rightarrow {}^3\mathrm{H} + {}^1\mathrm{H} + Q, \tag{4.6}$$

where the released energy, Q, here is as low as 0.764 MeV [42]. However, also capture of ^{6}Li and ^{10}B is often being used.

The charged products from these nuclear reactions give rise to an electrical signal, which is subsequently amplified by charge amplification in an Ar gas under high voltage (a few kV), as in a standard Geiger-Müller counter. The signal can then easily be detected.

Detectors may have just a single channel, or can be position sensitive in one or two dimensions. For particular applications, there exists area detectors with pixel sizes of around 1×1 mm^2 of sizes up to 1×1 m^2. Alternatively, one may use detector tubes with a diameter of the order 25 mm (one inch), being several meters long and linearly sensitive with a positioning accuracy of the order 5 mm.

At pulsed neutron sources, the detector electronics can in addition record the detection time of the neutron with a precision of a few μs. This is crucial in order to utilize the time-of-flight information, as will be described later.

4.3.2 Monitors

For controlling the possibly varying intensities of the beam, *monitors* are used at all neutron instruments for normalization purposes. A monitor is a deliberately

inefficient detector that interacts with only a small fraction of the neutron beam (of the order 10^{-3} to 10^{-4}). The counting efficiency is determined by the neutron absorption cross section and is hence proportional to λ. Monitors are typically placed at the end of a guide, just before the sample.

4.3.3 Background and background levels

Background is the general notion for all neutron detector counts that do not arise from the physical process under investigation.

One source of background comes from the sample itself, *e.g.* incoherent scattering, and is difficult to discriminate against.

Another background source is the experimental environment, *e.g.* neutrons from other experiments or fast neutrons from the source, that penetrate a series of shieldings to be counted in the detector. This background can always be improved by shielding, by moving the instrument far away from the source, and by eliminating line-of-sight between moderator and sample. Fast-neutron background is of particularly worry in spallation sources, due to the high energies in the spallation process itself.

At the end of a 30-100 m guide, the background count rates for a typical ^{3}He detector tube, 150 mm high, 25 mm diameter, at a medium-size source like PSI, is about 0.1 counts/minute with both the primary and secondary beam shutters closed [43]. This background is mostly due to electronic noise. During an experiment (both shutters open), the level of background not originating from the sample is 0.2 counts/minute in the best cases.

At pulsed sources, the fast-neutron background can in some cases dominate the elastical scattering from the sample. However, time-of-flight can be used to discriminate these fast neutrons.

4.4 Determining the incoming neutron wavelength

The famous Bragg law gives the relation between the wavelength, λ, of radiation diffracting off a crystal with lattice spacing d, and the scattering angle, 2θ:

$$n\lambda = 2d\sin(\theta), \tag{4.7}$$

as presented in equation (7.27) – and derived thoroughly in the adjacent text. According to the Bragg law, in order to interpret the neutron signal at a particular angle, 2θ (meaning determine the lattice spacing, d), it is necessary to know the neutron wavelength, λ. This is in practice done in two different ways: At continuous sources, the neutron beam is in general monochromatized, while at pulsed sources time-of-flight techniques are used to determine λ. We will here look in more detail on these two rather different methods.

4.4.1 Monochromating a continuous neutron beam

One method of monochromating a continuous neutron beam is to use a rotating velocity selector as presented in the SANS instrument, section 4.5.1. However,

this method only provides a crude degree of monochromaticity, of the order $\delta\lambda/\lambda \approx 10\%$. To obtain a better resolution one uses another method: Bragg reflection from a crystal.

Consider again the Bragg law (4.7), and imagine that now the lattice spacing, d, of the crystal is well known. In addition, the incident neutrons have a well-defined direction, but are polychromatic (a so-called *white beam*). In this case, only neutrons of certain wavelengths are scattered:

$$\lambda = \frac{1}{n} 2d \sin(\theta_{\mathrm{m}}). \tag{4.8}$$

A crystal used in this way is called a *monochromator*, represented by the subscript "m" on the scattering angle $2\theta_{\mathrm{m}}$. The monochromator reflects a series of wavelengths, given by the integer, n. The *first order* wavelength ($n = 1$) is usually the desired one, while the *higher order* wavelengths are undesired. Typically, one will try to suppress the higher order neutrons by transmission filters and/or by guide geometries which provide low transmission for shorter wavelength neutrons.

An order-of-magnitude estimate of the monochromaticity of the diffracted beam is given by considering the uncertainty in the scattering angle, $\delta\theta$, which is mostly determined by the experimental geometry, guides, and possible collimators. The uncertainty in the lattice spacing is in many cases negligible, leading to

$$\delta\lambda = \frac{1}{n} 2d \cos(\theta_{\mathrm{m}}) \delta\theta, \tag{4.9}$$

when θ is calculated in radians. One often considers the relative precision of the wavelength determination:

$$\frac{\delta\lambda}{\lambda} = \cot(\theta_{\mathrm{m}}) \delta\theta. \tag{4.10}$$

For 90° scattering ($\theta = 45°$) and a typical divergence value $\delta\theta = 0.5°$, we reach $\delta\lambda/\lambda \approx 1\%$.

Monochromators for thermal neutrons are often made from single crystals of Si, Ge, or Cu. For cold neutrons, pyrolytic graphite (PG) is the material of choice.

As with most other large single crystals, monochromator materials often consists of many crystallites, which have a small, random misalignment with respect to a "common" direction. This *mosaicity* is often close to being Gaussian (*i.e.* a normal distribution) and affects the monochromatizing properties of the material strongly. A small mosaicity (10'-20') reflects a smaller amount of the incoming neutrons than larger mosaicities (30'-60'). On the other hand, a small mosaicity is beneficial if one requires a good resolution, *i.e.* a narrow wavelength distribution of the beam.

Reflectivities of monochromators in Bragg condition depends both on the chosen material and on the neutron wavelength. Typical values range from 20% to 80%; the latter value achieved by PG with neutrons of $\lambda > 4$ Å [44].

4.4.2 Time-of-flight analysis

A completely different method of determining the neutron wavelength is by measuring the speed of the particle by time-of-flight analysis. Typical moderators at pulsed sources emit bursts of neutrons lasting $\tau = 10 - 100$ μs separated by intervals of $T \approx 20 - 100$ ms. The neutron start time at the moderator is thus very well defined. The neutron flight time from the moderator to the detector placed a distance, L, from the moderator is

$$\boxed{t = \frac{L}{v} = \frac{m_{\mathrm{N}}}{2\pi\hbar} L\lambda = \alpha\, L\, \lambda}, \tag{4.11}$$

where $\alpha = m_{\mathrm{n}}/h = 252.7\,\mu$ s/m/Å. The neutron wavelength can thus be determined directly from its time-of-flight. The uncertainty in the wavelength is in practice given by the pulse width τ through

$$\alpha L \delta\lambda \approx dt = \tau, \tag{4.12}$$

leading to

$$\frac{\delta\lambda}{\lambda} = \frac{\tau}{\alpha L \lambda}. \tag{4.13}$$

Hence, to have a good relative wavelength resolution, one would use a long instrument (large L), use a source with a short pulse length τ, and/or use a long wavelength.

In diffraction experiments, one typically allows a broad *wavelength band* from the incident beam to hit the sample, and later determine the wavelength of the detected neutrons from the time-of-flight at the (time-sensitive) detectors. The reason for not allowing the full white beam in the incident beam is to avoid *frame overlap*. This happens when the slow neutrons from one pulse are overtaken by fast neutrons from the following pulse, creating ambigiuity in the data analysis. This is best illustrated on a time-of-flight diagram; see Fig. 4.4. The spread in arrival times, Δt, cannot be allowed to exceed the time between pulses, T. From (4.11), the wavelength spread, $\Delta\lambda$ is limited by

$$\alpha L \Delta\lambda < T. \tag{4.14}$$

The (broad) wavelength band is usually limited by disk choppers, which are in this connection denoted *bandwidth definition choppers*. Similar choppers are placed slightly longer downstream to prevent very slow neutrons from entering the bandwidth chopper from a wrong source pulse. Such choppers are called *frame overlap choppers*.

It is possible by fast spinning choppers to define a (nearly) monochromatic neutron beam from a pulsed source. This is used for inelastic neutron scattering and will be discussed later.

The ESS will have a very long pulse, $\tau = 2.86$ ms. Hence, standard logic for pulsed sources does not apply, and many instrument concepts must be reconsidered. In particular, a shaping (shortening) of the pulse by choppers close the moderator is necessary for many instruments to avoid too large uncertainties in the determined value of λ.

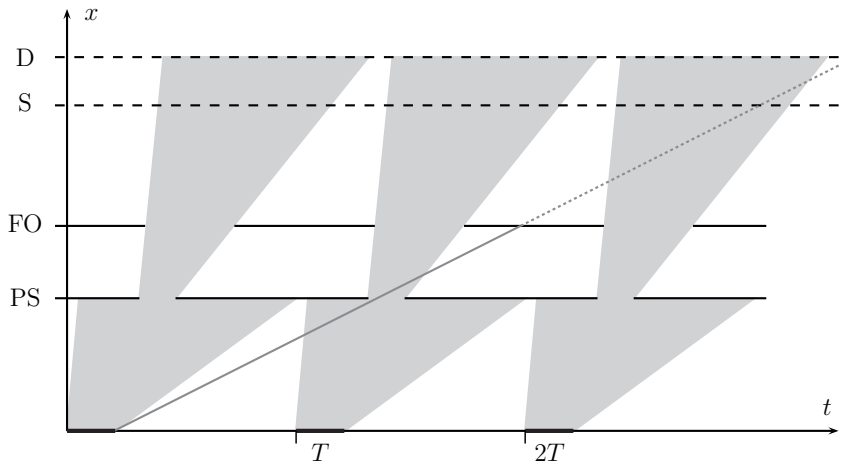

Figure 4.4: Time-of-flight diagram for a typical diffraction experiment. The horizontal axis denote time, t, where the initial pulses begin at $0, T, 2T$, etc. The vertical x-axis denote the position along the main axis of the instrument, where PS is the pulse shaping chopper, FO is the frame overlap chopper (that here also functions as bandwidth definition chopper), S the sample, and D the detector. Each neutron follows one path in the time-of-flight diagram, depending on its emission time and its velocity/wavelength; the shaded areas represent the continuum of allowed paths. At the moderator, a broad wavelength band is emitted, corresponding to a large spread in slopes in the (x, t) diagram. The PS and FO choppers selects a certain wavelength interval, which is narrow enough to avoid frame overlap (overlap between neutrons from different pulses at the detector).

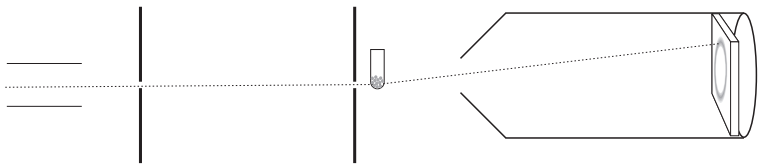

Figure 4.5: The principles of a SANS instrument. The pinholes (left) limit the beam divergence, while a position sensitive detector inside the vacuum tank (right) detects all neutrons scattered at small angles from the sample (middle).

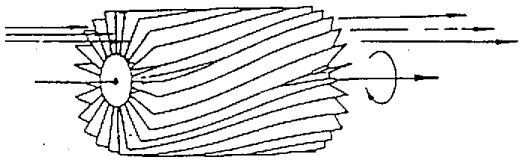

Figure 4.6: A principal sketch of a neutron velocity selector. The neutrons travel left-right, and the absorbing blades of the velocity selector rotate around an axis parallel to the neutron flight path.

4.5 Small-angle scattering instruments

4.5.1 A small-angle scattering instrument at a continuous source

The principle of an ordinary SANS instrument is rather simple. We will here present a SANS instrument for a continuous source, although a generalization to a time-of-flight instrument is straightforward. A sketch of a SANS instrument is shown in Fig. 4.5.

Source. A SANS instrument uses neutrons from a cold moderator and is situated at the end of a guide.

Velocity Selector. The neutrons are being monochromatized by a rotating velocity selector made from spinning absorbing blades, tilted from the main axis; see figure 4.6. This arrangement will allow passage of neutrons with velocities close to a particular value (see problem 4.10.3); typical values are 4-20 Å. The monochromatization is coarse; typically of the order of $\Delta\lambda/\lambda \approx 10\%$.

Collimator The divergence of the incident neutrons is limited by a pair of pinholes, that act as a collimator. Often, one can control the pinhole diameter and their distance, the *collimation length*, L_c, by inserting different pinholes at a number of fixed positions. The smallest collimation length is typically 1 m,

while the longest varies between 5 m and 20 m, depending on the particular instrument.

Sample. The sample is often flat and mounted perpendicular to the beam direction, so that all neutrons scattered at small angles will penetrate the full sample thickness. Hence, samples are often thin to limit absorption and multiple scattering.

Detector. The neutrons are detected by a position-sensitive detector (PSD), which can determine the position of an incident neutron, placed at a distance L_{d} from the sample. A typical PSD is 1×1 m^2 with a precision in positioning of 1-5 mm. The PSD is placed within an evacuated tank to avoid air scattering (which is mainly due to nitrogen), and the sample-detector distance can be varied by moving the PSD within the tank. The minimum PSD distance is around 1 m, while the maximum distance varies in the range 5-20 m determined by the length of the tank. Typically, one would match the sample-detector distance to the collimation length.

Beam stop. An absorbing beam-stop is placed in the direct beam just before the detector to limit the number of neutrons from the direct beam. This strong beam could otherwise saturate, or even damage, the detector. For correct placing of the beamstop, it is necessary to take into account how gravity affects neutrons of different wavelengths; see problem 15.2.5.

4.6 Powder scattering instruments

We will here present typical lay-out of powder scattering instruments for continuous and pulsed sources, respectively.

4.6.1 Continuous source powder diffractometers

A typical continuous-source powder diffractometer, the HRPT instrument at PSI, is illustrated in Fig. 4.7. It uses a beam of thermal neutrons straight from a beam port without use of neutron guides. The beam is reflected by a monochromator (see subsection 4.4.1), which selects the neutron wavelength, typically in the range 1-2 Å. The monochromatic beam passes through a narrow horizontal Soller collimator and hits the powder sample, which is often situated in a vacuum environment to reduce background from air scattering.

The neutrons are scattered according to Bragg's law, see chapter 7. Then, the neutrons are detected by a large arc-shaped detector bank, with typically hundreds of channels, each covering a narrow range of the scattering angle, 2θ.

Background neutrons flying around in the sample-detector area are suppressed by a radial collimator. The detectors have a limited height (perhaps 10-20 cm), to avoid a smearing effect in the data, caused by the blur in total scattering angle when the out-of-plane component is significant.

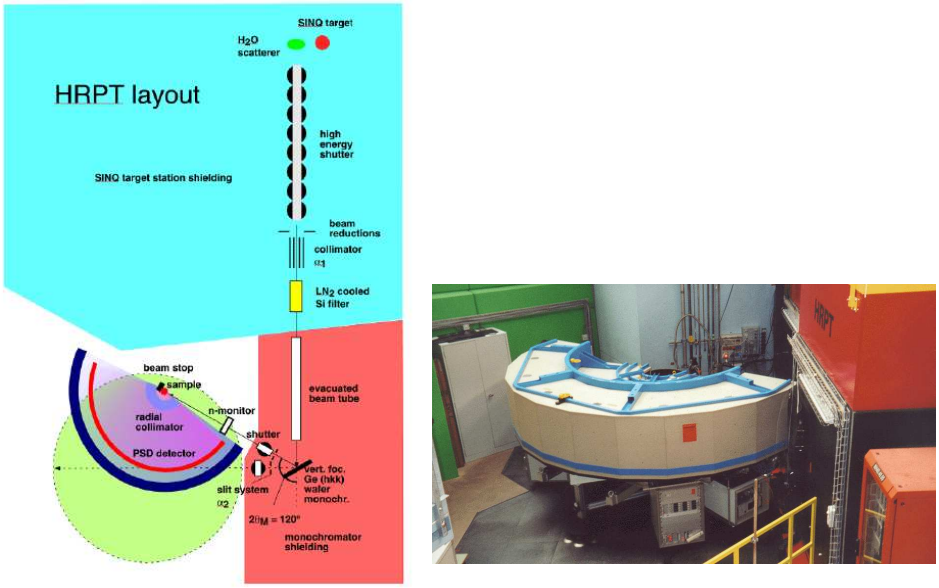

Figure 4.7: (left) Schematic lay-out of the typical high-resolution thermal powder diffractometer HRPT at SINQ, PSI. (right) Picture of the HRPT multidetector (white-blue) and its monochromator shielding (red).

A typical set of powder diffraction data is given in Fig. 4.8. Both the raw data and the data converted into scattering vector is shown. The background value between the peaks is mostly elastic incoherent scattering from the sample, but also thermal diffuse scattering contributes at larger scattering angles; see chapter 10. Towards low scattering angles, there is an increased background due to small-angle scattering of the direct beam.

As can be clearly seen, the *resolution* of the diffractometer (the width of the powder peaks) varies with scattering angle. In particular, the peaks are broadest at high scattering angles. This effect is well understood, but we will not go into details with it here.

4.6.2 A pulsed source powder diffractometer

In a time-of-flight diffraction experiment, the neutron wavelength will change with time, with the shortest wavelength arriving earliest. Hence, at a typical moment in time, there will be Bragg scattering from several lattice spacings. However, the scattering angle from any given reflection will increase with time as the wavelength increases.

To maximize count rate, a typical powder diffractometer is equipped with a large number of time- and position-sensitive detectors that cover a significant fraction of the 4π solid angle. The typical raw data from a time-of-flight powder diffraction experiment will be (transformed to be) two-dimensional: Neutron

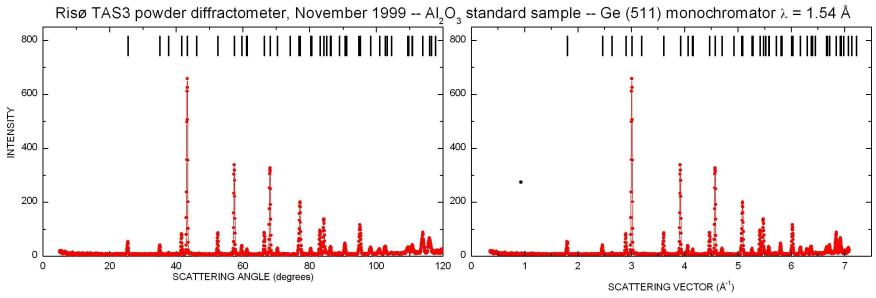

Figure 4.8: A typical powder diffraction pattern, taken by the TAS3 diffractometer at Risø (now placed at Kjeller(N)), which has a similar construction as HRPT. (left) The raw data shown as count vs. scattering angle, 2θ. (right) The data as counts vs. scattering vector, q.

counts vs. flight time, t, and detector angle, 2θ. In such a plot, powder lines will be seen as connected curves through $(2\theta, t)$ space. The processed data will contain only neutron intensity vs. q (or vs. lattice spacing, d), probably normalized in proper units of cross section.

The presently most powerful time-of-flight diffractometer is named GEM, and is placed at the 50 Hz source ISIS (UK). With this instrument, a complete powder diffraction pattern can be recorded within a single pulse (lasting 10-15 ms). In this way, it is possible to monitor diffraction signals from fast processes in real time, *e.g.* chemical reactions.

4.7 Instruments for inelastic neutron scattering

In inelastic neutron scattering, it is necessary to determine both the initial and the final neutron energy, E_i and E_f, in order to calculate the energy difference $\hbar\omega = E_\mathrm{i} - E_\mathrm{f}$. This is done differently for continuous and pulsed neutron beams, as we shall see below.

4.7.1 Continuous source instrumentation, triple-axis spectrometer

On instruments that uses a continuous beam of neutrons, it is necessary to directly select both E_i and E_f, in order to determine the neutron energy transfer, $\hbar\omega$. It is here customary to use Bragg diffraction from crystals for both purposes. Such a type of instrument is denoted a *triple-axis spectrometer*, since the neutron changes direction by scattering three times before being detected:

1. A *monochromator* crystal selects E_i of the incoming beam, as discussed in 4.4.1, by Bragg scattering an angle $2\theta_\mathrm{m}$.

2. The *sample* scatters the beam by the angle 2θ.

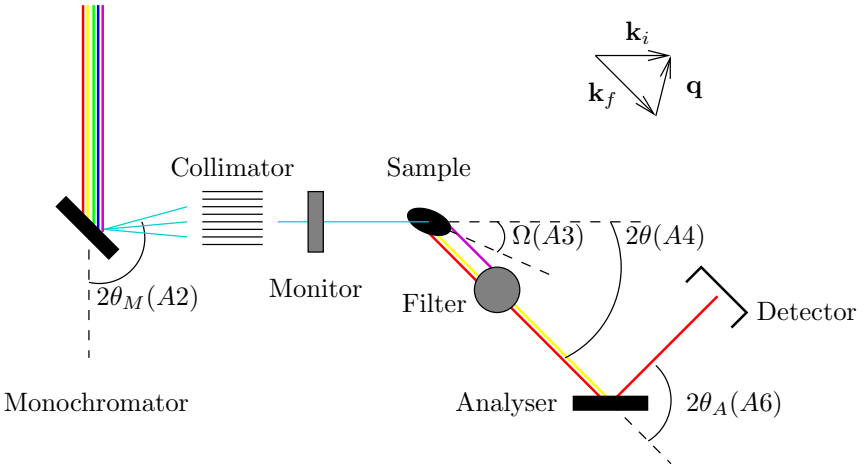

Figure 4.9: A sketch of a triple-axis spectrometer, showing the three scattering angles, $2\theta_\mathrm{m}$, 2θ, and $2\theta_\mathrm{a}$, and the sample rotation, Ω. The upper right part of the figure shows the scattering triangle for the particular configuration of the instrument. Note that $k_\mathrm{f} > k_\mathrm{i}$.

3. The *analyzer* determines E_f by Bragg scattering by an angle $2\theta_\mathrm{a}$, in the same way as the monochromator.

The path of the neutron beam is kept in the same horizontal plane, also denoted the *scattering plane*. The build-up of the triple-axis spectrometer is shown in Figure 4.9.

By correct selection of the three scattering angles, and the sample rotation around a vertical axis, ω, the triple-axis spectrometer can be adjusted to any value of scattering vector, $\mathbf{q}$, and energy transfer, $\hbar\omega$, allowed by the scattering condition (2.6). In fact, $\mathbf{q}$ can only obtain values within the scattering plane. This means that there are 4 free angles to determine only 3 parameters: $\hbar\omega$ and 2 dimensions of $\mathbf{q}$. In practice, this ambigiuity is solved by fixing either E_i or E_f to a predetermined value.

A thorough presentation of how to perform experiments with a triple-axis spectrometer is given in Ref. [45].

Experimental considerations. The 3 scattering angles, $2\theta_\mathrm{m}$, 2θ, and $2\theta_\mathrm{a}$, are often denoted by the less-obvious symbols $A2$, $A4$, and $A6$, respectively. The symbol $A3$ denotes the sample rotation ω, while the symbols $A1$ and $A5$ denotes the rotation of monochromator and analyzer crystals, respectively.

The fixed value of E_i or E_f is often selected, knowing which devices can be used to eliminate higher-order scattering from monochromator and/or analyzer. As one example, a block of PG will allow passage of only a few selected energies (or wavelengths). One example for PG is 14.7 meV. Other types of filters consist of cooled block of Be or BeO, which transmit energies below 5.2 meV

and 3.8 meV, respectively. See also problem 4.10.5.

Often, an experimental series consists of *scans* along a particular axis in $(\mathbf{q}, \hbar\omega)$ space. One speak about *constant-energy scans* and *constant-q scans*. For the latter, it is costumary to use a constant E_f for the scans and then measure each scan point until a constant count number in the beam monitor has been reached. Since the sensitivity of the monitor is proportional to wavelength, λ_i, the number of neutrons reaching the sample for each scan point is proportional to $1/\lambda_\mathrm{i}$ - or to k_i. These facts causes the factor $k_\mathrm{f}/k_\mathrm{i}$ in the final cross section (9.1) to be constant. Hence, the variation of this factor can be neglected, easing the subsequent data analysis.

4.7.2 Time-of-Flight inelastic spectrometers

On instruments at pulsed sources, one can utilize time-of-flight techniques as for diffraction. However, the time-of-flight cannot be used to determine both E_i and E_f. Either the initial or final energy must be selected by other means, typically by Bragg reflection from crystals or by chopping the beam in short time pulses close to the sample. This leads to two essentially different types of spectrometer geometries:

- **Direct geometry.** The incoming neutrons are monochromatized by a chopper system, E_i is fixed, and hits the sample in a short burst. Then, the time-of-flight is used to determine the variable E_f.

- **Indirect geometry.** The sample is hit by a "white" beam, and only outgoing neutrons with a particular energy is scattered by analyzer crystals on to the detector, *i.e.* E_f is fixed. The time-of-flight is then used to determine E_i.

The advantages with time-of-flight spectroscopy are so large, that at many continuous sources one chooses to chop the beam close to the source, producing pulses by sacrificing more than 99% of the neutrons coming through the guide system.

In later versions of these notes, there will be more material on time-of-flight spectrometers, including figures.

4.8 Instrumentation for investigation of magnetic diffraction

The study of magnetic diffraction uses the same instrumentation as described in the earlier chapters. For example powder diffractometers or single crystal diffractometers.

A special, and very powerful, addition to neutron instruments for the study of magnetic structures is the option of using polarized neutrons. This will be discussed in later versions of this text.

4.9 Instrumentation for investigation of magnetic excitations

The study of spin wave and other types of magnetic excitations uses the same instrumentation as described in chapter 10. In particular, time-of-flight spectrometers and triple-axis spectrometers are useful.

As for the study of magnetic structures, also the study of magnetic excitations benefits from the use of polarized neutrons. This will be discussed in later versions of this text.

4.10 Problems in neutron instrumentation

4.10.1 The neutron guide system

Consider a 20 m long Ni ($m = 1$) guide with a constant square cross section 50×50 mm^2, illuminated by a moderator of area $d^2 = 150 \times 150$ mm^2 at a distance, L. We can assume that $L \gg d$.

1. Calculate the critical scattering angle at the guide for 4 Å and 20 Å neutrons.

2. What is the maximal (horizontal or vertical) divergence of neutrons that passes through the guide without being reflected? Compare this to the previous question.

3. A guide is "underilluminated" when the moderator size, not the guide reflectivity, limits the divergence of the transmitted neutrons in any direction. How close must the guide be to the moderator in order not to be underilluminated at 4 Å and 20 Å wavelengths?

4. The guide entry is placed at $L = 1.5$ m. Compare the neutron flux at $\lambda = 4$ Å at the end of the guide to the flux in the situation where the guide entry is replaced with a beam port of the same size (equivalent to removing the reflecting mirrors from the guide).

5. Can you imagine why guides are often not used for instruments using thermal or hot neutrons?

4.10.2 The collimator

A horizontal collimator consists of a number of thin, parallel, equidistant sheets (like every n'th page in a book) of a neutron absorbing material, so that neutrons traveling in the "wrong" directions are eliminated. The distance between sheets is denoted D and the length of the sheets L.

1. Calculate the transmission, T, as a function of horizontal neutron divergence, η_h (the horizontal deviation from the beam axis). You can assume

that the sheets are infinitely thin. Further, assume that the position of individual collimator sheets are unknown (or equivalently that the collimator oscillates sidewards during the experiment).

2. A collimator is described by the FWHM (full width at half maximum) of the transmission curve. Calculate the FWHM in terms of D and L.

3. A typical collimator is 30' (or 0.5°) and has a length of $L = 200$ mm. What is the distance, D, between the absorbing sheets?

4. A 60' collimator is inserted after the guide in 4.10.1 (question 4). How does that affect the neutron flux for 4 Å and for 20 Å neutrons?

4.10.3 Neutron velocity selector

A neutron velocity selector is a drum that spins around an axis parallel to the beam. This axis lies below the guide. From the drum, a series of absorbing neutron blades sticks out radially. The ends of the drum are twisted with respect to each other. A principal sketch is shown in figure 4.6. This effect of the selector is that only neutrons around a certain velocity (or wavelength) can pass through.

Assume a selector length of $L = 0.25$ m, $n = 68$ blades, and a twisting angle of 48.3°, as for the selector at the SANS-2 instrument at PSI. Calculate the rotation speed you should use to select 10 Å neutrons.

4.10.4 Pinhole collimation

The collimation in a typical SANS instrument is performed by two pinholes separated by a distance. Consider a circular pinhole (made from an absorbing material), $d = 8$ mm, placed in the centre of a neutron beam and an identical circular pinhole a distance $L = 6$ m further down the beam. Calculate the maximal divergence in the x and y direction.

4.10.5 The Be filter

Beryllium crystallizes in the hcp structure with a lattice constant $a = 2.27$ Å. A thick block of Be powder is often used as a neutron attenuator, since it Bragg scatters neutrons away from the beam.

1. Why is the Be powder transparent for long wavelength neutrons?

2. Calculate the critical wavelength for neutron transmission. What is the corresponding energy? Hint: use the results of problem 7.7.2.

3. How can you utilize this to eliminate higher order neutrons scattered from a monochromator?

Part III

Structure of materials

Chapter 5

Small angle neutron scattering, SANS

co-authors: Jakob Kirkensgaard and Lise Arleth, Univ. Copenhagen, Niels Bohr Institute

Elastic neutron scattering, or *neutron diffraction*, was first used to reveal the crystal structure of materials, as will be presented in chapter 7. First, however, we consider the conceptually simpler - but historically later developed - field of (elastic) small angle neutron scattering (SANS), which provides information on the size and shape of objects on length scales from 1 nm to 1000 nm.

As we shall see later, scattering at small angles - or small values of the scattering vector, q - is a signature larger objects, while scattering at larger q-values probes the atomic distance. This is illustrated in Fig. 5.1.

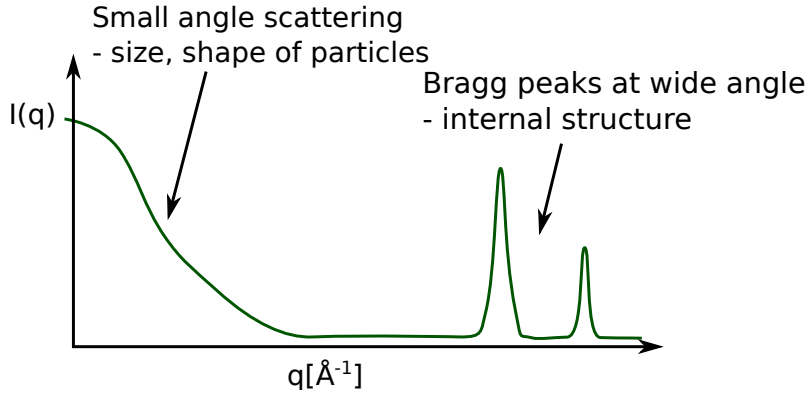

Figure 5.1: Illustration of small-angle scattering signal and diffraction peaks in the same data.

5.1 Applications of SANS in nanoscience

We here start with a few introductory examples to the types of science, where small-angle neutron scattering is useful.

5.1.1 Polymers

A very important class of molecules are polymers. As the name suggests, a polymer is built by assembling many chemical building blocks: *monomers*. Typically, this would be into single long chains, although a number of branched architectures also exist. The chains are formed by chemical bonds between the monomers. Conceptually you can think of polymers as beads on a string. Almost everything surrounding us in our daily life is made of polymers, for example plastics, rubber (typically built from one or two types of monomers), and biological molecules like DNA and proteins/peptides (built from several to many types of monomers). Fig. 5.2 shows examples of two simple plastic types (polyethylene and PVC), as well as an example of a peptide/protein-like structure.

Some of the most important characteristics of polymers are structural signatures like their size, shape and flexibility, often under different circumstances like varying temperature. For example, polyethylene is very flexible, while DNA is very stiff. The size of the polymer relates to its length, also called the *degree of polymerization*, *i.e.* how many monomers, N, it is built from. A typical size measure in polymer science is the radius of gyration which is generally defined as the root mean square distance of an objects' parts from its center of mass

$$R_g^2 = \frac{1}{N}\sum_{n=1}^{N}\langle(\bar{R}_n - \bar{R}_G)^2\rangle, \tag{5.1}$$

where R_n and R_G are the position vectors for the object parts and its centre of mass respectively. For a so-called ideal chain polymer this is given by

$$R_g^2 = \frac{1}{6}Nb^2, \tag{5.2}$$

where b is the polymer segment (bond) length. For non-ideal (real) chains the size scaling does not obey $R_g \propto N^{1/2}$ but depends on external parameters, for example whether it is surrounded by a solvent. The structural properties of polymers are typically investigated by scattering methods.

5.1.2 Lipids and surfactants

Other polymer-related classes of materials comprise lipids and surfactants, which play a significant role in biology and nano-science. These consists of amphiphilic molecules, *i.e.* they are made from components that are for example hydrophobic and hydrophilic (water hating and loving, respectively). Examples of such molecules are shown in Fig. 5.3(a).

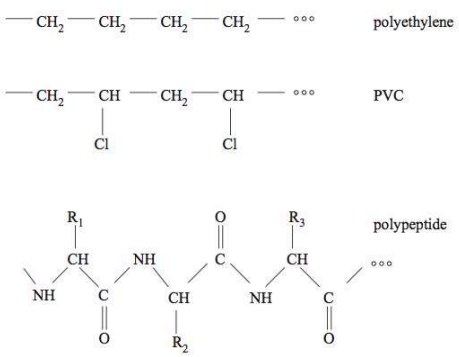

Figure 5.2: Examples of polymers: PE and PVC are synthetic polymers produced industrially, the polypeptide is an example of a biological polymer. Figures from [46].

Lipids are extremely important in biology as they are the building blocks of cells and membranes. Amphiphilic molecules self-assemble in solution to form aggregated structures. The shape and size of these structures can be explored in detail using scattering methods. Fig. 5.3(b) show examples of some of the simplest lipid aggregates, namely micelles and vesicles.

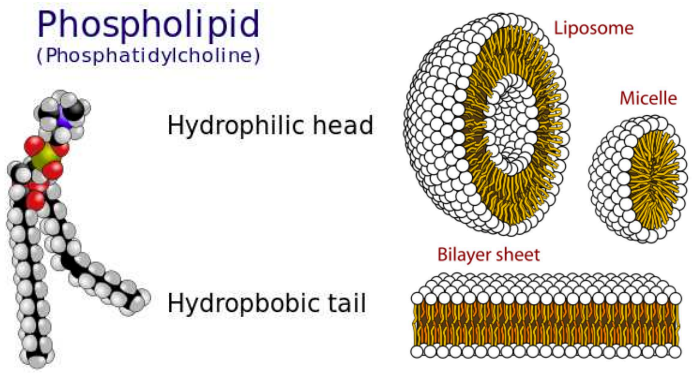

(a) (b)

Figure 5.3: (a) Example of amphiphile: a phospholipid. (b) Aggregates formed by self-assembled lipids. A vesicle or liposome, a micelle and a bilayer sheet. Figures from wikipedia.

5.2 The neutron scattering cross section from nano-sized particles

We will now describe in mathematical terms the scattering from a system of nano-sized particles.

5.2.1 The cross section for neutron diffraction

Our starting point is the expression for the coherent elastic scattering cross section for a system of nuclei, (2.56):

$$\left.\frac{d\sigma}{d\Omega}\right|_{\text{nucl. coh. el.}} = \left|\sum_{j'} b_{j'} \exp(i\mathbf{q}\cdot\mathbf{r}_{j'})\right|^2. \tag{5.3}$$

We have here considered the nuclei as being fixed in position. This is a very good approximation for small-angle scattering. For more details on this *static approximation* and on the necessary corrections to the equation, see the description in chapter 10 on the effect of nuclear vibrations.

5.2.2 The structure factor

For a sample of N identical nano-sized particles, we can divide the sum of the scattering nuclei into a sum over particles and a sum over the nuclei within each particle. We now write the nuclear coordinates, $\mathbf{r_j}$ in terms of the center of its host particle, $\mathbf{R}_J$, as $\mathbf{r}_{j'} \equiv \mathbf{r}_j + \mathbf{R}_J$. This gives:

$$\begin{aligned}
\left.\frac{d\sigma}{d\Omega}\right|_{\text{nucl. coh. el.}} &= \left|\sum_{j'} b_{j'} \exp(i\mathbf{q}\cdot\mathbf{r}_{j'})\right|^2 \\
&= \left|\sum_{j,J} b_j \exp(i\mathbf{q}\cdot(\mathbf{R}_J+\mathbf{r}_j))\right|^2 \\
&= \left|\sum_{J} \exp(i\mathbf{q}\cdot\mathbf{R}_J)\right|^2 \left|\sum_{j} b_j \exp(i\mathbf{q}\cdot\mathbf{r}_j)\right|^2 \\
&\equiv NS(\mathbf{q})\left|\sum_{j} b_j \exp(i\mathbf{q}\cdot\mathbf{r}_j)\right|^2,
\end{aligned} \tag{5.4}$$

where $S(\mathbf{q})$ is called the *structure factor*. For random, dilute systems, the relative phase between scattering from the particles, $\exp(i\mathbf{q}\cdot(\mathbf{R}_J-\mathbf{R}_K))$, takes a random value. Hence, the interference vanishes on average, leading to $S(\mathbf{q}) = 1$. The derivation is left as an exercise to the reader; see problem 5.4.1. With $S(\mathbf{q})$ known, the cross section from the scattering patters is thus seen to be directly proportional to that from the individual particles.

In practice, the particles are often dispersed in a solution, which will also scatter the neutrons. This case is treated in section 5.2.4.

5.2.3 The small-angle approximation

We will here only consider scattering vectors of sufficiently small length, q, so that the phase of the exponential, $i\mathbf{q}\cdot\mathbf{r}_j$, does not vary significantly between neighbouring atoms. The condition for this is

$$qa \ll 2\pi, \tag{5.5}$$

where a is a typical interatomic distance. For larger values of q, we are in a regime where the crystalline structure of the sample is responsible for the scattering. This leads to diffraction as will be explained in detail in chapter 7.

Studying (5.4), we see that when $i\mathbf{q}\cdot\mathbf{r}_j$ varies slowly between neighbouring nuclei, the scattering from the individual nuclei can not be distinguished, and the sample scatters approximately as a continuum. Hence it becomes valid to transform the sum in (5.4) into an integral

$$\sum_j b_j \exp(i\mathbf{q}\cdot\mathbf{r}_j) \longrightarrow \int_V \rho_b \exp(i\mathbf{q}\cdot\mathbf{r})dV, \tag{5.6}$$

where ρ_b is the effective *scattering length density* for the sample. The scattering length density is defined as the sum of the coherent scattering lengths over all atoms within a given volume, V_0, divided by this volume,

$$\boxed{\rho_b = \frac{1}{V_0}\sum_{j\in V_0} b_j}, \tag{5.7}$$

where j represents the position of the nuclei in the volume (which could be a formula unit). After the transformation, the SANS cross section reads

$$\left.\frac{d\sigma}{d\Omega}\right|_{\text{SANS}} = NS(\mathbf{q})\left|\int \rho_b(\mathbf{r})\exp(i\mathbf{q}\cdot\mathbf{r})dV\right|^2. \tag{5.8}$$

Experimental considerations. In a typical SANS experiment $q \leq q_{\max} = 0.3$ Å^{-1}. Hence, only structures larger than around $2\pi/q_{max} \approx 20$ Å are well resolved.

Instruments specialized in SANS can also be used to study periodic (crystalline) arrangements where the period is larger than the typical 2-10 Å, known from simple crystal structures. This could be crystals of very large molecules, superstructures, magnetic structures with long repetition length, *etc.*

5.2.4 SANS from particles in solution

One of the main applications of SANS is the study of nano-sized objects, suspended in a solution. In practice, the objects could be polymers or micelles, described in section 5.1, and the solvent could be water or an organic liquid.

As a start, we first consider one single nano-sized particle. For the combined system, it is convenient to separate the volume integration into an integral over the particle and an integral over the solvent,

$$\left.\frac{d\sigma}{d\Omega}\right|_{\text{SANS, 1 particle}} = \left|\int_{\text{particle}} \rho_b(\mathbf{r}) \exp(i\mathbf{q}\cdot\mathbf{r})dV + \rho_s \int_{\text{solvent}} \exp(i\mathbf{q}\cdot\mathbf{r})dV\right|^2 . \tag{5.9}$$

By using the *scattering length density contrast*,

$$\boxed{\Delta\rho(\mathbf{r}) = \rho_b(\mathbf{r}) - \rho_s}, \tag{5.10}$$

the solvent integration is replaced by an integration over the entire sample volume, V_s,

$$\left.\frac{d\sigma}{d\Omega}\right|_{\text{SANS, 1 particle}} = \left|\int_{\text{particle}} \Delta\rho(\mathbf{r}) \exp(i\mathbf{q}\cdot\mathbf{r})dV + \rho_s \int_{V_\text{s}} \exp(i\mathbf{q}\cdot\mathbf{r})dV\right|^2 . \tag{5.11}$$

Typically, the sample dimensions are on the order mm. This is roughly 4-6 orders of magnitude larger than the length scale of typical nano-sized particles. Hence, the contribution to small-angle scattering from the entire volume V is almost a δ-function in q – or to be more accurate has a width of the order 10^{-6} Å^{-1}. Such low q-values are not at all visible in the SANS measurements, where the typical minimum scattering vector is $q_{min} \approx 10^{-3}$Å^{-1}. We can therefore neglect the total volume scattering. Taking into account that the sample consists of N particles, the scattering cross section reads

$$\left.\frac{d\sigma}{d\Omega}\right|_{\text{SANS, particles}} = NS(\mathbf{q}) \left|\int_{\text{particle}} \Delta\rho(\mathbf{r}) \exp(i\mathbf{q}\cdot\mathbf{r})dV\right|^2 . \tag{5.12}$$

Notice that the scattering cross section depends essentially on the square of the contrast in scattering length density. Hence, the scattered intensity can be changed strongly by, *e.g.*, varying the scattering length density of the solvent. This is typically done by deuteration, as illustrated in Fig. 1.2.

In a different formulation, we describe the scattering in terms of the particle density $n = N/V_\text{s}$ and the volume specific cross section $\Sigma = \sigma/V_\text{s}$. The volume specific differential scattering cross section then becomes

$$\boxed{\left.\frac{d\Sigma}{d\Omega}\right|_{\text{SANS, particles}} = nS(\mathbf{q}) \left|\int_{\text{particle}} \Delta\rho(\mathbf{r}) \exp(i\mathbf{q}\cdot\mathbf{r})dV\right|^2}. \tag{5.13}$$

5.2.5 The particle form factor

For monodisperse, homogeneous particles, the cross section (5.13) simplifies to

$$\left.\frac{d\Sigma}{d\Omega}\right|_{\text{SANS, simple}} = n\Delta\rho^2 S(\mathbf{q}) \left|\int_{\text{particle}} \exp(i\mathbf{q}\cdot\mathbf{r})dV\right|^2 , \tag{5.14}$$

leading to

$$\left.\frac{d\Sigma}{d\Omega}\right|_{\text{SANS, simple}} \equiv n\Delta\rho^2 V^2 S(\mathbf{q})P(\mathbf{q}), \tag{5.15}$$

where V is the particle volume and $P(\mathbf{q})$ is known as *the particle form factor*,

$$\boxed{P(\mathbf{q}) = \left|\frac{1}{V}\int dV e^{i\mathbf{q}\cdot\mathbf{r}}\right|^2}, \tag{5.16}$$

which takes its maximum value of 1 as $q \to 0$.

When defining the *particle volume fraction* as $\phi = NV/V_s = nV$, the cross section reads

$$\boxed{\left.\frac{d\Sigma}{d\Omega}\right|_{\text{SANS, simple}} \equiv \phi\Delta\rho^2 V S(\mathbf{q})P(\mathbf{q})}. \tag{5.17}$$

Sometimes in the SANS literature, the volume specific cross section is denoted loosely $I(\mathbf{q}) = d\Sigma/d\Omega$, as if it were the observed intensity.

5.2.6 The form factor of a solid sphere

For a solid sphere of radius R, the form factor is isotropic and is easily calculated (see problem 5.4.2). The result is

$$P_{\text{sphere}}(q) = \left(3\,\frac{\sin(qR) - qR\cos(qR)}{(qR)^3}\right)^2, \tag{5.18}$$

which is illustrated for different radii in Figure 5.4.

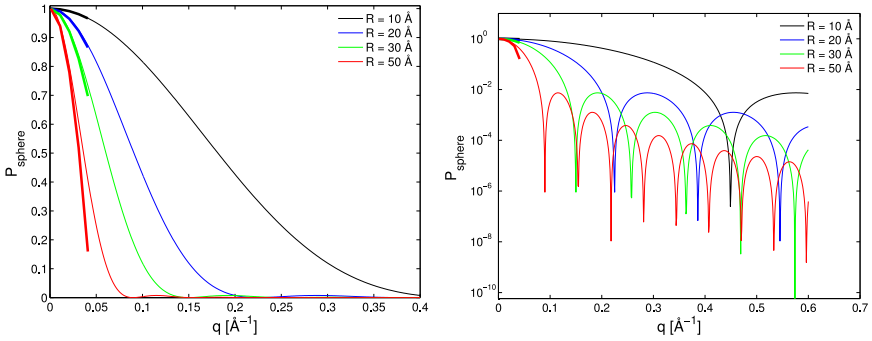

Figure 5.4: Plots of the form factor (5.16) for solid spheres of radii $R = 10, 20, 30$ and 50 Å respectively (thin lines). The Guinier approximation (5.27), see section 5.3.2, for small q is shown by fat lines. Left panel shows the function on a linear scale, while a semilogarithmic plot is used in the right panel.

5.2.7 The form factor of a spherical shell

From the calculations leading to the form factor for a sphere (5.18) it is straightforward to show that the form factor amplitude for a thin spherical shell is:

$$\boxed{P_{\text{shell}}(q) = \left(\frac{\frac{4\pi}{3} R_{\text{out}}^3 P_{\text{sphere}}(qR_{\text{out}}) - \frac{4\pi}{3} R_{\text{in}}^3 P_{\text{sphere}}(qR_{\text{in}})}{\frac{4\pi}{3}(R_{\text{out}}^3 - R_{\text{in}}^3)} \right)^2}, \tag{5.19}$$

where R_{out} is the outer radius of the shell and the inner radius of the shell is $R_{\text{in}} = R_{\text{out}} - D$, where D is the thickness of the shell. $P_{\text{sphere}}(qr)$ is here the form factor of a sphere (5.18), as calculated in problem 5.4.2.

The calculation leading to this result comes directly by expanding (5.16), using (5.25),

$$\begin{aligned} P(\mathbf{q}) &= \left| \frac{1}{V} \int dV e^{i\mathbf{q}\cdot\mathbf{r}} \right|^2 = \frac{(4\pi)^2}{V^2} \left| \int_{R_{\text{in}}}^{R_{\text{out}}} r^2 \frac{\sin(qr)}{qr} dr \right|^2 \\ &= \left(\frac{3}{q^3(R_{\text{out}}^3 - R_{\text{in}}^3)} \right)^2 \left| \int_{qR_{\text{in}}}^{qR_{\text{out}}} (rq)\sin(rq) d(rq) \right|^2 \\ &= \left(\frac{R_{\text{out}}^3 P_{\text{sphere}}(qR_{\text{out}}) - R_{\text{in}}^3 P_{\text{sphere}}(qR_{\text{in}})}{R_{\text{out}}^3 - R_{\text{in}}^3} \right)^2 . \end{aligned} \tag{5.20}$$

5.2.8 Polydispersity

Above, we have considered monodisperse (identical) particles only. If, however, the particles in the thin solution are not all the same size, we denote them *polydisperse*, and we ascribe them a *size distribution*, $D(R)$, defined as the probability of finding a particle of size R. Since $D(R)$ is a probability, $\int D(R)dR = 1$. For dilute, polydisperse particles, the form factor (5.16) is modified according to

$$P(q) = \int \mathrm{d}R \; D(R) \; P(q, R). \tag{5.21}$$

Hence the total SANS cross section per sample volume is

$$\frac{d\Sigma}{d\Omega}(q) = n(\Delta\rho)^2 \int \mathrm{d}R \; V(R) \; D(R) \; P(q, R), \tag{5.22}$$

where $P(q, R)$ is the size-dependent form factor and $V(R) = (4\pi/3)R^3$.

One of the most simple – but not generally the most correct – ways of including the structure factor is by using the so-called locally monodisperse approximation [47], where we approximate the particle volume, $V(R)$, by its average value, $V = (4\pi/3)R_{\text{av}}^3$, to reach

$$\frac{d\Sigma}{d\Omega}(q) = nV(\Delta\rho)^2 \int \mathrm{d}R \; D(R) \; P(q, R). \tag{5.23}$$

As the concentration of particles increases, the inter-particle interaction becomes increasingly important. Hence, the structure factor $S(q, R)$ can no longer be considered to be unity. The total SANS cross section per sample volume can then be written

$$\frac{d\Sigma}{d\Omega}(q) = nV(\Delta\rho)^2 \int \mathrm{d}R\ D(R)P(q, R)S(q, R). \tag{5.24}$$

The effect of polydispersity will be explored in Exercise 5.4.5.

5.2.9 Complementarity of neutrons and X-rays

SANS is often used in combination with its sister technique, Small-Angle X-ray Scattering (SAXS), and the fundamental theories for SANS and SAXS are very similar. In addition, the experimental setup of a SAXS instrument is in principle very similar to that of the SANS instrument. The main difference between the two methods is that in SANS, the incoming neutrons are scattered by the nuclei of the studied sample, whereas in SAXS the incoming photons are scattered by the electrons.

The scattering length of an electron, b_e is given by the classical electron radius (also known as the Compton radius or the Thompson scattering length). It is given by $b_\mathrm{e} = r_0 = e^2/(4\pi\varepsilon_0 m_\mathrm{e} c^2) = 2.82$ fm, where ε_0 is the vacuum permittivity, e and m_e are the charge and mass of the electron and c is the speed of light. Thus the scattering length of an atom with atomic number Z is simply Zb_e.

SAXS has a major advantage in the easy access to very intense, well-collimated and well-focused X-ray beams, both in home-based laboratories and at large scale synchrotron facilities.

As mentioned in chapter 1, the major advantage of SANS as compared to SAXS is the access to contrast variation via the exploitation of the difference in scattering length between hydrogen (H) and deuterium (D). This opens up for systematic contrast variation SANS measurements, where domains of specific interest in the system under investigation is enhanced at the same time as other domains are made practically invisible. This opportunity is widely applied within the investigation of biological and other organic materials and the contrast variation SANS approach has been used for investigating the internal organization of large protein complexes, to determine the finer details of phospholipid membranes, and to obtain insight into the conformation of the single polymer-chains in soft condensed materials.

5.3 Useful model-free approximations in SANS

We here present a number of useful approximations and limiting cases for small and large values of the scattering vector, q. These approximations are important for the analysis and understanding of SANS data.

5.3.1 The Debye formula

For a randomly oriented particle of general shape, Debye was able to show a highly useful expression for the average value of the complex phase

$$\boxed{\langle \exp(i\mathbf{q}\cdot\mathbf{r})\rangle = \frac{\sin(qr)}{qr}}. \tag{5.25}$$

This formula is often used for calculating the form factor of particles in solution; the proof is sketched below.

Consider a $\mathbf{q}$, fixed in the laboratory system, and let us define the z axis along $\mathbf{q}$. We consider the particles fixed in space and randomly oriented.

Hence, the position, $\mathbf{r}$, of one particular nucleus can be found anywhere on a sphere of radius r, described by the spherical coordinates, (θ, ϕ). We can now write $\mathbf{q}\cdot\mathbf{r} = qr\cos(\theta)$. The average value of the complex exponential function is given by the spherical integral

$$\begin{aligned}\langle \exp(i\mathbf{q}\cdot\mathbf{r})\rangle &= \frac{1}{4\pi}\int d\theta d\phi \sin(\theta)\exp(i\mathbf{q}\cdot\mathbf{r}) \\ &= \frac{1}{2}\int_0^\pi d(\cos\theta)\exp(iqr\cos\theta) \\ &= \frac{\sin(qr)}{qr}.\end{aligned} \tag{5.26}$$

5.3.2 The Guinier approximation

We will now present an important approximation for particle structure factors in small-angle scattering: the *Guinier approximation* for small values of q.

Let us first study the hard-sphere form factor (5.18) for small values of q, *e.g.* $qR \ll 1$. We expand the trigonometric functions to 5th(!) order in qR, reaching

$$P_{\text{sphere}}(q) \approx 1 - \frac{1}{5}(qR)^2. \tag{5.27}$$

This function has the same series expansion (to second order) as the expression $\exp(-(qR)^2/5)$, which is what we define as the Guinier approximation for the sphere form factor.

To generalize from this example, we can cast the equation in terms of the radius of gyration. The radius of gyration of the sphere is easily calculated by converting (5.1) into an integral, reaching

$$R_{\text{g}}^2 = 3R^2/5. \tag{5.28}$$

This leads to

$$\boxed{P(q) \approx \exp\left(-\frac{1}{3}(qR_{\text{g}})^2\right)}. \tag{5.29}$$

In fact, this is the general Guinier approximation valid for any particle shape. We will, however, not show it in the general case here.

5.3.3 The Porod law

We here present the important *Porod law*, which is valid for large q values. We again consider the sphere form factor (5.18), this time for large values of q, *i.e.* $qR \gg 2\pi$. To leading value of qR, this becomes

$$P_{\text{spheres}}(q) \approx \frac{9\cos^2(qR)}{(qR)^4}. \tag{5.30}$$

Now, for large q, even very small variations in the particle size, R, will lead to a variation of the cosine argument (qR) by an amount comparable to, or larger than, 2π. For such a sample, we will observe approximately the average value of the cosine, *i.e.*, $\left\langle \cos^2(qR) \right\rangle = 1/2$, leading to $P(q) \approx 9/(2q^4R^4)$ or

$$\boxed{P(q) \propto q^{-4}}. \tag{5.31}$$

This is, in fact, the generally valid Porod law for small-angle scattering. We will not show the Porod law directly here. Intuitively, however, it is reasonable to generalize from the example of the spheres. Here, the real-space structures (the particle radius) probed at a scattering vector of q is of the order π/q, as judged from the position of the first "dip" in the expression for the form factor, (5.18). Hence, at much larger values of q, the measurement is sensitive to smaller real-space structures. However, the only small real-space structures visible are sharp surfaces: The boundary between two different scattering length densities. And the reflectivity from a surface is in fact proportional to q^{-4}, as will be shown in chapter 6.

5.4 Problems

5.4.1 The structure factor for dilute systems

For a dilute system of identical nano-objects, it can be assumed that the relative phase between two of the objects, $\exp(i\mathbf{q}\cdot(\mathbf{R}_J - \mathbf{R}_K))$, assumes a random value.

Derive from this assumption that $S(q) = 1$ for dilute systems.

5.4.2 Scattering form factor for spheres

A sample of dilute, identical spheres with radius R dispersed in a solvent will scatter uniformly with the form factor given by (5.18).

1. Show by direct integrations that this form is correct. Hint: Use spherical coordinates or the Debye formula (5.25).

2. Implement the obtained form factor in MatLab or a similar program and calculate and plot the form factor for spheres with radii, $R = 20$ Å, $R = 40$ Å, $R = 60$ Å, and $R = 80$ Å as functions of q.

3. Estimate numerically the smearing due to a polydispersity if there is an uncertainty in these radii of the magnitude $\Delta R/R = 10\%$ (assume a uniform distribution of sizes in the range $[R - \Delta R; R + \Delta R]$).

5.4.3 Radius of gyration for a sphere

Show that the radius of gyration from a solid sphere is given by (5.28).

5.4.4 SANS q-range and resolution

Imagine a SANS instrument with a 1 m diameter PSD, a 40 mm diameter beam stop, pinhole collimation of diameter 20 mm (first) and 10 mm (at the sample), and equal collimation-detector lengths, $R_c = R_d$, in the range 1-20 m.

- Calculate the q-range of this instrument for wavelengths of 4 Å and 20 Å.
- Calculate the maximum divergence of the incoming beam in the two extreme settings of R_c.
- Calculate the relative uncertainty in the value of q due to the beam divergence, and compare to the total q-range in the two settings of R_c.

5.4.5 Polydisperse spheres

We imagine a solution of polydisperse spheres with volume fraction ϕ. When we can assume $S(q) = 1$ (typically for low concentrations, $\phi \ll 1$), the total SANS cross section per sample volume is given by (5.17).

1. Assume that the volume fraction is $\phi = 0.01$ and that the excess scattering length density is $\Delta\rho = 3 \cdot 10^{14}\text{m}^{-2}$. Using the form factors found in 5.4.2, calculate the volume specific cross section from spherical particles of radii $R = 20$ Å, $R = 40$ Å, $R = 60$ Å, and $R = 80$ Å, respectively, if they are considered monodisperse and dilute.

2. Now, assume instead that your sample of spheres is weakly polydisperse, and that it basically follows a Gaussian distribution, with $R_{av} = R$ and with a relative standard deviation of $\sigma/R = 20\%$. Plot the form factor in the polydisperse case for (at least) the $R = 60$ Å sample.

3. For higher particle concentrations, the particle-particle interactions generally have to be taken into account in the modeling of the scattering intensity via the structure factor, $S(q)$. The particles interact with a hard-sphere volume fraction ϕ. The expression for $S(q)$ has been calculated (using the Percus-Yevick approximation for the closure relation [48])

$$S(q, R) = \frac{1}{1 + \frac{24\phi}{2R} \cdot G(2Rq)}, \tag{5.32}$$

where in this equation

$$G(A) = \frac{\alpha(\sin A - A\cos A)}{A^2} + \frac{\beta(2A\sin A + (2-A^2)\cos A - 2)}{A^3} + \frac{\gamma(-A^4\cos A + 4((3A^2-6)\cos A + (A^3-6A)\sin A + 6))}{A^5}$$

and

$$\alpha = \frac{(1+2\phi)^2}{(1-\phi)^4}, \quad \beta = \frac{-6\phi(1+\phi/2)^2}{(1-\phi)^4}, \quad \gamma = \frac{\phi\alpha}{2}. \tag{5.33}$$

This structure factor may be combined with the form factor to yield the total volume specific scattering cross section. Use the locally monodisperse approximation (5.24). An appropriate integration range might be $R \in [R_{av} - 3\sigma; R_{av} + 3\sigma]$.

4. Calculate and plot the scattering intensity for the $R = 60$ Å polydisperse spheres for volume fractions of 1%, 5%, 10%, 25%, and 50%.

5.4.6 Phospholipid bilayer liposomes

The volume specific cross section from diluted monodisperse liposomes is given by (5.17), where here $S(q) = 1$, $V = V_{\text{out}} - V_{\text{in}}$ is the volume of the liposome and $P(q)$ is the form factor for a (thin) spherical shell, eq. (5.19).

1. Calculate and plot the scattering form factor, $P(q)$, for the thin spherical shell. Use $R_{\text{out}} = 400$ Å and $D = 30$ Å. NB: Note that, in general, $\lim_{q\to 0} F(q) = 1$.

2. In order to estimate the scattering from bilayer liposomes it is necessary to take a closer look at the geometrical cross section of the bilayer and develop a reasonable model for the $\Delta\rho(r)$-function. This includes considering whether the liposomes can be represented by a 1-shell model (green curve in Figure 5.5) or if it is more correct to use a 3-step model (red curve). In the 3 step model we are considering the excess scattering length density of the hydrophobic core, the hydrophilic shell and D_2O-buffer. Locate the hydrophobic and hydrophilic parts of the bilayer in Figure 5.5.

3. In order to estimate the correct $\Delta\rho(r)$-function, we need to calculate the excess scattering length density of the hydrophobic core, the hydrophilic shell and the D_2O-buffer. Use the chemical composition and partial specific molecular volumes in Table 5.1 to calculate the scattering length densities of D_2O, DMPC hydrophobic and hydrophilic parts, as well as the total average scattering length density for the DMPC. Calculate the excess scattering length densities of DMPC (hydrophobic, hydrophilic and total) as seen on a background of D_2O.

4. Assume an area per headgroup of DMPC of 59 Å^2. Use the (geometrical) expression for the volume of a cylinder and calculate the thickness of the hydrophobic bilayer and the two hydrophilic shells.

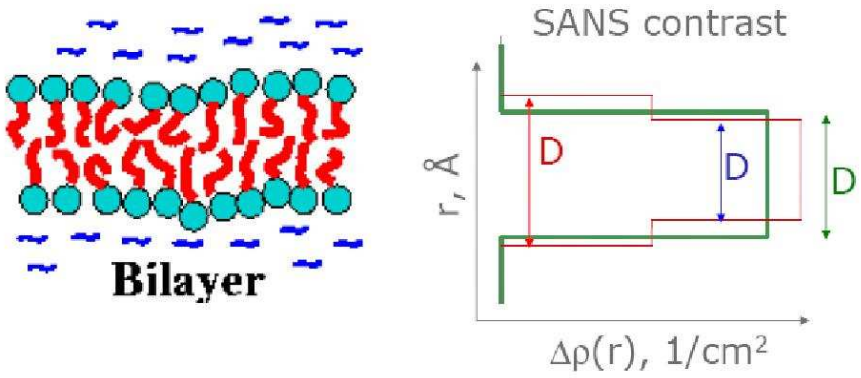

Figure 5.5: A schematic drawing of a phospolipid bilayer (left) and its scattering length density as function of position in the bilayer (right).

Constituent	Chemical composition	Partial specific molecular volume [Å^3]
D_2O	D_2O	30
DMPC, hydrophobic chains	2× $C_{14}H_{29}$	808
DMPC, hydrophilic headgroups	$C_8H_{14}NO_8P$	319

Table 5.1: Table of data for DMPC (Di-Myristyl Phospatidyl Choline).

5. Use the information obtained in the two previous questions to make a correctly scaled plot of the $\Delta\rho(r)$-function in the two cases (distinction and no distinction between hydrophobic and hydrophilic parts).

   From these calculations it should be visible that the $\Delta\rho(r)$ functions obtained in the two cases look slightly different. Not surprisingly, it is most correct to use the 3-step model. However, for simplicity, we will use the 1-step/1-shell model in the following.

6. Use the average $\Delta\rho$ -value for the DMPC liposomes (NB: This should be a number close to $-6 \cdot 10^{14}$ m^{-2}) and calculate the total scattering intensity for a sample of bilayer liposomes with $R_{\text{out}} = 400$ Å. Use the bilayer thickness calculated in the previous question. Assume that the liposome concentration is 10 mg/ml corresponding to $\phi = 0.01$.

7. Use the simple approach (diluted spheres, $S(q) = 1$) as in question 2 of 5.4.5 to include a polydispersity of the liposomes of $\sigma/R_{\text{av}} = 50\%$. Plot the resulting scattering intensity for the liposomes.

8. (Optional) Use the same approach (interacting spheres) as in question 3 of 5.4.5 to incorporate the hard spheres structure factor $S(q)$ into the

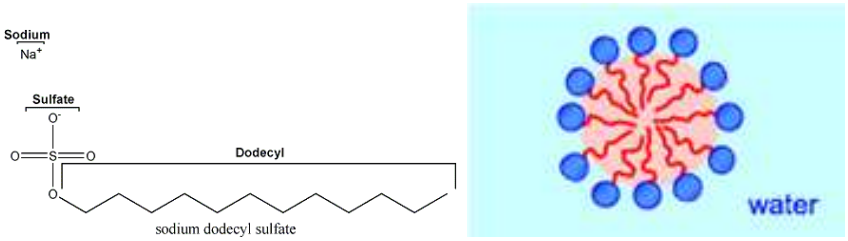

Figure 5.6: (left) Molecular structure of the surfactant Sodium Dodecyl Sulphate (SDS). (right) Illustration of the cross-section of a spherical micelle.

calculations of the volume specific cross section $d\Sigma/d\Omega$. NB: Note that the relevant hard-spheres volume fraction, ϕ, in the $S(q)$ calculations for the liposomes is the volume fraction of liposomes plus their encapsulated water cores.

9. (Optional) What is $\lim_{q\to 0} S(q)$ under the used sample conditions? Is it reasonable to ignore the structure factor effects and set S(q) to unity in the modelling of the data?

5.4.7 SANS and SAXS from spherical surfactant micelles

The anionic surfactant Sodium Dodecyl Sulphate (SDS) (see Fig. 5.6, left) is one of the main active components in ordinary dishwasher detergent. When dissolved in water, the SDS molecules self-organize into small spherical micelles, with the hydrophobic alkyl chains in the core of the micelles and the hydrophilic sodium sulphate head-groups surrounding the micelles (see Fig. 5.6, right). Assume that the aggregation number of the micelles, *i.e.* the average number of surfactant molecules per micelle, is 55 and that the micelles are perfectly monodisperse.

The partial specific mass density of SDS in water is 1.03 g/cm^3. The maximal extension, $l_{\max}$, and partial specific molecular volume, ν, of alkyl chains with n carbon atoms can be estimated from the so-called Tanford's formulas:

$$l_{\max} = (1.54 + 1.265 \times n)\text{Å},$$
$$\nu = (27.4 + 26.9 \times n)\text{Å}^3. \tag{5.34}$$

A combined SANS and SAXS experiment on SDS micelles in deuterated water (D_2O) is being planned (see section 5.2.9). Use the above information to calculate and sketch the excess scattering length density profiles, $\rho(r)$ of the micelles in water for neutrons and for X-rays (hint: See Fig. 5.7 for an example of an excess scattering length density profile from another surfactant micelle system.).

Calculate and plot the expected SAXS and SANS scattering intensity curves, i.e. the particle form factor in a q-range from 0.001 Å^{-1} to 0.5 Å^{-1}.

Estimate how a spread of the wavelength of the incoming beam, $\Delta\lambda/\lambda$ of 10% FWHM will affect the SAXS and SANS intensity curves.

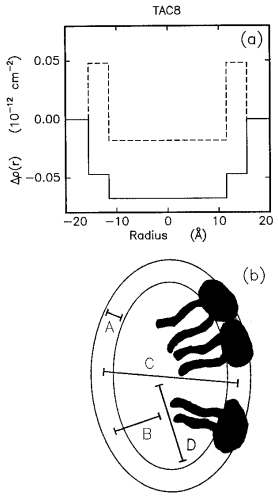

Figure 5.7: (a) Excess scattering length density profiles corresponding to a simple model of the TAC8 micelles assuming no hydration of the hydrophilic shell. The continuous line is for neutrons, and the broken line is for X-rays. (b) Cross-section of the prolate ellipsoidal TAC8 micelles. From Ref. [49].

In practice the micelles are polydisperse and can be described by a Gauss distribution with a reduced standard deviation $\sigma(R)/R = 20\%$. Discuss how this polydispersity affects the SAXS and SANS intensity curves, respectively.

Chapter 6

Neutron reflectivity

Author: Andrew Wildes, Institut Laue-Langevin

Reflectometry probes the properties of thin films and their interfaces, even if they are buried within a sample. The technique is non-destructive and it is straight-forward to present the measurements in absolute, dimensionless units.

The technique consists of measuring the reflected intensity of a beam from a flat sample as a function of the momentum transfer given by the beam to the sample. Reflectometry probes the refractive index, which is a quantity used to describe the propagation of waves in a medium relative to the propagation of waves in a vacuum. The refractive index can change significantly from medium to medium, and thus reflectometry determines the refractive index as a function of depth in the sample. The rate at which the refractive index changes as a function of depth will also depend on the quality and smoothness of the interfaces between media, and interface effects are also probed with reflectometry. As a result, reflectometry measurements with neutrons (and X-rays) are extremely important in the study of thin films and stratified media.

6.1 Thin films and interfaces

The definition of a "thin film" is certainly ambiguous. However in current scientific discussion "thin" refers to nanometer-sized length scales. Films with thicknesses of this order of magnitude are extremely important. In biology, examples include membranes and cell walls. In chemistry, examples include surfactants and catalysts. In physics there is a great deal of interest in low-dimensional magnetism and confinement effects. In addition, films and multilayers of these thicknesses are extensively used for information technology.

In all these scientific fields, it is important to determine what occurs at the interfaces on the properties of the film, and the influence of having a severe spatial constraint on the physical properties of the film. A thin film of a material

is highly unlikely to have the same properties of the same material in bulk, and the morphology of an interface can significantly change any interactions that can occur between two materials. Films can also be stacked to produce stratified layers, giving global properties to the material that are very different to the properties of the individual constituents.

6.2 The refractive index

The refractive index of a medium is a concept that is heavily used in optics. It relates to the fact that the traveling speed of a wave can vary when it travels though a medium. The refractive index of the material, n_m, is defined by

$$n_\mathrm{m} = \frac{\lambda_0}{\lambda_\mathrm{m}} = \frac{k_\mathrm{m}}{k_0}, \tag{6.1}$$

where λ_0 is the wavelength in the vacuum, λ_m is the wavelength in the medium, and likewise for the wavenumbers.

6.2.1 * Quantum mechanical derivation

The refractive index may be derived by solving a wave equation with the kinetic and potential energies for the wave in the medium. Neutron motion can be described by waves using quantum mechanics, and the relevant wave equation to describe their motion is given by:

$$\frac{\hbar^2}{2m_\mathrm{n}}\frac{d^2\psi}{dr^2} + \left(E - \overline{V}\right)\psi = 0, \tag{6.2}$$

where E is the total neutron energy.

The quantity $\overline{V}$ is the spatial average of the neutron potential, $V(\mathbf{r})$. A neutron propagating in a medium will see the average scattering length of all the nuclei in the medium,

$$\overline{V} = \frac{1}{\text{volume}}\int V(\mathbf{r})\, d\mathbf{r}. \tag{6.3}$$

This quantity is insensitive to the atomistic structure of the medium, hence the refractive index will be the same irrespective of whether the medium is liquid, amorphous, polycrystalline of monocrystalline. This is very different to the topic of neutron diffraction, which measures the arangement of the individual atoms (crystal structure). Equation (6.3) can be shown to rigorously hold, and the proof can be summarized by interpreting the solution of (6.2) as diffraction in the limit $q = 0$. The length scales probed by a diffraction experiment are proportional to q^{-1}. As $q \to 0$, the length scale thus becomes much larger than the distances between atoms. In the limit $q = 0$, all atoms scatter coherently, and thus (6.3) is valid.

Equation (6.2) may be rewritten in terms of its wavenumber, k,

$$\frac{\hbar^2}{2m}\frac{d^2\psi}{dr^2} + k^2\psi = 0, \tag{6.4}$$

where

$$k^2 = \frac{2m}{\hbar^2}\left(E - \overline{V}\right). \tag{6.5}$$

The mean potential for the neutron in a vacuum is equal to zero, $\overline{V} = 0$. The total energy, E, must always be conserved and is therefore always equal to the kinetic energy of the neutron when it travels in a vacuum,

$$E = \frac{\hbar^2 k_0^2}{2m}, \tag{6.6}$$

and thus the refractive index may be written

$$n^2 = 1 - \frac{\overline{V}}{E}. \tag{6.7}$$

6.2.2 Index of refraction from materials

In the absence of magnetism, the potential for the interaction of a neutron with a nucleus is given by the Fermi pseudo-potential

$$V_j(\mathbf{r}) = \frac{2\pi\hbar^2}{m_{\mathrm{n}}} b_j \delta\left(\mathbf{r} - \mathbf{r}_j\right). \tag{6.8}$$

Integrating equation (6.8) over the volume of the medium gives

$$\overline{V} = \frac{1}{\text{volume}} \int V_N\left(\mathbf{r}\right) d\mathbf{r} = \frac{2\pi\hbar^2}{m}\rho\bar{b}, \tag{6.9}$$

where ρ is the atomic number density and $\bar{b}$ is the average scattering length of all the nuclei in the medium. The refractive index is therefore sensitive to $\rho\bar{b}$, the *average scattering length density*, and is given by

$$n^2 = 1 - \frac{4\pi\rho\bar{b}}{k_0^2} = 1 - \frac{\lambda_0^2}{\pi}\rho\bar{b} \tag{6.10}$$

The refractive index is sometimes Taylor expanded and written

$$n \approx 1 - \frac{\lambda_0^2}{2\pi}\rho\bar{b}_c. \tag{6.11}$$

It may be noted that equations (6.1) to (6.7) also hold for X-rays, and that the final expression for the X-ray refractive index is very similar equation (6.10) with the difference that the scattering length density, $\rho\bar{b}_c$ for X-rays is given by the electron density multiplied by the classical electron radius, $\rho_e r_0$. The absorption cross-sections for X-rays is also much larger than those for neutrons and must always be included in the final expression for the refractive index.

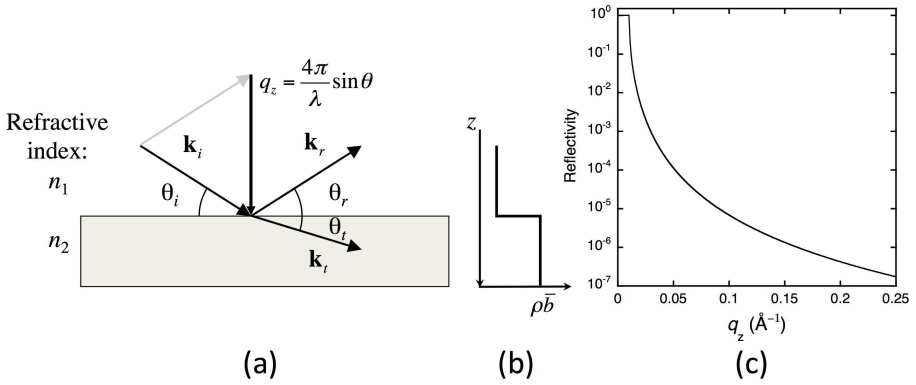

Figure 6.1: Schematics showing (a) the reflection and refraction of a wave at an interface between two media; (b) the scattering length density of the two media along the normal to the interface; (c) the calculated neutron reflectivity expected from an air/silicon interface.

6.3 Reflection from a smooth, flat interface

The potential for a wave changes at an interface between two media with different refractive indices. Through conservation of energy and momentum, the wave front at the interface splits in to a reflected part and a transmitted, or refracted, part. A schematic showing the effect is given in figure 6.1(a).

The incident wave is described by the wavevector $\mathbf{k}_i$ and subtends an angle θ_i with the interface. Part of the wave is reflected at the interface to give a reflected wave vector, $\mathbf{k}_r$, with a subtended angle θ_r. In the case of a perfectly flat interface the reflected angle equals the incident angle, $\theta_i = \theta_r$, and the momentum transfer to the wave is normal to the interface, hereafter defined as the z direction. This is known as *specular scattering*.

The solution to the wave equations describing the reflected and transmitted waves depends on only one spatial direction, and this is the z direction. An exact algebraic solution is known, and it comes from matching the amplitudes and phases of the incident, reflected, and transmitted waves at the interface. Because the equations are one-dimensional, articles often show the refractive index, and more specifically the scattering length density $\rho\bar{b}$, as a function of the depth z in the sample. These plots show the neutron potential, $\overline{V}$. An example for a single interface is shown in figure 6.1(b).

Part of the wavefront may be transmitted with angle θ_t to give a refracted wavevector $\mathbf{k}_t$. The wavelengths and angles in the two media are related through Snell's Law

$$n_1 \cos\theta_1 = n_2 \cos\theta_2. \tag{6.12}$$

In the schematic shown in figure 6.1, $\theta_1 = \theta_i$ and $\theta_2 = \theta_t$.

The amplitudes of the two waves are given by the Fresnel formulae from

classical optics theory. These give a reflectivity coefficient, r, and transmission coefficient, t, via the formulas

$$r = \frac{n_1 \sin\theta_1 - n_2 \sin\theta_2}{n_1 \sin\theta_1 + n_2 \sin\theta_2} = \frac{k_{1z} - k_{2z}}{k_{1z} + k_{2z}}, \tag{6.13}$$

$$t = \frac{2n_1 \sin\theta_1}{n_1 \sin\theta_1 + n_2 \sin\theta_2} = \frac{2k_{1z}}{k_{1z} + k_{2z}}, \tag{6.14}$$

where $k_{jz} = k_j \sin\theta_j$ is the component of the wavevector, $\mathbf{k}_j$, along the direction normal to the interface, z. The reflectivity, $\mathcal{R}$, is defined as the reflected intensity, I_r, divided by the incident intensity, I_0. It is an absolute, unitless quantity which can be measured experimentally in a relatively straightforward manner. It is related to the Fresnel reflectivity coefficient through the equation

$$\mathcal{R}(q_z) = \frac{I_r(q_z)}{I_0} = |r|^2. \tag{6.15}$$

The reflectivity is a function of the momentum components of the incident and refracted waves normal to the interface, and is here expressed as a function of the momentum transfer of the reflected wave, q_z. This momentum transfer is also normal to the interface and is equal to

$$q_z = \frac{4\pi}{\lambda_i} \sin\theta_i. \tag{6.16}$$

The calculated reflectivity of a neutron beam at the interface between air and a block of silicon is shown in figure 6.1(c). It shows a remarkable feature at small q_z and has a characteristic behaviour at large q_z that warrant closer inspection.

6.3.1 Total reflection

If $n_1 > n_2$, equation (6.12) shows that θ_2 can only be a real number for $n_2 \geq n_1 \cos\theta_1$. Beyond this limit the Fresnel reflection coefficient becomes imaginary and the reflectivity $\mathcal{R} = 1$. This commonly occurs for neutrons as equation (6.11) shows that the refractive index of a material with $\overline{b}_c > 0$ is less than one, and is therefore less than the refractive index for a vacuum. All the neutrons below a critical q_z will therefore be reflected.

The critical edge below which total reflection is observed is given by

$$q_c = \sqrt{16\pi\left(\rho_2\overline{b}_2 - \rho_1\overline{b}_1\right)}. \tag{6.17}$$

Equation 6.17 often expressed as a critical angle

$$\theta_c = \lambda_1\sqrt{\frac{\rho_2\overline{b}_2 - \rho_1\overline{b}_1}{\pi}} = \frac{\sqrt{4\pi\left(\rho_2\overline{b}_2 - \rho_1\overline{b}_1\right)}}{k_1}. \tag{6.18}$$

Equations (6.17) and (6.18) are generic, and they become simpler when one of the media is air or vacuum for which $\rho\overline{b} = 0$.

6.3.2 Reflection far from q_c

The approximation

$$k_{1z} + k_{2z} \approx q_z \tag{6.19}$$

is valid for $q_z >> q_c$. Rewriting the reflectivity coefficient as

$$r = \frac{k_{1z}^2 - k_{2z}^2}{(k_{1z} + k_{2z})^2} = \frac{q_c^2}{4(k_{1z} + k_{2z})^2} \tag{6.20}$$

leads to the observation that the reflectivity for large q_z will follow the relation

$$\mathcal{R}(q_z) \propto q_z^{-4}. \tag{6.21}$$

This expression is known as the *Porod Law* [50, 51]. It also holds for reflection from interfaces that do not have total reflection. We also saw this as the large q limit of the small angle scattering cross section in the previous chapter. At these values of q the beam is scattering from the interfaces between the liquid used as the solute and the objects suspended in the solute. In effect, these data represent the reflectivity from spherically averaged single interfaces.

6.3.3 Reflectivity as a scattering phenomenon

When describing reflectivity in terms of the sum of scattering from nuclei, the cross-section is given by the square of the Fourier transform of the function used to describe the object that scatters the neutrons. In the case of reflectivity, the function describes the refractive index as a function of depth. An example for a single interface is given in 6.1(b).

The Fourier transform of this function is proportional to q_z^{-1}. Squaring this function, and accounting for the surface area of the sample, gives the result that the cross-section is proportional to q_z^{-4}, which is the Porod Law. The first Born approximation can therefore be used to calculate reflectivity far from q_c.

However, a principal assumption of this formalism, known as the first Born approximation, is that the scattering must be weak. This is certainly not true as $q_z \to 0$. Even in samples without a critical edge, $\mathcal{R}(0) = 1$. The scattering at small q_z is always strong, and the first Born approximation fails in this regime. It does not predict total reflection or the presence of a critical edge, and gives $\mathcal{R}(0) \to \infty$.

6.4 Reflectivity of stratified media

Materials with numerous thin film overlayers are known as *stratified media*. These materials have numerous interfaces. Reflectivity methods are very useful for characterizing the sharpness of the interfaces and the scattering length densities, which give rise to the refractive index of the layers.

Calculating the reflectivity from stratified layers usually involve numbering the layers from the top of the sample to the bottom in the manner shown in figure

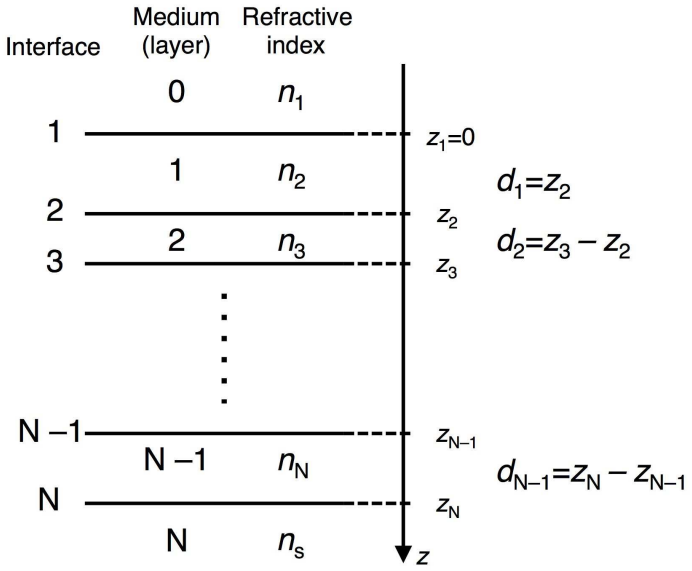

Figure 6.2: The numbering of a layered sample with N interfaces. The thickness of layer j is given by d_j.

6.2. Equations (6.13) and (6.14) may be adapted to give the Fresnel reflection and transmission coefficients at an interface between layers j and $j+1$, however this is insufficient to calculate the reflectivity. In addition to the reflected wave, the refracted wave, and the incident wave from above the interface horizon that were all described in section 6.3, a second incident wave from below the interface horizon must also be considered. This second incident wave is the reflected wave from interfaces deeper in the sample. The only interface where the second incident wave does not need to be considered is the deepest. Beyond this interface the sample is assumed to be infinitely thick.

Figure 6.3(a) shows a schematic example of the waves that must be considered when calculating the reflectivity from a single film on a substrate. The four waves that must be accounted for at the top interface between the refractive indices n_1 and n_2 are shown. The phase and the amplitude of the reflected wave from the bottom interface will be modified by the path length through the film and hence depends on the thickness, d, of the film. The amplitude of the wave is thus modified by the factor

$$a_j = \exp\left(-2ik_{jz}d_j\right). \tag{6.22}$$

The value of k_{jz} can be expressed as a function of the wavenumber in the topmost layer,

$$k_{jz} = k_j\sqrt{(1-\cos^2\theta_j)} = k_1\sqrt{\left(\frac{n_j^2}{n_1^2} - \cos^2\theta_1\right)}. \tag{6.23}$$

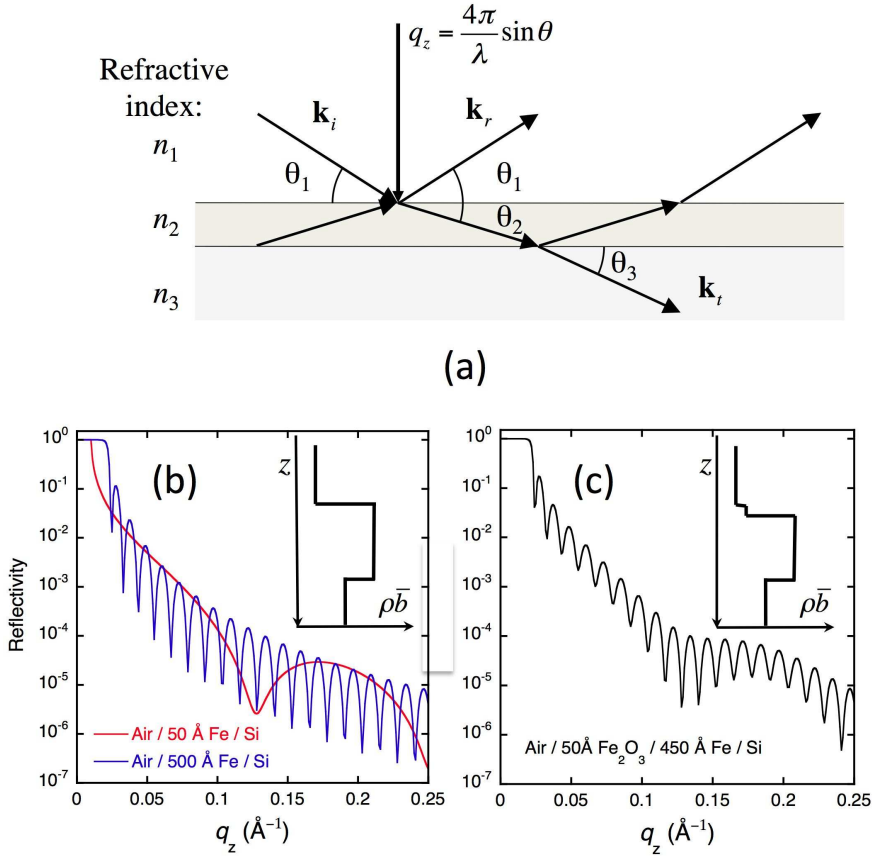

Figure 6.3: Figure showing reflection from stratified media. (a) Schematic showing the reflected and transmitted waves from a thin film sample. Note that four waves are needed to describe the scattering from each interface except the bottom-most interface where three waves are sufficient. (b) Example of reflection from a single iron film on silicon. Note that there are 10 minima from the 500 Å Fe film for every one from the 50 Å Fe film. (c) Example of reflection from a bilayer, with a 50 Å iron oxide film on 500 Å iron on silicon. The scattering length densities as a function of depth is shown in the inserts of (b) and (c).

The reflections from the different interfaces will interfere to give beats in the reflectivity. These beats are also known as 'Keissig' fringes. Figure 6.3(b) shows calculated examples of the reflectivity from a thin film of iron on silicon. The spacing between these fringes is approximately equal to 2π divided by the thickness of the film. This approximation becomes much better far from the critical edge. Nevertheless, the figure shows that the 500 Å film, being ten times thicker than the 50 Å film, always has 10 minima in the Keissig fringes for every one of the thinner film.

Further overlayers lead to further interference, and the final reflectivity comes from a coherent summation of the reflected and transmitted waves at every interface. Separate thicknesses cannot be explicitly determined just by looking at the data, however if the thicknesses of the layers and their refractive indices are sufficiently different (i.e. the *contrast* between the layers is sufficiently large) then some information can be inferred. Figure 6.3(c) shows a calculation for a thin oxide layer on a thicker iron layer. There are clearly two sets of beats present in the Keissig fringes and, from these, the thicknesses of the two layers can be inferred.

It is necessary to perform the complete summation in order to quantitatively analyse reflectivity data. There are two common methods of performing this calculation. The methods are mathematically identical.

6.4.1 The recursive method

This method is described by Parratt [52]. The layers of the sample are numbered as in figure 6.2, and the Fresnel reflection coefficients for each interface, j, are calculated after modifying equation 6.13 for reflection between layers $j-1$ and j,

$$r_{j-1,j} = \frac{k_{(j-1)z} - k_{jz}}{k_{(j-1)z} + k_{jz}}. \tag{6.24}$$

The reflection from the Nth interface is given by this Fresnel coefficient multiplied by the appropriate amplitude factor (equation (6.22))

$$R_{N-1,N} = a_{N-1} r_{N-1,N}. \tag{6.25}$$

This reflected wave is included in the calculation from the $j = (N-1)$th interface using a recursion formula

$$R_{j-1,j} = a_{j-1}^2 \left(\frac{R_{j,j+1} + r_{j-1,j}}{R_{j,j+1} r_{j-1,j} + 1} \right). \tag{6.26}$$

This recursion is continued to the first interface, noting that $a_0 = 1$, and the sample reflectivity is given by

$$\mathcal{R} = |R_{0,1}|^2 . \tag{6.27}$$

6.4.2 The characteristic matrix method

This method is described by Born and Wolf [53] from the work of Abelès [54]. A matrix is written for each of the layers $j = 1...N-1$ in figure 6.2, and has the form

$$\mathbf{M}_j = \begin{bmatrix} \cos(k_{jz}d_j) & -\frac{i}{p_j}\sin(k_{jz}d_j) \\ -ip_j\sin(k_{jz}d_j) & \cos(k_{jz}d_j) \end{bmatrix}, \tag{6.28}$$

with the definition that $p_j = n_j \sin\theta_j$. Note that this can be expressed as a function of the wavenumber and angle at the topmost layer in a similar manner to $k_j z$ in equation (6.23).

The matrices are then multiplied to give a final 2×2 matrix,

$$\mathbf{M}_{\mathcal{R}} = \mathbf{M}_1\mathbf{M}_2...\mathbf{M}_{N-1} = \begin{bmatrix} M_{11} & M_{12} \\ M_{21} & M_{22} \end{bmatrix}. \tag{6.29}$$

The resulting reflectivity coefficient is given by

$$r = \frac{(M_{11} + M_{12}p_N)\,p_1 - (M_{21} + M_{22}p_N)}{(M_{11} + M_{12}p_N)\,p_1 + (M_{21} + M_{22}p_N)}. \tag{6.30}$$

The matrix may also be expressed in terms of the Fresnel coefficients in equation (6.24),

$$\mathbf{C}_j = \begin{bmatrix} \exp ik_{jz}d_j & r_{j,j+1}\exp ik_{jz}d_j \\ r_{j,j+1}\exp -ik_{jz}d_j & \exp -ik_{jz}d_j \end{bmatrix}. \tag{6.31}$$

The matrices are then multiplied,

$$\mathbf{C}_{\mathcal{R}} = \mathbf{C}_1\mathbf{C}_2...\mathbf{C}_{N-1} = \begin{bmatrix} C_{11} & C_{12} \\ C_{21} & C_{22} \end{bmatrix}, \tag{6.32}$$

and the reflectivity coefficient is given by

$$r = \frac{C_{21}}{C_{11}}. \tag{6.33}$$

In both cases the reflectivity $\mathcal{R}$, is calculated from the reflectivity coefficient, r, using equation (6.15).

6.4.3 The relative merits of the two methods

Mathematically, the two methods are identical. The choice of which to use is essentially a question of which is the more efficiently written as computer code. Matrices, trigonometry, and the algebra of complex numbers are often complicated to code and slower to run when using low level computer languages, hence the recursive method is probably faster and easier to code. High level languages often have matrix algebra and complex numbers included in a software package, hence it may be easier to code reflectivity calculations when using the characteristic matrix method.

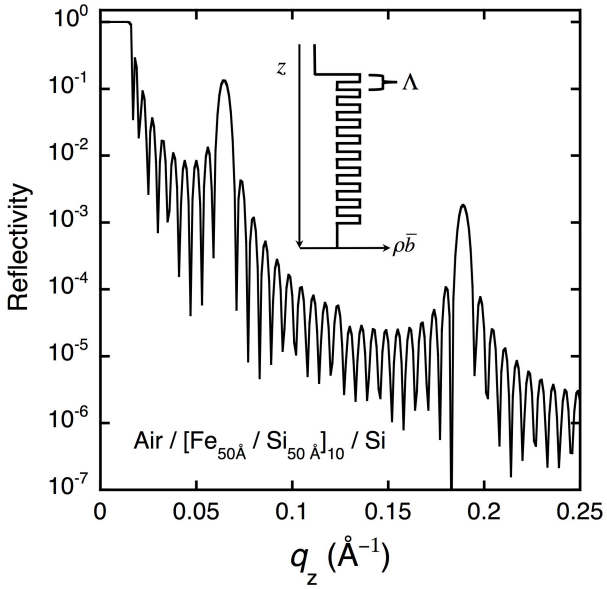

Figure 6.4: The reflectivity from a periodic iron/silicon multilayer. The insert shows a schematic of the scattering length density as a function of depth in the sample. The bilayer repeat distance is given be Λ.

6.5 Reflectivity of periodically stratified media

Periodically stratified media represent an important category of thin multilayer materials as certain physical aspects, for example optical or electronic properties, can be enhanced or suppressed depending on their structure. This behaviour can be exploited in technology, or in reflectivity experiments when the contribution from certain structural components in the sample can be increased.

An example of the scattering length density of a periodically stratified sample is shown in figure 6.4. The sample is formed of ten bilayers, each bilayer consisting of 50 Å Fe and 50 Å Si. The total thickness of the bilayer is therefore $\Lambda = 100$ Å.

The figure also shows the calculated reflectivity from the sample. Kiessig fringes are clearly visible with a spacing that corresponds roughly to the total thickness of the film. The reflectivity also shows peaks at multiples of $q_z \approx 2\pi/\Lambda$. These peaks are analogous to Bragg peaks, given by the periodicity of the layers in the sample. They are quite broad in q_z in the example, but become sharper as more bilayers are added. These peaks are usually quite far from q_c and can often be analysed using the first Born approximation. It must be noted that reflectivity is not sensitive to the atomic structure of the layers, and that these peaks will appear whether the layers are amorphous or monocrystalline. However, analysis of these peaks can give sensitive information about the structure of an individual period in the sample, in much the same

way as the analysis of Bragg peaks from single crystals can be used to determine atomic positions in a diffraction experiment.

In the example, the thicknesses of the two components of the bilayer are equivalent. This results in the even harmonics of the Bragg peaks to be suppressed, i.e. the Bragg peaks appear at $q_z \approx 2\pi M/\Lambda$, where $M = 1, 3, 5, ...$ If the thicknesses are not equivalent, the even harmonics will begin to appear. Reflectivity measurements at these positions are therefore very sensitive to the structural quality of the sample.

It may be noted that the reflectivity of the first harmonic is quite large. This has been exploited in modern neutron optics. If many bilayers are deposited such that Λ is slowly varied as a function of depth, the reflectivity will show many such intense Bragg peaks with slightly different q_z. The peaks will add together and give a high reflectivity that decreases slowly with increasing q_z. The net effect is almost as good as having a film with a very large q_c, even beyond $q_z = 0.1$ Å^{-1}. These films are the supermirrors we discussed in the chapter on neutron guides.

6.6 Rough and diffuse interfaces

Interfaces are never perfect, and the scattering length densities will never take the form of the step functions shown in figures 6.1(b), 6.3(b) and (c) and 6.4. In reality, the scattering length density will vary more continuously with depth either due to some level of grading across the interface, or due to roughness at the interface. Specular reflectivity cannot distinguish between interdiffusion and roughness, and in either case the scattering length variation must be accounted for in a valid reflectivity model.

In principle, the methods in sections 6.4.1 and 6.4.2 can explicitly be used. There is no upper or lower limit on the thicknesses, d_j, of each layer required for these methods. Interfaces can be modeled by introducing many thin layers with smoothly varying scattering length densities. This procedure is impractical, however, particularly if data are to be fitted.

A simpler method of accounting for interface width was proposed by Névot and Croce [55] and extended by Cowley and Ryan [56]. A model for the sample is constructed, much as has been the case in the previous examples. Each interface in the sample is assumed to have a Gaussian profile in z. Applying an appropriate Fourier transform over the interface modifies the Fresnel coefficients to:

$$\begin{aligned} r_{j-1,j} &= \frac{k_{(j-1)z}-k_{jz}}{k_{(j-1)z}+k_{jz}} \exp\left(-2k_{(j-1)z}k_{jz}\left\langle\sigma_j\right\rangle^2\right) \\ &\approx \frac{k_{(j-1)z}-k_{jz}}{k_{(j-1)z}+k_{jz}} \exp\left(-0.5\left[q_z\left\langle\sigma_j\right\rangle\right]^2\right), \end{aligned} \tag{6.34}$$

where σ_j defines the width of the Gaussian profile for the jth interface.

Equation (6.34) can be substituted directly for the Fresnel coefficients in equations (6.28) and (6.31) to include roughness in the calculations.

Chapter 7

Diffraction from crystals

Co-author: Bente Lebech, Technical University of Denmark

In crystalline solids, the atoms are organised in a regular pattern. We will here show how the interference between neutrons scattered elastically from atoms in a crystal leads to scattering only at particular "non-small" values of $\mathbf{q}$. This type of scattering is known as *diffraction* and is governed by the celebrated Bragg law.

By analyzing diffraction patterns from powders (a sample of randomly oriented μm- or nm-sized crystallites) or single crystals, it is possible to determine the crystal structure, lattice parameters, and atomic positions in crystalline materials. Neutron diffraction on powders and single crystals can be used also to determine magnetic structures, as briefly described in chapter 11.

7.1 Basic crystallography

We here give a brief introduction to the scientific field of *crystallography*, which is the study of the atomic arrangements in crystals, often seen in connection with organic and inorganic chemistry, mineralogy, or molecular biology (protein crystallography). Crystallography is a vast field in itself, and here we only touch the basics of it.

Crystal structures consist of ordered arrangements of groups of atoms (or molecules) placed within two- or three-dimensional space filling lattices. The overall symmetry of a crystal structure is determined by the underlying crystal lattice and by application of certain symmetry elements. In mathematical terms these symmetry elements are called congruent, isometric transformations. They may be translations, rotations and screws (direct congruent) or inversions, reflections and glides (opposite congruent). See reference [57] for further details.

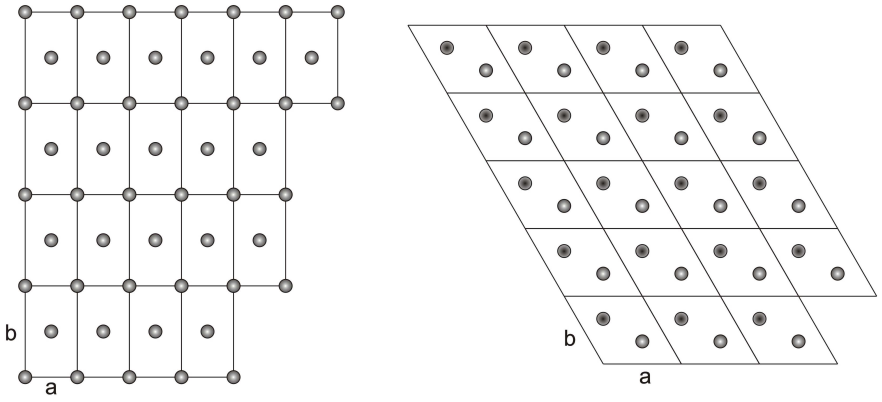

Figure 7.1: Examples of two-dimensional crystals formed by translation of two-dimensional unit cells, each consisting of two atoms, (a) $a \neq b$, $\gamma = 90°$ and (b) $a = b$, $\gamma = 120°$.

7.1.1 Lattice vectors

In a regular crystal, the atoms are arranged in a three-dimensional periodic structure; a *lattice*. It is possible to divide the crystal into a (large) number of identical unit cells, each containing one or more atoms. The position of a unit cell can be determined by just three integers, n_a, n_b, and n_c:

$$\boxed{\mathbf{r} = n_a\mathbf{a} + n_b\mathbf{b} + n_c\mathbf{c}}, \tag{7.1}$$

where the vectors $\mathbf{a}$, $\mathbf{b}$, and $\mathbf{c}$ are called the *lattice vectors*. The length of the lattice vectors are called the *lattice constants*, a, b, and c, respectively. Usually, but not always, the order is chosen so that $a \leq b \leq c$.

Two-dimensional crystal lattices are simple to visualise, and two examples are shown in Fig. 7.1. More realistic crystal lattices are three-dimensional, where the shape of a unit cell is a parallelepiped spanned by the three (right handed) lattice vectors, as shown in Fig. 7.2. The angles in the unit cell are defined with α being the angle between $\mathbf{b}$ and $\mathbf{c}$, β being the angle between $\mathbf{c}$ and $\mathbf{a}$, and γ the angle between $\mathbf{a}$ and $\mathbf{b}$. The volume of a unit cell is given by the volume product

$$V_0 = \mathbf{a} \cdot \mathbf{b} \times \mathbf{c}. \tag{7.2}$$

This product is positive due to the right-handedness of the lattice vectors.

7.1.2 The reciprocal lattice

It is convenient to define the *reciprocal lattice vectors* by

$$\mathbf{a}^* = \frac{2\pi}{V_0}\mathbf{b} \times \mathbf{c}, \qquad \mathbf{b}^* = \frac{2\pi}{V_0}\mathbf{c} \times \mathbf{a}, \qquad \mathbf{c}^* = \frac{2\pi}{V_0}\mathbf{a} \times \mathbf{b}. \tag{7.3}$$

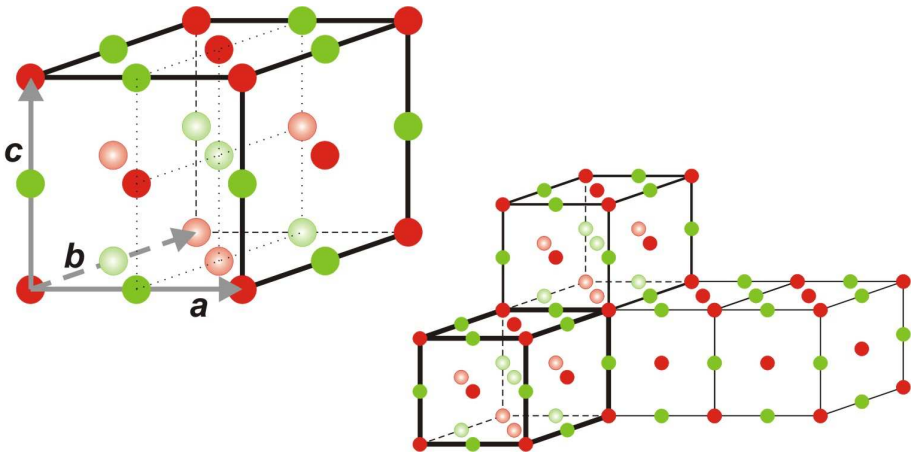

Figure 7.2: A typical three-dimensional cubic crystal structure (NaCl) with two kinds of atoms, in total 8 atoms in the unit cell. The figure shows one unit cell with three lattice vectors, $a = b = c$, and the three-dimensional lattice formed by repetition of the unit cell.

Each reciprocal lattice vector is perpendicular to two of the three real-space lattice vectors:

$$\mathbf{a}^* \cdot \mathbf{b} = \mathbf{a}^* \cdot \mathbf{c} = 0, \qquad \mathbf{b}^* \cdot \mathbf{a} = \mathbf{b}^* \cdot \mathbf{c} = 0, \qquad \mathbf{c}^* \cdot \mathbf{a} = \mathbf{c}^* \cdot \mathbf{b} = 0, \tag{7.4}$$

whereas

$$\mathbf{a}^* \cdot \mathbf{a} = 2\pi, \qquad \mathbf{b}^* \cdot \mathbf{b} = 2\pi, \qquad \mathbf{c}^* \cdot \mathbf{c} = 2\pi. \tag{7.5}$$

The three reciprocal lattice vectors span the *reciprocal lattice*, where a general lattice point is given by

$$\boxed{\boldsymbol{\tau}_{hkl} = h\mathbf{a}^* + k\mathbf{b}^* + l\mathbf{c}^*}. \tag{7.6}$$

The *Miller indices* h, k, and l are here integers. The *lattice spacing* corresponding to a set of Miller indices is defined as the distance between lattice planes perpendicular to $\boldsymbol{\tau}_{hkl}$ and is given by

$$d_{hkl} = \frac{2\pi}{|\boldsymbol{\tau}_{hkl}|}. \tag{7.7}$$

From (7.1) and (7.6), we calculate the dot product between a general lattice vector and a general vector of the reciprocal lattice:

$$\boldsymbol{\tau}_{hkl} \cdot \mathbf{r} = 2\pi(n_a h + n_b k + n_c l). \tag{7.8}$$

This result will be used in later derivations.

It can easily be shown that the volume of the reciprocal unit cell is given by

$$V_{\mathrm{r}} = \frac{(2\pi)^3}{V_0}. \tag{7.9}$$

It is possible to make a reciprocal space unit cell of volume V_r, which is centered around the origin and in which each point is located closer to the origin than to any reciprocal lattice vector. This cell is called the *Brillouin zone* and is discussed in detail in most textbooks on solid state physics [58].

7.1.3 Atomic positions in the unit cell

A particular simple class of lattices is the *Bravais lattice*, defined as a lattice where each unit cell contains only one atom. Hence, a Bravais lattices are found only among the pure elements, since each unit cell must contain at least one formula unit. In a Bravais lattice, the atomic positions are given directly by (7.1).

By far most lattices are non-Bravais lattices. Here, each unit cell consists of more than one atom, and their relative positions within the unit cell are given by their *basis*, denoted $\mathbf{\Delta}$. The absolute position of the i'th atom in the j'th unit cell is thus

$$\mathbf{r}_{i,j} = \mathbf{r}_j + \mathbf{\Delta}_i, \tag{7.10}$$

where $\mathbf{r}_j$ is the position of the j'th unit cell.

One often encountered example of a lattice with a basis is the *body-centered* cubic lattice (see figure 7.3). This lattice can be described as a simple cubic lattice of side length a with a two-atom basis. One atom is placed at $\mathbf{\Delta}_0 = (0, 0, 0)$, and the other at $\mathbf{\Delta}_1 = (1/2, 1/2, 1/2)\, a$.

7.1.4 Symmetry groups

According to the symmetry properties, ordered arrangements of atoms are divided into 17 two-dimensional and 230 three-dimensional space groups. Below we describe the 7 groups of crystal lattices covering all three-dimensional space-groups sorted by decreasing symmetry. The meaning of the parenthesized letters after the lattice names will be explained later.

1. **Cubic** (P, I, or F). This is the class of highest symmetry and has a 4-fold symmetry. All lattice constants are equal, and the lattice vectors are mutually perpendicular. Thus, the unit cells are cubes: $a = b = c$, $\alpha = \beta = \gamma = 90°$.

2. **Hexagonal** (P). This is a crystal class with a 6-fold symmetry axis: $a = b \neq c$, $\alpha = \beta = 90°$, and $\gamma = 120°$.

3. **Trigonal** (R). This can be seen as an angular distortion of the cubic lattice. Trigonal structures are often described by hexagonal cells with the c-axis along the rhombic body diagonal: $a = b = c$, $\alpha = \beta = \gamma \neq 90°$.

4. **Tetragonal** (P or I). This class can be seen as a distortion of a the cubic crystal along one axis, keeping all vectors perpendicular: $a = b \neq c$, $\alpha = \beta = \gamma = 90°$.

5. **Orthorhombic** (P, C, I, or F). This is a further distortion of a tetragonal crystal, still keeping the unit vectors perpendicular: $a \neq b \neq c$, $\alpha = \beta = \gamma = 90°$.

6. **Monoclinic** (PB or PC). An angular distortion of an orthorhombic crystal: $a \neq b \neq c$, $\alpha = \beta = 90°$, $\gamma \neq 90°$.

7. **Triclinic** (P). The lowest symmetry class, where the lattice is a parallepiped without any relation between axis and angles: $a \neq b \neq c$, $\alpha \neq 90°$, $\beta \neq 90°$, $\gamma \neq 90°$.

7.1.5 Crystal structures and symmetries

The knowledge of the classification in 230 space groups is highly useful when determining crystal structures. Details of the symmetry aspects of these space-groups are collected in various versions of "The International Tables for Crystallography" (in this text abbreviated "IT") [59, 60]. Here, we will give a rudimentary introduction to three-dimensional crystal structures and their classification and describe how to interpret the information given in IT and how to use it when refining a crystal structure from real experimental or simulated diffraction data.

In its simplest form a crystal structure is formed by placing one atom within a lattice and applying a number of symmetry elements which are consistent with the geometry of the underlying lattice to the coordinates of the first atom. Naturally, the symmetry of the structure increases with the number of symmetry elements. In [59], the site positions of atoms in the possible two- and three-dimensional space groups are listed according to the crystal lattices and the applied symmetry elements.

The space group with the lowest symmetry and space group number "1" is triclinic P1. Within the unit cell this space group has just one atom site position per atom type with coordinates (x, y, z). The symmetry element is a translation of the unit cell or, equivalently, rotation by 360°. The space group with the second lowest symmetry (translation of the unit cell) and space group number "2" is also triclinic $P\bar{1}$, but in addition to translation symmetry it has an inversion centre. Hence, within the unit cell this space group has two atom site positions per atom type with general coordinates (x, y, z) and $(-x, -y, -z)$.

The space group with the highest symmetry and space group number 230 is cubic $Ia\bar{3}d$. Within the unit cell this space group has 96 atom sites per atom type. The set of 96 coordinates (x_i, y_i, z_i) are generated by the coordinates of a single atom site per atom type (x_1, y_1, z_1) after application of the space group symmetry elements (see section 7.1.6).

The space group listings in IT are each described by a number and a combination of letters and numbers. The numbers represent the rotational symmetry (1-, 2-, 3-, 4- or 6-fold rotation) of the space group and small letters represent certain symmetry elements (e.g. m for mirror line or plane and represent 1- or 3-fold rotations plus inversions through centre). The first letter is always a capital. It indicates if some vectors in the crystal lattice are related in a non-trivial

way and possess symmetry other than the identity. These letters are shown in parenthesis in the listing (1 to 7) of the lattice types given above. The letter P means primitive, i.e. the only symmetry imposed by the lattice is the identity, F means face centered, *i.e.*, for the smallest possible unit cell, the lattice symmetry automatically generates atom sites at $(x, y, z) + \bar{d}_f$ where $\bar{d}_f$ equals half a face diagonal. The letter I means body centered which is a translation from German "innen zentrierte", *i.e.* the lattice symmetry automatically generates atom sites at $(x, y, z) + \bar{d}_b$ where $\bar{d}_b$ equals half a body diagonal. For more complicated crystal lattices other capitals are used to signify specific lattice related symmetries. The most important ones are R (rhombohedral) used for trigonal space groups and C (base centered) used for some orthorhombic and monoclinic space groups.

Fig. 7.3(a) shows a body centered cubic (bcc) structure. Figures 7.3(b) and (d) illustrates face centered cubic (fcc) structures with one and two types of atoms, respectively. Figures 7.3(a) and (b) also represents two of the 14 three-dimensional Bravais lattices. By definition, Bravais lattices contain only a single atom per unit cell which is obviously not the case for the cubic structures shown in 7.3(a) and (b). However, the smallest space filling units for fcc and bcc monoatomic crystals are not cubic, but rhombohedral as shown by the true yellow unit cell in 7.3(a) and indicated by the three yellow rhombohedral axes shown in 7.3(b). The bcc and fcc Bravais structures are to be considered in more detail in problem 7.7.2. Certain properties of structures with non-Bravais lattices will be considered in exercise 7.7.3.

Another important structure is the *hexagonal closed packed* (hcp) lattice, which is a cell with a two-atom basis. Regarding the hcp lattice, it is important to notice that the distance between all nearest neighbour atoms are equal, and that it represents the closest possible packing of spheres (a property it shares with the fcc lattice). The hcp crystal will also be treated in problem 7.7.2.

7.1.6 How to use the information in IT

To refine diffraction data with standard programs, you need information about the possible atom positions in the simulated structure and their approximate occupancies. An explanation of how to obtain this information by means of "IT" is given in the following and can be used to solve exercise 7.7.4.

Before attempting a structure refinement you will usually know the chemistry of your sample and have a rough idea about the crystal structure from other works (publications or databases) either obtained in the form of X-ray or neutron diffraction experimental data or, more unusual, from clever guesses. If the structure is known from publications as is the case for the tetragonal phase of the high-temperature superconductor $YBa_2Cu_3O_{6+x}$ shown in Fig. 7.4(b) for $x = 0.18$, the information may be in the form of a space group name or number (*e.g.* P4/mmm, (D^1_{4h}), or # 123, see fig. 7.5) with lattice parameters $a = b \neq c$ and $\alpha = \beta = \gamma = 90°$. The coordinates of the atoms are called site positions and written in an abbreviated form which will be described shortly. For $YBa_2Cu_3O_{6+x}$ the site positions are: Y-atoms at ($1d$), Ba-atoms at ($2h$),

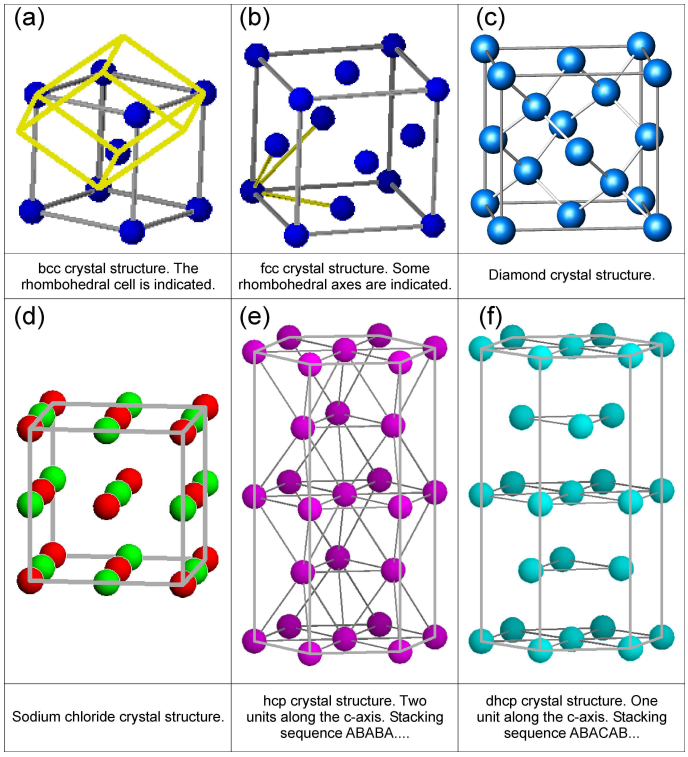

Figure 7.3: An illustration of some important simple crystal structures.

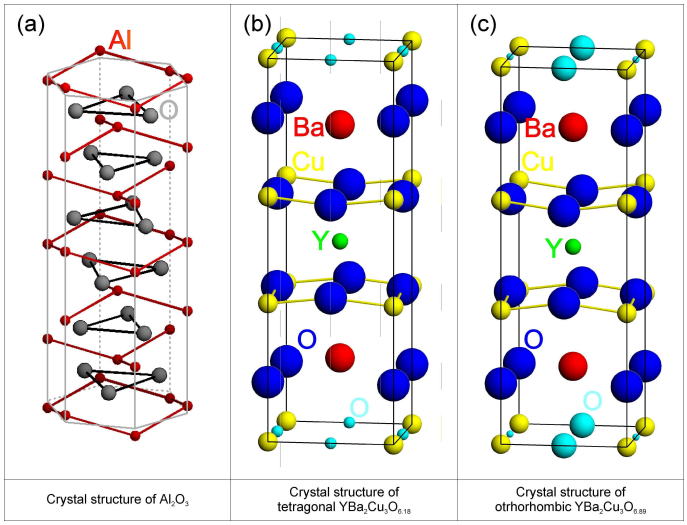

Figure 7.4: Illustration of some more complicated crystal structures. The small sized cyan O-atoms in (b) are not fully occupied. The small and medium sized cyan O-atoms in (c) indicate that some O-content are assumed to be statistically distributed between two sites.

Cu-atoms at $(1a)$ and $(2g)$, and O-atoms at $(2f)$, $(2g)$, and $(4i)$.

Depending on the O-concentration, x, and the temperature, $YBa_2Cu_3O_{6+x}$ undergoes a structural phase change from the tetragonal structure to an orthorhombic structure. The corresponding description of the orthorhombic structure usually named $YBa_2Cu_3O_{7-x}$ is shown in Fig. 7.4(c) for $x = 0.11$. The space group is Pmmm, (D^1_{2h}), or # 47 (see Fig. 7.6) with lattice parameters $a \neq b \neq c$ and $\alpha = \beta = \gamma = 90°$. The possible site positions for the atoms in $YBa_2Cu_3O_{7-x}$ are as follows: Y-atoms at $(1h)$, Ba-atoms at $(2t)$, Cu-atoms at $(1a)$ and $(2q)$ and O-atoms at $(1b)$ or $(1e)$, $(2q)$, $(2r)$, and $(2s)$.

In order to explain the meaning of the parenthesised number/letter codes for the site positions quoted above we use the space group example in Fig. 7.7. The figure lists the possible coordinates of atoms in the (fcc) cubic space group # 225, $Fm\bar{3}m$, or (O^5_h). The first column to the left shows the number of atoms with coordinates listed in columns 4 to 9. Because of the space group symmetry, one general atom coordinate set (x, y, z) results in 191 other atom coordinates (192 general sites) unless there are special relations between x, y, and z (denoted *special sites*). Thus, $x = y = z$ only results in 32 sets of atom coordinates. The 192 general sites are obtained by adding face centered coordinates to the 48 atom coordinates listed in the first group of coordinate sets in Fig. 7.7. The fact that the space group is face centered is indicated both by the F in the space group name and the four coordinates (0,0,0; 0,1/2,1/2; 1/2,0,1/2; 1/2,1/2,0)+ written just above the general site coordinates in Fig. 7.7. In the following we use N_G for the total number of positions at the general site and N_S for the total

CONTINUED **No. 123** $P4/mmm$

Generators selected (1); $t(1,0,0)$; $t(0,1,0)$; $t(0,0,1)$; (2); (3); (5); (9)

Positions

Multiplicity, Wyckoff letter, Site symmetry			Coordinates				Reflection conditions
							General:
16	u	1	(1) x,y,z (5) $\bar{x},y,\bar{z}$ (9) $\bar{x},\bar{y},\bar{z}$ (13) $x,\bar{y},z$	(2) $\bar{x},\bar{y},z$ (6) $x,\bar{y},\bar{z}$ (10) $x,y,\bar{z}$ (14) $\bar{x},y,z$	(3) $\bar{y},x,z$ (7) $y,x,\bar{z}$ (11) $y,\bar{x},\bar{z}$ (15) $\bar{y},\bar{x},z$	(4) $y,\bar{x},z$ (8) $\bar{y},\bar{x},\bar{z}$ (12) $\bar{y},x,\bar{z}$ (16) y,x,z	no conditions
							Special:
8	t	$.m.$	$x,\frac{1}{2},z$ $\bar{x},\frac{1}{2},\bar{z}$	$\bar{x},\frac{1}{2},z$ $x,\frac{1}{2},\bar{z}$	$\frac{1}{2},x,z$ $\frac{1}{2},x,\bar{z}$	$\frac{1}{2},\bar{x},z$ $\frac{1}{2},\bar{x},\bar{z}$	no extra conditions
8	s	$.m.$	$x,0,z$ $\bar{x},0,\bar{z}$	$\bar{x},0,z$ $x,0,\bar{z}$	$0,x,z$ $0,x,\bar{z}$	$0,\bar{x},z$ $0,\bar{x},\bar{z}$	no extra conditions
8	r	$..m$	x,x,z $\bar{x},x,\bar{z}$	$\bar{x},\bar{x},z$ $x,\bar{x},\bar{z}$	$\bar{x},x,z$ $x,x,\bar{z}$	$x,\bar{x},z$ $\bar{x},\bar{x},\bar{z}$	no extra conditions
8	q	$m..$	$x,y,\frac{1}{2}$ $\bar{x},y,\frac{1}{2}$	$\bar{x},\bar{y},\frac{1}{2}$ $x,\bar{y},\frac{1}{2}$	$\bar{y},x,\frac{1}{2}$ $y,x,\frac{1}{2}$	$y,\bar{x},\frac{1}{2}$ $\bar{y},\bar{x},\frac{1}{2}$	no extra conditions
8	p	$m..$	$x,y,0$ $\bar{x},y,0$	$\bar{x},\bar{y},0$ $x,\bar{y},0$	$\bar{y},x,0$ $y,x,0$	$y,\bar{x},0$ $\bar{y},\bar{x},0$	no extra conditions
4	o	$m2m.$	$x,\frac{1}{2},\frac{1}{2}$	$\bar{x},\frac{1}{2},\frac{1}{2}$	$\frac{1}{2},x,\frac{1}{2}$	$\frac{1}{2},\bar{x},\frac{1}{2}$	no extra conditions
4	n	$m2m.$	$x,\frac{1}{2},0$	$\bar{x},\frac{1}{2},0$	$\frac{1}{2},x,0$	$\frac{1}{2},\bar{x},0$	no extra conditions
4	m	$m2m.$	$x,0,\frac{1}{2}$	$\bar{x},0,\frac{1}{2}$	$0,x,\frac{1}{2}$	$0,\bar{x},\frac{1}{2}$	no extra conditions
4	l	$m2m.$	$x,0,0$	$\bar{x},0,0$	$0,x,0$	$0,\bar{x},0$	no extra conditions
4	k	$m.2m$	$x,x,\frac{1}{2}$	$\bar{x},\bar{x},\frac{1}{2}$	$\bar{x},x,\frac{1}{2}$	$x,\bar{x},\frac{1}{2}$	no extra conditions
4	j	$m.2m$	$x,x,0$	$\bar{x},\bar{x},0$	$\bar{x},x,0$	$x,\bar{x},0$	no extra conditions
4	i	$2mm.$	$0,\frac{1}{2},z$	$\frac{1}{2},0,z$	$0,\frac{1}{2},\bar{z}$	$\frac{1}{2},0,\bar{z}$	hkl : $h+k=2n$
2	h	$4mm$	$\frac{1}{2},\frac{1}{2},z$	$\frac{1}{2},\frac{1}{2},\bar{z}$			no extra conditions
2	g	$4mm$	$0,0,z$	$0,0,\bar{z}$			no extra conditions
2	f	$mmm.$	$0,\frac{1}{2},0$	$\frac{1}{2},0,0$			hkl : $h+k=2n$
2	e	$mmm.$	$0,\frac{1}{2},\frac{1}{2}$	$\frac{1}{2},0,\frac{1}{2}$			hkl : $h+k=2n$
1	d	$4/mmm$	$\frac{1}{2},\frac{1}{2},\frac{1}{2}$				no extra conditions
1	c	$4/mmm$	$\frac{1}{2},\frac{1}{2},0$				no extra conditions
1	b	$4/mmm$	$0,0,\frac{1}{2}$				no extra conditions
1	a	$4/mmm$	$0,0,0$				no extra conditions

Symmetry of special projections

Along [001] $p4mm$
$\mathbf{a}' = \mathbf{a}$ $\mathbf{b}' = \mathbf{b}$
Origin at $0,0,z$

Along [100] $p2mm$
$\mathbf{a}' = \mathbf{b}$ $\mathbf{b}' = \mathbf{c}$
Origin at $x,0,0$

Along [110] $p2mm$
$\mathbf{a}' = \frac{1}{2}(-\mathbf{a}+\mathbf{b})$ $\mathbf{b}' = \mathbf{c}$
Origin at $x,x,0$

(*Continued on preceding page*)

Figure 7.5: Sections from [59], for space groups no. 123 ($YBa_2Cu_3O_{6.18}$) showing

CONTINUED **No. 47** ***Pmmm***

Generators selected (1); $t(1,0,0)$; $t(0,1,0)$; $t(0,0,1)$; (2); (3); (5)

Positions

Multiplicity, Wyckoff letter, Site symmetry			Coordinates				Reflection conditions
							General:
8	α	1	(1) x,y,z (5) $\bar{x},\bar{y},\bar{z}$	(2) $\bar{x},\bar{y},z$ (6) $x,y,\bar{z}$	(3) $\bar{x},y,\bar{z}$ (7) $x,\bar{y},z$	(4) $x,\bar{y},\bar{z}$ (8) $\bar{x},y,z$	no conditions
							Special: no extra conditions
4	z	. . m	$x,y,\frac{1}{2}$	$\bar{x},\bar{y},\frac{1}{2}$	$\bar{x},y,\frac{1}{2}$	$x,\bar{y},\frac{1}{2}$	
4	y	. . m	$x,y,0$	$\bar{x},\bar{y},0$	$\bar{x},y,0$	$x,\bar{y},0$	
4	x	. m .	$x,\frac{1}{2},z$	$\bar{x},\frac{1}{2},z$	$\bar{x},\frac{1}{2},\bar{z}$	$x,\frac{1}{2},\bar{z}$	
4	w	. m .	$x,0,z$	$\bar{x},0,z$	$\bar{x},0,\bar{z}$	$x,0,\bar{z}$	
4	v	m . .	$\frac{1}{2},y,z$	$\frac{1}{2},\bar{y},z$	$\frac{1}{2},y,\bar{z}$	$\frac{1}{2},\bar{y},\bar{z}$	
4	u	m . .	$0,y,z$	$0,\bar{y},z$	$0,y,\bar{z}$	$0,\bar{y},\bar{z}$	
2	t	$m\,m\,2$	$\frac{1}{2},\frac{1}{2},z$	$\frac{1}{2},\frac{1}{2},\bar{z}$			
2	s	$m\,m\,2$	$\frac{1}{2},0,z$	$\frac{1}{2},0,\bar{z}$			
2	r	$m\,m\,2$	$0,\frac{1}{2},z$	$0,\frac{1}{2},\bar{z}$			
2	q	$m\,m\,2$	$0,0,z$	$0,0,\bar{z}$			
2	p	$m\,2\,m$	$\frac{1}{2},y,\frac{1}{2}$	$\frac{1}{2},\bar{y},\frac{1}{2}$			
2	o	$m\,2\,m$	$\frac{1}{2},y,0$	$\frac{1}{2},\bar{y},0$			
2	n	$m\,2\,m$	$0,y,\frac{1}{2}$	$0,\bar{y},\frac{1}{2}$			
2	m	$m\,2\,m$	$0,y,0$	$0,\bar{y},0$			
2	l	$2\,m\,m$	$x,\frac{1}{2},\frac{1}{2}$	$\bar{x},\frac{1}{2},\frac{1}{2}$			
2	k	$2\,m\,m$	$x,\frac{1}{2},0$	$\bar{x},\frac{1}{2},0$			
2	j	$2\,m\,m$	$x,0,\frac{1}{2}$	$\bar{x},0,\frac{1}{2}$			
2	i	$2\,m\,m$	$x,0,0$	$\bar{x},0,0$			
1	h	$m\,m\,m$	$\frac{1}{2},\frac{1}{2},\frac{1}{2}$				
1	g	$m\,m\,m$	$0,\frac{1}{2},\frac{1}{2}$				
1	f	$m\,m\,m$	$\frac{1}{2},\frac{1}{2},0$				
1	e	$m\,m\,m$	$0,\frac{1}{2},0$				
1	d	$m\,m\,m$	$\frac{1}{2},0,\frac{1}{2}$				
1	c	$m\,m\,m$	$0,0,\frac{1}{2}$				
1	b	$m\,m\,m$	$\frac{1}{2},0,0$				
1	a	$m\,m\,m$	$0,0,0$				

Symmetry of special projections

Along [001] $p2mm$
$\mathbf{a}' = \mathbf{a}$ $\mathbf{b}' = \mathbf{b}$
Origin at $0,0,z$

Along [100] $p2mm$
$\mathbf{a}' = \mathbf{b}$ $\mathbf{b}' = \mathbf{c}$
Origin at $x,0,0$

Along [010] $p2mm$
$\mathbf{a}' = \mathbf{c}$ $\mathbf{b}' = \mathbf{a}$
Origin at $0,y,0$

Maximal non-isomorphic subgroups

I [2] $Pmm2$ (25) 1; 2; 7; 8
[2] $Pm2m$ ($Pmm2$, 25) 1; 3; 6; 8
[2] $P2mm$ ($Pmm2$, 25) 1; 4; 6; 7
[2] $P222$ (16) 1; 2; 3; 4
[2] $P112/m$ ($P2/m$, 10) 1; 2; 5; 6
[2] $P12/m1$ ($P2/m$, 10) 1; 3; 5; 7
[2] $P2/m11$ ($P2/m$, 10) 1; 4; 5; 8

(*Continued on preceding page*)

Figure 7.6: Sections from [59], for space groups no. 47 ($YBa_2Cu_3O_{6.89}$) showing the

$Fm3m$ O_h^5

No. 225 $F\,4/m\,\bar{3}\,2/m$ $m\,3\,m$ Cubic

Origin at centre ($m3m$)

Number of positions, Wyckoff notation, and point symmetry			Co-ordinates of equivalent positions (0,0,0; 0,½,½; ½,0,½; ½,½,0)+	Conditions limiting possible reflections
				General:
192	l	1	x,y,z; z,x,y; y,z,x; x,z,y; y,x,z; z,y,x; $x,\bar{y},\bar{z}$; $z,\bar{x},\bar{y}$; $y,\bar{z},\bar{x}$; $x,\bar{z},\bar{y}$; $y,\bar{x},\bar{z}$; $z,\bar{y},\bar{x}$; $\bar{x},y,\bar{z}$; $\bar{z},x,\bar{y}$; $\bar{y},z,\bar{x}$; $\bar{x},z,\bar{y}$; $\bar{y},x,\bar{z}$; $\bar{z},y,\bar{x}$; $\bar{x},\bar{y},z$; $\bar{z},\bar{x},y$; $\bar{y},\bar{z},x$; $\bar{x},\bar{z},y$; $\bar{y},\bar{x},z$; $\bar{z},\bar{y},x$; $\bar{x},\bar{y},\bar{z}$; $\bar{z},\bar{x},\bar{y}$; $\bar{y},\bar{z},\bar{x}$; $\bar{x},\bar{z},\bar{y}$; $\bar{y},\bar{x},\bar{z}$; $\bar{z},\bar{y},\bar{x}$; $\bar{x},y,z$; $\bar{z},x,y$; $\bar{y},z,x$; $\bar{x},z,y$; $\bar{y},x,z$; $\bar{z},y,x$; $x,\bar{y},z$; $z,\bar{x},y$; $y,\bar{z},x$; $x,\bar{z},y$; $y,\bar{x},z$; $z,\bar{y},x$; $x,y,\bar{z}$; $z,x,\bar{y}$; $y,z,\bar{x}$; $x,z,\bar{y}$; $y,x,\bar{z}$; $z,y,\bar{x}$.	hkl: $h+k,k+l,(l+h)=2n$ hhl: $(l+h=2n)$; ↻ $0kl$: $(k,l=2n)$; ↻
				Special: as above, plus
96	k	m	x,x,z; z,x,x; x,z,x; $\bar{x},\bar{x},\bar{z}$; $\bar{z},\bar{x},\bar{x}$; $\bar{x},\bar{z},\bar{x}$; $x,\bar{x},\bar{z}$; $z,\bar{x},\bar{x}$; $x,\bar{z},\bar{x}$; $\bar{x},x,z$; $\bar{z},x,x$; $\bar{x},z,x$; $\bar{x},x,\bar{z}$; $\bar{z},x,\bar{x}$; $\bar{x},z,\bar{x}$; $x,\bar{x},z$; $z,\bar{x},x$; $x,\bar{z},x$; $\bar{x},\bar{x},z$; $\bar{z},\bar{x},x$; $\bar{x},\bar{z},x$; $x,x,\bar{z}$; $z,x,\bar{x}$; $x,z,\bar{x}$.	
96	j	m	$0,y,z$; $z,0,y$; $y,z,0$; $0,z,y$; $y,0,z$; $z,y,0$; $0,\bar{y},\bar{z}$; $\bar{z},0,\bar{y}$; $\bar{y},\bar{z},0$; $0,\bar{z},\bar{y}$; $\bar{y},0,\bar{z}$; $\bar{z},\bar{y},0$; $0,y,\bar{z}$; $\bar{z},0,y$; $y,\bar{z},0$; $0,\bar{z},y$; $y,0,\bar{z}$; $\bar{z},y,0$; $0,\bar{y},z$; $z,0,\bar{y}$; $\bar{y},z,0$; $0,z,\bar{y}$; $\bar{y},0,z$; $z,\bar{y},0$.	no extra conditions
48	i	mm	½,x,x; x,½,x; x,x,½; ½,x,$\bar{x}$; $\bar{x}$,½,x; x,$\bar{x}$,½; ½,$\bar{x}$,$\bar{x}$; $\bar{x}$,½,$\bar{x}$; $\bar{x}$,$\bar{x}$,½; ½,$\bar{x}$,x; x,½,$\bar{x}$; $\bar{x}$,x,½.	
48	h	mm	$0,x,x$; $x,0,x$; $x,x,0$; $0,x,\bar{x}$; $\bar{x},0,x$; $x,\bar{x},0$; $0,\bar{x},\bar{x}$; $\bar{x},0,\bar{x}$; $\bar{x},\bar{x},0$; $0,\bar{x},x$; $x,0,\bar{x}$; $\bar{x},x,0$.	
48	g	mm	x,¼,¼; ¼,x,¼; ¼,¼,x; x,¼,¾; ¾,x,¼; ¼,¾,x; $\bar{x}$,¼,¼; ¼,$\bar{x}$,¼; ¼,¼,$\bar{x}$; $\bar{x}$,¼,¾; ¾,$\bar{x}$,¼; ¼,¾,$\bar{x}$.	hkl: $h,(k,l)=2n$
32	f	$3m$	x,x,x; $x,\bar{x},\bar{x}$; $\bar{x},x,\bar{x}$; $\bar{x},\bar{x},x$; $\bar{x},\bar{x},\bar{x}$; $\bar{x},x,x$; $x,\bar{x},x$; $x,x,\bar{x}$.	no extra conditions
24	e	$4mm$	$x,0,0$; $0,x,0$; $0,0,x$; $\bar{x},0,0$; $0,\bar{x},0$; $0,0,\bar{x}$.	
24	d	mmm	0,¼,¼; ¼,0,¼; ¼,¼,0; 0,¼,¾; ¾,0,¼; ¼,¾,0.	hkl: $h,(k,l)=2n$
8	c	$\bar{4}3m$	¼,¼,¼; ¾,¾,¾.	
4	b	$m3m$	½,½,½.	no extra conditions
4	a	$m3m$	0,0,0.	

Figure 7.7: An example of a page in an old version [60] of "IT". The information in this table is equivalent to the information in [59], but simpler than the newer versions

number of positions at a special site in a given space group.

In addition to the number of site atoms and coordinates the second and third columns list a letter label and the point symmetry of the site. The letter label is assigned in alphabetical order where the site with the smallest number of site atoms is named "a". Hence, the special sites $x = y = z$ and $x = y = z = 0$ and the general sites are named $(32f)$, $(4a)$, and $(192l)$, respectively. The rightmost column contains information about space group or site imposed conditions for having non-zero structure factors. For the example in Fig. 7.7, the Miller indices for the space group allowed reflections must obey cyclic permutations of $h + k = 2n$ for general (h, k, l); $l + h = 2n$ for (h, h, l) and $k, l = 2n$ for $(0, k, l)$. Additional rules applies for contributions to the structure factors from atoms at the special sites at $(48g)$, $(24d)$ and $(8c)$.

In modern crystallography programs just one site position per atom type is needed as input because the remaining atoms are generated by the space group symmetry interactions included in the programs. The variables (x, y, z) in general or special sites are replaced by numbers when calculating structure factors and intensities in programs like FullProf (refinable numbers) and Crystallographica (fixed numbers).

7.1.7 Occupancy

From the description above we can see that there is a maximum number of atoms at each site position in a crystal structure (element or isotope). For example, the maximum is 32 atoms of type "i" at the f-sites of space group #225 (see Fig. 7.7). However, some of the atom sites may be empty (vacancies) or partly occupied by different elements (an alloy) or isotopes. The most obvious way to define the occupancy, $oc_{i,j}$ of a particular atom of type (i, j) is to set it equal to one if all site positions are occupied by the same type of atoms and less than one for sites occupied by vacancies, different elements or isotopes which is equivalent to defining occupancy as the ratio between the total number of atoms in the unit cell at a given site and the site multiplicity of that site.

In the examples described in section 7.1.6 (Figs. 7.5 and 7.6), some of the oxygen sites are only partly occupied. If all sites in either compound were fully occupied, the chemical formula would be $YBa_2Cu_3O_8$, and the number of formula units within the unit cell would be $Z = 1$. Hence, according to the above definition of occupancy, $oc_{ij} = 1$ for all atoms. However, not all sites are fully occupied for the compounds described in section 7.1.6.

In tetragonal $YBa_2Cu_3O_{6+x}$ the $2g$- and $4i$-oxygen sites are fully occupied while the $2f$-oxygen site contain the excess oxygens. Therefore, the total number of $2f$-atoms in the tetragonal unit cell is Zx and the occupancy $oc_{2f} = Zx/2$ because the site multiplicity of the $2f$-site is $N_S = 2$. In orthorhombic $YBa_2Cu_3O_{7-x}$ either the $1b$-, $1e$- or both of these oxygen sites may be oxygen deficient while all other sites are fully occupied. If we assume that the $1 - x$ excess oxygen atoms are distributed between $1 - x - y$ atoms at $1e$-sites and y atom at $1b$-sites with site multiplicity $N_S = 1$, the corresponding occupancies will be $oc_{1e} = Z(1 - x - y)$ and $oc_{1b} = Zy$.

For the examples above the ideal chemical formula represent structures with one formula unit per unit cell, but quite often this is not the case. One example could be $Pr_{2-x}Ca_xCuO_4$ where the chemical formula has been reduced to represent one formula unit which must be repeated four times in order to represent all atoms in the unit cell, i.e. $Z = 4$. The Pr- and Ca-atoms share the $8f$-site positions, and hence the chemical formula representing all atoms in the unit cell is $Pr_{8-4x}Ca_{4x}Cu_4O_{16}$. Therefore the occupancies of the $8f$-Pr and -Ca atoms are $oc_{Pr} = Z(2-x)/N_S$ and $oc_{Ca} = Zx/N_S$ ($N_S = 8$). The occupancies (oc_{ij}) of the fully occupied Cu-site and the two different O-sites are all 1. This relatively simple way of assigning occupancies is used in e.g. Crystallographica (Cgraf, [61]), Powdercell (PCW, [62]) and many other programs which calculate structure factors and intensities of diffraction peaks.

In the refinement program FullProf the occupancies (OC_{ij}) can be defined by the site multiplicity scaled by the concentration of the particular atom as given by the chemical formula, e.g. for fully occupied sites $OC_{ij} = N_S$. This method is appropriate when refining single phase diffraction patterns, e.g. diffraction patterns without impurities. For multi-phase diffraction patterns this will generally result in incorrect scaling of intensities from the different phases and give erroneous estimates of phase contents. In order to ensure correct scaling of intensities between compounds when using FullProf for refining multi-phase diffraction patterns, the occupancies OC_{ij} for each compound must be scaled by the site multiplicity for the general site (N_G) of the compound, e.g. $OCC_{ij} = OC_{ij}/N_G$. With these definitions, the occupancy for the $2f$-oxygen atoms in $YBa_2Cu_3O_{6+x}$ is either $OC_{2f} = Zx$ or $OCC_{ij} = Zx/N_G$ where $N_G = 16$. Similarly, the occupancies for the $1e$- and $1b$-oxygen atoms in $YBa_2Cu_3O_{7+x}$ is either $OC_{1e} = Z(1-x-y)$ and $OC_{1b} = Zy$ or $OC_{1e} = Z(1-x-y)/N_G$ and $OC_{1b} = Zy/N_G$ where $N_G = 8$. However, it is recommended to use the latter definition for occupancies even when refining single phase transitions.

7.2 Diffraction from crystalline materials

Our starting point for the description of crystal and powder diffraction is the expression for elastic scattering cross section for a system of nuclei, fixed in position (2.56), which we here repeat

$$\left.\frac{d\sigma}{d\Omega}\right|_{\text{nucl.}} = \left|\sum_j b_j \exp(i\mathbf{q}\cdot\mathbf{r}_j)\right|^2. \tag{7.11}$$

Our goal of this chapter is to describe the diffraction from crystals of macroscopic size and from nano-sized objects. Before this, we need to define some basic concepts in crystallography.

In the remainder of this section, however, we will expand (7.11) to add the effect of material temperature on the scattered neutrons.

7.2.1 Scattering from vibrating nuclei

We release the artificial restriction that the nuclei are immobile. This means that the nuclear positions, $\mathbf{r}_j$ can change in time. We write the nuclear position as the sum of the average positions and a (small) time-dependent deviation:

$$\mathbf{R}_j(t) = \mathbf{r}_j + \mathbf{u}_j(t), \tag{7.12}$$

where the time average of the displacement vanish, $\langle \mathbf{u}_j(t) \rangle = 0$. The full quantum mechanical treatment of (7.12) results in an interaction between the neutrons and the quantised lattice vibrations, the *phonons*, which is studied by inelastic scattering. This is described in chapter 10.

However, in this chapter we will consider only elastic scattering, so we can allow ourselves a more simple approach to estimate the effect of nuclear motion. Replacing $\mathbf{r}_j$ with $\mathbf{R}_j(t)$ in (7.11), we reach

$$\begin{aligned} \frac{d\sigma}{d\Omega} &= \left\langle \sum_{j,j'} b_j b_{j'} \exp(i\mathbf{q}\cdot\mathbf{R}_j(t)) \exp(-i\mathbf{q}\cdot\mathbf{R}_{j'}(t)) \right\rangle \\ &= \sum_{j,j'} b_j b_{j'} \exp(i\mathbf{q}\cdot\mathbf{r}_j) \exp(-i\mathbf{q}\cdot\mathbf{r}_{j'}) \left\langle \exp(i\mathbf{q}\cdot\mathbf{u}_j(t)) \exp(-i\mathbf{q}\cdot\mathbf{u}_{j'}(t)) \right\rangle . \end{aligned} \tag{7.13}$$

The vibration term in the brackets implies that the phase of the scattered neutron has a slight random variation. This has the effect of reducing the scattering intensity. To quantify this, we assume that the displacements are uncorrelated, $\langle \mathbf{u}_j(t)\mathbf{u}_{j'}(t) \rangle = 0$, and that the displacement amplitudes are isotropic and equal, $\langle \mathbf{u}_j(t)^2 \rangle = \langle \mathbf{u}_{j'}(t)^2 \rangle$. Then, we perform a second order series expansion of the complex exponential functions:

$$\begin{aligned} &\langle \exp(i\mathbf{q}\cdot\mathbf{u}_j(t)) \exp(-i\mathbf{q}\cdot\mathbf{u}_{j'}(t)) \rangle \\ &\quad \approx \left\langle \left(1 - i\mathbf{q}\cdot\mathbf{u}_j(t) - (\mathbf{q}\cdot\mathbf{u}_j(t))^2/2\right) \left(1 + i\mathbf{q}\cdot\mathbf{u}_{j'}(t) - (\mathbf{q}\cdot\mathbf{u}_{j'}(t))^2/2\right) \right\rangle \\ &\quad \approx \left\langle 1 - (\mathbf{q}\cdot\mathbf{u}_j)^2 \right\rangle \\ &\quad \approx \exp(-(\mathbf{q}\cdot\mathbf{u}_j)^2). \end{aligned} \tag{7.14}$$

The fourth (and higher) order terms in the series expansion agrees with the final result above, provided the displacement term $\mathbf{q}\cdot\mathbf{u}_j(t)$ follows a normal distribution.

7.2.2 The Debye-Waller factor

The correction term (7.14) is widely known as the *Debye-Waller factor*:

$$\exp(-2W_j) = \exp(-\langle \mathbf{q}\cdot\mathbf{u_j} \rangle^2). \tag{7.15}$$

In general, the Debye-Waller factor is site-dependent. However, one often uses the approximation where $\exp(-2W_j)$ is the same for all j. In this case, the

elastic nuclear scattering cross section reads:

$$\boxed{\left.\frac{d\sigma}{d\Omega}\right|_{\text{nucl.}} = \exp(-2W)\left|\sum_j b_j \exp(i\mathbf{q}\cdot\mathbf{r}_j)\right|^2}. \tag{7.16}$$

This implies that the expression (7.11) for immobile nuclei still holds, with the correction that we need to multiply by the site-independent Debye-Waller factor, $\exp(-2W)$.

At low temperatures, the temperature dependent displacement $\mathbf{u}_j$ has a small, but non-zero value due to zero-point fluctuations. This means that the Debye-Waller factor is always smaller than (but often close to) unity. All this is described in much more detail in chapter 10 and *e.g.* in the textbook by Squires [2].

Experimental consideration. The q-dependence of the Debye-Waller factor means that for large values of q (above 10 Å^{-1}), one generally prefers to cool the sample to avoid loosing signal. On the other hand, as $q \to 0$ the Debye-Waller factor goes quickly to unity. This means that this temperature-dependent factor can be neglected in SANS, as already anticipated in chapter 5.

7.2.3 The scattering cross section for a crystal

We can now calculate the expression for the elastic neutron cross section, equation (7.16), for a crystal, where we index the unit cells by j and the atoms within the unit cells by i:

$$\left.\frac{d\sigma}{d\Omega}\right|_{\text{nucl. el.}} = \exp(-2W)\left|\sum_{i,j} b_i \exp(i\mathbf{q}\cdot(\mathbf{r}_j + \mathbf{\Delta}_i))\right|^2. \tag{7.17}$$

A small rearrangement of terms leads to the basic equation for crystal diffraction:

$$\boxed{\left.\frac{d\sigma}{d\Omega}\right|_{\text{nucl. el.}} = \exp(-2W)\,|F_{\text{N}}(\mathbf{q})|^2\left|\sum_j \exp(i\mathbf{q}\cdot\mathbf{r}_j)\right|^2}, \tag{7.18}$$

where the *nuclear structure factor*, given by

$$\boxed{F_{\text{N}}(\mathbf{q}) = \sum_i b_i \exp(i\mathbf{q}\cdot\mathbf{\Delta}_i)}, \tag{7.19}$$

depends only on the arrangement of the atoms inside the unit cell. We will later see that it is possible to determine $|F_{\text{N}}(\mathbf{q})|^2$ experimentally and use it to deduce the atomic positions.

7.2.4 The lattice sum

To proceed, we like to calculate the sum over all unit cells: $|\sum_j \exp(i\mathbf{q}\cdot\mathbf{r}_j)|^2$, also known as *the lattice sum*. Let us as a start approach this intuitively. If $\mathbf{q}$ equals a reciprocal lattice vector, $\boldsymbol{\tau}$, all the complex exponentials equals unity, *c.f.* (7.8), and the squared sum must equal N^2, where N is the number of unit cells. If $\mathbf{q}$ is not a reciprocal lattice vector, many complex phases are present, and the sum should be small compared to N^2 or vanish completely. Let us show formally, that this is indeed what happens.

We assume that the lattice is "infinite", but we keep counting the number of lattice sites by N. Hence, the squared sum can be rewritten

$$\begin{aligned}\left|\sum_j \exp(i\mathbf{q}\cdot\mathbf{r}_j)\right|^2 &= \sum_{j,j'} \exp(i\mathbf{q}\cdot(\mathbf{r}_j-\mathbf{r}_{j'}))\\ &= \sum_{j,l} \exp(i\mathbf{q}\cdot\mathbf{r}_l)\\ &= N\sum_{l} \exp(i\mathbf{q}\cdot\mathbf{r}_l)\\ &= N\sum_{j} \exp(i\mathbf{q}\cdot\mathbf{r}_j). \end{aligned} \tag{7.20}$$

To perform the middle step, we utilize that the double lattice sum over $\mathbf{r}_j$ and $\mathbf{r}_{j'}$ can be transformed to a double sum over (i) one site, $\mathbf{r}_j$, and (ii) the difference between sites, $\mathbf{r}_l = \mathbf{r}_j - \mathbf{r}_{j'}$.

Now, equation (7.20) has the form $|x|^2 = Nx$. Solving for the unknown lattice sum, x, there are two possible solutions: N and 0. The value can only be N when all complex phases are multipla of 2π. Hence, this solution is found only when $\mathbf{q}$ equals a reciprocal lattice point; otherwise the zero solution must be chosen, as conjectured above. We can thus write (7.20) as a sum of Kronecker delta functions:

$$\sum_j \exp(i\mathbf{q}\cdot\mathbf{r}_j) = N\sum_{\boldsymbol{\tau}} \delta_{\mathbf{q},\boldsymbol{\tau}}. \tag{7.21}$$

However, it is more useful to write (7.20) in terms of Dirac delta functions. To do this, we write the sum as an unknown constant, c, times the delta function:

$$\sum_j \exp(i\mathbf{q}\cdot\mathbf{r}_j) = c\sum_{\boldsymbol{\tau}} \delta(\mathbf{q}-\boldsymbol{\tau}). \tag{7.22}$$

We now integrate over one unit cell of the reciprocal lattice - a Brillouin zone. The right hand side can be immediately integrated to give c, since the integration volume by definition contains exactly one reciprocal lattice vector. The left hand side is more elaborate; first we exchange sum and integration

$$\int_{\mathrm{BZ}} \sum_j \exp(i\mathbf{q}\cdot\mathbf{r}_j)d\mathbf{q} = \sum_j \int_{\mathrm{BZ}} \exp(i\mathbf{q}\cdot\mathbf{r}_j)d\mathbf{q}. \tag{7.23}$$

Now, the integral on the right hand side vanish if $\mathbf{r}_j \neq 0$. This can be seen by writing $\mathbf{r}_j = n_a\mathbf{a} + n_b\mathbf{b} + n_c\mathbf{c}$, $\mathbf{q} = h\mathbf{a}^* + k\mathbf{b}^* + l\mathbf{c}^*$, and integrate over h, k, and l (which are here no longer integers). The first one-dimensional integral is of the form $\int_0^1 \exp(ih\mathbf{a}^* \cdot \mathbf{r}_j)dh = \int_0^1 \exp(ihn_a 2\pi)dh = \delta_{n_a,0}$, and similar for the k and l integrals. Hence, the only contribution comes from the term with $\mathbf{r}_j = 0$. Therefore, the right hand side of (7.23) simply gives the volume of the Brillouin zone:

$$\sum_j \int_{\mathrm{BZ}} \exp(i\mathbf{q} \cdot \mathbf{r}_j)d\mathbf{q} = V_{\mathrm{r}} = \frac{(2\pi)^3}{V_0} = c. \tag{7.24}$$

Combining (7.18), (7.20), (7.22), and (7.24), the final equation for neutron diffraction from a crystal becomes

$$\boxed{\left.\frac{d\sigma}{d\Omega}\right|_{\mathrm{nucl.el.}} = N\frac{(2\pi)^3}{V_0}\exp(-2W)\,|F_{\mathrm{N}}(\mathbf{q})|^2 \sum_{\boldsymbol{\tau}} \delta(\mathbf{q} - \boldsymbol{\tau})}. \tag{7.25}$$

7.2.5 The Bragg law

We now turn to the qualitative understanding of the diffraction cross section (7.25). The delta-function in the equation gives rise to the so-called *Laue condition*

$$\boxed{\mathbf{q} = \boldsymbol{\tau}}. \tag{7.26}$$

This can also be expressed in terms of the lattice spacings, d, associated with the reciprocal lattice vectors (defined in (7.7)): through the *Bragg law*:

$$\boxed{n\lambda = 2d\sin(\theta)}, \tag{7.27}$$

where n is a positive integer and θ is the angle between the incoming neutron direction and the lattice planes, see figure 7.8. When scattering from a certain set of lattice planes, the scattering is *specular*, *i.e.* the incident angle equals the outgoing angle. The proof of equation (7.27) is left as exercise 7.7.1. The essence of the Bragg law is: Diffraction takes place only when (7.27) is fulfilled. However, the reverse is not always the case. Sometimes no neutrons are diffracted even though the Bragg condition is fulfilled. This happens for reflections with $|F_{\mathrm{N}}(\mathbf{q})|^2 = 0$, as illustrated *e.g.* in problem 7.7.2.

Experimental considerations When a crystal is oriented to fulfill Bragg's law, one often talks about the reflected neutrons as a *Bragg peak* or a *Bragg reflection*. The neutron intensity in a Bragg reflection can be considerable, and at times the neutron beam needs to be attenuated in order not to saturate the detector(s). Saturation effects start at around 10^4 to 10^6 counts per second, depending on detector details. Most often, the attenuation is performed in the incident beam, often by using plastic sheets, possibly with boron content.

The angle between the incoming and outgoing beam in Fig. 7.8 is seen to be 2θ. This is denoted *the scattering angle*, and is the primary observable to

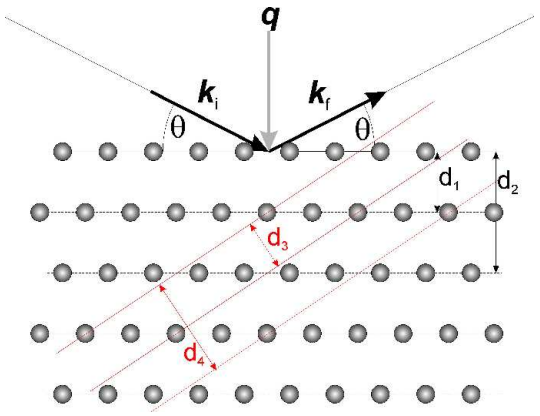

Figure 7.8: Diffraction in Bragg geometry. $\mathbf{k}_\mathrm{i}$ and $\mathbf{k}_\mathrm{f}$ are the incoming and outgoing wave vectors, respectively, $\mathbf{q}$ is the scattering vector, and d is the relevant lattice spacing in the crystal. The incoming and outgoing angles, θ, are equal. The labels d_1 through d_4 denote other possible lattice planes. Note that the planes with lattice spacing d_2 and d_4 do not give rise to diffraction, because the atoms between the planes make destructive interference (expressed as zero structure factor).

be measured in an experiment. Usually in diffraction experiments, this angle needs to be determined to precisions of the order 0.01°.

7.2.6 Integrals over the diffraction cross section

For the quantitative understanding of (7.25), the Dirac δ-function in the cross section is the crucial part. The infinite amplitude of the δ-function should not be taken litterally, since infinite amplitudes are unphysical. Instead, the δ-function symbolizes that the scattering is strongly peaked at very small intervals around the reciprocal lattice vectors. The integral of the δ-function does, however, have physical significance. Neutron scattering experiments are performed in non-ideal conditions, *e.g.* the incoming beam has a slight variation in wavelength (0.1% - 1%) and has a finite divergence (0.1° - 1°). In most cases, this makes the observed intensity depend on the integral over the scattering cross section. We will here show how to perform integrals over the δ-function. The derivation below is strongly inspired by Squires [2].

We will calculate the total cross section, *i.e.* the integral over all neutrons scattered by a particular Bragg peak.

$$\sigma_{\boldsymbol{\tau}} = \int \left(\frac{d\sigma}{d\Omega}\right)_{\text{nucl.el.},\,\boldsymbol{\tau}} d\Omega. \tag{7.28}$$

We consider a situation where the incoming neutron wave vector, $\mathbf{k}_\mathrm{i}$, and the reciprocal lattice vector in question, $\boldsymbol{\tau}$, are fixed. The angle between $\mathbf{k}_\mathrm{i}$ and $\boldsymbol{\tau}$ determines (one part of) the crystal orientation; this angle is most often denoted ω. The plane spanned by the two vectors $\mathbf{k}_\mathrm{i}$ and $\boldsymbol{\tau}$ is called the *scattering plane*.

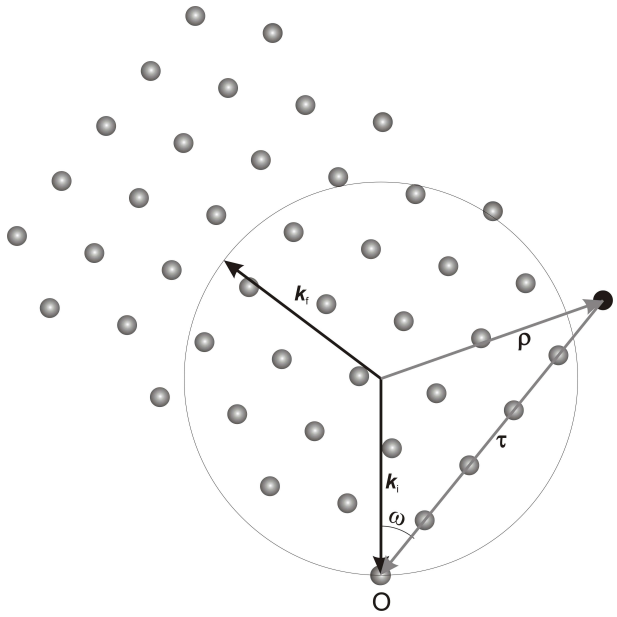

Figure 7.9: An illustration of the relevant vectors and angles in diffraction. $\mathbf{k}_\mathrm{i}$ and $\mathbf{k}_\mathrm{f}$ are the initial and final wave vectors, respectively, $\boldsymbol{\tau}$ is the reciprocal lattice vector in question, and $\boldsymbol{\rho} = \mathbf{k}_\mathrm{i} - \boldsymbol{\tau}$. All vectors reside in the scattering plane. Note that for this particular case it is not possible to fulfill the scattering requirement $\mathbf{q} = \boldsymbol{\tau}$.

The experimental geometry is often arranged so that the scattering plane is the horizontal plane. The factor $\delta(\mathbf{q} - \boldsymbol{\tau})$ in the scattering cross section (7.25) implies that the outgoing wave vector, $\mathbf{k}_\mathrm{f}$, also lies in the scattering plane, see Fig. 7.9. For very small crystallites, however, a spread of $\mathbf{k}_\mathrm{f}$ is seen, both in the in-plane and the out-of-plane directions. This is discussed in section 7.6.

The integral (7.28) boils down to an integral over the δ-function:

$$\int \delta(\mathbf{q} - \boldsymbol{\tau}) d\Omega = \int \delta(\boldsymbol{\rho} - \mathbf{k}_\mathrm{f}) d\Omega, \tag{7.29}$$

where we define $\boldsymbol{\rho} = \mathbf{k}_\mathrm{i} - \mathbf{q}$. The only variable in the integral is the direction of $\mathbf{k}_\mathrm{f}$, since the requirement of elastic scattering gives $|\mathbf{k}_\mathrm{i}| = |\mathbf{k}_\mathrm{f}|$. To calculate the two-dimensional integral over the three-dimensional δ-function, we employ a small trick. We first observe that the δ-function contributes only when

$$|\boldsymbol{\rho}| = |\mathbf{k}_\mathrm{f}|. \tag{7.30}$$

To be more precise: whenever (7.30) is fulfilled, the integral (7.29) will be non-zero. One could say that the crystal "chooses" one orientation of $\mathbf{k}_\mathrm{f}$ (or one solid angle $d\Omega$) that fulfills the scattering condition (7.30). We can therefore write

$$\int \delta(\boldsymbol{\rho} - \mathbf{k}_\mathrm{f}) d\Omega = -c' \delta(k_\mathrm{i}^2 + \tau^2 - 2k_\mathrm{i}\tau\cos(\omega) - k_\mathrm{f}^2), \tag{7.31}$$

where c' is a constant to be determined in the following. To proceed, we note that the integral of a δ-function over the full 3-dimensional space is unity. This leads to

$$\begin{aligned} 1 &= \int \delta(\boldsymbol{\rho} - \mathbf{k}_\mathrm{f}) d\mathbf{k}_\mathrm{f} \\ &= \int \left(\int \delta(\boldsymbol{\rho} - \mathbf{k}_\mathrm{f}) d\Omega \right) k_\mathrm{f}^2 dk_\mathrm{f} \\ &= \int c' \delta(k_\mathrm{i}^2 + \tau^2 - 2k_\mathrm{i}\tau\cos(\omega) - k_\mathrm{f}^2) k_\mathrm{f}^2 dk_\mathrm{f} \\ &= \frac{c'\rho}{2}. \end{aligned} \tag{7.32}$$

where $\rho^2 = k_\mathrm{i}^2 + \tau^2 - 2k_\mathrm{i}\tau\cos(\omega) = k_\mathrm{f}^2$. Hence, we can determine c'

$$c' = \frac{2}{\rho} = \frac{2}{k_\mathrm{f}}. \tag{7.33}$$

In this derivation, we have implicitly used (7.30). Now the integrals are dealt with, we can impose the condition of elastic scattering, $k_\mathrm{i} = k_\mathrm{f}$, and use (7.25) to reach the expression for the integrated cross section

$$\sigma_{\boldsymbol{\tau}} = \frac{N(2\pi)^3}{V_0} \frac{2}{k_\mathrm{i}} \exp(-2W) \left| F_\mathrm{N}(\tau) \right|^2 \delta(\tau^2 - 2k_\mathrm{i}\tau\cos(\omega)). \tag{7.34}$$

This equation still contains a δ-function and thus needs additional integration (over the crystal orientation, ω, or the initial wave vector, $\mathbf{k}_\mathrm{i}$) to give physical sense. Hence, (7.34) is only a stepping stone to calculate the cross sections for some particular experimental arrangements. These are discussed in sections 7.3, 7.5, and 7.6.

7.3 Diffraction from single crystals with monochromatic radiation

In the present version of the notes, we will only briefly touch upon the important topic of single crystal scattering.

7.3.1 Rotation of a crystal in the beam

Consider again the situation of a crystal in a monochromatic beam, shown by Fig. 7.9. We assume that the crystal is oriented so that the reciprocal lattice vector under consideration is kept within the scattering plane, which is spanned by $\mathbf{k}_\mathrm{i}$ and $\mathbf{k}_\mathrm{f}$. Scattering occurs when the crystal is oriented so that Braggs law is fulfilled, $\mathbf{q} = \boldsymbol{\tau}$.

The plot of the scattered intensity as a function of crystal orientation, ω, is known as a *rocking curve*. This curve is not shaped as a δ-function, but

has a non-zero width. There are a number of contributions to this broadening, including beam divergence, imperfect monochromaticity, imperfect sample (mosaicity), and wave-mechanical effects (dynamical diffraction). The two latter effects will be discussed in the subsections below.

The broadening of the peak makes it appropriate to calculate the integrated area under the rocking curve, also known as the *scattering power*:

$$P \equiv \Psi \int \boldsymbol{\sigma}_{\mathrm{tot},\boldsymbol{\tau}} d\omega. \tag{7.35}$$

This integral can be solved using (7.34):

$$\begin{aligned} P &= N\frac{(2\pi)^3}{V_0}\Psi|F_{\mathrm{N}}(\boldsymbol{\tau})|^2 \int \frac{2}{k_{\mathrm{i}}}\delta(\tau^2 - 2k_{\mathrm{i}}\tau\cos(\omega))d\omega \\ &= N\frac{(2\pi)^3}{V_0}\Psi\frac{|F_{\mathrm{N}}|^2}{k_{\mathrm{i}}^3\sin\theta}. \end{aligned} \tag{7.36}$$

It is seen that the unphysical δ-function has been integrated out. Equation (7.36) is alternatively written

$$\boxed{P = \Psi\frac{V}{V_0^2}\frac{\lambda^3}{\sin\theta}|F_{\mathrm{N}}(\boldsymbol{\tau})|^2.} \tag{7.37}$$

It is seen that the scattering power depends quite strongly upon the wavelength of the neutron beam.

7.3.2 Crystal mosaicity; secondary extinction

Most crystals used for neutron scattering experiments are imperfect. They can often be described by an assembly of small crystallites, aligned randomly around a mean orientation. We then talk about a *mosaic crystal*. Often the crystallite orientations can be well described by a normal distribution, and one talks about a *Gaussian mosaic*. The *mosaicity* of the crystal is given as the FWHM of this Gaussian curve, and is often denoted by η. The mosaicity will serve to broaden the rocking curve, which to first approximation will obtain the same integrated intensity as calculated above, and with a width equal to η.

Due to the scattering from the crystallites, the beam flux is attenuated while traveling through the crystal. On the other hand, the beam scattered inside the crystallite due to the reciprocal lattice vector, $\boldsymbol{\tau}$, can be scattered back to the original beam by a reciprocal lattice vector $-\boldsymbol{\tau}$. This complex dampening of the original beam is denoted *secondary extinction* and will be described in vol. 2 of these notes.

Experimental considerations: When a crystal is used as a monochromator, some amount of mosaicity is required, in order to let the crystal reflect a larger part of the incoming beam. Due to the secondary extinction, the peak reflectivity is often similar for a low-mosaic as for a high-mosaic crystal. Real mosaic

crystals used for monochromators often have a mosaicity of $0.1^\circ - 1^\circ$. The smaller the mosaic, the smaller the divergence, wavelength spread, and total flux of the outgoing beam.

Extinction can result in the effect that the width of the rocking curve can be somewhat different from the true crystalline mosaicity, η. For monochromators, one uses the width of the rocking curve to describe the mosaicity.

7.3.3 Perfect crystals; primary extinction

Some materials can be produced with perfect crystallinity, *i.e.* with zero mosaicity over several millimeters - or even centimeters. Typical examples are the semiconductors Si and Ge. Even in these cases, the rocking curve is not truly shaped as a δ-function. A detailed calculation of the wave propagation within the crystal shows that the wave is strongly attenuated within the crystal. This effect is denoted *primary extinction* and it ruins the assumption of interference between nuclei of the whole crystal. This again produces an effective mosaicity of the crystal of the order a fraction of an arc minute.

The calculation of primary extinction, also known as *dynamical diffraction*, can be found in most textbooks of X-ray diffraction; for example in [4]. However, it is often not important for neutron scattering, due to its smaller scattering cross section, and hence longer attenuation depth within the crystal. In this version of the notes, we will not dig deeper into the topic of primary extinction.

7.4 Laue diffraction

In Laue diffraction, one places a crystal with fixed orientation within a polychromatic beam of neutrons. Ideally, for each reciprocal lattice point, there exists a neutron wavelength that fulfill the Bragg law. In this way, all reciprocal lattice points will contribute with scattering peaks for the same experiment.

To calculate the scattering power of the Bragg reflections, we define

$$\begin{aligned} P &= \int \Psi(\lambda)\sigma_{\mathrm{tot},\boldsymbol{\tau}} d\lambda \\ &= N\frac{(2\pi)^3}{V_0}\left|F_{\mathrm{N}}(\boldsymbol{\tau})\right|^2 \int \frac{2}{k}\delta(\tau^2 - 2k\tau\cos(\omega))\Psi(\lambda)d\lambda. \end{aligned} \tag{7.38}$$

By using the substitution $x = 2k_{\mathrm{i}}\tau\cos(\omega)$, we reach the result

$$\boxed{P = N\frac{(2\pi)^3}{V_0}\frac{\pi\Psi(\lambda_{\mathrm{i}})|F_{\mathrm{N}}(\boldsymbol{\tau})|^2}{k_{\mathrm{i}}^4\cos^2(\omega)} = \frac{V}{V_0^2}\Psi(\lambda_{\mathrm{i}})\frac{\lambda^4}{2\sin(\theta)}|F_{\mathrm{N}}(\boldsymbol{\tau})|^2}. \tag{7.39}$$

We will not at this point in time go deeper into Laue diffraction. This section may later be expanded through input from from Mogens Christensen, Univ. Århus.

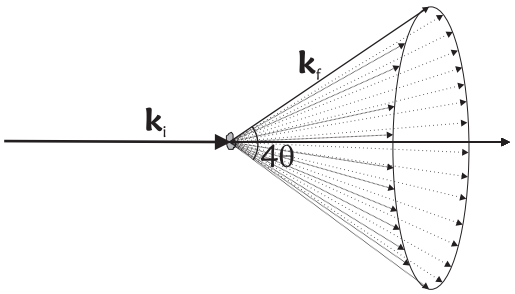

Figure 7.10: Illustration of the Debye-Scherrer cone for the diffraction from one powder line.

7.5 Diffraction from a powder

In a powder, there are billions of randomly oriented crystal grains, typically of μm size. Hence, it is safe to assume that all lattice orientations are represented equally and that extinction effects are absent (see sect. 7.3.2 and 7.3.3). Bragg scattering of an incoming monochromatic beam will thus happen in all possible ways that fulfill the Bragg law (7.27). The resulting scattering will occur on cones of opening angles of 4θ, the *Debye-Scherrer cones*. This is illustrated in Fig. 7.10.

To obtain the total scattering cross section from a powder, we average the cross section (7.34) over all orientations of a given lattice vector, $\boldsymbol{\tau}$. We use polar coordinates, (ϕ, ω), where ω is the angle between $\mathbf{k}_\mathrm{i}$ and $\boldsymbol{\tau}$ as in Fig. 7.9 and ϕ is the (unimportant) rotation angle around $\mathbf{k}_\mathrm{i}$.

$$\begin{aligned}\sigma_\tau &= \frac{1}{4\pi}\int \sigma_{\boldsymbol{\tau}} d\Omega = \frac{1}{4\pi}\int \sigma_{\boldsymbol{\tau}} d\phi \sin(\omega) d\omega \\ &= \frac{N(2\pi)^3}{V_0}\frac{2}{k_\mathrm{i}}\exp(-2W)\left|F_\mathrm{N}(\boldsymbol{\tau})\right|^2 \frac{1}{4\pi}\int 2\pi\sin(\omega)\delta(\tau^2 - 2k_\mathrm{i}\tau\cos(\omega))d\omega \\ &= V\exp(-2W)\frac{1}{V_0^2}\frac{\lambda^3}{4\sin\theta} j_\tau \left|F_\mathrm{N}(\boldsymbol{\tau})\right|^2 . \end{aligned} \tag{7.40}$$

In the last step, we have included j_τ, which is the *multiplicity* of the reflection, meaning the number of crystallographically equivalent lattice planes that all contribute to the scattering. One example is the cubic (100) reflection, with crystallographically equivalent reflections (010), (001), $(\bar{1}00)$, $(0\bar{1}0)$, and $(00\bar{1})$, giving $j_{100} = 6$.

In high-symmetry crystal structures, there may be non-equivalent reflections with the same length of $\boldsymbol{\tau}$. Examples are the cubic (221) and (300) reflections - and the cubic (333) and (511) reflections. In a powder, there is no way to separate these contributions to the scattering. Hence, to reach a description of the scattered intensity at a particular value of q, we must sum over all reflections

of same length of τ, reaching

$$\boxed{\sigma_q = \sum_{|\boldsymbol{\tau}|=q} \sigma_{\boldsymbol{\tau}} = V \exp(-2W) \frac{1}{V_0^2} \frac{\lambda^3}{4 \sin\theta} \sum_{|\boldsymbol{\tau}|=q} j_\tau \left|F_{\mathrm{N}}(\boldsymbol{\tau})\right|^2}. \tag{7.41}$$

Experimental considerations A closer look at (7.41) reveals that the only sample-dependent quantity is the nuclear structure factor, $F_{\mathrm{N}}(\boldsymbol{\tau})$. It is thus possible to determine the relative nuclear structure factor for a number of reflections from the relative *intensity* of the scattered neutrons. This can be used to determine the position of the atoms within the unit cell. The size and shape of the unit cell (the lattice parameters) are, in turn, determined by the *position* of the reflections, via the Bragg law. A number of standard programs exist to perform this analysis.

7.6 Diffraction from nano-sized systems

If the crystal grains are very small, often meaning below 100-500 nm, the "infinite crystal" approximation leading to the Bragg law (7.27) breaks down. It is then important to reconcile (7.16) for a nano-sized particle. The resulting mathematics is tedious, but the result is rather simple. The Bragg peaks broaden to a width (FWHM) of approximately

$$\Delta q \approx \frac{2\pi}{L}, \tag{7.42}$$

where L here is a typical dimension of the particle. We now dig a little deeper into the effect nano-sizes have on the diffraction signal.

7.6.1 A cubic nanoparticle

We first illustrate (7.42) with an example. Consider a simple cubic Bravais crystal with lattice constant a. Let also the outer shape of the particle be cubic with side length d. The atoms along a side are numbered from 0 to $m-1$, where $m = d/a$. The scattering cross section for $\mathbf{q}$ parallel to one side of the cube (here taken as the x-direction) reads:

$$\begin{aligned}
\frac{d\sigma}{d\Omega} &= \exp(-2W) \left| b m^2 \sum_{n=0}^{m-1} \exp(i q_x n a) \right|^2 \\
&= \exp(-2W) m^4 b^2 \left| \frac{1 - \exp(i q_x m a)}{1 - \exp(i q_x a)} \right|^2 \\
&= \exp(-2W) m^4 b^2 \left| \frac{\sin(m q_x a/2)}{\sin(q_x a/2)} \right|^2 .
\end{aligned} \tag{7.43}$$

This expression peaks around $q_x = 2\pi/a$, which is just the Bragg condition. However, the peak has a width of $\Delta q_x = 2\pi/(ma) = 2\pi/L$ as anticipated above. (The width of the reflection in the y and z directions are identical.)

It should be noticed that the squared term in (7.43) has a peak amplitude of m^2, meaning that the total peak amplitude is proportional to $m^6 = N^2$. We should, however, also take into account that the total broadening of the reflection in reciprocal space scales as $m^{-3} = N^{-1}$. Hence, the integrated intensity of the diffraction peak is proportional to N - and hence to the particle volume, V - as was also found in the infinite system, *c.f.* (7.25).

7.6.2 The Scherrer equation

The literature goes one step further into this problem. We will not go into any details with the derivation, but the "apparent" size of the particle is found to be given by the *Scherrer* equation originally derived for X-ray diffraction [63]:

$$\epsilon = \frac{\lambda}{b\cos(\theta)}, \tag{7.44}$$

where b is the angular broadening of the peak in radians. Identifying $b = \delta(2\theta) = 2\delta\theta$, we reach $\epsilon = \pi/(k\cos(\theta)\delta\theta)$. From the identity $q = 2k\sin(\theta)$ we reach $\delta q = 2k\cos(\theta)\delta\theta$, leading to

$$\boxed{\epsilon = \frac{2\pi}{\delta q}}, \tag{7.45}$$

as we anticipated in (7.42).

The relation between the "true" particle size, $p = (V)^{1/3}$ and the "apparent" size, ϵ is given by

$$p = K\epsilon, \tag{7.46}$$

where K is a constant of the order unity. This is discussed in great detail for different particle shapes in [63].

7.7 Problems

7.7.1 Simple Bragg scattering, the monochromator

Consider the Bragg law (7.27) for scattering of waves by a crystal. A reciprocal lattice vector, $\boldsymbol{\tau}$, is always perpendicular to a set of lattice planes, and has the length

$$|\boldsymbol{\tau}| = n\frac{2\pi}{d}, \tag{7.47}$$

where n is an integer.

1. Argue why n is needed in (7.47).
2. Show that the Bragg law can be written as $\tau = 2k\sin\theta$, following Fig. 7.8.

3. Show that the Bragg law can be derived from the (crystal) momentum conservation law $\hbar\mathbf{k}_\mathrm{i} = \hbar\mathbf{k}_\mathrm{f} + \hbar\boldsymbol{\tau}$.

4. Determine the scattering angle, 2θ, for 5 meV neutrons scattering off a pyrolytic graphite monochromator crystal with $\tau_{(002)} = 1.8734$ Å^{-1}.

7.7.2 Bragg scattering from Bravais lattices

We will here investigate the effect of the nuclear structure factor (7.19) in the total diffraction cross section (7.25) for Bravais lattices. However, as we shall see, some Bravais lattices can with advantage be described as a lattice with a basis.

1. For a simple cubic lattice, atom distance a, the reciprocal lattice points are also simple cubic, with point distance $\tau_{(001)} = 2\pi/a$. Calculate the squared structure factor $|F_\mathrm{N}(\boldsymbol{\tau}_{hkl})|^2$ in units of the nuclear scattering length b. Which reflections are allowed (non-zero structure factors)? Do the allowed reflections have different structure factors?

2. A body centered cubic (bcc) lattice can be described as a simple cubic lattice (side length a) with a second atom placed in the centre of the cube. The metallic elements Cr and Fe are two examples. Calculate the distance between nearest lattice sites. Calculate the expression for the nuclear structure factor of a bcc structure using $b = 1$. Which reflections (h, k, l) are allowed? Do they have different structure factors?

   The structure factors you have calculated using $b = 1$ are also called the geometrical structure factors. Can you think of a reason why?

3. A face centered cubic (fcc) lattice (side length a) has atoms in the cube corners and at the centre of the cube faces. One example of an fcc system is Al. Calculate the distance between nearest neighbour lattice sites. Calculate the expression for the geometrical structure factor of the fcc structure. Which reflections are allowed? Do they have different structure factors?

4. How many lattice sites (atoms) are present in the unit cell of the simple cubic, the bcc, and the fcc lattices, respectively?

5. The hexagonal lattice is described by the lattice vectors $\mathbf{a} = a(1, 0, 0)$, $\mathbf{b} = a(-1/2, \sqrt{3}/2, 0)$, and $\mathbf{c} = c(0, 0, 1)$ in orthogonal coordinates. Calculate the expression for the corresponding reciprocal lattice vectors.

6. The hexagonal closed-packed (hcp) lattice can be described as a hexagonal unit cell with a two-atom basis, where $\mathbf{d}_1 = (0, 0, 0)$ and $\mathbf{d}_2 = (a/2, a/(2\sqrt{3}), c/2)$ in cartesian coordinates. Calculate the ratio c/a, knowing that the distance between an atom and all 12 nearest neighbours must be equal. In the hexagonal crystal coordinates, the relative atom coordinates may be given as (0,0,0) and (2/3, 1/3, 1/2), *i.e.* in units of the three real-space lattice vectors. Explain how the value (2/3, 1/3, 1/2) appears.

7. Calculate the expression for the structure factor of the hcp lattice using $b = 1$ and the atom positions in the hexagonal cell. Use the expression to calculate the geometrical structure factors for $(hkl) = (100)$, (101), (102), (103), (001), (002), (110), (111) and (112). Explain the regularities in the structure factors.

7.7.3 Bragg scattering from non-Bravais lattices

We will here continue to investigate the nuclear structure factor (7.19), but this time for non-Bravais lattices.

1. The NaCl crystal structure consists of two interpenetrating fcc sublattices (side length a) displaced by half a cube diagonal with respect to each other. The Na atoms are placed on the lattice sites of one of the lattices and the Cl atoms on the lattice site of the other. What are the relative coordinates of the Na and Cl atoms, respectively?

2. The NaCl crystal may also be constructed by placing Na and Cl atoms alternating on a simple cubic lattice with side length a. What is the side length (lattice parameter) of the combined structure? How many simple cubic lattices are needed for the NaCl structure? What are the relative coordinates of the Na and Cl atoms in this unit cell?

3. Calculate the expression for the structure factor of the NaCl crystal structure. Which reflections are allowed? What causes the difference between the structure factor of the allowed reflections?

4. The crystal structure of CeSb is also the NaCl structure. Why are the structure factors of some reflections almost zero?

5. Another compound of the sodium chloride structure is LiH. Calculate the squared structure factors of the three shortest allowed scattering vectors. What happens to the mean scattering length, $\bar{b}$, for H if the naturally occuring H is enriched with 17% D? Which consequences does that have for the structure factors, and how do you understand that?

6. Si and Ge has the same structure as diamond where the atoms are placed in two interpenetrating fcc lattices (side length a). One of the lattices is displaced by 1/4 body diagonal with respect to the other, $\mathbf{d} = (1/4, 1/4, 1/4)a$. What is the distance between nearest neighbour sites? Calculate the structure factor of the diamond cubic structure of Si. Which reflections are allowed? Do they have different structure factors? Can you think of some familiarities between the NaCl and the diamond structure?

7. Why is it impossible to define a geometrical structure factor for NaCl and other compounds containing more than one element?

8. Neutron scattering lengths can be positive or negative. Describe the effect on the nuclear structure factor at a Bragg reflection, when the crystal

contains an atom with a positive scattering length on one site and an atom with a negative scattering length on another site? What would the effect be on the nuclear structure factor, if the atoms hypothetically were placed on the same site?

7.7.4 Use of International Tables for Crystallography

This exercise is intended to illustrate how the symmetry information of a particular crystal lattice and space group listed in "International Tables for Crystallography" can be used to visualise and understand the crystal structures of very different chemical compounds.

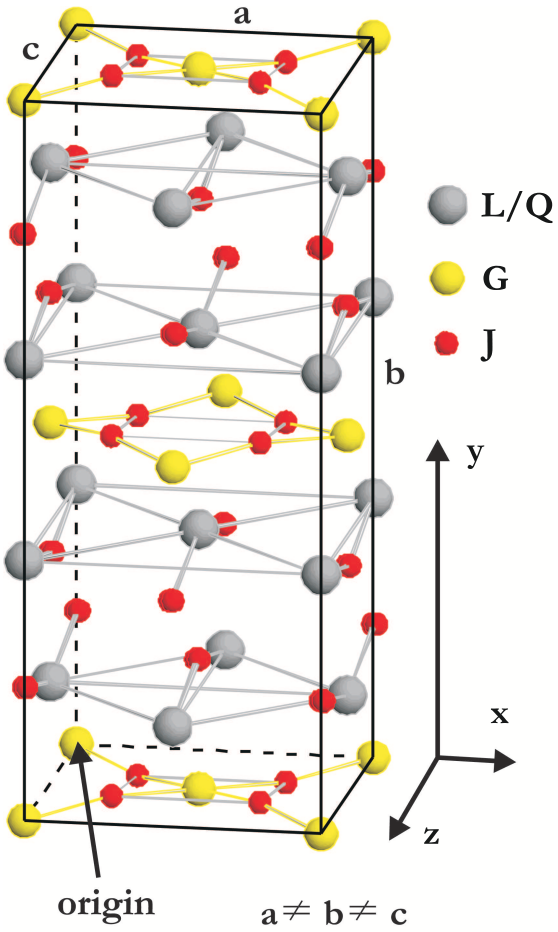

Figure 7.11: The unit cell crystal structure for one of the structures listed in Table 7.1.

#	Space group Crystal type	"Chemistry"	Element	Site type	x	y	z
1		$\mathbf{AR_2}$ a 9.863, α 90 b 7.791, β 90 c 7.833, γ 90	A1		0.2146	0	0
			A2		1/2	0.3086	0.1851
			R1		0.1282	0.2746	0.0512
			R2		0.3727	0.0450	0.2261
2		$\mathbf{L_3Z_3}$ a 5.113, α 90 $b = 9.731$, $\beta = 90$ c 7.907, γ 90	L		1/2	0.1563	0.0904
			Z1		1/4	0.419	1/4
			Z2		0	0	0
3		$\mathbf{L_{2-x}Q_xGJ_4}$ $a - 5.2431$, $\alpha - 90$ b 12.7848, β 90 $c - 5.2931$, $\gamma - 90$	L		0	0.1392	0.4898
			Q		0	0.1392	0.4898
			C		0	1/2	1/2
			J1		0	0.516	1/4
			J2		0	0.318	0.489
4		$\mathbf{L_{2-x}Q_xGJ_4}$ a 3.9746, α 90 $b - 3.9746$, $\beta - 90$ c 12.3647, γ 90	L		0	0	0.3506
			Q		0	0	0.3506
			G		1/2	0	0
			J1		0	1/2	0
			J2		0	1/2	1/4
5		$\mathbf{L_{2-x}Q_xGJ_4}$ a 3.765, α 90 b 3.765, β 90 c 13.27, γ 90	L		0	0	0.360
			Q		0	0	0.360
			C		0	0	0
			J1		1/2	0	0
			J2		0	0	0.169
6		$\mathbf{TM_2G_3J_{7-x}}$ a 3.8210, α 90 $b - 3.8826$, $\beta - 90$ c 11.6720, γ 90	T		1/2	1/2	1/2
			M		1/2	1/2	0.1851
			G1		0	0	0
			G2		0	0	0.3557
			J1		0	0	0.1600
			J2		1/2	0	0.3776
			J3		0	1/2	0.3778
			J4		0	1/2	0
7		$\mathbf{TM_2G_3J_{7-x}}$ $a - 3.8192$, $\alpha - 90$ $b - 3.8730$, $\beta - 90$ c 11.656, γ 90	T		1/2	1/2	1/2
			M		1/2	1/2	0.1839
			G1		0	0	0
			G2		0	0	0.3556
			J1		0	0	0.1586
			J2		1/2	0	0.3793
			J3		0	1/2	0.3783
			J4		0.046	1/2	0
			J5		1/2	0.046	0
8		$\mathbf{TM_2G_3J_{6-x}}$ a 3.8519, α 90 b 3.8519, β 90 $c - 11.8037$, $\gamma - 90$	T		1/2	1/2	1/2
			M		1/2	1/2	0.1952
			G1		0	0	0
			G2		0	0	0.3605
			J1		0	0	0.1518
			J2		0	1/2	0.3974
			J3		0	1/2	0
9		$\mathbf{L_{2-x}Q_XGJ_1}$ $a - 3.776$, $\alpha - 90$ $b - 3.776$, $\beta - 90$ c 13.246, γ 90	T		1/4	1/4	0.8889
			M		1/4	1/4	0.6090
			G1		1/4	1/4	0.6090
			G2		3/4	3/4	0.7487
			J1		3/4	1/4	0.7513
			J2		1/4	1/4	0.1348
			J3		1/4	1/4	0.0666

Table 7.1: Table to be filled in during problem 7.7.4.

1. Table 7.1 contains six filled and two unfilled columns. The first column is just a running number used to identify the different compounds. The third column quotes a fictitious chemical formula for the compound and the lattice parameters. The fourth and last three columns list the individual elements with the corresponding crystal lattice coordinates x, y, z. Simple letter synonyms are used for the elements. A selection of information sheets from "International Tables for Crystallography" can be found in the course material. Use the information for space groups #47, #64, #123, #129, #139, #194 and #225 in conjunction with section 7.1.6 to fill in the missing information in column two (space group and lattice type) and five (type of site). When this is done, answer the following questions.

2. Must all atoms of the same element be on the same site? Why can chemically very different compounds be described in by the same space group?

3. In some of the compounds, the coordinates are identical for different elements. What does that mean? Many of the compounds have different elements in the same site positions. How is that possible?

4. The space groups #6, 7 and 8 (Table 7.1) contain the same elements ($x > 1$). What is the difference between these structures? How many atom sites of the element **J** does each structure contain? Are these numbers consistent with the chemistry? What does this conclusion imply?

5. Figure 7.11 shows the unit cell crystal structure for one of the structures listed in Table 7.1. Look at the figure and compare the atom positions with the site positions listed in the filled in Table 7.1. Determine the number (first column of Table 7.1) and space group for this structure. Argue for the result.

6. From a symmetry point of view, it seems that the structure from the previous question contains more than one type (site) of **J**-atoms. How many types are there? Is there a simple way to describe them in relation to the crystal lattice[1]? Is this consistent with the filled Table 7.1? Does the total number of each atom type agree with number of site positions in Table 7.1?

7. What are the occupancies of the **L**-, **Q**-, **G**- and **J**-atom sites if $x = 0.14$ and the information is to be used as input in a FullProf refinement (see section 7.1.7)? Answer the same question if the information will be used as input in Crystallographica.

[1] E.g. central, face centre, body centre, in planes parallel to a lattice plane or on lines parallel to a direction.

Chapter 8

Imaging

Authors:
Maria Thomsen, Niels Bohr Institute, University of Copenhagen
Markus Strobl, European Spallation Source, Lund, Sweden

8.1 Introduction

In neutron imaging the interior structure of a sample is visualised in real space with a resolution of the order 10-100 micrometer, unlike scattering experiments where the information is obtained in reciprocal space and is an average over the sample volume illuminated. Like the scattering techniques, the imaging method is non-destructive and has been used in a wide variety of applications ranging from inspection of objects of preservation interest (*e.g.* cultural heritage) and industrial components to visualization and quantification of interior dynamical processes (*e.g.* water flow in operational fuel cells).

Neutron imaging is in general restricted to take place at large scale facilities. One example is the ICON beamline at SINQ, PSI, where a schematic illustration is shown in Figure 8.1 [64].

One aspect of imaging is radiography. Here, a two-dimensional (2D) map of the transmitted neutrons are obtained at the detector screen, similar to X-ray radiography known from the hospitals. Section 8.2 deals with the instrumentation needed for neutron imaging, including spatial and temporal image resolution and the detector system. Another aspect of imaging is computed tomography (CT), which is well known for X-rays, but also feasible with neutrons. Here, the sample is rotated around an axis perpendicular to the beam direction and radiographic projection images are obtained stepwise from different view angles. These images are combined mathematically to give the three-dimensional (3D) map of the attenuation coefficient in the interior of the sample. This will be explained in detail in section 8.3.

8.1.1 Attenuation

The neutron attenuation can happen either by absorbtion or scattering. The corresponding cross sections are given in Table 2.1 for some elements. In Figure 8.2, we show the attenuation coefficient for all elements as a function of atomic number for thermal neutrons (25 meV), compared to the absorption cross section for X-rays (100 keV). Whereas neutrons interact with the nuclei of matter, X-rays interact with its electrons. With X-rays, the attenuation is higher, the higher the electron density (the higher the atomic number). There is no such regular correlation for the interaction between neutrons and matter, and hence the attenuation coefficients are irregularly distributed independent of the atomic number. In the figure the mass attenuation coefficients are given as μ/ρ, with ρ being the density. The linear attenuation coefficient, μ, has the unit of reciprocal length. The relationship between the attenuation coefficient and the cross section is given by

$$\frac{\mu}{\rho} = \frac{N_a}{M}\sigma \tag{8.1}$$

where N_a is Avogadros number, M is the molar mass, and σ is the total cross section.

It is seen from the figure that the light elements, such as hydrogen and boron, have a very low absorption cross section for X-rays while they strongly scatter (blue) or absorb (red) neutrons. In contrast, many important metals can much easier be penetrated by neutrons than by X-rays (Al, Fe, Sn, and Pb are marked in Figure 8.2 as examples).

Neutron imaging can in many cases be used as a complementary technique to the X-ray radiography. This is illustrated in Figure 8.3, which shows a radiographic image of an analog camera obtained with X-rays (a) and neutrons (b). In the X-ray image the metal parts from the battery are attenuating strongly, but seem totally transparent to neutrons. Neutrons, on the other hand, display strong contrast to image the lighter polymer (plastic) parts containing significant amounts of hydrogen. Because neutrons interact directly with the nuclei, the attenuation coefficient differs even between isotopes (unlike the X-ray attenuation), making is possible to distinguish for example the water types: hydrogen oxide (normal water, H_2O) and deuterium oxide (heavy water, D_2O), because the total cross section for hydrogen is 40 times that of deuterium, see Table 2.1.

8.2 Radiography

We first repeat the result from section 2.1.5 that the neutron flux, Ψ, inside a sample is exponentially damped (the Beer - Lambert law):

$$\Psi(z) = \Psi(0)\exp\left(-\int_0^z \mu(z')dz'\right) \tag{8.2}$$

where z is the depth in the sample and $\mu(z')$ is the total attenuation coefficient at the given position in the sample. The total attenuation is the sum of the

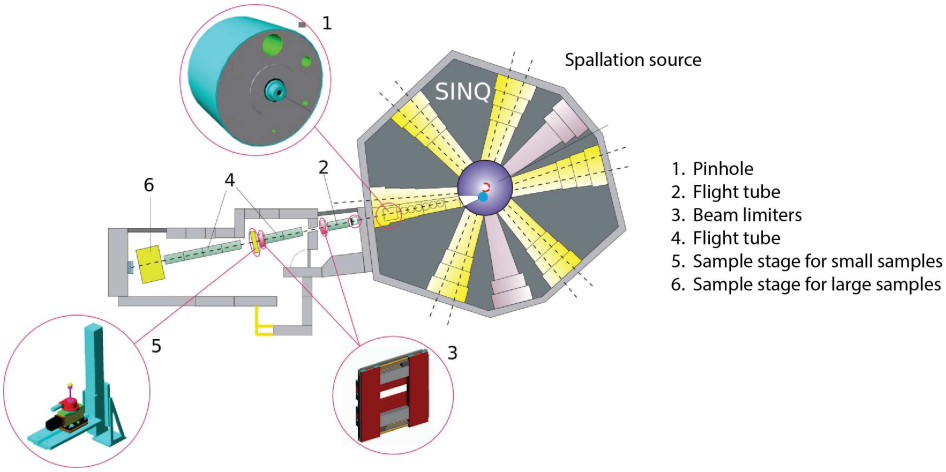

Figure 8.1: Schematic illustration of the ICON beamline at SINQ, PSI. Figure is adapted from [64].

absorption and scattering attenuations.

$$\mu = \mu_a + \mu_s, \tag{8.3}$$

Hydrogen and boron both give a strong attenuation of the neutron beam, but in the case of hydrogen the attenuation is mainly due to scattering, while for boron the attenuation is dominated by absorption, see Figure 8.2. The two processes can not be distinguished in the radiographic images, as only the transmitted neutrons are detected.

The experimental set-up is relatively simple, as it is a basic pinhole geometry due to the limited potential of optics with neutrons. The set-up is illustrated in Figure 8.4. In such a set-up the available flux is strongly coupled with the achievable spatial resolution. Like in many other cases and techniques, increasing resolution directly implies a trade-off in available flux and hence increases the exposure time.

The spatial resolution in an image gives the size of the structures that can be investigated, e.g. how close points in an object can be to each other but still be distinguished. The temporal resolution in a series of radiographic images is related to the acquisition time for a single image and is especially important when considering dynamic processes. Both the temporal and spatial resolution depend on the pinhole size, the collimation length (flight path), and the detector system, to be explained in the following.

8.2.1 Spatial resolution

Currently, the spatial resolution at state-of-the-art instruments is of the order of 100 μm down to 20 μm. The spatial resolution is limited by two factors:

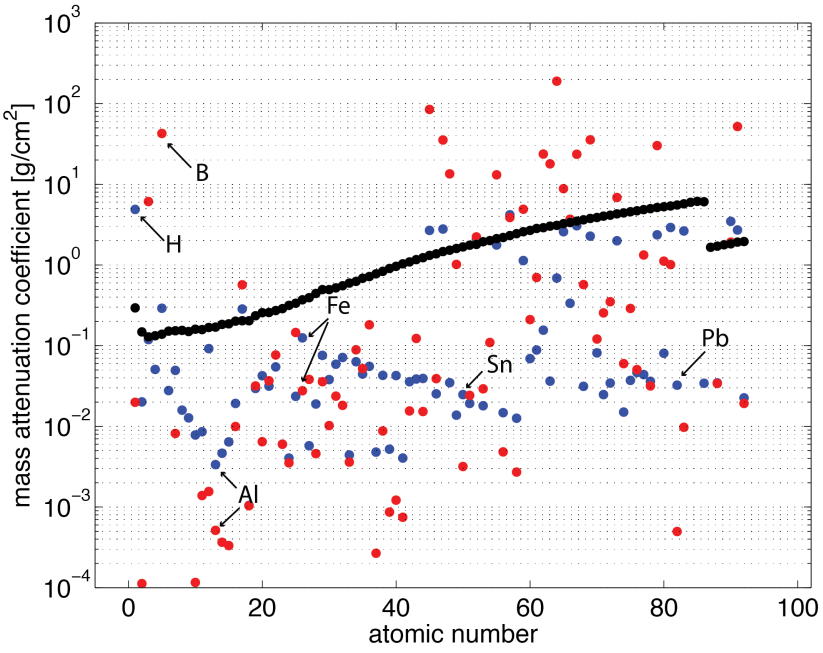

Figure 8.2: Absorption (red) and scattering (blue) coefficients for thermal neutrons with energy 25 meV (2200 m/s), compared to the attenuation coefficient for X-rays with energy 100 keV. Adapted from `http://www.psi.ch/niag/what-is-neutron-imaging`.

- The geometry of the pinhole set-up, including the pinhole size, the pinhole-sample and sample-detector distances.
- The intrinsic detector resolution, i.e. the uncertainty of the determination of the position in the physical and digital detection process.

In the basic pinhole geometry, illustrated in Figure 8.5, the optimum source for imaging is a point source, but at a real beam line, a pinhole with a finite size has to be used. For such a geometry it can easily be derived that for a pinhole with diameter D, the resolution is limited geometrically by the image blur, given by [65]

$$d = D\frac{l}{L}. \tag{8.4}$$

where L and l is the pinhole-sample and sample-detector distance, respectively, defined in Figure 8.5.

The collimation ratio is defined as the ratio between the pinhole-sample distance and the pinhole size, L/D, and is a key parameter for a set-up. The higher the collimation ratio, the better the spatial resolution for a finite sample-

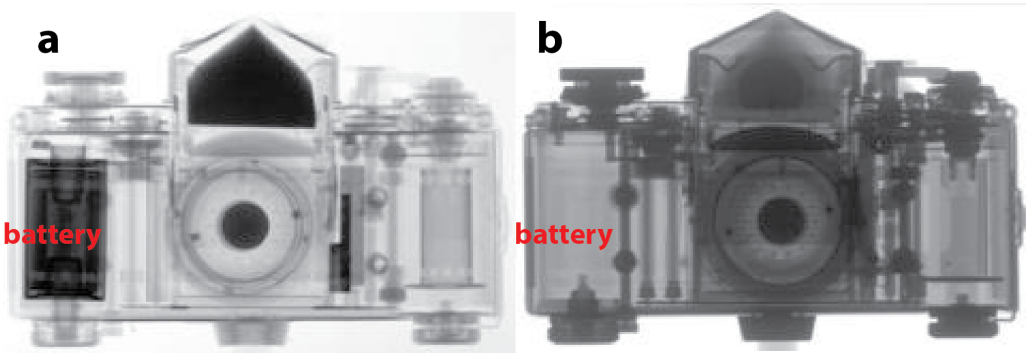

Figure 8.3: Radiography image of a camera obtained with X-rays (a) and neutrons (b). Adapted from `http://www.psi.ch/niag/what-is-neutron-imaging`.

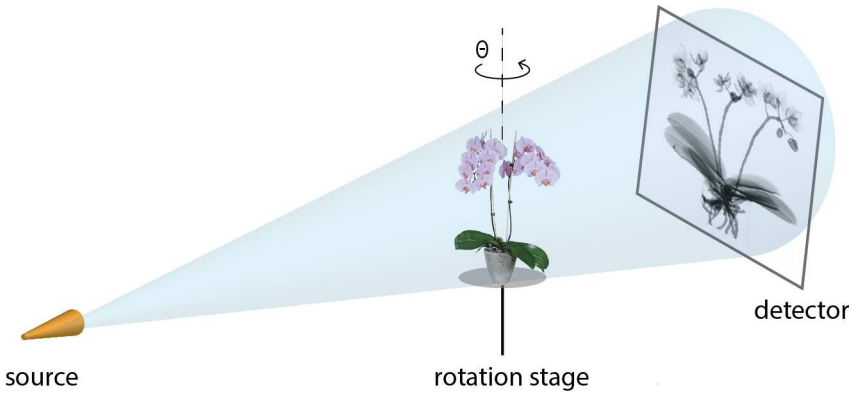

Figure 8.4: Schematic illustration of the experimental set-up for neutron imaging.

detector distance, l. The sample is placed as close as possible to the detector system, in order to achieve high resolution.

The collimation ratio can be increased by decreasing the pinhole diameter or increasing the pinhole-sample distance. Due to the divergence of the beam in the pinhole (of magnitude a few degrees), the beam opens into a cone and the flux decreases as the inverse square of the distance from the pinhole. Therefore, increasing the collimation ratio by a factor of two, either by increasing the distance or decreasing the pinhole diameter, reduces the flux by a factor four.

The second aspect of the spatial resolution is related to the detector system and depends on the size of the pixel elements and the precision in position by with the neutron can be detected. A neutron hitting one pixel element might also be counted in neighbouring pixels, meaning that the spatial resolution often is less than the actual detector pixel size will allow. By definition, the spatial resolution cannot be better than two times the pixel size. The basic principles will be explained in section 8.2.3.

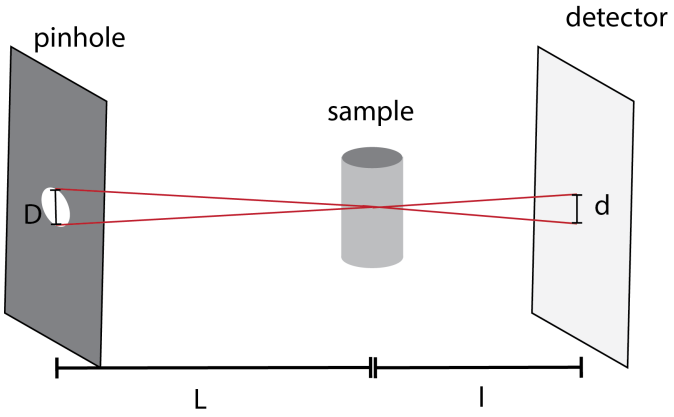

Figure 8.5: Schematic illustration of the geometric resolution (d) and its dependence on the size of the pinhole (D), the source to sample distance (l) and the sample to detector distance (L).

8.2.2 Temporal resolution

The achievable time resolution in kinetic studies depends on the available flux and the detector efficiency. The required exposure time is ruled by the signal-to-noise ratio. The relative image noise decreases when the number of counts in a detector pixel increases. Hence, the signal-to-noise ratio depends on the source flux, the size of the pinhole, the source-detector distance, the exposure time, the attenuation of the sample, the detector efficiency and additional detection noise, e.g. dark current and read out noise. Therefore the best trade off between spatial resolution and the signal-to-noise ratio has to found for each (in particular kinetic) experiment. Other sources of noise are, however, given by e.g. gamma radiation and fast neutrons reaching the detector. These background noise sources are to be avoided as much as possible through instrumentation means like shielding, filters, and avoiding a direct line of sight from the detector to the neutron source.

Neglecting the detector and background noise, it can be assumed that the counting statistics of the detector is Poisson distributed and the signal-to-noise ratio is given by $\sigma(N)/N = 1/\sqrt{N}$, where N is the number of counts in a single detector pixel.

To improve the spatial resolution both the geometric resolution, d, and the effective pixel size must be reduced. Both decrease the counting number in each detector pixel, meaning that the exposure time has to be increased correspondingly to have unchanged signal-to-noise ratio. In the most efficient case the resolution of the detector system matches the geometric resolution of the set-up. The higher the signal-to-noise ratio the better objects with similar attenuation coefficients (and thickness's) can be distinguished in a radiographic image. The neutron flux at most beam lines is of the order $10^6 - 10^8$ neutrons/cm^2/s and with a pixel size of the order 100 μm the number of counts per pixel is $10^3 - 10^6$

neutrons/s.

8.2.3 Detection

As outlined above, the main parameters characterizing an imaging detector are the detection efficiency, the electronic noise and the intrinsic spatial resolution. The most common detectors used for neutron imaging are scintillator screens in conjunction with CCD (charge-couple-device) cameras and flat amorhous-Si detectors[65, 66], but meanwhile also MCP (microchannel plate) based detectors [67]. In the scintillator screen the neutrons are absorbed and visible light is emitted, which can be detected by the CCD. The most commonly used scintillator material is crystalline ^{6}LiF/ZnS:Ag, where the neutrons are converted by the Li-atoms in order to produce light by the ZnS scintillator material [68]. The doping with silver shifts the light emission to be around 450 nm, which is in the range where the CCD is most efficient. The thickness of the scintillator screen is between 0.03 mm and 0.2 mm. The thicker the screen the more neutrons are absorbed, but the spatial resolution decreases correspondingly.

Not all neutrons will be absorbed in a scintillator screen and the CCD chip will suffer from radiation damage if placed directly behind the scintillator screen. Therefore a mirror is placed in an angle of 45° behind the scintillator screen and the light is reflected to the CCD chip. A lens system is placed between the mirror and the CCD in order to record an image of the light from the scintillator on the chip, illustrated in Figure 8.6.

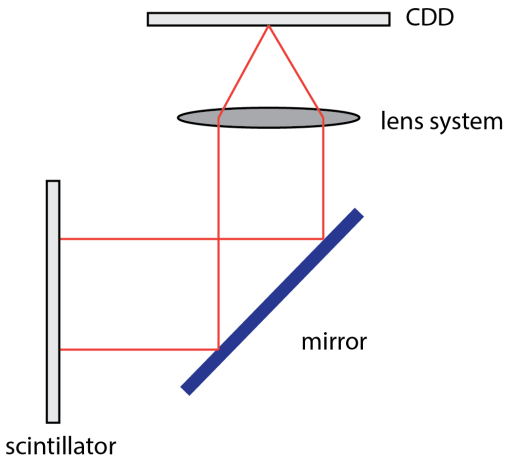

Figure 8.6: Schematic illustration of the scintillator screen coupled to a CCD detector.

Amorphous Si-detectors and MCP detectors can be placed directly in the beam and function without optics. Both the amorhous-Si and the MCP detectors require a converter, typically based on ^{10}B, which has a high absorption cross section for thermal neutrons. The neutrons are captured by ^{10}B to produce

^{7}Li and α-particles. For the Si-detector, the α-particles pass on to the detection layer, a biased silicon layer [69]. For the MCP detector the α-particles and lithium nuclei liberate free secondary electrons into the adjacent evacuated channel, illustrated in an animation (http://www.novascientific.com/neutron.html).

Experimental considerations. In the experimental set-up factors such as electronic noise and inhomogeneities in the detector efficiency and variation in the incident beam intensity both temporally and in time, effects the image quality.

To improve image quality three images are combined to form the final image; a projection image of the sample, a dark-field and a flat-field image. The dark-field image is a image with the beam turned off used to corrected for dark-current in the detector system, meaning counts in the detector not related to the neutron beam. These counts must be subtracted from the projection images. A flat-field image is an image with open beam shutter, but without the sample placed in the beam path. The flat-field image is used to correct for inhomogeneities in the beam profile and in the detector screen. The projections (transmission image) are for each pixel corrected with both the dark-field and the flat-field images.

$$T_\theta = \frac{I_\theta - DF}{FF - DF} \tag{8.5}$$

with I_θ being the original projection image, DF is the dark field image and FF is the flat-field image.

8.3 Computed tomography

Computed tomography (CT) is most commonly know for X-rays in the field of medical imaging, which is extensively used for diagnostics at hospitals. In computed tomography the interior 3D structure is reconstructed from a series of radiographic images obtained from different angles and have successfully been applied for neutrons.

Consider the case of a 2D sample, shown in 8.7(a) with the gray scale representing the interior attenuation coefficient, $\mu(x, y)$. When illuminated by the neutron beam the projection image, $T_\theta(x')$ is given by Eq. (8.5) and shown in 8.7(b). Projections taken from several angles are collected in a *sinogram*, shown in Figure 8.7(c).

The aim of the tomographic reconstruction is to go from the projections back to the function $\mu(x, y)$. The algorithm used for that is called the Filtered Backprojection Algorithm and will be derived in the following sections for a 2D sample and in the case where the beam rays are all parallel. To obtain the 3D reconstruction of the attenuation coefficient, $\mu(x, y, z)$, the projections are measured stepwise in height and the reconstructed 2D slices are stacked to obtain the 3D structure. The derivation given below follows [70].

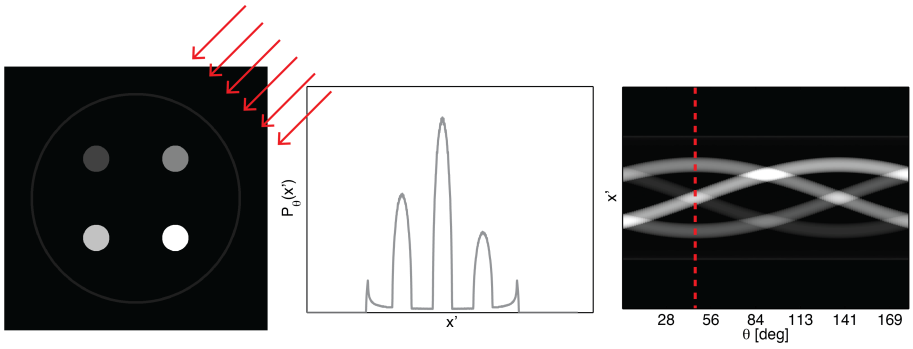

Figure 8.7: 2D object (a) projected from an angle of 45° degrees (b). The beam direction is shown as red arrows. Projections from 128 angles covering 180° collected in a sinogram (c). The red line indicates the projection at 45°.

8.3.1 Tomographic reconstruction

A projection image can be mathematically expressed as an integral of the object function, $f(x, y)$, along the beam path

$$\begin{aligned} P_\theta(x') &= \int_{-\infty}^{\infty} dx \int_{-\infty}^{\infty} dy f(x,y)\delta(x\cos(\theta) + y\sin(\theta) - x') \\ &= \int_{-\infty}^{\infty} f(x', y')dy' \end{aligned} \tag{8.6}$$

where the variables are defined in Figure 8.8 and $\delta(x)$ is the Dirac-delta function. The total projection is obtained by measuring $P_\theta(x')$ for all x'.

The coordinate system (x', y') is the coordinate system (x, y) rotated by the angle θ:

$$\begin{pmatrix} x' \\ y' \end{pmatrix} = \begin{bmatrix} \cos\theta & \sin\theta \\ -\sin\theta & \cos\theta \end{bmatrix} \begin{pmatrix} x \\ y \end{pmatrix} \tag{8.7}$$

The projection, $P_\theta(x')$, is known as the Radon transformation of the function of $f(x, y)$ [71]. In the case of neutron (or X-ray) imaging the object function, $f(x, y) = \mu(x, y)$, the interior attenuation coefficient. For the projection to be the Radon transformation of $\mu(x, y)$ it is seen from Eq. (8.2) that $P_\theta(x') = -\ln(T_\theta(x'))$.

The Fourier Slice Theorem

The Filtered Backprojection Algorithm is based on the Fourier Slice Theorem, which states that: *The Fourier transformation of projection $\tilde{P}_\theta(w)$ is equal to the Fourier transformation of the object, $\tilde{f}(u, v)$, along a line through the origin in the Fourier domain.*

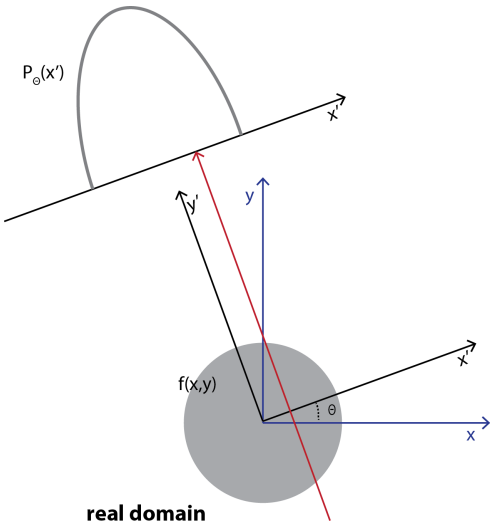

Figure 8.8: Projection, $P_\theta(t)$, of the object $f(x, y)$, along a line parallel to y'.

The theorem is illustrated in Figure 8.9(a), where the Fourier transformation of $P_\theta(x')$ is shown as a grey line in the Fourier domain. The line is rotated an angle θ with respect to the u-axis.

The Fourier Slice Theorem can be proven directly, by taking the Fourier transform of the projection of the object, $P_\theta(x')$ with respect to the spatial frequency w:

$$\begin{aligned}
\tilde{P}_\theta(w) &= \int_{-\infty}^{\infty} dx' P_\theta(x') \exp\left(-i2\pi(x'w)\right) \\
&= \int_{-\infty}^{\infty} dx' \int_{-\infty}^{\infty} dy' f(x', y') \exp\left(-i2\pi(x'w)\right) \\
&= \int_{-\infty}^{\infty} dx \int_{-\infty}^{\infty} dy f(x, y) \exp\left(-i2\pi w(x\cos\theta + y\sin\theta)\right) \\
&= \int_{-\infty}^{\infty} dx \int_{-\infty}^{\infty} dy f(x, y) \exp\left(-i2\pi(xu + yv)\right) \\
&= \tilde{f}(u, v) \qquad (8.8)
\end{aligned}$$

We here identify the spatial frequencies u and v as: $(u, v) = (w\cos\theta, w\sin\theta)$, meaning that

$$\tilde{P}_\theta(w) = \tilde{f}(w\cos\theta, w\sin\theta) \qquad (8.9)$$

8.3.2 Filtered Backprojection Algorithm

Before going into the mathematical derivation of the Filtered Backprojection Algorithm the main idea will be summarized.

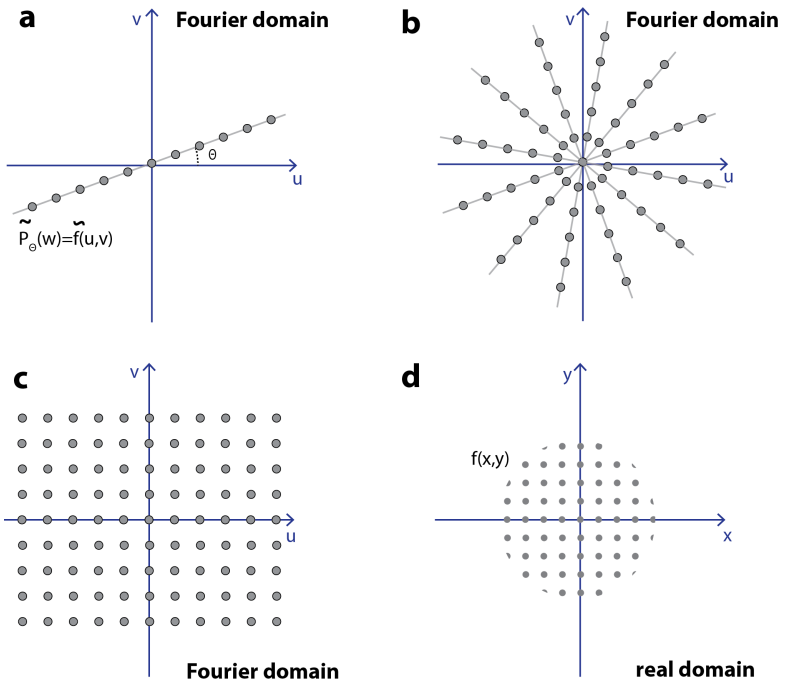

Figure 8.9: a) The Fourier transformation of the projection, $\tilde{P}_\theta(w)$ equals the Fourier transformation of the object, $\tilde{f}(u,v)$, along a single line in Fourier domain. **b)** Measuring $P_\theta(t)$ for different angles gives $\tilde{f}(u,v)$ in a number of lines in the Fourier domain. **c)** Interpolation of $\tilde{f}(u,v)$ in the parts of the Fourier domain not covered by the projection measurement. **d)** Inverse Fourier transformation to recover the object function.

Having obtained the projection from several angles, the Fourier transform of the object is known along several lines in the Fourier domain, shown in Figure 8.9(b). In order to calculate the object function by taking the inverse Fourier transformation, the Fourier transformation must be known regularly in the whole Fourier domain, as shown in Figure 8.9(c).

For this to be the case the Fourier transformation of each projection should form a pie shape in the Fourier domain, as shown in Figure 8.10(a). However, the Fourier Slice Theorem says that the Fourier Transformation is only known along a line, as illustrated in Figure 8.10(b). To approximate the ideal situation in Figure 8.10(a) a filter of the form $|w|$ is applied to $\tilde{f}(u,v)$ before taking the inverse Fourier transform, shown in Figure 8.10(c). From the mathematical derivation it is seen that the filter appears as the Jacobian determinant when changing from Cartesian to polar coordinates in the Fourier Domain.

The mathematical derivation of the algorithm goes backwards and starts by

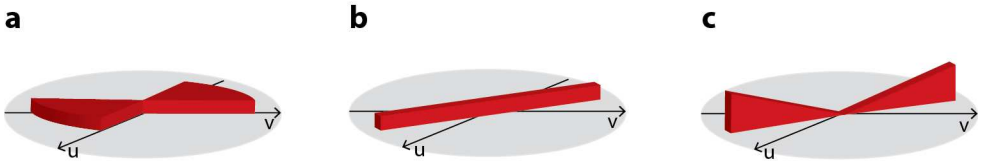

Figure 8.10: Schematic illustration of the Fourier transformation of the projections. **a)** The ideal case where the data covers a pie shape in Fourier domain and the object can be obtained by taking the inverse Fourier transform. **b)** Fourier transformation of a measured projection. **c)** In the Filtered Backprojection Algorithm a filter is applied to the data in (b) to approximate the situation in (a).

taking the inverse Fourier Transform of $\tilde{f}(u, v)$.

$$f(x,y) = \int_{-\infty}^{\infty} du \int_{-\infty}^{\infty} dv \tilde{f}(u,v) \exp\left(i2\pi(xu+yv)\right) \tag{8.10}$$

$$= \int_{0}^{2\pi} d\theta \int_{0}^{\infty} dw w \tilde{f}(w,\theta) \exp\left(i2\pi w(x\cos\theta + y\sin\theta)\right) \tag{8.11}$$

$$= \int_{0}^{\pi} d\theta \int_{-\infty}^{\infty} dw |w| \tilde{f}(w,\theta) \exp\left(i2\pi w(x\cos\theta + y\sin\theta)\right) \tag{8.12}$$

where the coordinate transformation from (u, v) to (w, θ) have introduced the Jacobian determinant, w. Note that the integration limits are changed from step 2 to 3, due to the periodic properties of the Fourier Transform, which gives the filter $|w|$.

$$\tilde{f}(w, \theta + \pi) = \tilde{f}(-w, \theta) \tag{8.13}$$

Substituting in the projection, using the Fourier Slice Theorem gives that

$$f(x,y) = \int_{0}^{\pi} d\theta \int_{-\infty}^{\infty} dw |w| \tilde{P}_\theta(w) \exp\left(i2\pi w x'\right) \tag{8.14}$$

The Fourier transform of the projection, $\tilde{P}_\theta(w)$ is filtered by $|w|$, before taking the inverse Fourier transform and backprojected by integrate over all angles in the real domain. Therefore the name Filtered Backprojection. The filter $|w|$ is called the Ram-Lak filter, but for some applications other filters is used in order to reduce noise in the reconstructed images [70].

To use this formula, the projection must be known continuously for the angle θ in the interval $[0, \pi]$ and in space x' in the interval $[-\infty, \infty]$. In practice the projections are measured in discrete points corresponding the pixel size of the detector and for a finite number of angle steps. Therefore the integrals in Eq. (8.14) are replaced by sums, illustrated by the point in Figure 8.9.

In summary, the Filtered Backprojection Algorithm goes in the following steps:

- Collect the projections $P_\theta(x')$ from a number of angle steps and number of points.

- Calculate the (discrete) Fourier Transformation, $\tilde{P}_\theta(w)$ of each projection, Figure 8.9(a-b)
- Apply the filter $|w|$ in Fourier domain, to approximate the ideal case where the measured points are equally distributed in Fourier space, Figure 8.9(c).
- Take the inverse Fourier Transformation of the filtered projection $|w|\tilde{P}_\theta(w)$ and make a sum over all angles to make the reconstruction, Figure 8.9(d).

Figure 8.11 shows the reconstruction of a 2D object, using 4 (a), 8 (b), 32 (c) and 128 projections (d) over 180°. It is seen how the reconstruction algorithm smear the projection images back on the image plane and that the reconstruction is improved when using more projections.

To speed up the measurements a cone beam instead of a parallel beam is used in practice, illustrated in Figure 8.4. The change in beam geometry effects the reconstruction algorithm in Eq. (8.14), since the path of the beam is changed, but the basic principle is the same. The derivation can be found in [70]. For most neutron imaging set-ups the distance between be pinhole and the detector is so large that for practical implementation the beam can be considered parallel.

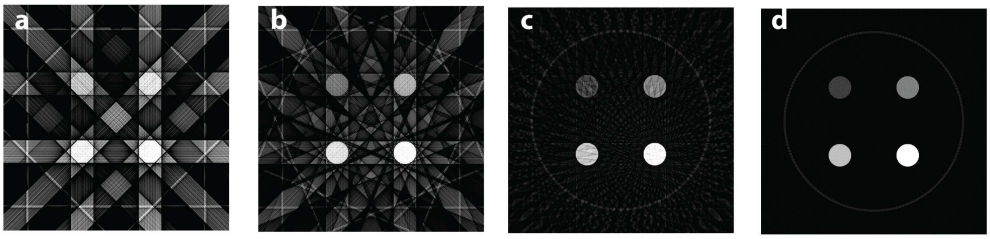

Figure 8.11: Reconstruction of the 2D object shown in Figure 8.7(a) using 4, 8, 32 and 128 projections (a-d) over 180 degrees.

8.4 Applications of neutron imaging

A particular strength of neutron imaging is the sensitivity to hydrogen, combined with the ability to penetrate bulk metal parts. Therefore water, plastic, glues, hydrogen, and organic materials can be detected in even small amount and in dense materials. This section presents examples, where neutron imaging gives novel insight.

8.4.1 Water transport in fuel cells

Fuel cells operate by converting a fuel into electrical power via a chemical reaction. One type of fuel cells is the hydrogen-oxygen proton exchange membrane fuel cell (PEMFCs), where hydrogen is used as the fuel and reacts with oxygen

to form water. A schematic presentation of a PEMFC is shown in Figure 8.12 [72]. The water must be removed through flow channels for the fuel cell to work properly and if water is not formed in an area of the fuel cell it indicates a defective area. The metallic shell of the fuel cell is almost transparent to neutrons and the interior water content can be quantified due to the high scattering cross section of hydrogen. Therefore the dynamics of the water can be quantified in a unmodified and full functional fuel cell (*in situ*) by neutron radiography or tomography [73].

To follow the dynamics, good temporal resolution is required, as the exposure time for each projection image is limited by the time scale of the transport process. The time resolution for neutron radiography is of the order of seconds, which is well suited for these processes [74]. The difference in the attenuation coefficient of water (H_2O) and heavy water (D_2O), makes it possible not only to study the water accumulation, but also the water exchange in operational fuel cells by neutron radiography, demonstrated by [75]. Switching from hydrogen to deuterium gas, the deuterium gas is reduced to D_2O in the catalyst layer and gradually replaced water, seen in the radiographic images as a decrease in neutron attenuation. Thereby the exchange time can be measured by measuring the change in image intensity, shown in Figure 8.13(left).

The radiographic images are normalized to the dry fuel, such that only the water content is seen and the color scale displays the local water thickness. At time $t = 0$ the fuel cell is saturated and the H_2 feed gas is exchange with the D_2 gas. After 24.75 min (Figure 8.13 (left)(d)) nearly all the water has been replace by heavy water, and the gas feed in again switched back to H_2. The neutron beam attenuation increases, seen in Figure 8.13 (left)(e)-(f). The amount of water is calculated from the attenuation in the red marked area in Figure 8.13 (left)(a) for about the first 10 sec, shown in Figure 8.13 (right). This show that neutron radiography can be used not only to visualize but also quantify the flow process *in situ*.

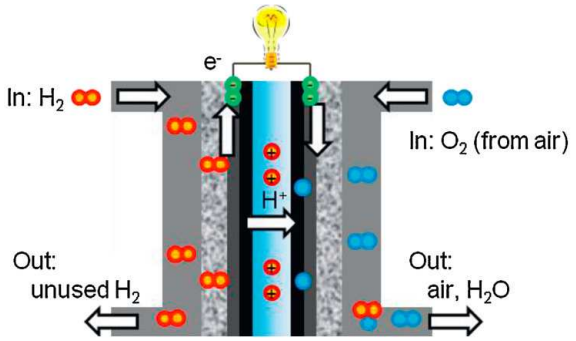

Figure 8.12: Schematic illustration of a PEMFC. Figure is adapted from [72].

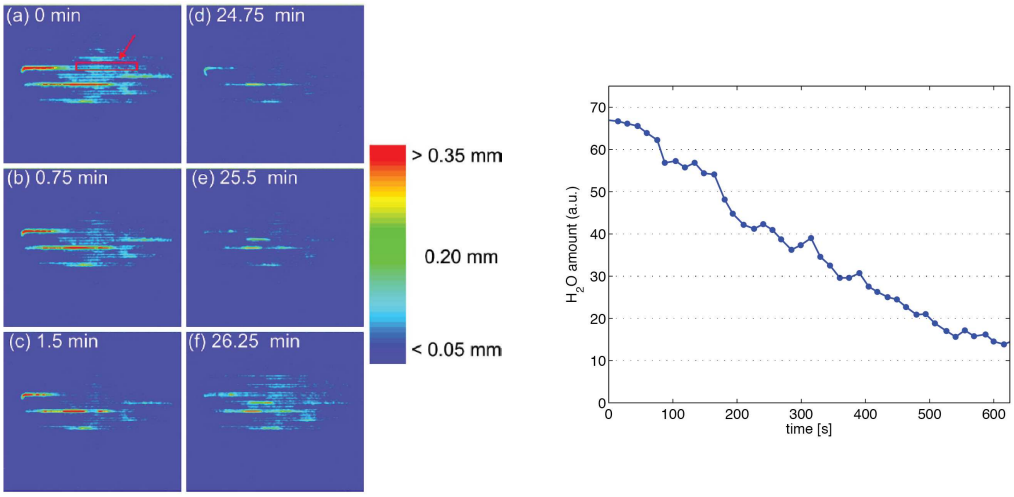

Figure 8.13: Left: Radiographic neutron images normalized to the dry fuel cell. Color scale display the water thickness. Figures are adapted from [75]. **Right:** Change in the water thickness in area marked by the red box in (a) after switching the gas feed from H_2 to D_2. Data is digitalized from [75].

8.4.2 Water uptake in plants

The difference in the attenuation coefficient of light and heavy water also makes it possible to study the water uptake in plants [76, 77, 78]. Figure 8.14(left)**a** shows a neutron radiographic image of roots in soil. The surface is irrigated with 3 mL of D_2O and radiographic images are obtained 15 min, 30 min, 6 h and 12 h after irrigation, shown at Figure 8.14 (left)**b-e**. The images are normalized to the original images, meaning that in the white areas H_2O has been replaced by D_2O. The soil to the left becomes wet and the roots takes up water (WR). The soil to the right side remains dry (S) for the whole experiment, but water is transported to the roots (DR). The relative change in neutron transmission makes it possible to compare the water uptake in the different areas of the roots, Figure 8.14 (right). The water uptake by the roots placed in the moist soil is significant higher, than in the dry soil. After 6-12 h it is seen that water is transported to the stem, Figure 8.14 (left)**d-e**.

8.4.3 Cultural heritage

Imaging of cultural heritage ranges from archaeological objections to pieces of art. Here, the preserving interest is important and non-destructive testing techniques are required. Therefore, neutron tomography is a well-suited technique.

El violinista (1920) is a sculpture by the Catalan artist Pablo Gargallo. The sculpture is composed of the wooden core on which thin sheets of lead is fixed by needles and soldering. Figure 8.15 shows a photography of the sculpture (a)

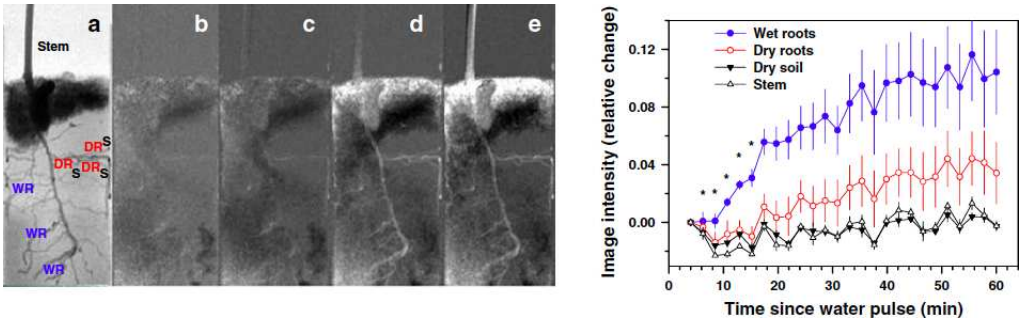

Figure 8.14: Left: (**a**) Roots system from Zea mays, prior to exposure of 3 mL of D_2O to the surface. (**b-e**) The same plant 0.25, 0.5, 6 and 12 h after the surface has been irrigated with D_2O. The images are divided by the initial image (a). Light areas represent displacement of H_2O with D_O. **Right:** Relative change in image intensity for roots placed in moist soil (WR), dry soil (DR) and the dry soil (S). The figures are adapted from [76].

and the 3D rendering of the tomographic reconstruction, showing the wooden core (b). The sculpture shows signs of corrosion, which is most likely due to organic vapours from the wood. This can be visualized by neutron tomography, due to the hydrogen sensitivity, shown as red areas in Figure 8.15(c).

Figure 8.15: The lead and wood sculpture *El violinista* (1920) (a). 3D rendering of the wood core (b) and map of the areas (c) effected by corrosion (red) and needle fixations (blue) obtained by neutron tomography. Figure adopted from [79].

An other example is a Buddhist bronze statue. Figure 8.16 (top row) shows a photograph (left) and neutron radiography image (right) of a 15th century Bodhisattva Avaloktesvara [79]. The objects placed inside the statue can be investigated closely by neutron tomography without effecting the statue, shown in Figure 8.16 (bottom raw). Three objects are identified. A small heart-shaped capsuled (turquoise) wrapped in a piece of close is placed in the chest of the statue. A scroll (brown) probably containing a religious text, and a pouch

(violet) containing some spherical objects and tied up with string.

Figure 8.16: Top: Photography (a) and neutron radiography image (b) of a Buddhist bronze statue. **Bottom**. 3D rendering obtained by neutron tomography. (a) shows a virtual cut through the sculpture. (b) and (c) show the segmentation of three discernable objects; a small wrapped capsule (turquoise), a scroll (brown) and a pouch (violet) containing some spherical objects (green, grey, yellow) and tied up with string (red). Figure adopted from [79].

Part IV

Dynamics of materials

Chapter 9

Inelastic nuclear neutron scattering

One of the early successes of neutron scattering was the study of dynamics of matter, in particular phonon dispersion relations. Here, the vibrational frequency (or phonon energy) is deduced from the change in neutron energy through the principle of energy conservation. Hence, for the study of dynamics we are dealing with inelastic neutron scattering.

This chapter naturally leads to the description in chap. 10 of neutron scattering from quantised lattice vibrations, or *phonons*. The related topic of inelastic neutron scattering from diffusion and molecular motion is not covered in this version of the notes.

Instrumentation for the general field of inelastic neutron scattering is described in section. 4.7.

9.1 * Scattering theory for nuclear dynamics

We will now return to the basic scattering theory from chapter 2 to derive the equations that govern all inelastic scattering from nuclei.

9.1.1 * Scattering from initial to final state

In (2.49), we derived the starting equation for the inelastic cross section:

$$\left.\frac{d^2\sigma}{d\Omega dE_{\mathrm{f}}}\right|_{\lambda_{\mathrm{i}}\to\lambda_{\mathrm{f}}} = \frac{k_{\mathrm{f}}}{k_{\mathrm{i}}}\left(\frac{m_{\mathrm{n}}}{2\pi\hbar^2}\right)^2 \left|\left\langle\lambda_{\mathrm{i}}\psi_{\mathrm{i}}\middle|\hat{V}\middle|\psi_{\mathrm{f}}\lambda_{\mathrm{f}}\right\rangle\right|^2 \delta(E_{\lambda_{\mathrm{i}}} - E_{\lambda_{\mathrm{f}}} + \hbar\omega). \tag{9.1}$$

We begin by expanding the expression for the nuclear potential (2.60):

$$\hat{V} = \frac{2\pi\hbar^2}{m_{\mathrm{n}}}\sum_j b_j\delta(\mathbf{r}-\mathbf{R}_j), \tag{9.2}$$

where $\mathbf{R}_j$ is now the operator for the position of the j'th nucleus. We use this to expand the matrix element in the inelastic cross section:

$$\begin{aligned}
&\left|\left\langle \lambda_\mathrm{i}\psi_\mathrm{i}\middle|\hat{V}\middle|\psi_\mathrm{f}\lambda_\mathrm{f}\right\rangle\right|^2 \qquad (9.3)\\
&= \left(\frac{2\pi\hbar^2}{m_\mathrm{n}}\right)^2 \left[\sum_j b_j \left\langle \lambda_\mathrm{i}\middle|\int \psi_\mathrm{i}^*\delta(\mathbf{r}-\mathbf{R}_j)\psi_\mathrm{f} d^3\mathbf{r}\middle|\lambda_\mathrm{f}\right\rangle\right]^2\\
&= \left(\frac{2\pi\hbar^2}{m_\mathrm{n}}\right)^2 \sum_{j,j'} b_j b_{j'} \left\langle \lambda_\mathrm{i}\left|\exp(-i\mathbf{q}\cdot\mathbf{R}_j)\right|\lambda_\mathrm{f}\right\rangle \left\langle \lambda_\mathrm{f}\left|\exp(i\mathbf{q}\cdot\mathbf{R}_{j'})\right|\lambda_\mathrm{i}\right\rangle .
\end{aligned}$$

If all nuclei were fixed in position, we would now reach the diffraction cross section by summing over the (in practice unmeasurable) finite states of the lattice, $|\lambda_\mathrm{f}\rangle$, since the δ-function in (9.1) would factorize out and vanish by integration. However, we cannot do this simple calculation now, so we need to take a more difficult path. We rewrite the troublesome delta-function in (9.1), using $2\pi\delta(a) = \int_{-\infty}^{\infty}\exp(iax)dx$ (following Squires 2.3):

$$\boxed{\delta(E_{\lambda_\mathrm{i}} - E_{\lambda_\mathrm{f}} + \hbar\omega) = \frac{1}{2\pi\hbar}\int_{-\infty}^{\infty}\exp\left(\frac{i(E_{\lambda_\mathrm{f}} - E_{\lambda_\mathrm{i}})t}{\hbar}\right)\exp(-i\omega t)dt}. \qquad (9.4)$$

Now, we utilize a rather intuitive identity from quantum mechanics, valid when $|\lambda\rangle$ is an eigenstate of the Hamiltonian H with eigenvalue E_λ:

$$\exp\left(\frac{iHt}{\hbar}\right)|\lambda\rangle = \exp\left(\frac{iE_\lambda t}{\hbar}\right)|\lambda\rangle. \qquad (9.5)$$

We can then rewrite the inelastic scattering cross section (9.1) into

$$\begin{aligned}
&\left.\frac{d^2\sigma}{d\Omega dE_\mathrm{f}}\right|_{\lambda_\mathrm{i}\to\lambda_\mathrm{f}} \qquad (9.6)\\
&= \frac{k_\mathrm{f}}{k_\mathrm{i}}\sum_{j,j'}\frac{b_j b_{j'}}{2\pi\hbar}\int_{-\infty}^{\infty}\left\langle \lambda_\mathrm{i}\left|\exp(-i\mathbf{q}\cdot\mathbf{R}_j)\right|\lambda_\mathrm{f}\right\rangle\left\langle \lambda_\mathrm{f}\left|\exp(i\mathbf{q}\cdot\mathbf{R}_{j'})\right|\lambda_\mathrm{i}\right\rangle\\
&\quad\times\exp\left(\frac{iE_{\lambda_\mathrm{f}}t}{\hbar}\right)\exp\left(-\frac{iE_{\lambda_\mathrm{i}}t}{\hbar}\right)\exp(-i\omega t)dt\\
&= \frac{k_\mathrm{f}}{k_\mathrm{i}}\sum_{j,j'}\frac{b_j b_{j'}}{2\pi\hbar}\int_{-\infty}^{\infty}\left\langle \lambda_\mathrm{i}\left|\exp(-i\mathbf{q}\cdot\mathbf{R}_j)\right|\lambda_\mathrm{f}\right\rangle\\
&\quad\times\left\langle \lambda_\mathrm{f}\middle|\exp\left(\frac{iHt}{\hbar}\right)\exp(i\mathbf{q}\cdot\mathbf{R}_{j'})\exp\left(-\frac{iHt}{\hbar}\right)\middle|\lambda_\mathrm{i}\right\rangle\exp(-i\omega t)dt\\
&= \frac{k_\mathrm{f}}{k_\mathrm{i}}\sum_{j,j'}\frac{b_j b_{j'}}{2\pi\hbar}\int_{-\infty}^{\infty}\left\langle \lambda_\mathrm{i}\left|\exp(-i\mathbf{q}\cdot\mathbf{R}_j(0))\right|\lambda_\mathrm{f}\right\rangle\\
&\quad\times\left\langle \lambda_\mathrm{f}\left|\exp(i\mathbf{q}\cdot\mathbf{R}_{j'}(t))\right|\lambda_\mathrm{i}\right\rangle\exp(-i\omega t)dt.
\end{aligned}$$

In the last step, we have employed the time-dependent Heisenberg operators, $\mathbf{R}(t) = \exp(iHt/\hbar)\mathbf{R}\exp(-iHt/\hbar)$; in particular, $\mathbf{R}(0) = \mathbf{R}$.

9.1.2 * The observable nuclear cross section

In an experiment, we observe only the final state of the neutron, not of the sample. Thus, we can find the total cross section by summing over all final states of the system, using the completeness rule:

$$\sum_{\mathrm{f}} |\lambda_{\mathrm{f}}\rangle\langle\lambda_{\mathrm{f}}| = 1, \tag{9.7}$$

We consider systems in thermal equilibrium and hence the contribution from a thermal average of initial states. We denote the thermal average by the notation $\langle A \rangle \equiv \sum_i p_i \langle\lambda_i|A|\lambda_i\rangle$, where p_i is the Boltzmann probability for the individual states. After these observations, we can specify the observable cross section for nuclear scattering:

$$\begin{aligned}\frac{d^2\sigma}{d\Omega dE_{\mathrm{f}}} = \frac{k_{\mathrm{f}}}{k_{\mathrm{i}}} \sum_{j,j'} \frac{b_j b_{j'}}{2\pi\hbar} \\ \times \int_{-\infty}^{\infty} \left\langle \exp(-i\mathbf{q}\cdot\mathbf{R}_j(0)) \exp(i\mathbf{q}\cdot\mathbf{R}_{j'}(t)) \right\rangle \exp(-i\omega t) dt.\end{aligned} \tag{9.8}$$

It should be noted that this is a rather general result, valid for any kind of nuclear motion.

Chapter 10

Scattering from lattice vibrations

In chapter 7, we worked under the assumption that the nuclei of the crystalline material were fixed in position, when investigating diffraction from the lattice planes. This is, of course, not a realistic description. In this chapter, we will investigate how the motion of the nuclei can scatter neutrons inelastically. However, as we shall see, a large fraction of the scattering will still take place as diffraction, as described in chapter 7.

First, we will treat the physics of lattice vibrations in crystalline materials purely classically, later a quantum mechanical treatment is given, leading to quantized vibrations, or *phonons*. The latter is necessary for the detailed understanding of the inelastic neutron scattering cross section from crystals.

Along with the description of phonons, we will discover how lattice vibrations affect the intensity of the diffraction signals, leading to the Debye-Waller factor described in chapter 7.

10.1 Lattice vibrations, classical treatment

We will here describe lattice vibrations in general. This section deals with the purely classical description, while section 10.2 introduces the quantum mechanical treatment.

10.1.1 Dynamical description of nuclei in crystals

Let us as before denote the equilibrium position of the nuclei with $\mathbf{r}_j$ – or for a non-Bravais lattice $\mathbf{r}_j + \mathbf{\Delta}_i$ with j being the index for the unit cell and i labeling the atom within the unit cell. These atomic positions are constant in time (assuming that the crystal center-of-mass is at rest). We describe the motion of the nuclei with the (small) displacement vector $\mathbf{u}_{ij}(t)$. The time-

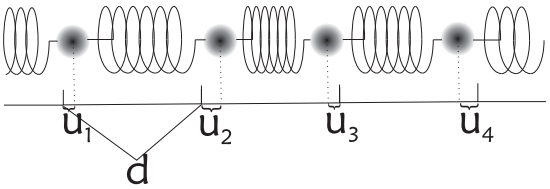

Figure 10.1: A classical illustration of a system showing lattice vibrations in one dimension. A series of equal masses (atoms) are connected by identical harmonic forces and can vibrate around their equilibrium positions.

dependent nuclear position now reads

$$\mathbf{R}_{ij}(t) = \mathbf{r}_j + \mathbf{\Delta}_i + \mathbf{u}_{ij}(t). \tag{10.1}$$

We approximate the potential energy between two neighbour atoms by a quadratic form in the difference between their displacements:

$$V_{jj'} = \frac{1}{2} K_{jj'} (\mathbf{u}_j(t) - \mathbf{u}_{j'}(t))^2 + V_0, \tag{10.2}$$

where $K_{jj'}$ is the spring constant for the (in this case isotropic) atom-atom interaction, V_0 is a zero point of the energy, and we have dropped the subscripts i for convenience.

10.1.2 The one-dimensional nearest neighbour model

We will now turn to a few concrete one-dimensional examples, which will give much insight in the physics of phonons. We first consider a model of N identical particles (atoms) of mass M, with equilibrium spacing a, and identical nearest neighbour spring constants K. This system is illustrated in figure 10.1. The equilibrium distance between atoms is a, so we can write $r_j = ja$.

The net spring force between two particles is zero in equilibrium (where all $u_j = 0$). In the general case, the force on particle j from particle $j+1$ reads:

$$F_{j,j+1}(t) = K\big(-u_j(t) + u_{j+1}(t)\big), \tag{10.3}$$

where K is the spring constant of one spring. Including also the similar coupling $F_{j-1,j}(t)$, the equation of motion for u_j can be written using Newton's second law:

$$M\frac{d^2}{dt^2}u_j(t) = K\big(u_{j-1}(t) + u_{j+1}(t) - 2u_j(t)\big). \tag{10.4}$$

To simplify the calculations, we assume periodic boundary conditions, *i.e.* we assume that atom 1 is connected with atom N with a force term equivalent to $F_{j,j+1}$. The error introduced by this so-called *Born-von Karman boundary*

conditions will vanish in the thermodynamic limit ($N \to \infty$) and hence it is safe for us to make this choice that makes the problem mathematically simple. The periodic boundary conditions are equivalent to defining $u_{N+1} \equiv u_1$.

We look for solutions to (10.4) of the plane wave form

$$u_j(t) = A\exp(iqja - i\omega_q t), \tag{10.5}$$

where the real value of $u_j(t)$ represent the physical displacement, while the imaginary part contains information on the phase of the vibrations. The amplitude for the vibrations, A, is chosen to be real. The periodic boundary conditions imply that the phase is invariant under a translation of N atoms. This gives a choice of possible values of the wave vector:

$$q = \frac{n}{N}a^*, \tag{10.6}$$

where n is an integer and the reciprocal lattice vector is $a^* = 2\pi/a$.

Inserting (10.5) into (10.4), we reach

$$-\omega_q^2 M u_j(t) = K u_j(t)\big(\exp(iqa) + \exp(-iqa) - 2\big). \tag{10.7}$$

This simplifies directly into the dispersion relation we are looking for

$$\boxed{\omega_q^2 = 2\omega_0^2\big(1 - \cos(qa)\big) = 4\omega_0^2 \sin^2(qa/2)}. \tag{10.8}$$

Here, the characteristic frequency, ω_0, is defined as the resonance frequency of the related single-particle harmonic oscillator,

$$\boxed{\omega_0 = \sqrt{K/M}}. \tag{10.9}$$

The dispersion relation for one Brillouin zone, $|\mathbf{q}| \leq \pi/a = |\mathbf{a}^*|/2$, is shown in figure 10.2. At small q, the dispersion is approximately linear, so it is meaningful to define a velocity of the lattice vibrations as

$$c = \frac{\partial \omega_q}{\partial q} \approx \omega_0 a. \tag{10.10}$$

These long-wavelength lattice vibrations are, in fact, the same as sound waves in materials. Therefore, this type of vibrations is known as *acoustic*.

As we shall see in section 10.2, the quantized lattice vibrations are known as phonons. The low-energy phonons are in analogy with the discussion above denoted *acoustic phonons*.

10.1.3 Optical lattice vibrations

A symmetry breaking in the Bravais crystal can cause a doubling of the unit cell, even if it may have little effect on the vibration physics. This leads to reduction of the Brillouin zone by a factor 2, $a_2^* = a^*/2$. The vibration modes

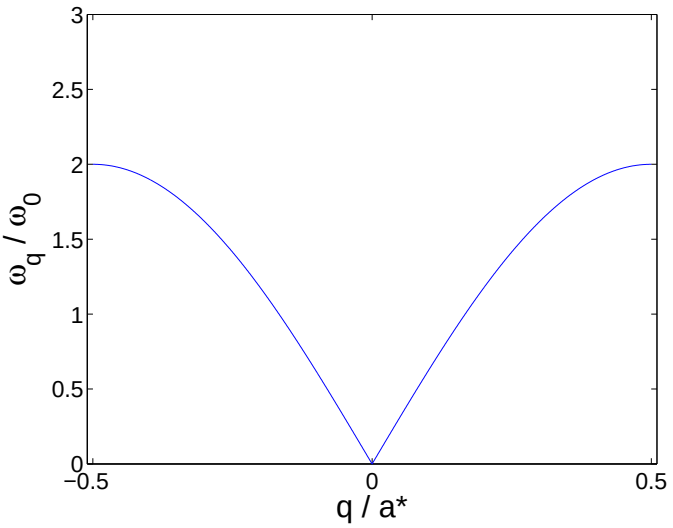

Figure 10.2: Dispersion relation for the nearest neighbour one-dimensional lattice model within one Brillouin zone.

are now denoted differently. The part of the dispersion relation that has the highest values of $|q|$ is "folded back" by $q_2 = q - a_2^*$ to create a second branch of the dispersion relation. This new, most often higher lying, branch is now denoted the *optical branch*. The optical and acoustic branches are shown in figure 10.3.

The optical mode for $q = 0$ is particularly easy to interpret: All unit cells behave identically, while the two atoms in the unit cell vibrate in counter phase. In the original system, figure 10.2, this corresponds to the zone boundary: $q = \pi/a$. The frequency at this position is $\omega_{\pi/a} = 2\omega_0$.

For the sake of self-consistency, let us calculate the above result explicitly. To describe this motion quantitatively, we denote the displacement of the first atom in the j'th unit cell $u_j(t)$, while the second atom is denoted $v_j(t)$. The equation of motion now reads

$$\begin{aligned} M\frac{d^2}{dt^2}u_j(t) &= K\big(v_{j-1}(t) + v_j(t) - 2u_j(t)\big), \\ M\frac{d^2}{dt^2}v_j(t) &= K\big(u_{j+1}(t) + u_j(t) - 2v_j(t)\big). \end{aligned} \tag{10.11}$$

Since $q = 0$, the motion is independent of j. Hence, we can reduce the expression to:

$$\begin{aligned} \omega^2 u(t) &= 2\omega_0^2\big(u(t) - v(t)\big), \\ \omega^2 v(t) &= 2\omega_0^2\big(v(t) - u(t)\big). \end{aligned} \tag{10.12}$$

This is the same equation of motion as for two identical particles connected by one spring with strength $2K$. When we take into account that the two atoms in

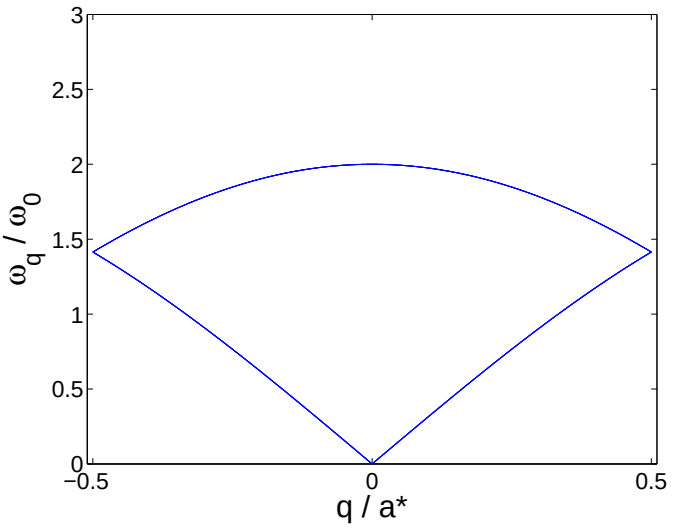

Figure 10.3: Dispersion relation for the nearest neighbour one-dimensional phonon model when the unit cell is doubled without change in the vibration physics. This means that the reciprocal lattice vector is halved with respect to Fig. 10.2, $a_2^* = a^*/2$. Note the occurence of a low (acoustic) and a high (optical) branch.

the unit cell move in counter phase, we have $u(t) = -v(t)$, leading to $\omega = 2\omega_0$, as we aimed to show.

In general, for a one-dimensional system with N atoms in the unit cell, there will be 1 acoustic and $N - 1$ optical modes.

10.1.4 One-dimensional models with two different atoms

Let us now treat the one-dimensional system with identical springs of constant K, but two different atoms per unit cell. This is illustrated in Figure 10.4.

The masses of the two atoms are denoted m and M, respectively, with M

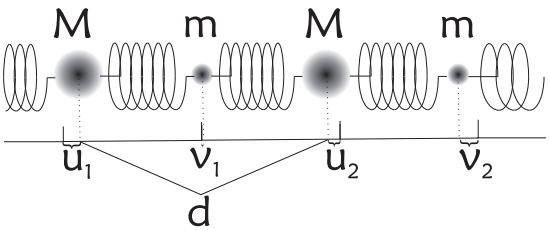

Figure 10.4: The two-atom phonon problem in one dimension. Two different masses (atoms) are connected by identical harmonic forces (springs).

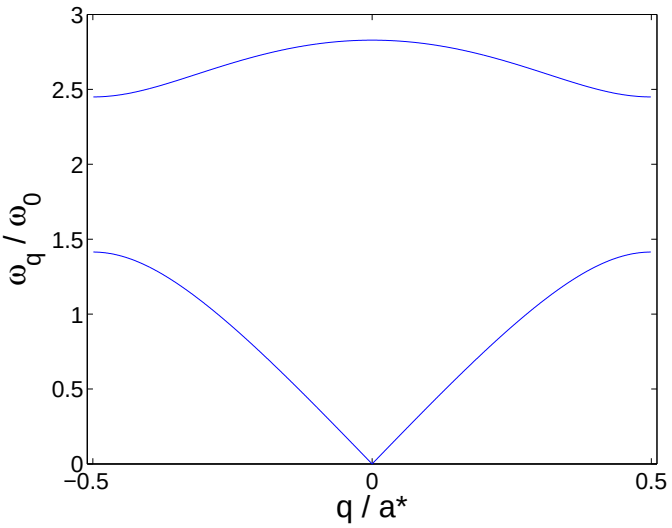

Figure 10.5: Dispersion relation for the simple two-atom one-dimensional phonon model with $\beta = 1/3$.

the largest of the two. We define

$$\beta = \frac{m}{M} < 1, \tag{10.13}$$

and ω_0 is defined as in (10.9).

Solving the equations of motion for the two atoms (see problem 10.4.2), we reach the dispersion relation

$$\boxed{\omega_q^2 = 2\omega_0^2\big(1 - \cos(qa/2)\alpha^{-1}\big)}, \tag{10.14}$$

where α is the ratio of vibration amplitudes for the two types of atoms:

$$\alpha = \frac{1 - \beta \pm \sqrt{(1-\beta)^2 + 4\beta\cos^2(qa/2)}}{2\cos(qa/2)}. \tag{10.15}$$

Note that for $q \to 0$, we have the solutions $\alpha_1 = 1$ (long-wave acoustic phonons) and $\alpha_2 = -\beta$; the $q = 0$ optical phonons, where the atoms move in counter phase and the light atoms vibrate with a larger amplitude. The resulting dispersion relation for $\beta = 1/3$ is shown in figure 10.5.

10.1.5 The role of lattice vibrations in materials

The lattice vibrations determine a number of properties of materials. A straigtforward example is the acoustic properties, where the acoustic phonons are equal to sound waves.

An important consequence of lattice vibrations is the thermodynamic properties of materials. In fact the heat capacity and thermal conductivity in insulating materials stem from the lattice vibrations.

As we shall see in section 10.2, the lattice vibrations quantize in energy units of $\hbar\omega_q$. These *quasiparticles* are denoted *phonons* and are approximately Bosons, *i.e.* there can be several phonons with the same $\mathbf{q}$; a larger number of phonons corresponds to larger classical vibration amplitudes. The occupation numbers of phonons are thus given by Bose-Einstein statistics,

$$n_q = n_{\mathrm{B}}(\hbar\omega_q/k_{\mathrm{B}}T). \tag{10.16}$$

where n_{B} is the Bose occupation number

$$n_{\mathrm{B}}\left(\frac{\hbar\omega}{k_{\mathrm{B}}T}\right) = \frac{1}{\exp\left(\frac{\hbar\omega}{k_{\mathrm{B}}T}\right) - 1}\,. \tag{10.17}$$

These equations form, together with knowledge of the dispersion relation, ω_q, the basis for the description of the thermal properties of phonons, which is elaborated on in many textbooks, *e.g.* the one by Kittel [69]. Is it therefore essential to measure the phonon dispersion relations in order to understand thermal properties of materials.

Another, and more complex part of phonon science is the study of crystal anharmonicities, caused by 4'th and higher order terms in the atomic potentials. Anharmonicities give rise to *e.g.* thermal expansion, and can be inferred from studies of phonon lifetimes, which in turn can be found by studying the energy spread in the phonon energies. This is, however, beyond the scope of these notes.

10.2 * Phonons, quantum mechanical treatment

With the discussion on lattice vibrations (last section) in mind, we now treat the problem of lattice vibrations quantum mechanically. We will show how the vibrations with frequencies ω_q of the classical solution quantize into bosonic *phonons*, which has wavenumber $\mathbf{q}$ and energy $\hbar\omega_q$.

10.2.1 * The harmonic oscillator

The solution to the phonon problem lends much from the standard example of one particle in a harmonic potential. Therefore, it is of value to summarize this solution here. A more thorough derivation is given in most textbooks on quantum mechanics.

We consider a particle of mass M in a one-dimensional periodic potential. The Hamiltonian is given as

$$H = \frac{p^2}{2M} + \frac{Kx^2}{2}, \tag{10.18}$$

where p is the momentum operator, $p = i\hbar\partial/\partial x$, and $[x, p] = i\hbar$. We recall that the classical oscillator frequency is given by (10.9) and define the creation and annihilation operators as

$$a^\dagger = \frac{1}{\sqrt{2\hbar\omega_0 M}} \left(M\omega_0 x + ip\right). \tag{10.19}$$

$$a = \frac{1}{\sqrt{2\hbar\omega_0 M}} \left(M\omega_0 x - ip\right). \tag{10.20}$$

These operators are normalized so that

$$[a, a^\dagger] = 1. \tag{10.21}$$

This commutation relation show that a and $a^\dagger$ are boson operators. We can obtain the position and momentum operators:

$$x = \sqrt{\frac{\hbar}{2\omega_0 M}} \left(a^\dagger + a\right). \tag{10.22}$$

$$p = -i\sqrt{\frac{\hbar\omega_0 M}{2}} \left(a^\dagger - a\right). \tag{10.23}$$

By substitution into (10.18), we reach

$$H = \hbar\omega_0 \left(a^\dagger a + \frac{1}{2}\right), \tag{10.24}$$

where $a^\dagger a$ is the number operator, n, with eigenvalues being integers from zero and upwards. The oscillation is thus quantized with energy quanta of $\hbar\omega_0$. Notice that even the ground state has a finite energy, $E_{\rm gs} = \hbar\omega_0/2$. This is called the *zero point energy*. The zero point energy is related to a "smearing" of the ground state, due to Heisenberg's uncertainty principle, which in this case is denoted *zero point motion*.

10.2.2 * The one-dimensional quantum model

This lattice model is solved in much the same way as for the one-particle harmonic oscillator. We can write the Hamiltonian as the sum of the kinetic energy and a harmonic potential of the form (10.2):

$$H = \sum_j \left(\frac{p_j^2}{2M} + \frac{K}{2}\left(u_j - u_{j+1}\right)^2\right). \tag{10.25}$$

We now perform a Fourier transform of the displacement operators:

$$u_q = \frac{1}{\sqrt{N}} \sum_j \exp(iqja) u_j, \tag{10.26}$$

$$u_j = \frac{1}{\sqrt{N}} \sum_q \exp(-iqja) u_q, \tag{10.27}$$

and similar for the p_j operators. We have here applied periodic Born-von Karman boundary conditions as in the classical case: $u_{N+1} \equiv u_1$, and used that the equilibrium positions are given by $r_j = ja$. Inserting this into (10.25), we reach

$$H = \sum_{jqq'} \exp\big(-i(q+q')ja\big) \times \left(\frac{p_q p_{q'}}{2MN} + \frac{K}{2N}\big(u_q u_{q'}[1-\exp(-iqa)][1-\exp(-iq'a)]\big)\right). \tag{10.28}$$

The sum over j depends only on the first exponential function. This is summed out to give $N\delta_{q,-q'}$. Next, the sum over q' is easily performed yielding

$$\begin{aligned} H &= \sum_q \left(\frac{p_q p_{-q}}{2M} + K\big(u_q u_{-q}[1-\cos(qa)]\big)\right) \\ &= \sum_q \left(\frac{p_q p_{-q}}{2M} + \frac{M}{2}\left(u_q u_{-q}\omega_q^2\right)\right), \end{aligned} \tag{10.29}$$

where we in the last step have used the expression for the classical vibration frequency, ω_q, from (10.8).

We now define the Fourier transformed creation and annihilation operators as

$$a_q^\dagger = \frac{1}{\sqrt{2\hbar\omega_q M}}\left(M\omega_q u_q + ip_q\right). \tag{10.30}$$

$$a_q = \frac{1}{\sqrt{2\hbar\omega_q M}}\left(M\omega_q u_q - ip_q\right). \tag{10.31}$$

It can be shown that these operators describe bosons, through

$$[a_q, a_q^\dagger] = 1. \tag{10.32}$$

The operators u_q and p_q are given by:

$$u_q = \sqrt{\frac{\hbar}{2\omega_q M}}\left(a_q^\dagger + a_q\right). \tag{10.33}$$

$$p_q = -i\sqrt{\frac{\hbar\omega_q M}{2}}\left(a_q^\dagger - a_q\right). \tag{10.34}$$

Inserting into the Hamiltonian (10.29), we reach the final solution

$$H = \sum_q \left(a_q^\dagger a_q + \frac{1}{2}\right)\hbar\omega_q. \tag{10.35}$$

This shows that the system is described by N independent oscillator modes (phonons), distinguished by their wave number q.

10.2.3 * Phonons in three dimensions

The problems has been treated in a number of textbooks, *e.g.* in Squires, Appendix G [2]. The solution is very similar to the one-dimensional case, except that the phonons now have both a (three-dimensional) $\mathbf{q}$ and a polarization vector, $\mathbf{e}_{q,p}$, which represents the direction of the vibration:

$$\mathbf{u}_j(t) = \sqrt{\frac{\hbar}{2MN}} \sum_{q,p} \frac{\mathbf{e}_{q,p}}{\sqrt{\omega_{q,p}}} \times \left[a_{q,p} \exp(i(\mathbf{q}\cdot\mathbf{r}_j - \omega_{q,p}t)) + a^\dagger_{q,p} \exp(-i(\mathbf{q}\cdot\mathbf{r}_j - \omega_{q,p}t)) \right], \quad (10.36)$$

where p is the polarization index, which runs over 3 times the number of atoms in the unit cell. The Hamiltonian for the phonon system reads

$$H = \sum_{q,p} \hbar\omega_{q,p} \left(a^\dagger_{q,p} a_{q,p} + \frac{1}{2} \right). \quad (10.37)$$

In general, there are two types of phonons:

- **Longitudinal.** The polarization vector $\mathbf{e}_{q,p}$ is parallel to $\mathbf{q}$.
- **Transverse.** The two polarization vectors $\mathbf{e}_{q,p}$ are perpendicular to $\mathbf{q}$. Usually, these modes have lower energies than the longitudinal ones.

For a non-Bravais lattice with m atoms per unit cell, there are only 3 acoustic modes. The remaining $3(m-1)$ are optical modes with a non-zero frequency (often a local maximum) at $q = 0$. A typical set of phonon dispersion curves for a two-atom unit cell (Ge) is presented in Fig. 10.6.

10.3 * The scattering cross section for phonons

We now aim to specialize the inelastic scattering cross section (9.8) to the case of phonons in a crystal. Along the way, we touch upon a proper derivation of the Debye-Waller factor (7.15).

10.3.1 * Inelastic cross section of atoms in a lattice

As a start, we make the assumption that the nuclei vibrate around their equilibrium position, eq. (10.1). Further, we use the translational symmetry of the crystal, so that (as for crystal diffraction) the sum over j and j' equals N times

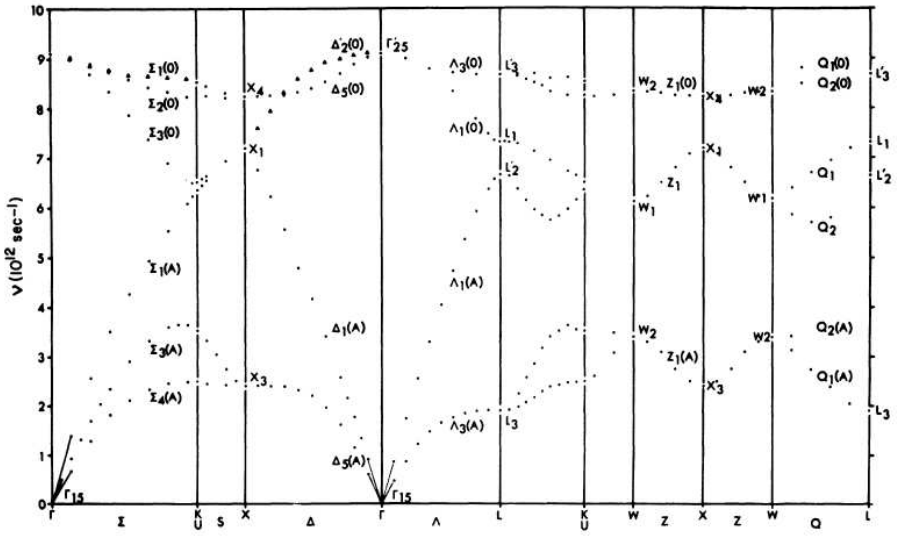

Figure 10.6: Phonon dispersions for crystalline Ge, measured by neutron scattering. The 6 branches are divided into 3 acoustic (reach zero af the Γ point) and 3 optical. The 3 acoustic branches are in turn divided into 1 (steep) longitudinal and 2 (shallow) transverse. The Γ point is the center of the Brillouin zone, while K, X, L, and W all lie on the zone boundary. Picture taken from from ref. [80].

the sum over j:

$$\begin{aligned}
&\sum_{j,j',i,i'} b_{j,i} b_{j',i'} \left\langle \exp(-i\mathbf{q}\cdot\mathbf{R}_{j,i}(0)) \exp(i\mathbf{q}\cdot\mathbf{R}_{j',i'}(t)) \right\rangle \qquad (10.38)\\
&\quad = N \sum_{i,i'} b_i b_{i'} \exp(i\mathbf{q}\cdot(\boldsymbol{\Delta}_{i'} - \boldsymbol{\Delta}_i)) \sum_{j'} \exp(i\mathbf{q}\cdot\mathbf{r}_{j'})\\
&\qquad \times \left\langle \exp(-i\mathbf{q}\cdot\mathbf{u}_{0,i}(0)) \exp(i\mathbf{q}\cdot\mathbf{u}_{j',i'}(t)) \right\rangle\\
&\quad = N|F_{\mathrm{N}}(\mathbf{q})|^2 \sum_{j',i,i'} \exp(i\mathbf{q}\cdot\mathbf{r}_{j'}) \left\langle \exp(-i\mathbf{q}\cdot\mathbf{u}_{0,i}(0)) \exp(i\mathbf{q}\cdot\mathbf{u}_{j',i'}(t)) \right\rangle.
\end{aligned}$$

The scattering cross section now becomes

$$\begin{aligned}
\frac{d^2\sigma}{d\Omega dE_{\mathrm{f}}} &= \frac{k_{\mathrm{f}}}{k_{\mathrm{i}}} \frac{N|F_{\mathrm{N}}(\mathbf{q})|^2}{2\pi\hbar} \sum_{j,i,i'} \exp(i\mathbf{q}\cdot\mathbf{r}_j) \qquad (10.39)\\
&\quad \times \int_{-\infty}^{\infty} \left\langle \exp(-i\mathbf{q}\cdot\mathbf{u}_{0,i}(0)) \exp(i\mathbf{q}\cdot\mathbf{u}_{j,i'}(t)) \right\rangle \exp(-i\omega t) dt.
\end{aligned}$$

For a Bravais lattice (one atom per unit cell), the sum over the i's disappear. Here, we can specialize the cross section to yield

$$\frac{d^2\sigma}{d\Omega dE_\mathrm{f}} = \frac{k_\mathrm{f}}{k_\mathrm{i}}\frac{Nb^2}{2\pi\hbar}\sum_j \exp(i\mathbf{q}\cdot\mathbf{r}_j) \tag{10.40}$$
$$\times \int_{-\infty}^{\infty} \left\langle \exp(-i\mathbf{q}\cdot\mathbf{u}_0(0))\exp(i\mathbf{q}\cdot\mathbf{u}_j(t))\right\rangle \exp(-i\omega t)dt.$$

10.3.2 * Details of phonon operators

The difficult portion of the phonon cross section (10.40) is now the operator exponential functions, which are of the type $\langle\exp(U)\exp(V)\rangle$. To study this, we follow Squires, ch. 3.4 [2]. Here, he proves a theorem stating that if $[U,V]$ is a c-number (in contract to being another operator), then

$$\langle\exp(U)\exp(V)\rangle = \langle\exp(U+V)\rangle\exp\left(\frac{1}{2}[U,V]\right). \tag{10.41}$$

Let us take a closer look at U and V. Both can be put in the form:

$$U = -i\mathbf{q}\cdot\mathbf{u}_0(0) = -i\sum_{q,p}(g_{q,p}a_{q,p} + g^*_{q,p}a^\dagger_{q,p}), \tag{10.42}$$

$$V = i\mathbf{q}\cdot\mathbf{u}_j(t) = i\sum_{q,p}(h_{q,p}a_{q,p} + h^*_{q,p}a^\dagger_{q,p}), \tag{10.43}$$

where the coefficients are given by

$$g_{q,p} = \sqrt{\frac{\hbar}{2MN}}\frac{\mathbf{q}\cdot\mathbf{e}_{q,p}}{\sqrt{\omega_{q,p}}}. \tag{10.44}$$

$$h_{q,p} = \sqrt{\frac{\hbar}{2MN}}\frac{\mathbf{q}\cdot\mathbf{e}_{q,p}}{\sqrt{\omega_{q,p}}}\exp(i\mathbf{q}\cdot\mathbf{r}_j)\exp(-i\omega_{q,p}t). \tag{10.45}$$

Now, we need to calculate $[U,V]$, which becomes a quadruple sum. To ease our task, we note that $[a_{q,p}, a^\dagger_{q',p'}]$ is nonzero only if $q=q'$ and $p=p'$. We can now show that $[U,V]$ is a c-number and calculate its value:

$$\begin{aligned}[U,V] &= \sum_{q,p,q',p'}[g_{q,p}a_{q,p} + g_{q,p}a^\dagger_{q,p}, h_{q',p'}a_{q',p'} + h^*_{q',p'}a^\dagger_{q',p'}] \\ &= \sum_{q,p} g_{q,p}h^*_{q,p}[a_{q,p}, a^\dagger_{q,p}] + g_{q,p}h_{q,p}[a^\dagger_{q,p}, a_{q,p}] \\ &= \sum_{q,p}(g_{q,p}h^*_{q,p} - g_{q,p}h_{q,p}).\end{aligned} \tag{10.46}$$

Squires proves that for any harmonic oscillator operator (*e.g.* U or V):

$$\langle\exp(U)\rangle = \exp\left(\frac{1}{2}\langle U^2\rangle\right). \tag{10.47}$$

We now use this theorem to show

$$\langle \exp(U+V)\rangle \exp(\frac{1}{2}[U,V]) = \exp\left(\frac{1}{2}\left\langle U^2+V^2+UV+VU+UV-VU\right\rangle\right)$$
$$= \exp(\langle U^2\rangle)\exp(\langle UV\rangle). \tag{10.48}$$

In the last step, we have used that $\langle U^2\rangle = \langle V^2\rangle$. This can be argued by noting that the only differences between these harmonic operators are the time and place of the atomic displacements. Since the system is translation- and time invariant, the two expectations values must be identical.

10.3.3 * The phonon expansion

We first summarize the expression for the (Bravais lattice) phonon cross section so far:

$$\frac{d^2\sigma}{d\Omega dE_\mathrm{f}} = \frac{k_\mathrm{f}}{k_\mathrm{i}}\frac{Nb^2}{2\pi\hbar}\exp(\langle U^2\rangle) \tag{10.49}$$
$$\times \sum_j \exp(i\mathbf{q}\cdot\mathbf{r}_j)\int_{-\infty}^{\infty}\exp(\langle UV\rangle)\exp(-i\omega t)dt.$$

The most significant part of this expression is the operator $\exp(\langle UV\rangle)$, which can create or annihilate a number of phonons. We proceed by a series expansion of the exponential:

$$\exp(\langle UV\rangle) \approx 1 + \langle UV\rangle + \frac{1}{2}\langle (UV)^2\rangle + \cdots \tag{10.50}$$

The zero'th order term we have dealt with before. Here, the time integral results in $2\pi\hbar\delta(\hbar\omega)$, *i.e.* elastic scattering. The cross section resulting from this term essentially equals (7.16), which for crystalline materials leads to the Bragg law, modified by the Debye-Waller factor. We will elaborate on the Debye-Waller factor in section 10.3.4.

The term UV in (10.50) corresponds to creation or annihilation of one single phonon. This will be discussed in section 10.3.6. Likewise, the term $(UV)^2$ describes processes involving two phonons, and so on. We will here discuss only one-phonon processes. The complications of multi-phonon processes are to some extent discussed in Squires [2].

10.3.4 * The Debye-Waller factor

We now look closer at the term $\langle U^2 \rangle$. Using the definition of U, we can write

$$\begin{aligned}
\langle U^2 \rangle &= -\sum_i p_i \left\langle \lambda_i \left| U^2 \right| \lambda_i \right\rangle \\
&= -\sum_i p_i \left\langle \lambda_i \left| \sum_{q,p,q',p'} g_{q,p} g_{q',p'} (a_{q,p} + a^\dagger_{q,p})(a_{q',p'} + a^\dagger_{q',p'}) \right| \lambda_i \right\rangle \\
&= -\sum_{q,p} g^2_{q,p} \sum_i p_i \left\langle \lambda_i \left| a_{q,p} a^\dagger_{q,p} + a^\dagger_{q,p} a_{q,p} \right| \lambda_i \right\rangle \\
&= -\sum_{q,p} g^2_{q,p} \left(2n_{\mathrm{B}} \left(\frac{\hbar \omega_{q,p}}{k_{\mathrm{B}} T} \right) + 1 \right) \\
&= -\frac{\hbar}{2MN} \sum_{q,p} \frac{(\mathbf{q} \cdot \mathbf{e}_{q,p})^2}{\omega_{q,p}} \left(2n_{\mathrm{B}} \left(\frac{\hbar \omega_{q,p}}{k_{\mathrm{B}} T} \right) + 1 \right),
\end{aligned} \tag{10.51}$$

where the expectation value $\left\langle a^\dagger_{q,p} a_{q,p} \right\rangle$ has been replaced by n_{B}, the Bose occupation number, eq. 10.17. In the derivation, we have also used that the expectation value is non-zero only when the number of a and $a^\dagger$ operators is the same for each (q,p). For example, the expression $a^\dagger_{q,p} a^\dagger_{q',p'} |\lambda\rangle$ gives you the state $|\lambda\rangle$ with two additional phonons, whence $\langle \lambda | a^\dagger_{q,p} a^\dagger_{q',p'} | \lambda \rangle = 0$.

It is customary to define $2W = -\langle U^2 \rangle$ and then define the *Debye-Waller* factor

$$\boxed{\exp(-2W) \equiv \exp(\langle U^2 \rangle)}. \tag{10.52}$$

This is used to describe the reduction in diffraction intensity due to lattice vibrations, as was anticipated in chapter 7. For a cubic crystal it can be shown [2][(3.63)] that

$$2W = \frac{1}{3} q^2 \langle u^2 \rangle, \tag{10.53}$$

where u is the mean atomic displacement from equilibrium. Using this as representative for all crystals, we can see that $2W$ is non-zero at zero temperature (due to zero-point motion) and increases with temperature. As a consequence, the resulting Debye-Waller factor is slightly below unity at low temperatures, decreasing at higher temperatures.

Since $2W$ is proportional to q^2, the Debye-Waller factor can be approximated by unity in small-angle scattering; as we did implicitly in chapter 5.

10.3.5 * Calculating $\langle UV \rangle$

Using (10.49) as a starting point, we continue to develop the operator values.

$$\begin{aligned}
\langle UV \rangle &= \sum_i p_i \langle \lambda_i | UV | \lambda_i \rangle \\
&= \sum_i p_i \left\langle \lambda_i \middle| \sum_{q,p} \left(g_{q,p} a_{q,p} + g_{q,p} a^\dagger_{q,p} \right) \left(h_{q,p} a_{q,p} + h^*_{q,p} a^\dagger_{q,p} \right) \middle| \lambda_i \right\rangle \\
&= \sum_{q,p} \sum_i p_i \left\langle \lambda_i \middle| \left(g_{q,p} a_{q,p} h^*_{q,p} a^\dagger_{q,p} + g_{q,p} a^\dagger_{q,p} h_{q,p} a_{q,p} \right) \middle| \lambda_i \right\rangle \\
&= \sum_{q,p} g_{q,p} h^*_{q,p} (n_{q,p} + 1) + g_{q,p} h_{q,p} n_{q,p}, \qquad (10.54)
\end{aligned}$$

where we have used that the expectation values for a pair of creation-annihilation operators is non-zero only if they have the same quantum numbers. Using the expression for the g's and h's, we reach

$$\begin{aligned}
\langle UV \rangle = \frac{\hbar}{2MN} \sum_{q,p} \frac{(\mathbf{q} \cdot \mathbf{e}_{q,p})^2}{\omega_{q,p}} \qquad (10.55) \\
\times \left(\exp(-i\mathbf{q} \cdot \mathbf{r}_j + i\omega_{q,p} t)(n_{q,p} + 1) + \exp(i\mathbf{q} \cdot \mathbf{r}_j - i\omega_{q,p} t) n_{q,p} \right).
\end{aligned}$$

We now insert this into (10.49). To avoid confusion of labels, we use $\mathbf{q}'$ for the phonon wave vector.

$$\begin{aligned}
\frac{d^2\sigma}{d\Omega dE_\mathrm{f}} = \frac{k_\mathrm{f}}{k_\mathrm{i}} \frac{b^2}{4\pi M} \exp(-2W) \sum_{q',p} \frac{(\mathbf{q}' \cdot \mathbf{e}_{q',p})^2}{\omega_{q',p}} \sum_j \exp(i\mathbf{q} \cdot \mathbf{r}_j) \qquad (10.56) \\
\times \int_{-\infty}^{\infty} \left(\exp(-i\mathbf{q}' \cdot \mathbf{r}_j + i\omega_{q',p} t)(n_{q',p} + 1) \right. \\
\left. + \exp(i\mathbf{q}' \cdot \mathbf{r}_j - i\omega_{q',p} t) n_{q',p} \right) \exp(-i\omega t) dt.
\end{aligned}$$

The Fourier transformations in time and space are immediately calculated, giving the final one-phonon cross section:

$$\begin{aligned}
\frac{d^2\sigma}{d\Omega dE_\mathrm{f}} = \frac{k_\mathrm{f}}{k_\mathrm{i}} \frac{b^2 (2\pi)^3}{2MV_0} \exp(-2W) \sum_{q,p,\tau} \frac{(\mathbf{q} \cdot \mathbf{e}_{q,p})^2}{\omega_{q,p}} \qquad (10.57) \\
\times \left[(n_{q,p} + 1) \delta(\omega - \omega_{q,p}) \delta(\mathbf{q} - \mathbf{q}' + \boldsymbol{\tau}) \right. \\
\left. + n_{q,p} \delta(\omega + \omega_{q,p}) \delta(\mathbf{q} + \mathbf{q}' + \boldsymbol{\tau}) \right].
\end{aligned}$$

10.3.6 * Understanding the one-phonon cross section

We now like to discuss the interpretation of the phonon cross section (10.57), starting with the last two lines. In the first term in the square brackets, the neutron looses energy, while the lattice gains the same amount, $\hbar\omega_{q,p}$. Hence, this corresponds to the creation of one phonon. Likewise, in the second term

the neutron gains energy, while the lattice loses, representing annihilation of one phonon. The population factors, $n_{q,p}$ and $n_{q,p}+1$ give the physically meaningful result that at zero temperature ($n_{q,p} = 0$), phonon annihilation has zero cross section (no phonons are present), while phonon creation is still allowed.

The term $(\mathbf{q}\cdot\mathbf{e}_{q,p})^2$ in (10.57) implies that the neutron only senses vibrations *parallel* to the total scattering vector. This intuitively makes sense, since a displacement of the nucleus perpendicular to $\mathbf{q}$ would not change the phase of the scattering.

Experimental considerations. The dependence of the scattering cross section on $(\mathbf{q}\cdot\mathbf{e}_{q,p})^2$ has strong implications on the experimental strategy. If, *e.g.*, in a cubic system you like to study longitudinal phonons, you first like to find the highest reasonable value of q, *e.g.* (0 0 4). Next, you like to investigate the scattering along $(0\,0\,4+l)$ to pick up the longitudinal vibrations. In contrast, for transverse phonons, you should look along another direction, *e.g.* $(h\,0\,4)$.

If one wants to study all vibration directions in a crystal of low symmetry, it may be necessary to investigate the phonon spectrum in different Brillouin zones to change the angle between the scattering vector, $\mathbf{q}$, and the phonon wave vector, $\mathbf{q}'$.

10.4 Problems

10.4.1 Classical lattice vibrations in one dimension

This problem is a simple illustration of classical lattice vibrations, as calculated in section 10.1. The problem owes much to Squires 3.1 [2].

We imagine a one-dimensional chain of atoms of lattice constant d, connected by springs with force constant K. We assume all atoms are equal, *i.e.* they have identical mass, M. The displacement of the atoms from equilibrium is denoted by $u_j(t)$ and can move only along the chain direction (longitudinal vibrations). This system is illustrated in Fig. 10.1.

1. Prove that
$$M\ddot{u}_j(t) = K\big(u_{j-1}(t) + u_{j+1}(t) - 2u_j(t)\big) \tag{10.58}$$
is the correct equation of motion for atom j.

2. We assume a vibrational motion of the plane wave type:
$$u_j(t) = A_q \exp\big(i(djq - \omega_q t)\big), \tag{10.59}$$
where A_q is an arbitrary amplitude. Prove that this trial function is a solution of the equation of motion with a vibration frequency of
$$\omega_q^2 = \frac{4K}{M}\sin^2(qd/2). \tag{10.60}$$

3. Argue that the potential energy can be written as

$$V = \frac{K}{2} \sum_j \left(\Re[u_{j+1}(t)] - \Re[u_j(t)] \right)^2. \tag{10.61}$$

4. Prove that the time average of the potential energy and the kinetic energy,

$$T = \frac{M}{2} \sum_j \Re[\dot{u}_j(t)]^2 \tag{10.62}$$

   are equal for any q.

10.4.2 Classical vibrations with a two-atom unit cell

We here consider the one-dimensional chain with two atoms per unit cell, of masses m and M, with one spring constant, K, and with distances between atoms of $d/2$. This system is illustrated in Figure 10.4, and the basic definition are given in (10.13).

1. Write down the equations of motion for each of the two atoms.
2. Write down the trial solutions for the two atoms of the type (10.5). Remember that there may be a phase shift, $\phi(q)$ between the two types of atoms.
3. Show that there are only two allowed values of $\phi(q)$, which differ by π.
4. Show that the vibration frequencies can be written by (10.14).

Part V

Magnetic materials

Chapter 11

Magnetic neutron scattering

Due to its magnetic dipole moment, the neutron can be affected by a variation of the local magnetic field inside materials. This magnetic field often originates from atomic magnetic moments. In this chapter, we treat the basic interaction and magnetic scattering theory. Main topics in elastic magnetic scattering is explained in chapter 12, while chapter 13 is devoted to magnetic excitations and inelastic magnetic scattering. Magnetic scattering can also be performed with spin-polarised neutrons, where additional information on magnetic properties can be obtained. This, however, falls outside the scope of these notes.

To simplify the presentation, we initially consider only magnetic fields arising from the spins of electrons in unpaired atomic orbitals. Later, we will describe the results from other types of magnetic fields, *e.g.* from orbital magnetic moments. A more complete treatment of magnetic neutron scattering theory is given in a number of textbooks, *e.g.* by Marshall and Lovesey[1].

11.1 Magnetic ions

We first describe briefly the origin of magnetic moment in materials before continuing to the scattering theory. Our presentation largely follows the textbook by S. Blundell [81].

11.1.1 Magnetic moments of electrons

The magnetic moment of atoms and ions stems from the angular moment of the electrons. The orbital angular moment, $\mathbf{l}$, generates a circular current, like a tiny coil. This produces a magnetic dipole moment of

$$\boldsymbol{\mu}_l = \mu_{\mathrm{B}}\mathbf{l}, \tag{11.1}$$

where the Bohr magneton is

$$\mu_{\mathrm{B}} = \frac{\hbar e}{2m_{\mathrm{e}}} = 9.274 \cdot 10^{-24}\mathrm{J/T} = 5.788 \cdot 10^{-5}\,\mathrm{eV/T}. \tag{11.2}$$

For similar reasons (enhanced by relativistic effects) the spin of the electron causes a magnetic dipole moment of

$$\boxed{\boldsymbol{\mu}_s = g\mu_{\mathrm{B}}\mathbf{s}}, \tag{11.3}$$

where $g = 2.0023$ is the gyromagnetic ratio of the electron and $\mathbf{s}$ is the electron spin.

We have above taken $\mathbf{l}$ and $\mathbf{s}$ to be unitless (*i.e.* the orbital angular moment is actually $\hbar\mathbf{l}$). We will remain with this definition in all of these notes.

11.1.2 Hund's rules

We now turn to the determination of the total angular moment of a free atom or ion. In general, we use the z-axis as the quantization axis of angular momenta.

General quantum mechanics gives us the addition rule of angular momenta

$$\mathbf{L} = \sum_i \mathbf{l}_i, \qquad \mathbf{S} = \sum_i \mathbf{s}_i, \qquad \mathbf{J} = \mathbf{L} + \mathbf{S}, \tag{11.4}$$

where $\mathbf{J}$ is the total angular momentum. The quantum numbers, L, S, and J take integer or half-integer values. J will assume a value between $S + L$ and $|S - L|$. In general, due to the coupling between the magnetic field from the orbital motion and the spin magnetic moment (the *spin-orbit coupling*), J is the only constant of motion.

We immediately note that closed shells represent $L = S = J = 0$, since all positive and negative values of l_i^z and s_i^z are represented. Hence, we only need to consider partially filled shells.

Due to electrostatic repulsion between atoms, combined with quantum mechanics (the Pauli principle and the spin-orbit coupling), it is energetically favourable for the electrons to occupy the partially filled shells in a particular way. This is described by *Hund's rules* (in order of highest priority):

1. Maximize S.
2. Maximize L.
3. For less-than-half-filled shells: Minimize J.
   For more-than-half-filled shells: Maximize J.

These rules are, however, only general rules of thumb that may be overruled by other effects, as discussed below.

11.1.3 Quenching

In materials, the ions cannot be considered free. In stead, they interact with their neighbouring ions through electrostatic forces. This implies a breaking of the rotational symmetry of the atomic orbitals. In many cases, $\mathbf{L}$ is then no longer a good quantum number, and the average contribution to the magnetic moment from $\mathbf{L}$ vanishes, whence $\mathbf{J} = \mathbf{S}$. This effect is denoted *quenching*.

Quenching is seen for ions of most of the 3d-metals, *i.e.* the metals with a partially filled 3d shell (transition metals), which are some of the most prominent magnetic ions in solids. The other prominent group, the 4f-metals (the rare-earth elements), are less often prone to quenching due to the relatively smaller spatial extend of the 4f orbitals.

In much of the text to follow, we assume a complete quenching of the magnetic ions, so that the only magnetic degree of freedom is the spin quantum number, **S**.

11.2 Scattering of neutrons from magnetic ions

We now develop the formalism for magnetic neutron scattering. This is performed in a general way that gives us an expression for the elastic and inelastic scattering simultaneously.

11.2.1 * The magnetic interaction

The interaction responsible for magnetic neutron scattering is the nuclear Zeeman term for a neutron in an external magnetic field:

$$H_{\mathrm{Z}} = -\boldsymbol{\mu} \cdot \mathbf{B} = -\gamma \mu_{\mathrm{N}} \hat{\boldsymbol{\sigma}} \cdot \mathbf{B}, \tag{11.5}$$

where $\hat{\boldsymbol{\sigma}}$ represents the three Pauli matrices for the neutron. The external field that scatters the neutron comes from the individial electrons that combine to ionic moments as described above.

The magnetic moment of an electronic spin, $\mathbf{s}_j$, is given by

$$\boldsymbol{\mu}_{\mathrm{e}} = -g\mu_{\mathrm{B}} \mathbf{s}_j. \tag{11.6}$$

Furthermore, the field from a dipole placed at the origin can be described as

$$B = \frac{\mu_0}{(4\pi)} \nabla \times (\boldsymbol{\mu} \times \mathbf{r}/r^3). \tag{11.7}$$

We now position the spin at position $\mathbf{r}_j$, and transform eq. (11.5) into

$$H_{\mathrm{Z},j} = \frac{\mu_0}{4\pi} g\mu_{\mathrm{B}} \gamma \mu_{\mathrm{N}} \hat{\boldsymbol{\sigma}} \cdot \nabla \times \left(\frac{\mathbf{s}_j \times (\mathbf{r} - \mathbf{r}_j)}{|\mathbf{r} - \mathbf{r}_j|^3} \right). \tag{11.8}$$

The neutron interaction with the magnetic ions is given as the total nuclear Zeeman interaction, summed over all magnetic sites, j. This we use as the scattering potential, $\hat{V}$, in the master equation for neutron scattering (2.49). We note that we do not measure the final state of the sample. Furthermore, we assume that the sample is initially in thermal equilibrium. Therefore, we perform a thermal average over the initial states of the sample, $|\lambda_{\mathrm{i}}\rangle$, and sum over those final states, $|\lambda_{\mathrm{f}}\rangle$, which are consistent with the observed momentum transfer, $\mathbf{q}$ and energy transfer, $\hbar\omega$. This treatment is similar to the derivation of the inelastic nuclear cross section, chap. 10.

By substitution, the resulting equation for the scattering cross section becomes

$$\left.\frac{d^2\sigma}{d\Omega dE_{\rm f}}\right|_{\sigma_{\rm i}\to\sigma_{\rm f}} = \frac{k_{\rm i}}{k_{\rm f}}\left(\frac{\mu_0}{4\pi}\right)^2\left(\frac{m_{\rm N}}{2\pi\hbar^2}\right)^2(g\mu_{\rm B}\gamma\mu_{\rm N})^2\sum_{\lambda_{\rm i},\lambda_{\rm f}}p_{\lambda_{\rm i}} \times\left|\left\langle \mathbf{k}_{\rm f}\lambda_{\rm f}\sigma_{\rm f}\right|\sum_j \hat{\boldsymbol{\sigma}}\cdot\nabla\times\left(\frac{\mathbf{s}_j\times(\mathbf{r}-\mathbf{r}_j)}{|\mathbf{r}-\mathbf{r}_j|^3}\right)\left|\mathbf{k}_{\rm i}\lambda_{\rm i}\sigma_{\rm i}\right\rangle\right|^2 \times\delta\left(\hbar\omega+E_{\lambda_{\rm i}}-E_{\lambda_{\rm f}}\right). \tag{11.9}$$

11.2.2 * The magnetic matrix element

We now turn to the calculation of the complicated matrix element in (11.9). We utilize a mathematical identity [2],

$$\nabla\times\left(\frac{\mathbf{s}\times\mathbf{r}}{r^3}\right)=\frac{1}{2\pi^2}\int\hat{\mathbf{q}}'\times(\mathbf{s}\times\hat{\mathbf{q}}')\exp(i\mathbf{q}'\cdot\mathbf{r})d^3\mathbf{q}' \tag{11.10}$$

to reach

$$\begin{aligned}
&\left\langle \mathbf{k}_{\rm f}\lambda_{\rm f}\sigma_{\rm f}\right|\sum_j\hat{\boldsymbol{\sigma}}\cdot\nabla\times\left(\frac{\mathbf{s}_j\times(\mathbf{r}-\mathbf{r}_j)}{|\mathbf{r}-\mathbf{r}_j|^3}\right)\left|\mathbf{k}_{\rm i}\lambda_{\rm i}\sigma_{\rm i}\right\rangle\\
&=\frac{1}{2\pi^2}\left\langle \mathbf{k}_{\rm f}\lambda_{\rm f}\sigma_{\rm f}\right|\sum_j\int d^3\mathbf{q}'\hat{\boldsymbol{\sigma}}\cdot(\hat{\mathbf{q}}'\times(\mathbf{s}_j\times\hat{\mathbf{q}}'))\exp(i\mathbf{q}'\cdot(\mathbf{r}-\mathbf{r}_j))\left|\mathbf{k}_{\rm i}\lambda_{\rm i}\sigma_{\rm i}\right\rangle\\
&=\frac{1}{2\pi^2}\left\langle \lambda_{\rm f}\sigma_{\rm f}\right|\sum_j\int d^3\mathbf{r}d^3\mathbf{q}'\exp(i\mathbf{q}\cdot\mathbf{r})\\
&\quad\times\exp(i\mathbf{q}'\cdot(\mathbf{r}-\mathbf{r}_j))\hat{\boldsymbol{\sigma}}\cdot(\hat{\mathbf{q}}'\times(\mathbf{s}_j\times\hat{\mathbf{q}}'))\left|\lambda_{\rm i}\sigma_{\rm i}\right\rangle\\
&=4\pi\left\langle \lambda_{\rm f}\sigma_{\rm f}\right|\sum_j\exp(i\mathbf{q}\cdot\mathbf{r}_j)\hat{\boldsymbol{\sigma}}\cdot(\hat{\mathbf{q}}\times(\mathbf{s}_j\times\hat{\mathbf{q}}))\left|\lambda_{\rm i}\sigma_{\rm i}\right\rangle.
\end{aligned}\tag{11.11}$$

In the last step we used that $\int\exp(i(\mathbf{q}+\mathbf{q}')\cdot\mathbf{r})d^3\mathbf{r}=(2\pi)^3\delta(\mathbf{q}+\mathbf{q}')$. The equation contains a term

$$\hat{\mathbf{q}}\times(\mathbf{s}_j\times\hat{\mathbf{q}})\equiv\mathbf{s}_{j,\perp}, \tag{11.12}$$

which is simply the component of the spin on site j perpendicular to the scattering vector. (11.11) therefore shows that the spin component parallel to $\mathbf{q}$ is invisible to neutrons. This is a completely general result and is essential to all magnetic neutron scattering.

11.2.3 * Matrix element for unpolarized neutrons

For the remainder of this chapter, we assume that the neutrons are unpolarized, $p_\uparrow=p_\downarrow=1/2$. We also assume that we do not observe the final spin state,

σ_f, of the neutron. To obtain the cross section for unpolarised neutrons, we therefore sum over σ_f and average over the initial spin state, σ_i.

We start with the spin part of the matrix element (11.9), transformed using (11.11) to reach

$$\sum_{\sigma_\mathrm{i},\sigma_\mathrm{f}} p_{\sigma_\mathrm{i}} \left|\langle \sigma_\mathrm{f}\lambda_\mathrm{f}\left|\hat{\boldsymbol{\sigma}}\cdot\mathbf{s}_\perp\right|\sigma_\mathrm{i}\lambda_\mathrm{i}\rangle\right|^2 . \tag{11.13}$$

Now, the dot product will contain terms of the type $\sigma^x s^x_\perp$, where the first factor depends only on the neutron spin coordinate, σ, and the second only on the sample coordinate, λ. We assume that the initial neutron state is not correlated with the initial state of the sample. Hence, we can factorize the two inner products:

$$\begin{aligned}
&\sum_{\sigma_\mathrm{i},\sigma_\mathrm{f}} p_{\sigma_\mathrm{i}} \left|\langle \sigma_\mathrm{f}\lambda_\mathrm{f}\left|\hat{\boldsymbol{\sigma}}\cdot\mathbf{s}_\perp\right|\sigma_\mathrm{i}\lambda_\mathrm{i}\rangle\right|^2 \qquad (11.14)\\
&= \sum_{\sigma_\mathrm{i},\sigma_\mathrm{f}} p_{\sigma_\mathrm{i}} \left|\sum_\alpha \langle\sigma_\mathrm{f}\left|\sigma^\alpha\right|\sigma_\mathrm{i}\rangle\,\langle\lambda_\mathrm{f}\left|\mathbf{s}^\alpha_\perp\right|\lambda_\mathrm{i}\rangle\right|^2\\
&= \sum_{\alpha,\beta,\sigma_\mathrm{i},\sigma_\mathrm{f}} p_{\sigma_\mathrm{i}} \langle\sigma_\mathrm{i}|\sigma^\beta|\sigma_\mathrm{f}\rangle\langle\sigma_\mathrm{f}|\sigma^\alpha|\sigma_\mathrm{i}\rangle\langle\lambda_\mathrm{i}|\mathbf{s}^\beta_\perp|\lambda_\mathrm{f}\rangle\langle\lambda_\mathrm{f}|\mathbf{s}^\alpha_\perp|\lambda_\mathrm{i}\rangle\\
&= \sum_{\alpha,\beta,\sigma_\mathrm{i}} p_{\sigma_\mathrm{i}} \langle\sigma_\mathrm{i}|\sigma^\beta\sigma^\alpha|\sigma_\mathrm{i}\rangle\langle\lambda_\mathrm{i}|\mathbf{s}^\beta_\perp|\lambda_\mathrm{f}\rangle\langle\lambda_\mathrm{f}|\mathbf{s}^\alpha_\perp|\lambda_\mathrm{i}\rangle,
\end{aligned}$$

where we in the last step have used the *completeness relation* $\sum_{\sigma_\mathrm{f}} |\sigma_\mathrm{f}\rangle\langle\sigma_\mathrm{f}| = 1$. For unpolarized neutrons, $\alpha = \beta$ leads to

$$\sum_{\sigma_\mathrm{i}} p_{\sigma_\mathrm{i}} \langle\sigma_\mathrm{i}|\sigma^\alpha\sigma^\beta|\sigma_\mathrm{i}\rangle = 1. \tag{11.15}$$

Likewise, if $\alpha \neq \beta$, we have that $\sum_{\sigma_\mathrm{i}} p_{\sigma_\mathrm{i}} \langle\sigma_\mathrm{i}|\sigma^\alpha\sigma^\beta|\sigma_\mathrm{i}\rangle = 0$. Using this to perform the sum over σ_i, we obtain

$$\sum_{\sigma_\mathrm{i},\sigma_\mathrm{f}} p_{\sigma_\mathrm{i}} \left|\langle \sigma_\mathrm{f}\lambda_\mathrm{f}\left|\boldsymbol{\sigma}\cdot\mathbf{s}_\perp\right|\sigma_\mathrm{i}\lambda_\mathrm{i}\rangle\right|^2 = \sum_\alpha \langle\lambda_\mathrm{i}|s^\alpha_\perp|\lambda_\mathrm{f}\rangle\,\langle\lambda_\mathrm{f}|s^\alpha_\perp|\lambda_\mathrm{i}\rangle . \tag{11.16}$$

When summed over the final states, $|\lambda_\mathrm{f}\rangle$, we obtain

$$\sum_{\sigma_\mathrm{i},\sigma_\mathrm{f},\lambda_\mathrm{f}} p_{\sigma_\mathrm{i}} \left|\langle \sigma_\mathrm{f}\lambda_\mathrm{f}\left|\boldsymbol{\sigma}\cdot\mathbf{s}_\perp\right|\sigma_\mathrm{i}\lambda_\mathrm{i}\rangle\right|^2 = \langle\lambda_\mathrm{i}\left|\mathbf{s}_\perp\cdot\mathbf{s}_\perp\right|\lambda_\mathrm{i}\rangle . \tag{11.17}$$

When this expression is used in the calculation for the cross section, we will encounter terms of the general type $\mathbf{s}_{j\perp}\cdot\mathbf{s}_{j'\perp}$. We here utilize that the perpendicular projection is defined as $\mathbf{s}_{j\perp} \equiv \mathbf{s}_j - (\mathbf{s}_j\cdot\hat{\mathbf{q}})\hat{\mathbf{q}}$, where $\hat{\mathbf{q}}$ is a unit vector in the direction of $\mathbf{q}$, to reach

$$\mathbf{s}_{j\perp}\cdot\mathbf{s}_{j'\perp} = \mathbf{s}_j\cdot\mathbf{s}_{j'} - (\mathbf{s}_j\cdot\hat{\mathbf{q}})(\mathbf{s}_{j'}\cdot\hat{\mathbf{q}}) = \sum_{\alpha\beta}\left(\delta_{\alpha\beta} - \hat{q}_\alpha\hat{q}_\beta\right) s^\alpha_j s^\beta_{j'}, \tag{11.18}$$

where the indices α and β run over the Cartesian coordinates (x, y, and z).

11.2.4 * The master equation for magnetic scattering

We now collect the prefactors from the calculations above, assuming that the proton and neutron masses are identical:

$$\frac{m_{\mathrm{N}}}{2\pi\hbar^2} g\mu_{\mathrm{B}}\gamma\mu_{\mathrm{N}}\mu_0 = \gamma\frac{\mu_0}{4\pi}\frac{e^2}{m_{\mathrm{e}}} = \gamma r_0, \tag{11.19}$$

where r_0 is the classical electron radius $r_0 = e^2\mu_0/(4\pi m_{\mathrm{e}}) = 2.818$ fm, as defined in Appendix A.2.1.

Collecting all equations from above, we end up with *the master equation* for the partial differential magnetic scattering cross section for unpolarized neutrons [1]:

$$\begin{aligned}\frac{d^2\sigma}{d\Omega dE_{\mathrm{f}}} &= (\gamma r_0)^2 \frac{k_{\mathrm{f}}}{k_{\mathrm{i}}} \sum_{\alpha\beta} (\delta_{\alpha\beta} - \hat{q}_\alpha \hat{q}_\beta) \\ &\times \sum_{\lambda_{\mathrm{i}}\lambda_{\mathrm{f}}} p_{\lambda_{\mathrm{i}}} \langle\lambda_{\mathrm{i}}|Q_\alpha|\lambda_{\mathrm{f}}\rangle \langle\lambda_{\mathrm{f}}|Q_\beta|\lambda_{\mathrm{i}}\rangle \, \delta\left(\hbar\omega + E_{\lambda_{\mathrm{i}}} - E_{\lambda_{\mathrm{f}}}\right),\end{aligned} \tag{11.20}$$

where we have defined $\mathbf{Q}$ as the Fourier transform of the spins $\mathbf{s}_j$ positioned at $\mathbf{r}_j$, with respect to the scattering vector, $\mathbf{q}$ [1]:

$$\mathbf{Q} = \sum_j \exp(i\mathbf{q}\cdot\mathbf{r}_j)\mathbf{s}_j. \tag{11.21}$$

11.2.5 The magnetic form factor

We assume the electrons causing the magnetism to be located in orbitals around particular ions as discussed in section 11.1. The electron coordinates are therefore replaced by the nuclear positions, $\mathbf{r}_j$, plus a small deviation from this, $\mathbf{r}$, representing the extension of the particular electron orbital. We thus make the substitution

$$\mathbf{Q} = \sum_j \int \exp(i\mathbf{q}\cdot(\mathbf{r}_j + \mathbf{r}))\mathbf{s}_j d^3\mathbf{r} = \sum_j \exp(i\mathbf{q}\cdot\mathbf{r}_j)\mathbf{S}_j F(\mathbf{q}). \tag{11.22}$$

Here, the *magnetic form factor* is given by

$$\boxed{F(\mathbf{q}) = \int \exp(i\mathbf{q}\cdot\mathbf{r}) s(\mathbf{r}) d^3\mathbf{r}}, \tag{11.23}$$

where $s(\mathbf{r})$ is the normalised spin density. For small values of q, the magnetic form factor is close to unity, $F(0) = 1$, and it falls off smoothly to zero for large scattering vectors.

In the following, we assume that the magnetic form factor is identical for all magnetic ions in the material under investigation, even though this may be too simple an approach, in particular for materials containing more than one magnetic element.

11.2.6 Orbital contributions

When taking contributions from orbital magnetism into account, *e.g.* from rare-earth ions, the term $g\mathbf{s}$ is replaced by $g_{\mathrm{L}}\mathbf{J}$, where g_{L} is the Landé factor:

$$g_{\mathrm{L}} = 1 + \frac{J(J+1) + S(S+1) - L(L+1)}{2J(J+1)}, \tag{11.24}$$

which is a number between 1 and 2, and $\mathbf{J}$ is the total angular momentum However, in the expressions to follow we keep the notation $\mathbf{s}$ for simplicity.

The derivation of the contribution from orbital moment is lengthy and adds nothing to the general understanding of magnetic neutron scattering, so we simply omit it here. Details of this derivation are found in Ref. [1].

11.2.7 The final magnetic cross section

Performing all replacements above, the final cross section for magnetic neutron scattering reads

$$\begin{aligned}\frac{d^2\sigma}{d\Omega dE_{\mathrm{f}}} = (\gamma r_0)^2 \frac{k_{\mathrm{f}}}{k_{\mathrm{i}}} \left[\frac{g}{2}F(q)\right]^2 \sum_{\alpha\beta} (\delta_{\alpha\beta} - \hat{q}_\alpha \hat{q}_\beta) \\ \times \sum_{\lambda_{\mathrm{i}}\lambda_{\mathrm{f}}} p_{\lambda_{\mathrm{i}}} \sum_{j,j'} \langle\lambda_{\mathrm{i}}| \exp(-i\mathbf{q}\cdot\mathbf{r}_j)\mathbf{s}_j^\alpha |\lambda_{\mathrm{f}}\rangle\langle\lambda_{\mathrm{f}}| \exp(i\mathbf{q}\cdot\mathbf{r}_{j'})\mathbf{s}_{j'}^\beta |\lambda_{\mathrm{i}}\rangle \\ \times \delta\left(\hbar\omega + E_{\lambda_{\mathrm{i}}} - E_{\lambda_{\mathrm{f}}}\right).\end{aligned} \tag{11.25}$$

In (11.25), $\mathbf{r}_j$ and $\mathbf{r}_{j'}$ denotes the nuclear positions, which are not fixed. The quantum mechanical way of handling this is by treating $\mathbf{r}_j$ as operators. This gives rise to phonon scattering, as described in chap. 10.

We will here only consider magnetic scattering that does not involves phonons, *i.e.* is elastic in the phonon channel. Hence, we can interpret $\mathbf{r}_j$ as the lattice positions, while multiplying the magnetic scattering cross section with the Debye-Waller factor $\exp(-2W)$.

$$\begin{aligned}\left.\frac{d^2\sigma}{d\Omega dE_{\mathrm{f}}}\right|_{\mathrm{magn}} = \exp(-2W)\,(\gamma r_0)^2 \frac{k_{\mathrm{f}}}{k_{\mathrm{i}}} \left[\frac{g}{2}F(q)\right]^2 \sum_{\alpha\beta} (\delta_{\alpha\beta} - \hat{q}_\alpha \hat{q}_\beta) \\ \times \sum_{\lambda_{\mathrm{i}}\lambda_{\mathrm{f}}} p_{\lambda_{\mathrm{i}}} \sum_{j,j'} \langle\lambda_{\mathrm{i}}| \exp(-i\mathbf{q}\cdot\mathbf{r}_j)\mathbf{s}_j^\alpha |\lambda_{\mathrm{f}}\rangle\langle\lambda_{\mathrm{f}}| \exp(i\mathbf{q}\cdot\mathbf{r}_{j'})\mathbf{s}_{j'}^\beta |\lambda_{\mathrm{i}}\rangle \\ \times \delta\left(\hbar\omega + E_{\lambda_{\mathrm{i}}} - E_{\lambda_{\mathrm{f}}}\right).\end{aligned} \tag{11.26}$$

11.3 * Inelastic magnetic neutron scattering

In this section we will specialize the master equation for magnetic scattering to describe spin waves. We start with repeating (11.26):

$$\begin{aligned}\frac{d^2\sigma}{d\Omega dE_{\rm f}} &= (\gamma r_0)^2 \frac{k_{\rm f}}{k_{\rm i}} \left[\frac{g}{2}F(q)\right]^2 \sum_{\alpha\beta}(\delta_{\alpha\beta}-\hat{\mathbf{q}}_\alpha\hat{\mathbf{q}}_\beta) \\ &\times \sum_{\lambda_{\rm i}\lambda_{\rm f}} p_{\lambda_{\rm i}} \sum_{j,j'} \langle\lambda_{\rm i}|\exp(-i\mathbf{q}\cdot\mathbf{r}_j)\mathbf{s}_j^\alpha|\lambda_{\rm f}\rangle\langle\lambda_{\rm f}|\exp(i\mathbf{q}\cdot\mathbf{r}_{j'})\mathbf{s}_{j'}^\beta|\lambda_{\rm i}\rangle \\ &\times \delta\left(\hbar\omega + E_{\lambda_{\rm i}} - E_{\lambda_{\rm f}}\right).\end{aligned} \tag{11.27}$$

The next step closely follows the treatment of phonon scattering. First, we rewrite the energy-conserving δ-function in terms of a time integral. To repeat (9.4):

$$\delta(\hbar\omega + E_{\lambda_{\rm i}} - E_{\lambda_{\rm f}}) = \frac{1}{2\pi\hbar}\int_{-\infty}^{\infty} dt \exp\left(-\frac{i(\hbar\omega + E_{\lambda_{\rm i}} - E_{\lambda_{\rm f}})t}{\hbar}\right). \tag{11.28}$$

Subsequently, we transform the stationary operators, here denoted $\hat{A}$, to time-dependent Heisenberg operators, $\hat{A}(t)$, through

$$\begin{aligned}&\left\langle \lambda_{\rm i}\middle| \exp\left(\frac{iE_{\lambda_{\rm i}}t}{\hbar}\right)\hat{A}\exp\left(-\frac{iE_{\lambda_{\rm f}}t}{\hbar}\right)\middle|\lambda_{\rm f}\right\rangle \\ &=\left\langle \lambda_{\rm i}\middle| \exp\left(\frac{i\hat{H}_\lambda t}{\hbar}\right)\hat{A}\exp\left(-\frac{i\hat{H}_\lambda t}{\hbar}\right)\middle|\lambda_{\rm f}\right\rangle \\ &= \langle\lambda_{\rm i}|\hat{A}(t)|\lambda_{\rm f}\rangle.\end{aligned} \tag{11.29}$$

Making this transformation and performing the closure sum over the final states, ($\sum_{\lambda_{\rm f}}|\lambda_{\rm f}\rangle\langle\lambda_{\rm f}| = 1$), we reach the equation for the magnetic scattering cross section in the Heisenberg picture:

$$\begin{aligned}\frac{d^2\sigma}{d\Omega dE_{\rm f}} &= (\gamma r_0)^2 \frac{k_{\rm f}}{k_{\rm i}} \left[\frac{g}{2}F(q)\right]^2 \sum_{\alpha\beta}(\delta_{\alpha\beta}-\hat{q}_\alpha\hat{q}_\beta) \\ &\times \frac{1}{2\pi\hbar}\sum_{j,j'}\int_{-\infty}^{\infty} dt \exp(-i\omega t) \\ &\times \left\langle \exp(-i\mathbf{q}\cdot\mathbf{r}_j(0))\mathbf{s}_j^\alpha(0)\exp(i\mathbf{q}\cdot\mathbf{r}_{j'}(t))\mathbf{s}_{j'}^\beta(t)\right\rangle,\end{aligned} \tag{11.30}$$

where $\langle\hat{A}\rangle$ means the thermal average of the expectation value of an operator $\hat{A}$, in the same way as the calculations leading to the phonon expression (9.8).

The nuclear positions $\mathbf{r}(t)$ and the atomic spin $\mathbf{s}(t)$ are both operators. Each of these gives rise to both an elastic and an inelastic contribution; in total the cross section becomes a sum of four terms. The one that is elastic in both channels is the magnetic diffraction signal, while the contribution that is elastic in

the nuclear positions (the phonon channel) and inelastic in the spins (the magnetic channel) is the true magnetic inelastic signal. The two other contributions involve creation/annihilation of phonons via the magnetic interactions, and are not discussed further here; we refer to Ref. [1, (8.10)].

The two contributions that are elastic in the phonon channel are reached in analogy with chapter 10. We replace the general nuclear position operators $\mathbf{r}_j$ with the nuclear equilibrium positions in a lattice and utilize the periodicity of the lattice. Furthermore, we multiply with the Debye-Waller factor, $\exp(-2W)$:

$$\left(\frac{d^2\sigma}{d\Omega dE_\mathrm{f}}\right)_\mathrm{magn.} = (\gamma r_0)^2 \frac{k_\mathrm{f}}{k_\mathrm{i}} \left[\frac{g}{2}F(q)\right]^2 \exp(-2W) \sum_{\alpha\beta} (\delta_{\alpha\beta} - \hat{\mathbf{q}}_\alpha \hat{\mathbf{q}}_\beta) \quad (11.31)$$
$$\times \frac{N}{2\pi\hbar} \int_{-\infty}^{\infty} \sum_{j'} \exp(i\mathbf{q}\cdot\mathbf{r}_j) \left\langle \mathbf{s}_0^\alpha(0) \mathbf{s}_{j'}^\beta(t) \right\rangle \exp(-i\omega t) dt.$$

This equation should be understood as the space and time Fourier transform of the spin-spin correlation function, and it is the starting point for most calculations of magnetic scattering cross sections.

11.4 Problems

11.4.1 Derivation of the cartesian formulation of the perpendicular spin component

Expand the steps in equation (11.18).

Chapter 12

Elastic magnetic scattering

The arrangement of the magnetism of magnetic ions in materials is a rich and diverse field, in which neutron scattering is a key technique. We will here turn to the study of magnetic structures by magnetic diffraction.

12.1 Magnetism in materials

We begin with a description of magnetic properties of materials. We will concentrate on materials where the magnetic moments are localised and interact via simple exchange interactions. We shall see how this interaction leads to a number of different magnetically ordered structures.

There exists a number of textbooks devoted to magnetic properties of materials. For a general introduction to the field, we recommend the textbook by S. Blundell [81].

12.1.1 Interactions between magnetic ions

Due to their magnetic moments, described in section 11.1, ions will interact with an external magnetic field. This is described by the *Zeeman Hamiltonian*:

$$H_{\mathrm{Z}} = -\boldsymbol{\mu} \cdot \mathbf{B} = -g\mu_{\mathrm{B}} S^z B\,, \tag{12.1}$$

where the z direction is here defined as the direction of the magnetic field.

In a similar way, magnetic ions interact with other magnetic ions through the dipole-dipole interaction. However, for most moments this is only a tiny effect that can be neglected. The major term deciding the interactions stem from the electrostatic forces. The combination of these forces and the Pauli principle will affect the energy levels of the system, resulting in the *exchange interaction*. There are a number of ways this interaction can appear, of which we mention only the two most important ones:

- **Direct exchange.** The electronic orbitals of the two ions overlap directly. If the spins of the electrons of the different ions have the same direction,

the Pauli principle will make sure that they stay apart (the spatial part of the two-particle wavefunction must be odd - and is therefore zero where the particles meet). Hence, the electrostatic energy is lowered, and parallel alignment of spins is preferred.

- **Indirect exchange.** Here, the electron orbitals on neighbouring magnetic ions do not overlap, but they are bridged by a non-magnetic ion (*e.g.* O^{2+}). If the electronic spins are different, they are able to "visit" one another by hopping over via the bridging ion. Despite the electrostatic repulsio, this hopping lowers the kinetic energy due to the Heisenberg uncertainty principle. If the spin quantum numbers are equal, the Pauli principle will prohibit such visits. In effect, an antiparallel spin alignment is (in most cases) energetically favourable.

The simple exchange interaction mechanisms described above are isotropic in spin space, since the underlying mechanisms do not depend upon a particular choice of coordinate system. These interactions are described by the *Heisenberg Hamiltonian*:

$$H_{ij} = -J_{ij}\mathbf{S}_i \cdot \mathbf{S}_j, \tag{12.2}$$

where i and j here represent two different ions in the material. A positive value of the exchange constant J_{ij} favours a parallel alignment of the two spins, while a negative value favours an antiparallel alignment.

If anisotropies are present, the effective Hamiltonian changes. In the most extreme case, two of the spin dimensions are suppressed, and we reach the *Ising Hamiltonian*

$$H_{ij} = -J^z_{ij}S^z_i S^z_j. \tag{12.3}$$

This Hamiltonian is much easier to deal with, as any state written in the S^z basis is immediately an eigenstate, and quantum mechanical effects vanish.

The values of J_{ij} and J^z_{ij} can be several meV, in particular if i and j are nearest neighbours. In general, the interaction falls off rapidly as a function of distance, and it is often sufficient to include the second (or in some case also the third) nearest neighbour.

12.1.2 Classical magnetic structures

In a magnetic solid, one must deal with the simultaneous interaction between all spins. This can give rise to many complex magnetic arrangements, or *magnetic structures*.

The physics can be described by the total Heisenberg Hamiltonian

$$\boxed{H = \sum_{\langle i,j\rangle} H_{ij} + \sum_j H_{\mathrm{Z,j}} = -\sum_{\langle i,j\rangle} J_{ij}\mathbf{S}_i \cdot \mathbf{S}_j - g\mu_{\mathrm{B}}B\sum_j S^z_j}, \tag{12.4}$$

where the summing convention here is so that the same pair, $\langle i, j\rangle$ is only counted once. The solution of this Hamiltonian is a severely complex problem, which has puzzled physicists for most of a century.

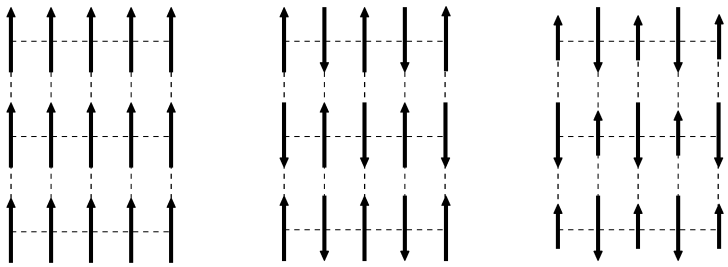

Figure 12.1: The three main types of magnetically ordered structures. (left) The ferromagnetic structure, where all spins are aligned. (middle) A simple antiferromagnetic structure, with antiparallel alignment of spins and no net magnetic moment. (right) One type of a ferrimagnetic structure with antiparallel spin alignment, but still a net moment, here due to a difference in the spin values on two different sites.

It is observed by a number of experimental methods that materials which can be described by (12.4) become magnetically ordered below a certain phase transition temperature, or *critical temperature*, T_c. Some magnetic structures are stable even up to around $T_c \approx 1000$ K.

A classical solution to (12.4) is often a good approximation to the physical reality. As we will see below, this gives rise to three main types of magnetically ordered structures, also illustrated in figure 12.1.

- **Ferromagnetism.** Here $J_{ij} > 0$, and all spins are (on average) aligned in the same direction, and the system has a resulting magnetisation.
- **Antiferromagnetism.** Here $J_{ij} < 0$, and the spins are divided into different *sublattices* (often two), each with the same magnetisation value. However, the total outer magnetisation of the antiferromagnet vanishes due to different orientation of the sublattice magnetisations. By convention, the critical temperature for a ferromagnet is denoted the *Nèel temperature*, T_N, after Louis Nèel who discovered antiferromagnetism.
- **Ferrimagnetism.** Here $J_{ij} < 0$, and the spins are divided into sublattices aligned in different directions, like the antiferromagnet. However, the ferrimagnet still possesses a net magnetic moment, since the magnetisation value of the sublattices are different. This could be due to a different number of spins in the sublattices or to different spin values (as illustrated in figure 12.1).

We will here make a brief introduction to magnetic structures for the simple case where all magnetic ions are crystallographically equivalent. This implies that the mean (thermal) magnitude of the ordered spin at a given site $\mathbf{r}_j$ is independent of j. We denote the thermal average by $\langle \mathbf{s}_j \rangle$.

We assume that we have a crystal of sufficiently large size that we can use periodic boundary conditions. Since all magnetic ions are equivalent, we have

complete translational symmetry. Hence, the spin-spin interaction can only depend upon the relative position of the spins:

$$J_{ij} = J(\mathbf{r}_i - \mathbf{r}_j). \tag{12.5}$$

The interaction part of the Hamiltonian can now be written in a slightly different form, where we first sum over all spins, and then over all neighbours relative to that spin. To compensate for double-counting, we must divide by a factor 2.

$$H = -\frac{1}{2}\sum_{j,\delta} J_\delta \mathbf{S}_j \cdot \mathbf{S}_{j+\delta}. \tag{12.6}$$

For simplicity, we have assumed that the external field is zero. We now decompose the spin structure in its Fourier components

$$\mathbf{S}_\mathbf{q} = \frac{1}{\sqrt{N}}\sum_j \mathbf{S}_j \exp(i\mathbf{q}\cdot\mathbf{r}_j), \tag{12.7}$$

and we further define the Fourier transform of the spin-spin interaction

$$J(\mathbf{q}) = \sum_\delta J_\delta \exp(i\mathbf{q}\cdot\mathbf{r}_\delta), \tag{12.8}$$

which is a real quantity (for each neighbour at $\mathbf{r}_\delta$, there is another neighbour at $-\mathbf{r}_\delta$ with the same interaction constant). It can be shown that (12.6) can be rewritten as [82]

$$H = -\sum_\mathbf{q} J(\mathbf{q})\mathbf{S}_\mathbf{q}\cdot\mathbf{S}_{-\mathbf{q}}. \tag{12.9}$$

Now, we Fourier transform the identity $S^2 = \mathbf{S}_j \cdot \mathbf{S}_j$, leading to

$$NS^2 = \sum_{\mathbf{q},\mathbf{q}'} \mathbf{S}_\mathbf{q}\cdot\mathbf{S}_{\mathbf{q}'}\exp(i(\mathbf{q}-\mathbf{q}')\cdot\mathbf{r}_j). \tag{12.10}$$

This must be satisfied simultaneously all lattice sites, j, which is a tedious task to test. However, summing (12.10) over all sites gives the relaxed condition

$$NS^2 = \sum_\mathbf{q} \mathbf{S}_\mathbf{q}\cdot\mathbf{S}_{-\mathbf{q}}. \tag{12.11}$$

Here, $\mathbf{S}_\mathbf{q}\cdot\mathbf{S}_{-\mathbf{q}}$ can be viewed as the square amount of the spin Fourier component of that particular $\mathbf{q}$. In this respect, (12.11) can be seen as a modified Pythagoras equation. Although a much weaker requirement than the original, it is often sufficient to fulfill (12.11) to solve the problem. In this case, the ground state is found where only one Fourier component, $S_\mathbf{Q}$, is non-zero. Here, the *magnetic ordering vector*, $\mathbf{Q}$, is the one that minimizes $J(\mathbf{q})$. The energy of the spin system is thus given by

$$E_{\min} = -NS^2 J(\mathbf{Q}). \tag{12.12}$$

The detailed calculation behind this can be found in [82]. Typical solutions to the minimization problem are

- $\mathbf{Q} = \mathbf{0}$: The ferromagnetic structure.
- $\mathbf{Q}$ is on a position of the Brillouin zone boundary, so that $\exp(\mathbf{Q}\cdot\mathbf{r}_j) = \pm 1$ always. This gives *two-sublattice commensurate* antiferromagnetic structures, as illustrated in figure 12.1. These structures are often found in nearest-neighbour dominated transition metal oxides.
- $\mathbf{Q}$ has another value. This often gives rise to *incommensurate* structures, *e.g.* helical (spiral) structures, often found in systems where interactions beyond nearest neighbours are substantial, *e.g.* in rare-earth metals. For a description of the magnetism of rare-earth elements, we refer to the book by Jensen and Mackintosh [83].

12.1.3 Magnetic phase transitions

Magnetically ordered structures have in common that upon heating, the average ordered magnetic moment, or *order parameter* decreases. When the order parameter reaches zero, at the *ordering temperature*, T_c, the system is said to be unordered, or *paramagnetic*.

In *first order phase transitions*, the order parameter discontinuously drops to zero, and latent heat and thermal hysteresis is connected with the phase transition.

In *second order phase transitions*, the order parameter decreases continuously to zero, and the phase transition is reversible. Second order phase transitions can in general be described by the same universal theory, valid close to the transition temperature, where *e.g.* the order parameter varies as

$$\langle \mathbf{S}_\mathbf{Q} \rangle \propto (1 - T/T_c)^\beta. \tag{12.13}$$

The full description of these *critical phenomena* is, however, outside the scope of these notes.

In more complex systems, the magnetic *phase diagram* will contain more than one magnetic phase, *e.g.* the ordering vector, $\mathbf{Q}$, may vary with temperature. We will, however, not discuss these more advanced cases here.

Perspectives. The detailed magnetic structure and its temperature dependence is of relevance for the classification of new magnetic materials, for example the multiferroic materials where the electric, magnetic and structural properties are strongly related. We also like to mention the use of magnetic phase transitions for magnetic cooling, and the many uses of magnetism in nanotechnology, *e.g.* for magnetic data recording.

12.2 Magnetic diffraction

We here present the magnetic scattering cross section for diffraction and show a few important examples.

12.2.1 The magnetic diffraction cross section

We will now consider the part of the magnetic scattering cross section (11.26), that is purely elastic in both the nuclear and the magnetic system. Hence, the energy δ-function falls out and the completeness sum, $\sum_f |\lambda_\mathrm{f}\rangle\langle\lambda_\mathrm{f}| = 1$, can be performed. We now obtain:

$$\left.\frac{d\sigma}{d\Omega}\right|_\mathrm{magn.el.} = (\gamma r_0)^2 \left[\frac{g}{2}F(q)\right]^2 \exp(-2W) \sum_{\alpha\beta} (\delta_{\alpha\beta} - \hat{q}_\alpha \hat{q}_\beta) \times \sum_{\lambda_\mathrm{i}} p_{\lambda_\mathrm{i}} \sum_{j,j'} \exp(i\mathbf{q}\cdot(\mathbf{r}_{j'} - \mathbf{r}_j)) \big\langle \lambda_\mathrm{i} | \mathbf{s}_j^\alpha \mathbf{s}_{j'}^\beta | \lambda_\mathrm{i} \big\rangle, \tag{12.14}$$

which for a static magnetic structure can be simplified to

$$\left.\frac{d\sigma}{d\Omega}\right|_\mathrm{magn.el.} = (\gamma r_0)^2 \left[\frac{g}{2}F(q)\right]^2 \exp(-2W) \left| \sum_j \exp(-i\mathbf{q}\cdot\mathbf{r}_j) \langle \mathbf{s}_{j,\perp} \rangle \right|^2, \tag{12.15}$$

where $\langle\,\rangle$ here denotes thermal average and $\mathbf{s}_\perp$ is the spin component perpendicular to $\mathbf{q}$.

Equation (12.15) plays the same pivotal role for magnetic diffraction as (2.56) does for nuclear diffraction.

12.2.2 Paramagnetic scattering

A paramagnet is a collection of magnetic spins, where there is no correlation between different spins, *i.e.*

$$\langle \mathbf{s}_j \cdot \mathbf{s}_{j'} \rangle = 0. \tag{12.16}$$

The scattering from a paramagnet is rather simple, since each spin scatters independently of the neighbouring spins. In fact, this is a magnetic version of incoherent scattering. In the second line of (12.14), only terms with identical position indices contribute to the double sum, for example $\mathbf{s}_j \cdot \mathbf{s}_j$. Hence, the dependence of $\mathbf{q}$ disappears. The five-fold sum can then be replaced with $2Ns(s+1)/3$, where N is the number of spins, and the factor $2/3$ comes from the fact that two out of three spin components are perpendicular to $\mathbf{q}$. Hence, the result reads:

$$\left.\frac{d\sigma}{d\Omega}\right|_\mathrm{paramagn.el.} = \frac{2}{3} N (\gamma r_0)^2 \left[\frac{g}{2}F(q)\right]^2 \exp(-2W) s(s+1). \tag{12.17}$$

12.2.3 Scattering from magnetically ordered structures

We will here investigate the magnetic scattering from ordered magnetic structures, as described in section 12.1. We assume the atoms to be located on an ordered lattice, as described in chapter 7. It should be noted that the *magnetic unit cell* used to describe ferri- and antiferromagnetically ordered structures is often larger than the structural unit cell. This is illustrated in Fig. 12.2.

Figure 12.2: An illustration of the unit cell of the two-dimensional antiferromagnet. Left panel shows the nuclear unit cell, middle panels shows a unit cell, which is a factor two enlarged in both directions, and right panel shows the minimal antiferromagnetic unit cell.

In analogy to nuclear diffraction, the magnetic scattering cross section from an ordered structure ends up being

$$\left.\frac{d\sigma}{d\Omega}\right|_{\text{magn.el.}} = (\gamma r_0)^2 \left[\frac{g}{2}F(q)\right]^2 \exp(-2W) \times \frac{N(2\pi)^3}{V_0}|F_{\text{M}}(\mathbf{q})|^2 \sum_{\boldsymbol{\tau}} \delta(\mathbf{q}-\boldsymbol{\tau}-\mathbf{Q}), \tag{12.18}$$

where $\mathbf{Q}$ is the ordering vector of the magnetic structure, and the magnetic structure factor is given by the sum over the magnetic unit cell:

$$F_{\text{M}}(\mathbf{q}) = \sum_{\mathbf{i}} \exp(-i\mathbf{q}\cdot\boldsymbol{\Delta}_i)\left\langle \mathbf{s}_{i,\perp}\right\rangle . \tag{12.19}$$

Equations (12.18) and (12.19) are equivalent to the description of nuclear diffraction if we make the replacement

$$b_j \longrightarrow \gamma r_0 \frac{g}{2} F(q)\mathbf{s}_{i,\perp}. \tag{12.20}$$

The magnitude of this *magnetic scattering length* is similar to the nuclear scattering lengths, since $\gamma r_0 = 5.39$ fm and $gF(q)s/2$ is of the order unity. Hence, the magnetic and nuclear scattering cross sections have similar magnitudes. For large values of S, *e.g.* in some transition metal salts, *e.g.* Fe-oxides, or in most rare-earth compounds, the magnetic scattering can completely dominate the diffraction patterns.

In conclusion, magnetic diffraction is seen when the scattering vector equals a magnetic ordering vector (modulo a reciprocal lattice vector), and the intensity of the scattering is proportional to the square of the ordered moment and of similar magnitude as nuclear scattering. Hence, neutron scattering is a clearcut way to determine magnetic structures. In contrast, techniques that measure the macroscopic magnetic response cannot determine the ordering vector.

Example. The existence of ordered antiferromagnets was predicted during the 1930'ies and 1940'ies, but the final proof was given by one of the first neutron diffraction experiments by C. Shull in Brookhaven in 1951 [84]. For this, and for the invention of neutron diffraction in the first place, C. Shull was awarded the Nobel prize in 1994. Some original data, showing the proof of antiferromagnetism in MnO, are shown in Fig. 12.3.

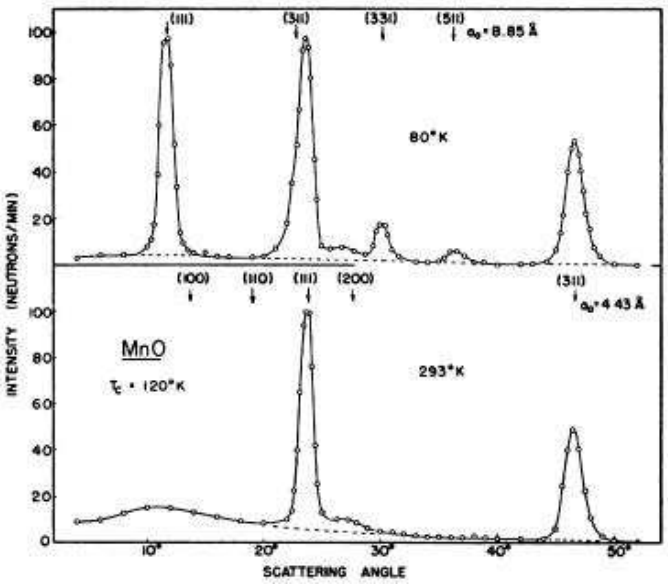

Figure 12.3: The first published neutron diffraction data was the determination of the antiferromagnetic structure in NiO, CoO, FeO, MnO, and α-Fe_2O_3. The data shown are scans on a two-axis diffractometer on a powder of MnO, (top) at 77 K (below $T_N = 120$ K) and (bottom) at 293 K. The low-temperature peak at $2\theta = 12^\circ$ shows antiferromagnetic order with an ordering vector along (111). Note that there is still a broad bump at the (111) position at 293 K, typical for short-range magnetic order present above the critical temperature. From Ref. [84].

12.3 Problems

12.3.1 A classical antiferromagnet in two dimensions

This problem is an illustration of antiferromagnetic order.

We imagine a two-dimensional square lattice with lattice constant d and one magnetic atom on each lattice point. The magnetic interactions is antiferromagnetic between nearest neighbours, with coupling constant J, and zero otherwise.

1. Calculate the energy of the antiferromagnetic state with alternating spin directions between nearest neighbours, as illustrated in Figs. 12.1(middle).

2. Argue that this energy is the minimum energy possible.

3. Calculate $J(q)$ and find in this way the Q-vector of the magnetically ordered structure.

12.3.2 Scattering from an antiferromagnet

This problem is a simple illustration of magnetic diffraction, as calculated in section 12.2.

We consider the two-dimensional square lattice with lattice constant d and antiferromagnetic interactions between nearest neighbours. In problem 12.3.1, we showed that this system is antiferromagnetic with alternating spin directions between nearest neighbours, as illustrated in Figs. 12.1(middle) and 12.2.

1. Argue that the square 4-atom cell with side length $2d$ is a valid magnetic unit cell for the system and that the reciprocal lattice then becomes a square lattice with side length π/d.

2. We define as usual the reciprocal lattice coordinates, (h, k), in terms of the nuclear reciprocal lattice vectors, $|\mathbf{a}^*| = |\mathbf{b}^*| = 2\pi/d$. Show that the points of the 4-atom magnetic reciprocal lattice can be reached by integer and half-integer values of h and k.

3. In the nuclear Brillouin zone, there are 4 different magnetic reciprocal lattice points: $(0, 0)$, $(0, 1/2)$, $(1/2, 0)$, and $(1/2, 1/2)$. Calculate the magnetic scattering structure factor for these 4 reflections when the spins are all pointing out of the plane (the l-direction). Draw a map of q-space, showing the allowed nuclear and magnetic reflections, respectively.

4. Compare to the value of the ordering Q-vector, $\mathbf{Q} = (1/21/2)$, found in problem 12.3.1.

Chapter 13

* Inelastic magnetic scattering

This chapter is devoted to inelastic neutron scattering from magnetic systems, which is one of the hallmarks of neutron scattering. For the investigation of magnetic excitations, neutron scattering is simply the technique of choice.

We begin with a general description of excitations in magnetic materials. Later sections contain a general description of the neutron scattering from magnetic excitations, including cross sections for ferro- and antiferromagnetic spin-waves, magnetic dynamics in nanoparticles, and scattering from quantum spin systems.

13.1 * Magnetic excitations

Here we discuss the coherent magnetic excitations known as *spin waves*. The first section deals with spin waves in a ferromagnet, then we extend the discussion to the much more difficult antiferromagnetic spin waves. We end the chapter by touching the topic of quantum magnets.

13.1.1 * Spin waves in a ferromagnet

Let us assume that the system can be described by a Heisenberg Hamiltonian of the form (12.4). We assume that the sign of the interaction, J_δ, is dominantly positive; *i.e.* that the Fourier transform of the spin-spin interaction, $J(\mathbf{q}')$ in eq. (12.8), is maximal at $\mathbf{q}' = \mathbf{0}$. In that case, $\mathbf{Q} = \mathbf{0}$, and the ground state of the system is the ferromagnet

$$|\mathrm{GS}\rangle = |\mathrm{FM}\rangle = |\uparrow\uparrow\uparrow\uparrow\rangle, \tag{13.1}$$

where all spins point along the positive z-axis. This quantization axis is in practice defined by the direction of an applied field or some small anisotropy

terms, not present in (12.4). We will here neglect anisotropies and just assume that a quantization axis exists even in zero field. We will describe the elementary excitations in the ferromagnet in two ways: The equation-of-motion method and the stationary operator method, both of which are described below.

* The equation-of-motion

Spin excitation frequencies can in general be determined by the "equation-of-motion" approach [1, 81]. We assume that the spin components perpendicular to the spin ordering z-direction, $s_j^x(t)$ and $s_j^y(t)$, can be non-zero, although their time average is zero. We shall then see that the perpendicular components will perform periodic motion.

To find the time derivative of the perpendicular components, one must take into account that the spins are angular momenta. Hence, a field (or interaction) trying to align the spin along the z-axis, instead causes the spins to precess around this axis. We could now write down the classical equations of motion for the spin system, but it turns out to be equally simple to perform the full quantum mechanical treatment, which we will do here.

We start by considering the operators along the ordering direction, $s_j^z(t)$. For the equation of motion of the spin operators, we use the Ehrenfest theorem:

$$\begin{aligned} i\hbar\frac{d}{dt}s_j^z &= [s_j^z, \hat{H}] \\ &= \sum_{j'}\left[s_j^z, J(\mathbf{r}_j-\mathbf{r}_{j'})(s_j^x s_{j'}^x + s_j^y s_{j'}^y)\right] \\ &= \sum_{j'} J(\mathbf{r}_j-\mathbf{r}_{j'})\left(s_{j'}^x s_j^y - s_{j'}^y s_j^x\right) \approx 0. \end{aligned} \tag{13.2}$$

We have in the derivation neglected commutator terms that immediately vanish. The last approximation to zero is valid since the terms inside the sum are all small to second order - and in fact can be shown to have a time average of exactly zero. Thus, the spin value along the ordering directions is a constant of motion.

Next, we consider the linear combination $s_j^+(t) = s_j^x(t) + is_j^y(t)$, also known as the spin raising operator, defined in (13.37). The Ehrenfest theorem yields:

$$\begin{aligned} i\hbar\frac{d}{dt}s_j^+ &= [s_j^+, \hat{H}] \\ &= \sum_{j'}\left[(s_j^x + is_j^y), J(\mathbf{r}_j-\mathbf{r}_{j'})(s_j^x s_{j'}^x + s_j^y s_{j'}^y + s_j^z s_{j'}^z - g\mu_{\mathrm{B}}Bs_j^z)\right] \\ &= g\mu_{\mathrm{B}}Bs_j^+ + \sum_{j'} J(\mathbf{r}_j-\mathbf{r}_{j'})\left(s_{j'}^z s_j^+ - s_{j'}^+ s_j^z\right). \end{aligned} \tag{13.3}$$

As often in solid state physics, we turn to the Fourier transform; this time

of the spin operators

$$S^+_{\mathbf{q}'} = \frac{1}{\sqrt{N}} \sum_j \exp(i\mathbf{q}' \cdot \mathbf{r}_j) s^+_j, \tag{13.4}$$

where N is the number of spins. Combined with (13.3), we arrive at

$$\hbar \frac{d}{dt} S^+_{\mathbf{q}'} = g\mu_{\mathrm{B}} B S^+_{\mathbf{q}'} + \frac{1}{\sqrt{N}} \sum_{j,j'} \exp(-i\mathbf{q}' \cdot \mathbf{r}_j) J(\mathbf{r}_j - \mathbf{r}_{j'}) \left(s^z_{j'} s^+_j - s^+_{j'} s^z_j \right). \tag{13.5}$$

Now, in the ground state, the operator s^z_j has the eigenvalue S. At finite temperatures, we approximate this operator by its thermal mean value, the *ordered moment* $\langle S^z \rangle$. Hence, we simplify (13.5)

$$\begin{aligned} \hbar \frac{d}{dt} S^+_{\mathbf{q}'} &= g\mu_{\mathrm{B}} B S^+_{\mathbf{q}'} + \frac{\langle S^z \rangle}{\sqrt{N}} \sum_{j,j'} \exp(i\mathbf{q}' \cdot \mathbf{r}_j) J(\mathbf{r}_j - \mathbf{r}_{j'}) \left(s^+_j - s^+_{j'} \right) \\ &= \big(g\mu_{\mathrm{B}} B + \langle S^z \rangle [J(\mathbf{0}) - J(\mathbf{q}')] \big) S^+_{\mathbf{q}'}. \end{aligned} \tag{13.6}$$

This differential equation shows that $S^+_{\mathbf{q}'}$ performs a periodic motion with the frequency

$$\hbar\omega_{\mathbf{q}'} = g\mu_{\mathrm{B}} B + \langle S \rangle [J(\mathbf{0}) - J(\mathbf{q}')]. \tag{13.7}$$

Now, let us investigate the significance of this result. Assume that $S^+_{\mathbf{q}'}$ is the annihilation operator of one elementary excitation of the system,

$$S^+_{\mathbf{q}'} |\mathbf{q}'\rangle = |\mathrm{GS}\rangle, \tag{13.8}$$

where the energy of the groundstate is E_0 and of the excited state $|\mathbf{q}'\rangle$ is denoted $E_0 + \hbar\omega_{\mathbf{q}'}$. The time dependent operator, $S^+_{\mathbf{q}'}(t)$, is then found directly by

$$S^+_{\mathbf{q}'}(t) |\mathbf{q}'\rangle = \exp\left(\frac{iHt}{\hbar} \right) S^+_{\mathbf{q}'} \exp\left(-\frac{iHt}{\hbar} \right) |\mathbf{q}'\rangle = \exp(-i\omega_{\mathrm{q}'} t) S^+_{\mathbf{q}'} |\mathbf{q}'\rangle. \tag{13.9}$$

Hence, $\omega_{\mathbf{q}'}$ is the frequency of the spin deviation, and $\hbar\omega_{\mathbf{q}'}$ is the energy of the elementary (*spin wave*) excitation of the system.

Example. For nearest neighbour interactions in one dimension, each spin interacts only with its two neighbours. Hence $J(q') = J(0)\cos(q'd)$, and $J(0) = 2J$, giving

$$\hbar\omega_{\mathbf{q}'} = g\mu_{\mathrm{B}} B + 2JS\big(1 - \cos(q'd)\big). \tag{13.10}$$

Hence, for small values of $|q'|$ (compared to the reciprocal lattice vector, $2\pi/d$), the spin wave energy in zero field becomes quadratic in q'. Furthermore, it can be seen that an applied field induces an energy gap of $\Delta = g\mu_{\mathrm{B}} B$. These effects are illustrated in Fig. 13.1.

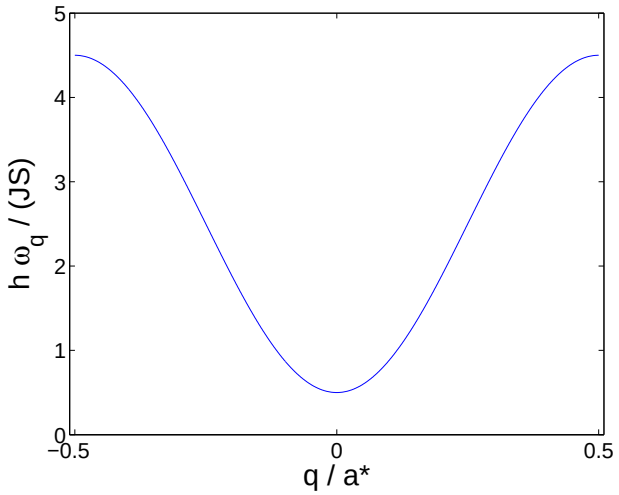

Figure 13.1: Dispersion relation for spin waves in a 1D nearest neighbour ferromagnet in an applied field, given by (13.10).

* The stationary operator method

If the ground state can be described (or approximated) in simple terms, it is in general possible to describe the lowest excited states by exact quantum mechanical calculations. For the ferromagnet, this is particularly simple. Let us first define the lowering operator in reciprocal space as

$$S^-_{\mathbf{q}'} = \frac{1}{\sqrt{N}} \sum_j \exp(i\mathbf{q}' \cdot \mathbf{r}_j) s^-_j . \tag{13.11}$$

It can be shown by direct application of the Hamiltonian (12.4) that the state

$$|\mathbf{q}'\rangle = S^-_{\mathbf{q}'}|\mathrm{GS}\rangle \tag{13.12}$$

is an eigenstate of the Hamiltonian,

$$\hat{H}|\mathbf{q}'\rangle = (E_0 + \hbar\omega_{\mathbf{q}'})|\mathbf{q}'\rangle. \tag{13.13}$$

Reassuringly, for zero temperature ($\langle S^z \rangle = S$) this gives the same spin wave frequency, $\omega_{\mathbf{q}'}$, as the equation-of-motion method (13.7).

13.1.2 * Spin waves in an antiferromagnet

We now proceed to the much more difficult task of calculating the spin waves in a two-sublattice antiferromagnet (AFM), as first described by P. W. Anderson [85]. We will use the equation-of-motion method as described in section 13.1.1.

* The anisotropic Hamiltonian

We assume that the ground state for the AFM is the classical *Neél state*, where the spins are fully aligned along the positive z-axis (sublattice m) or along the negative z-axis (sublattice n), as described in section 12.1.

We write the magnetic Hamiltonian as an isotropic Heisenberg term, an applied field, $\mathbf{B}$, and an effective anisotropy field, $\mathbf{B}_\mathrm{A}$, originating from the surrounding crystal. Both fields are parallel to the z-axis.

$$\begin{aligned}\hat{H} = &\sum_{\mathbf{m},\mathbf{r}} J(\mathbf{r})\mathbf{s}_\mathbf{m}\cdot\mathbf{s}_{\mathbf{m}+\mathbf{r}} + \sum_{\mathbf{n},\mathbf{r}} J(\mathbf{r})\mathbf{s}_\mathbf{n}\cdot\mathbf{s}_{\mathbf{n}+\mathbf{r}} \\ &+ \sum_{\mathbf{m},\mathbf{R}} J_1(\mathbf{R})\mathbf{s}_\mathbf{m}\cdot\mathbf{s}_{\mathbf{m}+\mathbf{R}} + \sum_{\mathbf{n},\mathbf{R}} J_1(\mathbf{R})\mathbf{s}_\mathbf{n}\cdot\mathbf{s}_{\mathbf{n}+\mathbf{R}} \\ &- g\mu_\mathrm{B}\left(B + B_\mathrm{A}\right)\sum_\mathbf{m} s^z_\mathbf{m} - g\mu_\mathrm{B}\left(B - B_\mathrm{A}\right)\sum_\mathbf{n} s^z_\mathbf{n},\end{aligned} \tag{13.14}$$

where $\mathbf{r}$ connects spins on opposite sublattices with coupling strength $J(\mathbf{r})$, and $\mathbf{R}$ connects spins on the same sublattice with coupling $J_1(\mathbf{R})$. Note that $\mathbf{B}_\mathrm{A}$ points in opposite directions in the two sublattices.

* The equations of motion

We now transform the spin operators on the "down" sublattice (n) by

$$s^x_\mathrm{n} = t^x_\mathrm{n}, \quad s^y_\mathrm{n} = -t^y_\mathrm{n}, \quad s^z_\mathrm{n} = -t^z_\mathrm{n}. \tag{13.15}$$

As a start, we recall the commutation relations (13.16):

$$[s^+_j, s^-_{j'}] = 2s^z_j\delta_{j,j'} \approx 2\langle S\rangle\delta_{j,j'}, \tag{13.16}$$

$$[s^z_j, s^\pm_{j'}] = \pm s^\pm_j\delta_{j,j'}, \tag{13.17}$$

$$[s^x_j, s^y_{j'}] = is^z_j\delta_{j,j'} \text{ and cyclic permutations.} \tag{13.18}$$

where $\langle S\rangle$ is here the ordered moment of the sublattice. This important approximation is of course valid only when the Neél state is a good approximation of the actual state of the system.

We now calculate the equations of motion, keeping only terms linear in the

operators:

$$\begin{aligned} i\hbar\frac{d}{dt}s^+_{\mathbf{m}} &= \left[s^+_{\mathbf{m}}, \hat{H}\right] \\ &\overset{\text{(1st order)}}{=} S\sum_{\mathbf{r}} J(\mathbf{r})(s^+_{\mathbf{m}} + t^-_{\mathbf{m}+\mathbf{r}}) \\ &\quad + S\sum_{\mathbf{R}} J_1(\mathbf{R})(-s^+_{\mathbf{m}} + s^+_{\mathbf{m}+\mathbf{R}}) + g\mu_{\mathrm{B}}(B + B_{\mathrm{A}})s^+_{\mathbf{m}}. \end{aligned} \tag{13.19}$$

$$\begin{aligned} i\hbar\frac{d}{dt}t^+_{\mathbf{m}} &= \left[t^-_{\mathbf{m}}, \hat{H}\right] \\ &\overset{\text{(1st order)}}{=} -2\sum_{\mathbf{r}} J(\mathbf{r})(t^-_{\mathbf{m}} + s^+_{\mathbf{m}+\mathbf{r}}) \\ &\quad - S\sum_{\mathbf{R}} J_1(\mathbf{R})(-t^-_{\mathbf{m}} + t^-_{\mathbf{m}+\mathbf{R}}) + g\mu_{\mathrm{B}}(B - B_{\mathrm{A}})t^-_{\mathbf{m}}. \end{aligned} \tag{13.20}$$

This calculation differs from that of the ferromagnet, section 13.1.1, by the complication that the equations of motion for the s^+ operators involve the t^- operators. Also the t^+ operators and the s^- operators are mixed. Below, we show how to deal with this problem.

* Fourier and Boguliobov transformations

We now solve the two coupled equations of motion, describing the spins in the two sublattices. First, Fourier transformation gives

$$\begin{aligned} i\hbar\frac{d}{dt}S^+_{\mathbf{q}'} &= \left[S(J(0) - J_1(0) + J_1(\mathbf{q}')) + g\mu_{\mathrm{B}}(B + B_{\mathrm{A}})\right] S^+_{\mathbf{q}'} \\ &\quad + SJ(\mathbf{q}')T^-_{\mathbf{q}'}, \end{aligned} \tag{13.21}$$

$$\begin{aligned} i\hbar\frac{d}{dt}T^-_{\mathbf{q}'} &= \left[S(-J(0) + J_1(0) - J_1(\mathbf{q}')) + g\mu_{\mathrm{B}}(B - B_{\mathrm{A}})\right] T^-_{\mathbf{q}'} \\ &\quad - SJ(\mathbf{q}')S^+_{\mathbf{q}'}. \end{aligned} \tag{13.22}$$

Second, we perform a *Boguliobov transformation*, which is a linear transformation of two operators:

$$S^+_{\mathbf{q}'} = u_{\mathbf{q}'}\hat{\alpha}_{\mathbf{q}'} + v_{\mathbf{q}'}\hat{\beta}^\dagger_{\mathbf{q}'}, \tag{13.23}$$

$$T^-_{\mathbf{q}'} = u_{\mathbf{q}'}\hat{\beta}^\dagger_{\mathbf{q}'} + v_{\mathbf{q}'}\hat{\alpha}_{\mathbf{q}'}. \tag{13.24}$$

The idea is that by a correct choice of the real coefficients $u_{\mathbf{q}'}$ and $v_{\mathbf{q}'}$, the new Boson operators, $\hat{\alpha}_{\mathbf{q}'}$ and $\hat{\beta}_{\mathbf{q}'}$ will perform independent oscillations. To determine the coefficients $u_{\mathbf{q}'}$ and $v_{\mathbf{q}'}$, we seek a number of boundary conditions. Firstly, Boson operators must fulfill the commutation relations:

$$[\hat{\alpha}^\dagger_{\mathbf{q}}, \hat{\alpha}_{\mathbf{q}'}] = \delta_{\mathbf{q},\mathbf{q}'}, \quad [\hat{\beta}^\dagger_{\mathbf{q}}, \hat{\beta}_{\mathbf{q}'}] = \delta_{\mathbf{q},\mathbf{q}'}. \tag{13.25}$$

Secondly, the "old" spin commutator relations must still be valid:

$$[s^+_{\mathbf{m}}, s^-_{\mathbf{m}'}] = 2s^z_{\mathbf{m}}\delta_{\mathbf{m},\mathbf{m}'}, \quad [t^+_{\mathbf{n}}, t^-_{\mathbf{n}-}] = 2t^z_{\mathbf{n}}\delta_{\mathbf{n},\mathbf{n}'}. \tag{13.26}$$

The resulting calculations are straightforward but tedious, and we will not list them here. We will proceed directly to the result for the energies.

* The spin wave energy

The antiferromagnetic spin waves have two branches, and their energies are

$$\hbar\omega_0(\mathbf{q}') = +g\mu_\mathrm{B}B + \Omega(\mathbf{q}'), \tag{13.27}$$
$$\hbar\omega_1(\mathbf{q}') = -g\mu_\mathrm{B}B + \Omega(\mathbf{q}'), \tag{13.28}$$

where the zero field spin wave energy is

$$\Omega(\mathbf{q}') = \sqrt{\left[SJ(\mathbf{0}) - S\left(J_1(\mathbf{0}) - J_1(\mathbf{q}')\right) + g\mu_\mathrm{B}B_\mathrm{A}\right]^2 - S^2J(\mathbf{q}')^2}. \tag{13.29}$$

The coefficients for the Boguliobov transformation can be written as

$$u^2_{\mathbf{q}'} - v^2_{\mathbf{q}'} = 2S, \tag{13.30}$$
$$u^2_{\mathbf{q}'} = 2S\,\frac{\Omega(\mathbf{q}') + 2SJ(\mathbf{0}) - 2S[J_1(\mathbf{0}) - J_1(\mathbf{q}')] + g\mu_\mathrm{B}B_\mathrm{A}}{2\Omega(\mathbf{q}')}, \tag{13.31}$$

leading to a few helpful expressions we will need later to determine the scattering cross section:

$$u^2_{\mathbf{q}'} + v^2_{\mathbf{q}'} = 2S\,\frac{2SJ(\mathbf{0}) - 2S[J_1(\mathbf{0}) - J_1(\mathbf{q}')] + g\mu_\mathrm{B}B_\mathrm{A}}{\Omega(\mathbf{q}')}, \tag{13.32}$$
$$u_{\mathbf{q}'}v_{\mathbf{q}'} = \frac{-(2S)^2J(\mathbf{q}')}{2\Omega(\mathbf{q}')}. \tag{13.33}$$

Example. It is worth contemplating equation (13.27). Let us consider the simple case of nearest neighbour couplings only, $J_1(\mathbf{q}') = 0$, zero applied field, $B = 0$, and zero anisotropy, $B_\mathrm{A} = 0$. Then, the spin wave energy becomes

$$\hbar\omega_\mathrm{simple}(q') = S\sqrt{J(0)^2 - J(\mathbf{q}')^2}. \tag{13.34}$$

For small values of $|\mathbf{q}'|$, this can be approximated by a linear dispersion of the form $\hbar\omega = c|\mathbf{q}'|$, where c is called the *spin wave velocity*.

With a small anisotropy, the spin wave energy becomes

$$\hbar\omega_\mathrm{simple,anis}(q') = S\sqrt{(J(0) + g\mu_\mathrm{B}B_\mathrm{A}/(2S))^2 - J(\mathbf{q}')^2}, \tag{13.35}$$

with a gap at $q' = 0$, as illustrated in figure 13.2.

13.1.3 * Quantum magnetism

Solving the Hamiltonian (12.4) quantum mechanically is an easy task for a ferromagnet. Let us first rewrite the spin product term:

$$\mathbf{S}_i \cdot \mathbf{S}_j = s_i^z s_j^z + \frac{1}{2}(s_i^+ s_j^- + s_i^- s_j^+), \tag{13.36}$$

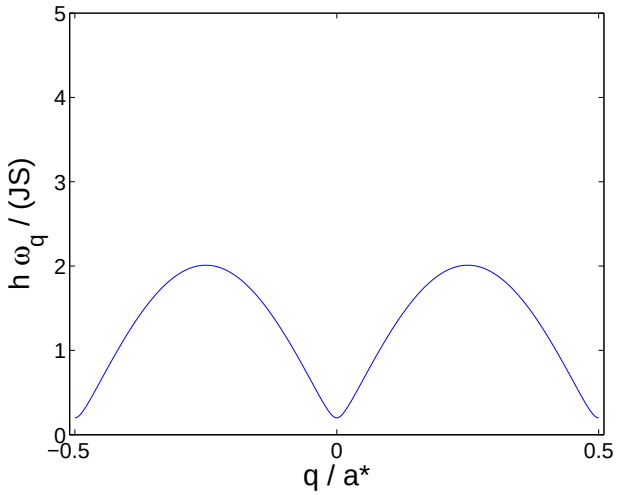

Figure 13.2: Dispersion relation for spin waves in a 1D nearest neighbour AFM in zero applied field. The anisotropy is given by $g\mu_B B_A = 10^{-2} \times 4SJ$, as defined in Eq. (13.29).

where the spin raising and lowering operators are defined as

$$s_j^+ = s_j^x + is_j^y, \tag{13.37}$$

$$s_j^- = s_j^x - is_j^y. \tag{13.38}$$

The raising/lowering operators have the effect of changing m, the eigenvalue of s^z for one spin, by one unit:

$$s_j^+|S,m\rangle_j = \sqrt{(S-m)(S+m+1)}|m+1\rangle_j, \tag{13.39}$$

$$s_j^-|S,m\rangle_j = \sqrt{(S-m+1)(S+m)}|m-1\rangle_j. \tag{13.40}$$

We can see that when using the Hamiltonian (12.4) on the ferromagnetic state, $|\mathrm{FM}\rangle = |\uparrow\uparrow\uparrow\uparrow\rangle$, all spin terms containing s^+ vanish, leaving only the diagonal $s_i^z s_j^z$ terms.

$$H|\mathrm{FM}\rangle = -\sum_{\langle ij\rangle} J_{ij} S^2 |\mathrm{FM}\rangle. \tag{13.41}$$

The ferromagnetic state is thus an eigenstate of the Hamiltonian, and is also the ground state. However, for antiferromagnetic couplings, (12.4) is a very difficult many-body problem. This can be seen from just considering the two-spin model for spins $S = 1/2$. Here, the classical ground states are $|\mathrm{AFM}_1\rangle = |\uparrow\downarrow\rangle$ and $|\mathrm{AFM}_2\rangle = |\downarrow\uparrow\rangle$. None of these states are eigenstates to (12.4), since terms in the Hamiltonian of the type $s_1^+ s_2^-$ mix the states:

$$H|\mathrm{AFM}_1\rangle = -\frac{J}{4}|\mathrm{AFM}_1\rangle + \frac{J}{2}|\mathrm{AFM}_2\rangle, \tag{13.42}$$

$$H|\mathrm{AFM}_2\rangle = +\frac{J}{2}|\mathrm{AFM}_1\rangle - \frac{J}{4}|\mathrm{AFM}_2\rangle. \tag{13.43}$$

The resulting ground state is a *spin singlet*:

$$|\mathrm{GS}\rangle = \frac{1}{\sqrt{2}}\left(|\mathrm{AFM}_1\rangle - |\mathrm{AFM}_2\rangle\right), \tag{13.44}$$

with a ground state energy of $-3J/4$, three times lower than (the expectation value of) the energy of the classical solution.

The antiferromagnetic quantum Heisenberg model for macroscopic systems has only been solved in a few simple one-dimensional cases, and only for spin values $S = 1/2$ and $S = 1$. The main conclusion is that there is no magnetic order in the classical sense, and that the ground state is a many-body quantum singlet state with short-range order. Three-dimensional systems are generally well described by a classical state with few modifications, whereas two-dimensional systems may show intermeditate (and highly interesting) behaviour, where the ground state could be described by a mixture of classical long-range order and quantum short-range order.

Magnetic quantum effects are revealed by the strength of the magnetic order, which is often smaller than expected classically (or completely absent). However, the fingerprint of quantum magnetism is found by inelastic magnetic neutron scattering.

Perspectives. Interest in magnetic quantum systems comes from the study of basic many-body quantum mechanics, entanglement of quantum systems with possible applications in quantum computing, in the study of zero-temperature "quantum phase transitions", as models for the string theory description of elementary particles, and as a basis for the study of correlated electron materials like the "heavy-fermion" systems and the high-temperature superconductors.

13.2 * Neutron cross section from ferromagnetic spin waves

For calculating the neutron scattering cross section for ferromagnetic spin waves, we begin with the master equation (11.31) and use the description of spin waves above.

We describe the spin-spin correlation functions in terms of the "coordinates" $+, -$ and z. The sum of the z-component of the spins, $S^z = \sum_j s_j^z$, commutes with $\hat{H}$, making this sum a constant of motion. Hence, the number of $+$ and $-$ operators must be the same for the correlation function to have a non-zero value. It is then easy to see that spin correlation functions of the types $\langle s^+(0)s^+(t)\rangle$ and $\langle s^+(0)s^z(t)\rangle$ vanish, leaving only three non-zero terms: $\langle s^z(0)s^z(t)\rangle$, $\langle s^+(0)s^-(t)\rangle$, and $\langle s^-(0)s^+(t)\rangle$. Since S^z is a constant of motion, we have $s_j^z(t) = s_j^z(0)$, and hence the zz term gives rise to elastic scattering only.

The spin wave cross section comes from the term

$$\begin{aligned}\langle s_j^-(0)s_{j'}^+(t)\rangle &= \frac{1}{N}\sum_{\mathbf{q}'}\exp(i\mathbf{q}'\cdot(\mathbf{r}_{j'}-\mathbf{r}_j))\langle S_{\mathbf{q}'}^-(0)S_{\mathbf{q}'}^+(t)\rangle \\ &= \frac{1}{N}\sum_{\mathbf{q}'}\exp(i\mathbf{q}'\cdot(\mathbf{r}_{j'}-\mathbf{r}_j))\exp(-i\omega_{\mathbf{q}'}t)\left\langle S_{\mathbf{q}'}^-(0)S_{\mathbf{q}'}^+(0)\right\rangle \\ &= \frac{2\langle S^z\rangle}{N}\sum_{\mathbf{q}'}\exp(i\mathbf{q}'\cdot(\mathbf{r}_{j'}-\mathbf{r}_j))\exp(-i\omega_{\mathbf{q}'}t)n_{\mathrm{B}}\left(\frac{\hbar\omega_{\mathbf{q}'}}{k_{\mathrm{B}}T}\right).\end{aligned} \tag{13.45}$$

In the second step of this calculation, we have used that the operator $S_{\mathbf{q}'}^-(0)S_{\mathbf{q}'}^+(0)$ is related to the number operator, so that its thermal average value is $\langle S_{\mathbf{q}'}^-S_{\mathbf{q}'}^+\rangle = 2\langle S^z\rangle n_{\mathrm{B}}(\hbar\omega_{\mathbf{q}'}/k_{\mathrm{B}}T)$, where the thermal population factor for Bosons, n_{B}, is given by (10.17).

Since $[S_{\mathbf{q}'}^+, S_{\mathbf{q}'}^-] = 2S^z$, we immediately find the value of the thermal average of the last operator pair.

$$\begin{aligned}\langle s_j^+(0)s_{j'}^-(t)\rangle &= \frac{1}{N}\sum_{\mathbf{q}'}\exp(-i\mathbf{q}'\cdot(\mathbf{r}_{j'}-\mathbf{r}_j))\langle S_{\mathbf{q}'}^-(0)S_{\mathbf{q}'}^+(t)+2S^z\rangle \\ &= \frac{2\langle S^z\rangle}{N}\sum_{\mathbf{q}'}\exp(-i\mathbf{q}'\cdot(\mathbf{r}_{j'}-\mathbf{r}_j))\exp(i\omega_{\mathbf{q}'}t)\left(n_{\mathrm{B}}\left(\frac{\hbar\omega_{\mathbf{q}'}}{k_{\mathrm{B}}T}\right)+1\right).\end{aligned} \tag{13.46}$$

To transform back to the x and y operators, we note that the x and y axes are equivalent, whence $\langle s_j^x(0)s_{j'}^x(t)\rangle = \langle s_j^y(0)s_{j'}^y(t)\rangle$. Moreover, the sum of the two mixed terms $\langle s_j^x(0)s_{j'}^y(t) + s_j^y(0)s_{j'}^x(t)\rangle$ is zero. We calculate directly

$$\langle s_j^x(0)s_{j'}^x(t)\rangle = \frac{1}{4}\langle s_j^+(0)s_{j'}^-(t) + s_j^-(0)s_{j'}^+(t)\rangle. \tag{13.47}$$

This allows us to calculate the coordinate sum entering the cross section expression:

$$\begin{aligned}\sum_{\alpha\beta}(\delta_{\alpha\beta}-\hat{q}_\alpha\hat{q}_\beta)\,\langle s_j^\alpha(0)s_{j'}^\beta(t)\rangle &= (2-\hat{q}_x^2-\hat{q}_y^2)\langle s_j^x(0)s_{j'}^x(t)\rangle \\ &= \frac{1}{4}(1+\hat{q}_z^2)\langle s_j^+(0)s_{j'}^-(t)+s_j^-(0)s_{j'}^+(t)\rangle.\end{aligned} \tag{13.48}$$

Inserting into (11.31), the expression for the inelastic neutron scattering cross section for a ferromagnet reads:

$$\begin{aligned}\left(\frac{d^2\sigma}{d\Omega dE_{\mathrm{f}}}\right)_{\mathrm{magn.}} &= (\gamma r_0)^2\,\frac{k_{\mathrm{f}}}{k_{\mathrm{i}}}\left[\frac{g}{2}F(q)\right]^2\exp(-2W)\left(1+\hat{q}_z^2\right)\frac{\langle S^z\rangle}{2} \\ &\quad\times\frac{(2\pi)^3}{v_0}\sum_{\mathbf{q},\boldsymbol{\tau}}\Bigg[\left(n_{\mathrm{B}}\left(\frac{\hbar\omega_{\mathbf{q}}}{k_{\mathrm{B}}T}\right)+1\right)\delta\left(\hbar\omega_{\mathbf{q}'}-\hbar\omega\right)\delta\left(\mathbf{q}'-\mathbf{q}-\boldsymbol{\tau}\right) \\ &\qquad + n_{\mathrm{B}}\left(\frac{\hbar\omega_{\mathbf{q}'}}{k_{\mathrm{B}}T}\right)\delta\left(\hbar\omega_{\mathbf{q}'}+\hbar\omega\right)\delta\left(\mathbf{q}'+\mathbf{q}-\boldsymbol{\tau}\right)\Bigg],\end{aligned} \tag{13.49}$$

where $\boldsymbol{\tau}$ is a reciprocal lattice vector and v_0 is the volume of the unit cell. We can see that the cross section depends upon energy and temperature only through the thermal population factor, n_{B}, and the ordered moment, $\langle S^z \rangle$. At low temperatures, compared to the spin wave energy, the spin wave spectral weight is constant, apart from the slow variation with q of the magnetic structure factor, $F(q)$, and the Debye-Waller factor, $\exp(-2W)$. Notice that the spin wave intensity is highest when $\mathbf{q}$ is in the direction of the ordered moment. This can be understood by the spin wave being a purely transverse excitation.

13.3 * Neutron cross section of antiferromagnetic spin waves

For the calculation of the neutron scattering cross section for antiferromagnetic spin waves, we again invoke the master equation (11.31) and use the solutions for the antiferromagnetic spin waves above.

Firstly, we calculate the correlation functions. As for the ferromagnetic spin waves, the zz term is elastic and other terms involving z vanish. also the $++$ and $--$ terms vanish. Hence, we need only to calculate

$$\left\langle S^-_{\mathbf{q}'} S^+_{\mathbf{q}'} \right\rangle = \left\langle (u_{\mathbf{q}'} \hat{\alpha}^+_{\mathbf{q}'} + v_{\mathbf{q}'} \hat{\beta}_{\mathbf{q}'})(u_{\mathbf{q}'} \hat{\alpha}_{\mathbf{q}'} + v_{\mathbf{q}'} \beta^+_{\mathbf{q}'}) \right\rangle \tag{13.50}$$

$$= u^2_{\mathbf{q}'} n_{\mathrm{B}}(\hbar\omega_{\mathbf{q}'}/k_{\mathrm{B}}T) + v^2_{\mathbf{q}'}(n_{\mathrm{B}}(\hbar\omega_{\mathbf{q}'}/k_{\mathrm{B}}T) + 1). \tag{13.51}$$

Transforming to real space and (x, y, z) coordinates, the final expression reads:

$$\begin{aligned}\left(\frac{d^2\sigma}{d\Omega dE_{\mathrm{f}}}\right)_{\mathrm{magn.}} &= (\gamma r_0)^2 \frac{k_{\mathrm{f}}}{k_{\mathrm{i}}} \left[\frac{g}{2} F(q)\right]^2 \exp(-2W) \left(1 + \hat{q}_z^2\right) \frac{1}{4} \frac{(2\pi)^3}{v_0} \\ &\times \sum_{\mathbf{q}', \boldsymbol{\tau}, a} \Bigg[\left(n_{\mathrm{B}} \left(\frac{\hbar\omega_{a,\mathbf{q}'}}{k_{\mathrm{B}}T} \right) + 1 \right) \delta\left(\hbar\omega_{\mathbf{q}'} - \hbar\omega\right) \delta\left(\mathbf{q}' - \mathbf{q} - \boldsymbol{\tau}\right) \\ &\qquad + n_{\mathrm{B}} \left(\frac{\hbar\omega_{a,\mathbf{q}'}}{k_{\mathrm{B}}T} \right) \delta\left(\hbar\omega_{\mathbf{q}'} + \hbar\omega\right) \delta\left(\mathbf{q}' + \mathbf{q} - \boldsymbol{\tau}\right) \Bigg] \\ &\times \left[u^2_{\mathbf{q}'} + v^2_{\mathbf{q}'} + 2 u_{\mathbf{q}'} v_{\mathbf{q}'} \cos(\boldsymbol{\rho} \cdot \boldsymbol{\tau}) \right],\end{aligned} \tag{13.52}$$

where $\boldsymbol{\tau}$ is a reciprocal lattice vector of a sublattice, $\boldsymbol{\rho}$ is a vector joining the sublattices, and a is the sublattice index. The difference between this cross section and the one for ferromagnetic spin waves is the presence of the *coherence factor*, $u^2_{\mathbf{q}'} + v^2_{\mathbf{q}'} + 2u_{\mathbf{q}'} v_{\mathbf{q}'} \cos(\boldsymbol{\rho} \cdot \boldsymbol{\tau})$. It should be noted that the term $\cos(\boldsymbol{\rho} \cdot \boldsymbol{\tau})$ assumes a value of unity for $\boldsymbol{\tau}$ being a nuclear peak and -1 for $\boldsymbol{\tau}$ being an AFM peak.

We now proceed to calculate the cross section in a few simple cases.

13.3.1 * The simple nearest neighbour antiferromagnet

In some lattice types, like the bcc lattice, all nearest neighbours are ions from the opposite sublattice. Hence, for a nearest neighbour system, $J_1(\mathbf{q}) = 0$. We

assume absence of anisotropy, $\mathbf{B}_\mathrm{A} = 0$. Hence, the expressions for the spin wave dispersion (13.29) and (13.32), simplify to

$$\Omega_\mathbf{q} = 2S\sqrt{J(\mathbf{0})^2 - J(\mathbf{q})^2}, \tag{13.53}$$

$$u_\mathbf{q}^2 + v_\mathbf{q}^2 = \frac{(2S)^2 J(\mathbf{0})}{\Omega_\mathbf{q}}, \tag{13.54}$$

$$2u_\mathbf{q}v_\mathbf{q} = \frac{-(2S)^2 J(\mathbf{q})}{\Omega_\mathbf{q}}. \tag{13.55}$$

For scattering close to an AFM peak ($\cos(\boldsymbol{\rho}\cdot\boldsymbol{\tau}) \approx -1$), the coherence factor, which essentially determines the strength of the scattering cross section (13.52), can be written as

$$\left[u_\mathbf{q}^2 + v_\mathbf{q}^2 + 2u_\mathbf{q}v_\mathbf{q}\cos(\boldsymbol{\rho}\cdot\boldsymbol{\tau})\right] = 2S\sqrt{\frac{J(\mathbf{0}) + J(\mathbf{q})}{J(\mathbf{0}) - J(\mathbf{q})}}, \tag{13.56}$$

which diverges as $1/\Omega_\mathbf{q}$ for low values of $|\mathbf{q}|$. Close to a nuclear Bragg peak ($\cos(\boldsymbol{\rho}\cdot\boldsymbol{\tau}) = 1$), the solution is the reciprocal of (13.56), having a value of zero for $|\mathbf{q}| = 0$. At the zone boundary, $J(\mathbf{q}) = 0$, and the coherence factor equals $2S$.

13.3.2 * Antiferromagnetic nanoparticles in zero field

In nanoparticles, the spin wave spectrum is quantized, since the boundary consitions makes the spin waves essentially standing waves within the particles. However, only the $\mathbf{q} = 0$ mode has ever been observed [86]. The energy of the lowest mode, the *collective magnetic precessions*, is then completely determined by the anisotropy:

$$\Omega_\mathbf{0} = g\mu_\mathrm{B}B_\mathrm{A}. \tag{13.57}$$

The coherence factors are found from

$$u_\mathbf{0}^2 + v_\mathbf{0}^2 = \frac{(2S)^2 J(\mathbf{0}) + g\mu_\mathrm{B}B_\mathrm{A}}{\Omega_\mathbf{0}}, \tag{13.58}$$

$$2u_\mathbf{0}v_\mathbf{0} = \frac{-(2S)^2 J(\mathbf{0})}{\Omega_\mathbf{0}}. \tag{13.59}$$

For $\boldsymbol{\tau}$ being an AFM Bragg peak, $\cos(\boldsymbol{\rho}\cdot\boldsymbol{\tau}) = -1$, the coherence factor is approximately

$$\left[u_\mathbf{0}^2 + v_\mathbf{0}^2 + 2u_\mathbf{0}v_\mathbf{0}\cos(\boldsymbol{\rho}\cdot\boldsymbol{\tau})\right] \approx 2S\frac{2J(\mathbf{0})}{g\mu_\mathrm{B}B_\mathrm{A}}, \tag{13.60}$$

which usually is a very large number, since the exchange interaction is much larger than the anisotropy. On the other hand, for $\boldsymbol{\tau}$ being a nuclear Bragg peak, $\cos(\boldsymbol{\rho}\cdot\boldsymbol{\tau}) = 1$, the coherence factor equals unity, much lower than for the AFM Bragg peak. This explains why collective magnetic excitations are not observed at the position of nuclear Bragg peaks.

Part VI

Ray-tracing simulation of neutron scattering

Chapter 14

Monte Carlo simulation of neutron instruments

Even in the simplest cases, it is not straightforward to calculate the optics of a neutron instrument. This is illustrated, *e.g.*, by considering multiple bounces in a neutron guide system, see problem 4.10.1. An accurate calculation of the properties of a realistic neutron instrument becomes almost hopeless, and various other schemes must be applied.

One approach beyond back-of-the-envelope estimates is the approximate, analytical calculations, made for determining the instrument resolution, which was performed around 1970 by Cooper and Nathans [87] and Popovici [88]. Calculations of this type have been extremely useful for many types of neutron instruments over the past decades, in particular triple-axis spectrometers, which are mostly used for elastic and inelastic measurements on single crystals, with high q-resolution. The triple-axis spectrometer was presented in section 4.7.

The alternative way to describe neutron instruments, which we here will present, is to perform computer simulations of neutron trajectories. This can give essentially correct descriptions of neutron instrument models. The results are, however, subject to statistical sampling errors, always present in computer simulations (as in real experiments).

The present chapter gives an introduction to Monte Carlo simulations and to existing Monte Carlo ray-tracing packages for neutron scattering.

14.1 Introduction to the Monte Carlo technique

Monte Carlo simulations are in general a way to perform approximate solutions to complex problems by use of random sampling. The phrase "Monte Carlo" comes from the generous use of random numbers, which resembles the gambling of the famous Monaco casino. The method was, in fact, originally designed to facilitate calculations of neutron physics - more precisely for the Manhattan

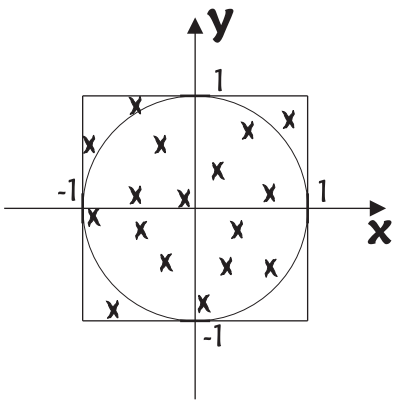

Figure 14.1: A simple example of Monte Carlo simulations. Random points are chosen within the 2×2 square, and the area of the enclosed figure (the unit circle) is estimated from the fraction of points that lie inside the figure. See also the discussion in the text.

project. For the history of the Monte Carlo technique, we refer to an excellent essay by one of its inventors [89].

14.1.1 A simple example of Monte Carlo simulations

As an introduction, we consider a simple example. We intend to estimate the area of an object. For simplicity let us consider the unit circle, $x^2 + y^2 \leq 1$, as shown in Fig. 14.1. We now select N points randomly in the square that contains the circle fully, with area $A_\mathrm{s} = 4$. The points (x, y) inside the square are defined by

$$-1 \leq x \leq 1 \ \wedge \ -1 \leq y \leq 1. \tag{14.1}$$

We now select a number of points, N, inside the square by retrieving independent, random values of x and y from a (pseudo-) random number generator. We will not here dwell on the issue of random number generation, which is described elsewhere [90], we only mention that such generators exist with specifications useful for our purpose.

We now count the number of points, N_i, that fall inside the unit circle. For large N, the fraction of accepted points will according to the law of large numbers approach the ratio of the areas:

$$\frac{N_i}{N} \rightarrow \frac{A_\mathrm{c}}{A_\mathrm{s}}. \tag{14.2}$$

Hence, this "numerical experiment" can be used to estimate the value of the circle area, A_c. Of course, the answer to this simple problem is well known: $A_\mathrm{c}/A_\mathrm{s} = \pi/4$.

14.1.2 On Monte Carlo methods

Monte Carlo techniques can be used to solve problems much more complex than the example above. This may involve multiple dimensions, complex figures, and/or a number of branches (choices between different possibilities). Here, analytical solutions are often close to impossible, making the Monte Carlo method show its full virtue.

In general, Monte Carlo techniques can be used for problems in different fields:

- In Physics, the method can describe a number of many-body problems. *E.g.* in high-energy physics where each particle under consideration can be either absorbed, scattered, or converted into other particles.

- In Mathematics, the method can be used to solve complex integrals in many dimensions with complex boundary conditions.

- In Finance Theory, the method is used to estimate the effect of uncertainties in market values.

- In Computer Science, the method has been used to optimize multi-variable functions.

14.1.3 Methods for variance reduction

As with all stochastical methods (including experiments), Monte Carlo methods are prone to statistical errors or *variances*. To reduce the statistical errors of simulations, a number of *variance reduction* methods have been designed. We here mention

- **Stratified sampling.** To ensure that the sampling is spread evenly, one would divide the parameter space up into mutually exclusive strata, and sample a given amount of each strata. In the circle example above, one could divide the area up into smaller squares and sample equally often from each.

- **Importance sampling.** When it can be shown that sampling from some places in parameter space is more crucial to the final result than others, one can choose to sample more often in the important regions. If the problem was *e.g.* to calculate the average height over sea level of a landscape, one would measure the mountain more careful than the lake, *i.e.* the Monte Carlo sampling would be denser at the mountain. In the stratified version of the circle example, one would sample more often in areas that contain a part of the circle rim, while completely filled or empty areas need little sampling.

Package	Origin	Start	Platform	Home page
NISP	Los Alamos Nat. Lab. (US)	1970'ies	Windows	[93]
IDEAS	Oak Ridge Nat. Lab. (US)	2000	Windows	[94]
McStas	Risø (DK) and ILL (F)	1999	Unix, Windows, Mac	[95]
VITESS	Helmholtz Center Berlin (D)	1999	Unix and Windows	[96]
RESTRAX	Nuclear Physics Institute, Rez (CZ)	1996	Unix and Windows	[97]

Table 14.1: Actively developed simulation packages for thermal/cold neutrons, as of September 2012. It is uncertain if IDEAS will still be maintained in the future.

14.1.4 Monte Carlo Ray-tracing

We will not explain the general Monte Carlo technique in further detail, this information can be found in a number of textbooks, *e.g.* [91]. Rather, we specialize immediately to the method relevant for our purpose. This is known as *Monte Carlo ray-tracing* and can be performed to study objects which travel along a path (*a ray*), and can be (partially) absorbed or scattered into another direction, but not converted into other types of radiation. The most known example of this is visible light, and this type of ray-tracing is frequently used to generate realistic illumination in 3D computer graphics.

In a scientific environment, ray-tracing can be used to study non-interacting radiation, *e.g.* neutrons or X-rays. We will now dive into the description of ray-tracing simulations for this purpose.

14.2 Monte Carlo ray-tracing packages for neutrons

In the early 1990'ies, simulation of the optics in a neutron instrument was performed mostly by monolithic Monte Carlo codes. Although being marvelous pieces of work, these codes were mostly written as one-person projects with limited manpower resources. Hence, the codes were designed to solve only one particular problem. They were thus subject to lack of generality, possible programming mistakes, low documentation level, and limited user-friendliness. (One notable exception from this is the package NISP.)

Today, a fair number of well-tested and documented general freeware packages exists for neutron ray-tracing simulations. Each package has the aim of enabling neutron scientists and students to quickly set up simulations. The development projects of the package co-exist in an atmosphere of collaboration and friendly competition for users. The collaboration between the three European packages were 2004-2012 supported by a European Union research project, MCNSI [92]. The 5 currently maintained packages are listed in table 14.1.

The main author of these notes is also a co-author of the McStas package. However, we have kept the text part of these notes free from reference to any particular package, to the extent possible. The hands-on problems on simulations found in chapter 15 are related directly to the McStas package, but could with little effort be "converted" into covering any other simulation package.

14.2.1 Describing the neutron optical components

In the simulation packages, the individual optical *components* (or *modules*), like source, guide, sample, and detector, are parametrized and pre-programmed. Each package contains a library of well-tested components that cover the most often used optical ones, as well as some model samples. It is, however, possible for the user to program additional components when needed. Some of these components may later find their way into the corresponding library, which is thus strengthened by user contributions.

Some of the components contain a full quantum mechanical treatment of the neutron as a wave on the microscopic length scales to compute the correct physics of the component, *e.g.* diffraction from a crystal. However, it should be emphasized that quantum mechanics is only present in the simulations at this level of description. The transport of rays between components is performed by classical kinematics, possibly including gravity.

14.2.2 Describing and visualizing the neutron instrument

It is the task of the user (*the simulator*) to assemble the components into a full working instrument. The Monte Carlo simulation itself is then performed by the simulation package on the basis of the instrument description.

All packages have features to visualize the instrument geometry, the simulated rays, and the monitor/detector data.

14.2.3 Varying and optimizing the instrument parameters

The packages all facilitate the performance of a series of simulations, where one or more instrument parameters are systematically varied. In this way, it is possible to perform a scan of one or more instrument parameters and plot some key data, *e.g.* the neutron counts in a monitor, as a function of the scanned parameter(s). The packages can automatically produce such plots.

In addition, some packages are able to vary a number of instrument parameters to perform optimization of the instrument settings. Many numerical optimization methods exist, and we will not here go into details.

General about the optimizations is, however, that the user should define a certain *Figure of Merit* (FoM) for the optimizer to maximize. This could be the number of neutrons at the sample, the reciprocal of the beam spot size (if a narrow beam is wanted), the reciprocal width of the neutron energy distribution (if a monochromatic beam is desired), or any combination of these. The optimal parameter settings depend upon the choice of the FoM, and hence a careful selection is necessary.

14.2.4 Virtual experiments

Using a detailed instrument description with a realistic sample component, it is possible to produce a computer model of a complete neutron scattering experiment. This virtual instrument can then be controlled with software that

resembles the actual instrument control program, and the simulation data can be analyzed with the same tools as used for real experimental data. This is known as a *virtual experiment*. It is foreseen by many scientists in the field that virtual experiments can be used to support and complement experimental activities in a number of ways [11]:

- In the design phase of an instrument it can be investigated how the instrument will perform certain key experiments. This can in turn be used to optimize the instrument design [98].
- When applying for beam time at a facility, the experimentalists can estimate whether the experiment will be feasible at a given instrument and how much beam time is needed.
- Experiments (and experimentalists) can be prepared prior to performing the actual experiment by analyzing the optimal instrument configuration [99].
- Running experiments can be diagnosed "on the fly" to faster react on various mistakes and unexpected results.
- Analysis of the data can be conducted in more detail by including instrument-related features in the data analysis [100].
- New data analysis programs can be benchmarked against virtual data from known samples [101].
- Students and new users can be trained before their first actual experiment. This is, in fact, the general idea behind the simulation problems in these notes.

14.2.5 Parallel ray-tracing simulations

Since the (neutron) rays in the simulations are non-interacting and in principle statistically independent, the simulations can without methodological problems be carried out in parallel on several computers. Many packages are equipped to parallize the simulations automatically, and the performance has been seen to scale linearly with the number of processors up to at least 1000.

Hence, the technique of neutron ray-tracing simulations can take full advantage of the large parallel supercomputers emerging in many research facilities and universities.

14.3 Techniques for neutron ray-tracing

The neutron ray-tracing packages have a common philosophy in the way simulations are described and performed, and in the way the neutrons are represented. We here describe this in some detail.

14.3.1 Representing the neutrons in simulations

In simulations, a neutron is represented semiclasically by simultaneously well-defined position, $\mathbf{r}$, velocity, $\mathbf{v}$, time, t, and all three components of the neutron spin vector, $\mathbf{s}$. Formally, this violates the laws of quantum mechanics, in particular the Heisenberg uncertainty relations [17], given for the conjugate position/momentum variables by

$$\delta x \delta p \geq \frac{\hbar}{2}, \tag{14.3}$$

and similar for the conjugate variables energy,time. However, as we shall illustrate in problem 14.4.1, the semiclassical approximation is very good for describing instruments that use "typical" neutrons with velocities of the order $100-10000$ m/s. The validity of the semiclassical approach is discussed in detail in Ref. [102].

One important region where the semiclassical approximations breaks down is for very slow (or "ultra-cold") neutrons, where quantum effects become prominent in the optical properties [103, 104, 105, 106]. Ultra-cold neutrons will not be discussed in this version of the notes.

The neutrons are simulated in "rays", by which we mean the neutron trajectory; position as a function of time, $\mathbf{r}(\mathrm{t})$. Therefore, at any point in the simulation of one ray, t is a necessary parameter. This is of particular importance when simulating pulsed neutron sources.

14.3.2 The neutron weight factor

To represent realistic values for neutron numbers, a neutron ray in general represents more than a single physical neutron. As a consequence, the ray contains an additional parameter, the *weight factor*, p. This generally has the unit of neutrons per second. When the ray begins at the source, p has a typical initial value of thousands to millions of neutrons per second.

To improve simulation speed, the weight factor can be manipulated through the simulation. For example, when some physical neutrons are "lost" due to *e.g.* finite reflectivity or absorption, the simulated ray will in general continue in the simulations, while p is adjusted to reflect the correct average physical behaviour. When (if) the neutron ray reaches the detector, p may be only a fraction of a neutron per second. This weight factor adjustment is a very efficient implementation of importance sampling, as presented in section 14.1.

To quantify the method, we consider a surface perpendicular to the beam in the simulated instrument. Here, the neutron intensity is given by the sum of all rays reaching this surface, again with units neutrons per second:

$$I_j = \sum_{i=1}^{N} p_{i,j-1} \tag{14.4}$$

where i is the ray index, N is the total number of rays, and j is the index of the given component. The index $j-1$ on p indicate that we consider the intensity

being emitted by the previous component. If the ray does not reach this point, we take $p_{i,j-1} = 0$. The weight of the neutrons emitted from this point in the simulations, *i.e.* after interacting with component j, is expressed by

$$p_j = w_j p_{j-1}, \tag{14.5}$$

where the ray index, i, is omitted for simplicity. The *weight multiplier* of the j'th component, w_j, is calculated by the probability rule

$$\boxed{f_{\mathrm{MC,b}} w_j = P_{\mathrm{b}}}, \tag{14.6}$$

where P_{b} is the physical probability for the event "b", and $f_{\mathrm{MC,b}}$ is the probability that the Monte Carlo simulation selects this event.

Often, there is only one allowed event, giving $f_{\mathrm{MC}} = 1$, whence $w_j = P$. This may, *e.g.*, be the case for neutrons being attenuated when passing through absorbing materials. When a Monte Carlo branch point is reached (selection between several events), we have $f_{\mathrm{MC,b}} < 1$ for each branch, b. However, since f_{MC} is a probability function, we must have

$$\sum_b f_{\mathrm{MC,b}} = 1. \tag{14.7}$$

14.3.3 Estimates of simulation uncertainty

In a stochastical simulation, it is important to be able to estimate the uncertainty, in the same way as for experiments. We here present a simple derivation of the uncertainty in simulations with weight factors.

As a simple start, let us imagine M rays, all with weight factor p. Each ray is imagined to have an overall probability, P_{d}, of reaching the detector. The distribution of observed rays will be binominally distributed with a mean value $\bar{N} = MP_{\mathrm{d}}$ and variance $\sigma^2(N) = MP_{\mathrm{d}}(1-P_{\mathrm{d}})$. Very often, we will have $P_{\mathrm{d}} \ll 1$ and large values of M, so that $MP_{\mathrm{d}} \gg 1$. In this case, the distribution will be approximately Gaussian with a standard deviation

$$\sigma(N) = \sqrt{MP_{\mathrm{d}}} = \sqrt{N}, \tag{14.8}$$

where the observed value, N, is used as the best estimate for the true average, $\bar{N}$. Recalling that the rays have weight factors, the total simulated intensity becomes

$$I = Np, \tag{14.9}$$

with a variance

$$\sigma^2(I) = Np^2. \tag{14.10}$$

We now allow the rays to have (discrete) different weight factors, p_i. The simulated number of rays in each class is denoted n_i (standard deviation $\sqrt{n_i}$). The total simulated result is now

$$I = \sum_i n_i p_i. \tag{14.11}$$

Using that the variance of a sum is the sum of its variances, we reach the statistical variance of the simulated result:

$$\sigma^2(I) = \sum_i n_i p_i^2. \tag{14.12}$$

Now, let the simulations occur with rays of arbitrary weight factors, p_j, different for each ray, *i.e.* $n_i \equiv 1$, corresponding to a continuous distribution of p_i. If the distribution of these weight factors is reasonably well behaved, we can generalize the equations above to reach

$$\boxed{I = \sum_i p_i}, \tag{14.13}$$

with a variance:

$$\boxed{\sigma^2(I) = \sum_i p_i^2}, \tag{14.14}$$

which is consistent with (14.10) and (14.12). This is the way uncertainties of simulation results are calculated in all detectors (sometimes denoted monitors) in the McStas package.

14.3.4 Scattering from a sample

One of the places where most Monte Carlo choices are made is when the neutron ray interacts with a sample. First, it must be decided whether the ray scatters or not. If scattering takes place, the algorithm must select the point in the sample for the scattering event, the scattered direction, and (for inelastic scattering) the final energy. Finally, there is potentially an issue of multiple (repeated) scattering, accompanied by additional Monte Carlo choices.

To simplify the description, let us just study the scattering direction. Assume we have a sample that only scatters elastically and isotropically with a volume specific cross section, Σ, and that no absorption is present. Then, the attenuation factor for the direct beam is $\mu = \Sigma$, and the physical probability for scattering at some point along the beam path is

$$P_{\text{scatt}} = 1 - \exp(-\Sigma L), \tag{14.15}$$

where L is the length of the particular ray within the sample. However, we must also consider the outgoing ray. The probability for scattering into the solid angle $d\Omega$ is

$$P(\Omega)d\Omega = P_{\text{scatt.}} \frac{d\Omega}{4\pi}. \tag{14.16}$$

Let us require that the ray must always scatter, and let us select the outgoing ray direction with uniform probability. Then we have

$$f_{\text{MC uniform}} d\Omega = \frac{d\Omega}{4\pi}. \tag{14.17}$$

We must now calculate the weight multiplied, and (14.6) gives

$$\boxed{w_{\text{uniform}} = \frac{P(\Omega)d\Omega}{f_{\text{MC phys.}}d\Omega} = 1 - \exp(-\Sigma L) \approx \Sigma L}, \tag{14.18}$$

where the rightmost approximation is valid only for "thin" samples, $\Sigma L \ll 1$. Note that we have here not taken into account the attenuation of the outgoing neutron ray. This must be done seperately.

14.3.5 Focusing in sample scattering

Some neutron instruments have a geometry such that only rays scattered in certain "interesting directions" have any chance of being detected. In such cases, one will employ the technique of *focusing* to improve simulation efficiency. This implies a need to modify (14.18), as we discuss below.

In focusing, the ray will be emitted only within a certain solid angle, $\Delta\Omega$. This solid angle must contain all the directions contributing to the detector counts, otherwise the focusing will give false results. Assuming uniform selection within $\Delta\Omega$, the Monte Carlo probability will be given by

$$f_{\text{MC focus}}d\Omega = \frac{d\Omega}{\Delta\Omega}, \tag{14.19}$$

and (14.6) gives

$$\boxed{w_{\text{focus}} = \frac{P_{\text{scatt.}}}{f_{\text{MC focus}}} = \frac{\Delta\Omega}{4\pi}\big(1 - \exp(-\Sigma L)\big) \approx \frac{\Delta\Omega}{4\pi}\Sigma L}. \tag{14.20}$$

Comparing to the uniform case, the focusing method gives smaller weight factors per ray, but a larger number of rays traveling towards the detector. This gives the same final result, but with a smaller statistical error. The focusing technique is an important example of importance sampling.

14.4 Problems

We now present a number of pen-and-paper problems, which illustrate the basics of simulation methods. Proper hands-on simulation problems and larger projects are presented in chapter 15.

14.4.1 Validity of the semiclassical approximation

Cold and thermal neutrons are considered as classical particles at the instrument level, saving the wave description to the component level. We will now look closer at the soundness of this semiclassical approximation.

1. In a typical high-angular-resolution experiment to measure diffraction from single crystals, the neutron direction is determined within 10' (10 arc minutes) in the horizontal direction. Consider a set-up with a low neutron energy of 3.7 meV, where the beam is limited in space by a slit (or diaphragm) with a width (horizontally) of 1 mm. How does this set-up agree with the uncertainty relations? And how small a beam would still be consistent with the present value of collimation?

2. At the high-energy-resolution neutron scattering instrument BASIS at SNS, the neutron energy can be measured with an accuracy of 2.2 μeV, using backscattering from Si analyzer crystals, while the neutron energy itself is $E = 2.08$ meV. Since SNS is a pulsed neutron source, the energy resolution of the incoming neutrons is determined by the pulse length, which is around 40 μs. How does that match the Heisenberg uncertainty relations? (Similar instruments operate at reactor sources, *e.g.* the instrument SPHERES at FRM-2, Munich, that has an energy resolution of 0.6 μeV.)

14.4.2 Simulation of incoherent scattering

We will now excercise the rule of weight transformations, (14.6). First, consider a thin sample of an incoherent scatterer, area A, thickness t with $d\Sigma/d\Omega = \rho\sigma_{\rm inc}/(4\pi)$, where ρ is the number density per unit volume and $d\Sigma/d\Omega$ is the differential scattering cross section per unit volume.

1. Show from (2.4) that the scattering probability for a given neutron ray is $P = \sigma_{\rm inc}\rho t$. Calculate the value for vanadium, where $\rho^{-1} = 13.77$ Å^3.

2. In a particular simulation, we choose to focus the neutron rays into an area of $\Delta\Omega$ in the following way: (a) pick a random direction inside $\Delta\Omega$, (b) scatter all incident neutrons. Argue that the weight factor adjustment should be $w = \rho\sigma_{\rm inc}t\Delta\Omega/(4\pi)$.

3. For a general sample, the cross section per unit volume is denoted $(d\Sigma/d\Omega)(\mathbf{q})$. Argue that the weight factor adjustment will be $w = (d\Sigma/d\Omega)(\mathbf{q})t\Delta\Omega$, also if the cross section varies with $\mathbf{q}$ across $\Delta\Omega$.

14.4.3 Simulation of SANS scattering

Calculate an equation for the Monte Carlo weight factor adjustment, w, in a sample component for spheres, where all neutrons are scattered, $f_{\rm MC} = 1$. The form factor for spheres is discussed in problem 5.4.2. You may like to consult the text in the present chapter.

Chapter 15

McStas simulation projects

This chapter contains simulation problems and projects of different sizes, which all require the use of the McStas simulation package. It should with little effort be possible to convert these projects to being performed with any other simulation tool, although this has not yet been done.

For technical details about the use of the McStas package, we refer the the user manual found at the home page [95].

15.1 Simple simulation problems

The simple problems below can be solved using the McStas components `Source_simple`, `Source_Maxwell3`, `Slit`, `Guide`, `PSD_monitor`, `Div_monitor`, `L_monitor`, and `Div_L_monitor`. Please note that all McStas monitors can be used as ideal detectors.

15.1.1 Estimating the circle area

1. Construct a simulation with a square neutron source, which emits neutrons in a preferred direction. Focus the source output to a position-sensitive detector, which is much further away than the source size. Verify that the detector is completely illuminated, but that still all emitted neutrons rays are detected. Then place a circular slit very close to the detector.

2. Use your results to estimate the value of π. Perform the simulations for a varying number of neutron rays, N, in the interval $10^4 - 10^8$. Make a few simulations for each value of N and estimate the variance of the result. Determine how the simulation uncertainty depends on N and compare with the uncertainty estimate given directly by McStas. Make a graph of the estiated circle value and its standard deviation as a function of (the logarithm of) N.

15.1.2 A neutron guide system

The neutron flux from a moderator can be described by the temperature of a Maxwellian distribution. Assume that we have a square cold neutron source 15×15 cm^2 with $T = 30$ K with a flux of 10^{12} neutrons/s/cm^2/steradian, corresponding to values for ESS or ILL. Use this moderator to construct a 20 m neutron guide system with $m = 1$ starting 1.5 m from the moderator, similar to the one in problem 4.10.1.

1. Simulate this system and try to reproduce the analytical results of problems 4.10.1. Use the McStas guide values $\alpha = 0$, $W = 0$, $R_0 = 1$, and $m = 1$ (to remove the effect of the guide, use $m = 0$).

2. Exchange the $m = 1$ guide with a multilayer guide of $m = 2$ with the parameters (McStas defaults): $\alpha = 4.38$ and $W = 0.003$. Repeat the simulations to investigate the effect of the new guide material. One suggestion could be to investigate how intensity and divergence behave as a function of neutron wavelength for the two different guides.

15.2 Simulation project: SANS-2

SANS-2 is a small-angle neutron scattering instrument situated at the neutron source SINQ, PSI, Switzerland. SANS-2 is placed at the SINQ cold source.

In this project, you should construct a model of SANS-2, insert a SANS sample component modelling nano-sized objects, perform a virtual SANS experiment, and analyze the data. You will also study the q-resolution of the spectrometer.

15.2.1 The source-guide system

The SINQ cold source is made from liquid deuterium, D_2. The outgoing neutrons are not brought into complete thermal equilibrium with the cold source, so the energy/wavelength spectrum is not completely Maxwellian. However, it can be described as a sum of three Maxwellians. This is implemented in the source component `source_maxwell_3`. The correct parameters for this component are `width=0.085, height=0.16, T1=150.42, T2=38.74, T3=14.84, I1=3.67E11, I2=3.64E11, I3=0.95E11`.

The opening in the biological shielding, which we use for the SANS-2 beam port, is 0.050 m high and 0.050 m wide and starts 1.5 m from the cold source, which is 0.08 m wide and 0.16 m tall.

The SANS-2 guide system first has a 4.5 m long straight section. Then follows a 20 m curved section made from 40 0.5 m straight pieces, placed so that the radius-of-curvature is 2.4 km, then a 10 m long straight guide. However, here we make the simplification that the guide is straight and is in one piece.

The guide material has $m = 2$ with same parameters as in problem 15.1.2. The guide has measures 0.05 m times 0.05 m along its whole length.

Update your simulation of the guide system and measure the wavelength and energy spectrum at the end of the guide. You can neglect neutrons with a wavelength below 1 Å (corresponding to an energy above 82 meV).

15.2.2 Velocity selector

Insert a velocity selector, centered 0.2 m after the guide. Use the default parameters, except for the aperture size (which you adjust to be "large enough"). Another exception is the number of blades which is 68, and the rotation, which you use as an input parameter of the instrument.

Adjust the rotation speed to select neutrons of $\lambda = 10$ Å. Perform the simulation and verify that the correct wavelength is chosen. Measure the wavelength spread, $\Delta\lambda/\lambda$.

McStas hint: The wavelength monitor performs simple statistics when you perform a single plot from the plot menu. The plotted width is the statistical (or Gaussian) variance. In case the distribution is Gaussian, the FWHM is found by multiplying with $2\sqrt{2\ln(2)}$.

15.2.3 Pinhole collimation

Place one pinhole (circular slit), 8 mm diameter, right after the exit of the velocity selector, and place an identical one 6 m downstream. Simulate the divergence of the beam after the second slit. Compare to the calculated values.

Perform the same task for the case of $L_c = 3$ m (move the first slit 3 m further downstream). Does it make a difference to place a 3 m guide piece after the velocity selector? Why?

McStas hint: You may like to store the results of your two simulations by `virtual_output` to ease the simulations in the problems below. You will probably need $1 \cdot 10^9$ rays or more to reach reasonable statistics. It might be a good idea to produce the virtual sources over the weekend.

15.2.4 Detector

The detector is a circular PSD, diameter 64 cm, with a pixel size of 8×8 mm^2, placed in an evacuated tank that begins 0.5 m after the second slit. The distance between the second slit and the detector is either $L_d = 3$ m or $L_d = 6$ m. Calculate and simulate the size of the direct beam for $L_c = L_d = 3$ m and $L_c = L_d = 6$ m.

Place a circular beamstop of an appropriate diameter just before the detector to avoid the direct beam. Control whether this beamstop blocks the whole of the direct beam.

McStas hint: As preliminary treatment of isotropic SANS data, one would normally perform an average of the measured $d\sigma/d\Omega(\mathbf{q})$ for positions of the detector with equal value of $|\mathbf{q}|$. This corresponds to a radial average of the pixels in concentric circles. The monitor component `PSD_monitor_rad` performs

this radial average. Perform the simulation with this component at the detector position.

15.2.5 The effect of gravity

Until now, the effect of gravity has been neglected. Estimate the effect of gravity on neutrons in a SANS instrument with $L_c = L_d = 6$ m for neutrons of 10 Å and 20 Å. Comment on the result, but continue to not include gravity in the next problems.

15.2.6 A full virtual experiment - spheres sample

The component `Sans_spheres_new` uses the formfactor derived earlier. Use this sample and the simulated set-up to make a full virtual SANS experiment. Insert a `Sans_spheres_new` sample 0.05 m behind the last slit and perform a simulation. Use the particle size $R = 100$ Å, and the excess scattering length density $\Delta\rho \approx -0.6\text{fm/Å}^3$ as calculated as the average scattering length density for the liposomes in problem 5.4.6.

Try a few settings of collimation length and detector length to simulate the result in various ranges of q. Try also particles of sizes $R = 200$ Å and 400 Å. Plot the theoretical total scattering intensity for $R = 100$ Å and 400 Å.

McStas hint: Use if possible similar collimation length and detector distance. Convert position at the radially averaging detector to q for each detector distance.

15.2.7 A full virtual experiment - Liposome sample

The component `Sans_liposomes` uses the formfactor for a spherical shell

$$F_{\text{shell}}(q) = \frac{\frac{4\pi}{3}R_{\text{out}}^3 f(qR_{\text{out}}) - \frac{4\pi}{3}R_{\text{in}}^3 f(qR_{\text{in}})}{\frac{4\pi}{3}(R_{\text{out}}^3 - R_{\text{in}}^3)}, \tag{15.1}$$

where $f(x)$ is the formfactor of a sphere as found in the previous problem. The intensity from diluted monodisperse liposomes is given by

$$I(q) = \phi V(\Delta\rho)^2 F^2(q), \tag{15.2}$$

where $V = V_{\text{out}} - V_{\text{in}}$ is the volume of the liposome and $\Delta\rho$ is the excess scattering length density in the shell.

Use the average $\Delta\rho$ that you calculated for the phospholipid bilayer liposomes ($\Delta\rho \approx -0.6\frac{\text{fm}}{\text{Å}^3}$, include your derivation in the report), and the volume-fraction $\phi = 0.01$. Each unit of the phospholipid bilayer consists of two DMPC groups with the hydrofobic chains facing each other. Calculate the thickness of the phospholipid bilayer by assuming an area of 64 Å^2 of each DMPC headgroup and a cylindrical shape of the DMPC bilayer unit. The volume of a DMPC headgroup is 302 Å^3 and 808 Å^3 for the tails. Use the liposome bilayer thickness in the `Sans_liposomes` component and simulate the total scattering

intensity for $R_{\text{out}} = 100$ Å and $R_{\text{out}} = 400$ Å. Plot also the theoretical total scattering intensity for $R_{\text{out}} = 100$ Å and $R_{\text{out}} = 400$ Å.

15.2.8 Normalizing data

Extrapolate the intensity of the forward scattering from the two samples ($I(q \to 0)$) and use the spheres to normalize the liposome intensity. Compare to the theoretical ratio of the forward scattering intensities of the two samples.

15.2.9 Data analysis

Fit the 1-dimensional data from `PSD_monitor_rad`. Determine the particle size both of the spheres and liposomes from the virtual data using the Guinier approximation.

Compare the obtained radius of gyration, R_g, with the particle radius R.

For the largest particles, try to fit the data to the Porod law. Comment on the results.

15.2.10 Resolution of the SANS instrument

A thin sample that scatters the beam with a fixed value of $|\mathbf{q}|$ can be used to simulate the q-resolution of the instrument. Argue that this is the case and that the component `Powder1` can be used for this purpose.

Insert this component and simulate the results for $L_{\text{c}} = L_{\text{d}} = 6$ m for two values of q, representative for the q-range of the instrument. Perform the same simulations for $L_{\text{c}} = L_{\text{d}} = 3$ m. Comment on the results.

15.3 Simulation project: Powder diffraction

DMC is a cold-neutron powder diffractometer situated at PSI. This instrument is optimized for high intensity, it has a medium q-resolution and a small-to-medium q-range. This makes DMC well suited for the study of magnetic structures. However, we will here discuss only nuclear structures.

This assignment takes you through the construction of a full DMC simulation. Then, you will perform a virtual powder diffraction experiment. At last, you will use the state-of-the-art analysis package FULLPROF to analyze the data and determine the crystal structure of an unknown substance.

If time allows, you are encouraged to suggest and investigate improvements to the spectrometer.

15.3.1 The guide system

DMC is placed at the cold source. For the cold source and surroundings you can use same parameters as for the SANS instrument in problem 15.2. The opening for the DMC beam port is 0.120 m high and 0.020 m wide. The DMC guide system begins at the DMC beam port. The guide is 40 m long and curved to

avoid line-of-sight to the source. You can assume the guide to be straight and with constant measures 0.120 m high and 0.020 m wide.

Simulate the neutron beam profile (using a PSD), its intensity, energy distribution, and divergence at the exit of the guide.

15.3.2 Monochromator

The monochromator is placed just after the guide exit (0.5 m downstream). You can assume it is a flat piece of PG crystal with a reflectivity of 80%. You will use the (002) reflection ($\tau = 1.8734$ Å^{-1}) to scatter the neutrons. The height of the monochromator is 0.120 m and the width is 0.200 m. The mosaicity of the PG crystal is 30' in both directions. Use the McStas component `monochromator_flat`.

You should select the "DMC standard" neutron wavelength of 2.4 Å. Calculate the scattering angle, 2θ and place a monitor at the sample position, 1.8 m from the monochromator centre. The monitor should have the typical sample dimensions, 2 cm high and 1 cm wide. Now, scan the monochromator orientation to obtain the maximum signal at the sample position (which is kept fixed in space, at an angle calculated from the Bragg law). Comment on the outcome.

Using the best setting found above, simulate the intensity, divergence and the energy distribution at the sample position. Do the same for the other "DMC standard" wavelength of 4.2 Å. Comment on the results.

15.3.3 Collimator

Insert a "Soller" collimator (component `Collimator_Linear`) between monochromator and sample. Investigate collimations of 20' and 60' and simulate intensity, divergence and energy distribution at the sample position. Compare to the situation without collimation and comment on the results.

15.3.4 Sample

You are now ready to insert a sample. First, use the simple component `Powder1` as documented in the component manual. You may use the default settings, but for the q value use the innermost peak of Al_2O_3: 1.8049 Å^{-1}. Calculate the scattering angle for the first reflection. Position a PSD monitor 1.0 m away from the sample at this angle and find the signal.

15.3.5 DMC multi-detector

The DMC detector has 400 channels with a 0.2° spacing, each 0.1 m tall. It is often run in two settings, 0.1° apart. In this way the effective angular spacing between adjacent channels is 0.1°, and the distance between detector channels 1 and 800 is 79.9°. The detector can rotate around the sample until the highest detector channel is at approx. 140°. In McStas, this detector can be inserted by means of `Monitor_nD` with input parameters (exactly)

```
options = "banana, theta bins=800 limits=[20 100]",
xwidth = 2, yheight = 0.1, filename = "My_datafile"
```

Test the new detector set-up. Simulate incoherent background counts in all detector channels. Then vary the collimation of the incoming beam and see how this affects the powder signal.

15.3.6 A full virtual experiment

Insert a realistic sample component, `PowderN`, at the sample position. The parameters, in the form of an input file, `"secret.lst"`, which will be provided on the course home page in the document "Recipe for Crystallographica-McStas-FullProf interplay".

Perform a full virtual experiment by running a long simulation of the counts in the multi-detector. Use a 20' collimator after the monochromator.

15.3.7 Emulating real experimental data

All McStas simulations is performed in units of counts per unit time. Hence, to reach "real" count numbers, one should multiply the simulated intensity, I, by the virtual measuring time, t. There is, however, an upper limit to this value. If the Monte Carlo errorbar scaled with virtual counting time: $t\delta I$ exceeds the equivalent experimental counting statistics: $\sqrt{tI}$, the accuracy of the simulation is not sufficient to allow scaling to the given time value. The criterion reads

$$t\delta I \leq \sqrt{tI}, \tag{15.3}$$

or

$$t \leq \left(\frac{I}{\delta I}\right)^2 \tag{15.4}$$

for every data point.

The McStas tool `mcrealistic` performs the transformation from intensities to counts under the observation of this rule. Further, it adds "real" counting statistics if some simulation points are "too accurate". This tool will be explained in the class.

Run `mcrealistic` on your simulated data in the way described in the note "Recipe for Crystallographica-McStas-FullProf interplay". Assume one hour of experimental time (if this is possible with the simulated statistics).

Display the results as a function of q with errrobars.

15.3.8 Determine the crystal structure of the sample

It is now time to use your virtual data, in the format produced in problem 15.3.7, as input to the FullProf structure refinement program. Your aim is to determine the crystal structure of the sample. Information on the use of FullProf is given in the note "Recipe for Crystallographica-McStas-FullProf interplay".

15.3.9 Optional: Improve your instrument

In this problem, you should optimize your instrument with respect to intensity and/or q-resolution. Anything goes as long as it works.

A few suggestions: It may be possible to optimize guide parameters and geometry, monochromator parameters and geometry, distances, collimations, detector dimensions. Note that McStas has a built-in optimizer function. The details of this is best explained in the class.

The DMC instrument will be upgraded over the next few years, and you may be able to find a suggestion for improvement that is better than the planned. Perhaps you can save PSI a few million Swiss Francs?

Anyway, there is a round of C-credits at stake for the best instrument, i.e. the instrument that gives the best results in terms of intensity and resolution combined. A good figure-of-merit could be peak intensity squared divided by peak width (and it is not allowed to increase the structure factor).

15.4 Simulation project: A triple-axis spectrometer

RITA-2 is a triple-axis spectrometer situated at PSI, Switzerland. RITA-2 is placed at the cold source and is optimized for medium energy resolution and high q resolution.

In this assignment, you will use McStas to construct a model of RITA-2 and perform a virtual inelastic phonon experiment. You will then use the state-of-the-art analysis package MFIT to analyze the data and determine the phonon dispersion relation. You will also be asked to study the energy and (optionally) the q resolution of the spectrometer.

15.4.1 The source-guide system

We use the same cold source as for project 15.3. The opening we are using for the RITA-2 beam port is 0.120 m high and 0.030 m wide.

The RITA-2 guide system starts 1.5 m from the source. It has a 4.5 m long straight section, followed by a 20 m curved section made from 40 0.5 m straight pieces, placed so that the radius-of-curvature is 2408 m. This eliminates the line-of-sight, so to avoid neutrons with very small wavelengths. However, in this assignment we make the simplification that the guide is straight and is in one piece. The guide material has $m = 2$ and same parameters as in project 15.3. The guide has height 0.120 m and width 0.030 m along its whole length.

Simulate the neutron beam intensity at the exit of the guide for neutrons in the range 0.5 Å - 20 Å.

15.4.2 A focusing monochromator

The RITA-2 monochromator is placed just after the guide exit (0.4 m downstream). It consists of 5 slabs of pyrolytic graphite (PG) crystals with a mosaicity of $\eta = 37$ arc minutes, a scattering vector of $q = 1.87325$ Å^{-1}, 0.15 m wide

and 0.025 m tall, displaced $h = 0.026$ m vertically with respect to the neighbour slabs. We denote the scattering angle at the monochromator $2\theta_{\mathrm{M}}$ - often given as TTM in McStas.

The five slabs can be rotated individually around their horizontal axis by the angle ϕ. The idea behind this is to focus the beam vertically on to the sample, which is positioned $L_{\mathrm{MS}} = 1.54$ m from the monochromator center.

Analyze the geometry to find an expression for the optimal tilting angle of one blade in a vertically focusing monochromator as a function of neutron wave vector, k_{i} (or $2\theta_{\mathrm{M}}$). Show that the rotation angle of a slab centered at the height h above the beam center is given by (in a small-angle approximation):

$$\phi = \frac{hk_{\mathrm{i}}}{qL_{\mathrm{MS}}} = \frac{h}{2\sin(\theta_{\mathrm{M}})L_{\mathrm{MS}}}. \tag{15.5}$$

Hint 1: You can consider the beam leaving the guide to be parallel and horizontal. Hint 2: It is an advantage to consider the neutron wave vectors, k_{i} and k_{f} - and to focus on their y-component. Hint 3: Remember that the **q**-vector is fixed within the monochromator crystal and therefore changes when the crystal rotates. For example, $q_y = 0$ for $\phi = 0$.

15.4.3 Tuning the RITA-2 monochromator

Make a model of the 5-blade monochromator using the component `Monochromator_flat`. You should then select the "RITA-2 standard" neutron energy of 5.0 meV. Scan the monochromator curvature to obtain the maximum signal at the sample, which is 0.02 m high and 0.01 m wide. Compare to the value from eq. (15.5).

Using the best setting found above, simulate the intensity, divergence and the energy distribution at the sample position. Compare with the situation where the monochromator is flat (zero curvature).

Perform the same tuning for the other "standard" energies of 3.7 meV and 14 meV and compare to the results for a flat monochromator. Try also the energy 7.0 meV, which you will need later. Comment on the results.

Hint 1: To simulate a component rotated around two axes, you can use two Arm's, rotated with respect to one another. This allows you to visualize in which order the rotations are performed (Remember, rotations do not commute). Hint 2: To optimize the simulations now and later, you should choose a limited wavelength interval at the source. Check at your wavelength monitor that this interval is still broad enough to simulate all neutrons that would have hit the sample.

15.4.4 Collimator

Insert a linear collimator between monochromator and sample. The collimation should be 80' in the horizontal direction; open vertically. A typical dimension is 10 cm width, 20 cm height, and 20 cm length. Simulate the intensity, divergence and energy distribution (in particular: the energy width) at the sample position for 5.0 meV neutrons and focusing monochromator. Try also a 40' and

a 20' horizontal collimator. Compare to the situation without collimation and comment on the results.

From now on, use a 80' horizontal collimator.

15.4.5 Filter

To avoid contamination by second order neutrons, one often uses a powder filter, as described in Problem 4.10.5. For 5.0 meV, the choice is Be. A 10 cm thick powder sample of this light metal is placed either between the monochromator and the "physical" sample, or right after the sample. Such a Be filter will scatter away neutrons with energies above a certain cut-off energy. A filter is typically cooled to avoid inelastic scattering due to phonons.

The filter shall not be simulated, since a useful McStas component does not yet exist.

15.4.6 Analyzer and detector

The second axis in a triple axis spectrometer is the sample, from where the neutrons are scattered in an angle, we here denote TT. Use first a radius 10 mm / inner radius 6 mm hollow vanadium sample (`V_sample`) and focus the outgoing scattering (in the simulations) on the analyzer below.

To form the third axis in the RITA-2 spectrometer, a PG analyzer crystal is placed 1.26 m from the sample. The size of the analyzer crystal is 0.150 m high and 0.025 m wide. Use the `monochromator_flat` component with the same parameters as for the monochromator.

The neutrons are scattered from the analyzer into the detector, which is a PSD detector, 0.30 m wide and 0.50 m high, 128×128 pixels, placed 0.350 m from the analyzer. Usually, only the middle 19 mm of the detector is used.

Position the analyzer-detector to perform Bragg scattering for 5.0 meV neutrons. The scattering angle at the analyzer is denoted TTA. Confirm that neutrons reach the detector and that it is reasonable to use only 19 mm detector width. Estimate the effective detector height and use this value from here on.

Hint: You may like to test the set-up by inserting a 4π monitor, centered at the vanadium sample.

Experimental note: At the RITA-2 instrument, several analyzer blades are used. We will, however, not go into details with that here.

15.4.7 Energy resolution

Investigate the energy resolution of your spectrometer by performing a scan of the energy transfer. Vary E_i by moving TTM/OMM, keeping all other angles constant. Use 5.0 meV for E_f and a non-zero value for TT. Plot the simulated intensity (*e.g.* E-monitor with only one channel) as a function of $\hbar\omega$ and find the energy resolution (FWHM of the peak) using MatLab.

Where would you place the Be filter in such an experiment?

Hint: Remember to stretch the lambda interval in the source to allow for the change in E_i. If it is a help, you can safely assume that the optimal curvature does not change significantly over the scan. Multiple McStas simulations can be run from the command line by typing a series of `mcrun` commands into a file and the excecuting the file by the command `source ./<filename>`. The syntax for the McStas command line `mcrun` is given in the manual.

15.4.8 Phonon sample

You should now simulate lattice vibrations (phonons) in a single crystal sample of Pb: cubic lattice constant $a = 4.95$ Å, scattering length $b = 9.4$ fm, and velocity of sound $c = 10$ meV Å .

Position an energy monitor 1.26 m away from the sample (use *e.g.* an interval of 0-8 meV) and position the crystal at the (200) Bragg reflection by a proper value of the sample rotation OM. Try to turn OM 2° away from this reflection and measure the energy of the neutrons that now leave the sample in the direction of the analyzer. Comment on the result.

McStas hints: In this project you will use the sample `phonon_simple`, which is documented in the component manual. When unrotated, the crystal is oriented with the (001) axis (lying in the scattering plane) perpendicular to the beam and the (100) axis along the beam direction.

To optimize simulation time and avoid second order scattering, you may like to limit your simulated wavelength interval in the source component. Take care that you do not make the interval too narrow!

15.4.9 A full virtual experiment

You should now perform the virtual experiment. The idea is to perform a scan in reciprocal space with a constant energy transfer, $\hbar\omega = 2.0$ meV. You should move the spectrometer along a line in reciprocal space through the (200) position, intersecting the phonon branch twice.

However, before you can perform the scan, you should calculate the setting of the spectrometer. First, construct the scattering triangle, given by the known wave vectors $\mathbf{k}_\mathrm{i}$, $\mathbf{k}_\mathrm{f}$, and $\mathbf{q}$ and use it to calculate the scattering angles, TT and OM. Use $E_f = 5.0$ meV, $\hbar\omega = 2.0$ meV, and $\mathbf{q} = \boldsymbol{\tau}$=(2,0,0). (Scattering angles should in general be calculated with a precision of 0.01°.)

Convince yourself that by rotating the sample (by ΔOM), you will make a close-to-transverse constant-E_i scan in reciprocal space, without changing the angles of the scattering triangle. (Hint: The scattering triangle, and hence $\mathbf{q}$, is fixed in the laboratory coordinate system, but you need to describe $\mathbf{q}$ in the coordinate system of the sample.)

Calculate how (h, k, l) and ΔOM corresponds to one another. (Hint: You need only go to first order in ΔOM.)

Perform the virtual close-to-transversal scan. Perform the scan also in the opposite orientation, changing the sign of both OM and TT (the "+-+" configuration).

For the best of the two configurations found above, perform scans for a few other energy transfers, *e.g.* $\hbar\omega = 1.0$ meV and 3.0 meV.

Fit the processed data and use the fitting results to calculate the measured velocity of sound in Pb.

15.4.10 Optional 1: Determine the full phonon dispersion of the sample

For higher energy transfers, the dispersion is no longer linear. Perform constant-q scans to measure the dispersion in the $(h, 0, 0)$ direction across the Brillouin zone. Fit the results and plot $\hbar\omega(q)$ vs. q.

15.4.11 Optional 2: The resolution function

You may have noticed that your two phonon peaks are not identical, e.g. for 2.0 meV. The reason for this is hidden in the "resolution function", which is a measure of the precision of the spectrometer. In more precise terms, it is the distribution $\hbar\omega$ and q of the scattered neutrons that actually hit the detector for one particular setting. The "resolution ellipse" is the contour in $(\hbar\omega, q)$-space, where the transmission has fallen to half the value of the nominal point.

In experiments, the resolution function at $\hbar\omega = 0$ can be measured by e.g. elastic scattering from single crystals, but direct measurements of the inelastic resolution function cannot be performed. Often, the resolution is calculated from the analytical Popovici approximation, by means of the program RESCAL [107].

The resolution function may, however, be calculated by McStas. Replace your sample by component `res_sample` and replace your detector by `res_monitor`. The sample then scatteres neutrons inelastically into a focusing direction and energy interval determined by you, and the monitor records the values of $\hbar\omega$ and q of the neutrons that hits. After the simulation, the outcome can be shown with the McStas tool `mcresplot`.

Determine your resolution function at both 2.0 meV inelastic peaks and discuss why the peak shapes and peak intensities were not equal.

Appendix A

Appendix

A.1 Mathematical identities

A.1.1 Vector analysis

By using the identities

$$\frac{\mathbf{r}}{|\mathbf{r}|^3} = -\nabla\left(\frac{1}{|\mathbf{r}|}\right) \tag{A.1}$$

$$\frac{1}{|\mathbf{r}|} = \frac{1}{2\pi^2}\int d\mathbf{q}\frac{1}{q^2}\exp(i\mathbf{q}\cdot\mathbf{r}) \tag{A.2}$$

We utilize the mathematical identity [2]:

$$\nabla\times\left(\frac{\mathbf{s}\times\mathbf{r}}{r^3}\right) = \frac{1}{2\pi^2}\int \hat{\mathbf{q}}'\times(\mathbf{s}\times\hat{\mathbf{q}}')\exp(i\mathbf{q}'\cdot\mathbf{r})d\mathbf{q}'. \tag{A.3}$$

A.2 Electrodynamics

A.2.1 The classical electron radius

We will here calculate an expression for the "radius", r_0, of the electron, which it would have if its electrostatic energy was equal to its relativistic energy, $m_e c^2$. In other words, we assume that the electron charge, $-e$, is evenly distributed over a sphere of radius r_0. We know that for such an arrangement, the electrostatic force on a small test charge, dq outside the sphere of charge q is the same as if the charge was concentrated in the centre:

$$F_{\text{el}} = \frac{1}{4\pi\epsilon_0}\frac{qdq}{r^2}. \tag{A.4}$$

Of course, we here assume that the hypothetical test charge is much smaller than e. To move the test charge from infinity (where the potential is zero) to

the sphere surface, we need to add a mechanical energy

$$dE = \int_{\infty}^{r_0} F_{\mathrm{el}} dr = \int_{\infty}^{r_0} \frac{1}{4\pi\epsilon_0} \frac{qdq}{r^2} dr = \frac{1}{4\pi\epsilon_0} \frac{qdq}{r_0}.. \tag{A.5}$$

We can thus see that the potential of the surface of the sphere is

$$U = \frac{1}{4\pi\epsilon_0} \frac{q}{r_0}. \tag{A.6}$$

Hence, the sphere has a capacitance of

$$C = \frac{U}{q} = \frac{1}{4\pi\epsilon_0} \frac{1}{r_0}, \tag{A.7}$$

and the charging energy of this sphere to the total charge, e, reads

$$E = \frac{1}{2} C e^2 = \frac{1}{4\pi\epsilon_0} \frac{e^2}{2r_0}. \tag{A.8}$$

When this energy is equalled with $m_{\mathrm{e}}c^2$, we reach

$$r_0 = \frac{e^2}{8\pi\epsilon_0 m_{\mathrm{e}} c^2} = \frac{\mu_0}{4\pi} \frac{e^2}{2m_{\mathrm{e}}} = 2.818\,\mathrm{fm}, \tag{A.9}$$

where we have utilized that $\epsilon_0\mu_0 = 1/c^2$.

?ER DER IKKE EN FAKTOR 2 GALT?

A.3 Quantum mechanics

A.3.1 The Fermi Golden Rule

Bibliography

[1] W. Marshall and S.W. Lovesey. *Theory of Thermal Neutron Scattering*. Oxford, 1971.

[2] G.L. Squires. *Thermal Neutron Scattering*. Cambridge University Press, 1978.

[3] See the home page of the Nobel price committee `www.nobelprize.org`.

[4] D. F. McMorrow and J.-A. Nielsen. *Modern X-ray scattering*. Wiley, 2001.

[5] J. Chadwick. Possible existence of a neutron. *Nature*, 129:312–312, 1932.

[6] A. Garcia, J.L. Garcia-Luna, and G.L. Castro. *Phys. Lett. B*, 500:66, 2001.

[7] R. P. Feynman. *The Feynman Lectures on Physics*. Addison Wesley Longman, 1970.

[8] See also the home pages for the major neutron facilities: `www.ill.fr`, `www.isis.rl.ac.uk`, `www.sns.gov`, `http://j-parc.jp/index-e.html`.

[9] See `http://www.ess-scandinavia.eu`.

[10] M. Enderle *et al. Phys. Rev. Lett.*, vol:page, year.

[11] K. Lefmann *et al. Journal of Neutron Research*, 16:97–111, 2008.

[12] Eugen Merzbacher. *Quantum Mechanics*. Wiley, 3rd edition, 1998.

[13] A.-J. Dianoux and G. Lander. *ILL Neutron Data Booklet*. ILL, 2003.

[14] See the NIST neutron cross section home page `http://www.ncnr.nist.gov/resources/n-lengths/`.

[15] J. Howard. *J. Appl. Cryst.*, 20:120–122, 1987.

[16] P. Henry. *(in preparation)*, 2011.

[17] E. Merzbacher. *Quantum Mechanics*. Wiley, 1998.

[18] W.W.T Crane, G.H. Higgins, and S.G. Thompson. *Phys. Rev.*, 97:242, 1955.

[19] B. Naranjo, J.K. Gimzewski, and S. Putterman. *Nature*, 434:1115, 2005.

[20] See the home page `www.aip.org/tip/INPHFA/vol-9/iss-6/p22.html`.

[21] J. Duderstadt and L. Hamilton. *Nuclear Resactor Analysis*. Wiley, 1976.

[22] See the SNS web page `http://www.sns.gov`.

[23] See J-PARC web page `http://j-parc.jp/MatLife/en/index.html`.

[24] See the home page of the NMI3 project `www.neutron-eu.net`.

[25] See the Neutron Sources home page `www.neutronsources.org`.

[26] G.S. Bauer. Neutron sources. In *Lecture Notes of the Introductory Course to the ECNS99*, pages 12–26. Report KFKI-1999-04/E.

[27] L.D. Landau and E.M. Lifshitz. *Course in Theoretical Physics*, volume 5 of *Statistical Physics*. Butterworth-Heinemann, 1951.

[28] K.H. Klenø. *Exploration of the challenges of neutrons optics and instrumentation at long-pulsed spallation sources*. PhD thesis, Niels Bohr Institute, University of Copenhagen, 2013.

[29] D.J. Picton, S.M. Bennington, T.A. Broome, and T.D. Benyon. *Nucl. Instr. Meth. A*, 545:363, 2005.

[30] E. Padovani, S.A. Pozzi, S.D. Clarke, and E.C. Miller. MCNPX-PoliMi User's Manual, C00791 MNYCP, Radiation Safety Information Computational Center, Oak Ridge National Laboratory, 2012.

[31] Geant 4.9.5 Physics Reference Manual, `http://geant4.web.cern.ch/geant4/UserDocumentation/UsersGuides/PhysicsReferenceManual/BackupVersions/V9.5/fo/PhysicsReferenceManual.pdf`, December 2012.

[32] H. Maier-Leibnitz and T. Springer. *J. Nucl. En. A/B*, 17:217, 1963.

[33] F. Mezei. *Communications in Physics 1*, 81, 1976.

[34] Information from Swiss Neutronics Ltd. See `http://swissneutronics.ch`.

[35] D.F.R. Mildner. *Nucl. Instr. Meth. A*, 290:189, 1990.

[36] K.H. Klenø. *(in preparation)*, 2011.

[37] C. Schanzer et al. *Nucl. Instr. Meth. A*, 529:63, 2004.

[38] S. Muehlbauer et al. *Physica B Cond. Matt.*, 385:1247, 2006.

[39] L.D. Cussen et al. *Nucl Instr. Meth. A*, 705:121, 2013.

[40] L. Chapon et al. *Neutron News*, 22:25, 2011.

[41] J.J X-ray Aps, private communication (2013); `http://www.jjxray.dk`.

[42] See e.g. the home page: `http://www.lanl.gov/quarterly/q_sum03/neutron_detect.shtml`. We will soon find more references here...

[43] K. Lefmann *et al. Physica B*, 385-386:1083–1085, 2006.

[44] T. Riste and K. Otnes. *Nucl. Instr. Meth.*, 75:197, 1969.

[45] G. Shirane, S.M. Shapiro, and J.M. Tranquada. *Neutron scattering with a Triple-Axis Spectrometer*. Cambridge, 2002.

[46] Kim Sneppen and Giovanni Zocchi. *Physics in Molecular Biology*. Cambridge University Press, 2005.

[47] J.S. Pedersen. *J. Appl. Cryst.*, 27:595–608, 1994.

[48] J.S. Pedersen. ? In *Neutrons, X-rays, and Light*, page ? Elsevier, 2002.

[49] L. Arleth *et al. Langmuir*, 13:1887–1896, 1997.

[50] G. Porod. *Kolloid Z.*, 124, 1951.

[51] G. Porod. *Kolloid Z.*, 125, 1952.

[52] L.G. Parratt. *Phys. Rev.*, 95:359, 1954.

[53] M. Born and E. Wolf. *Principles of Optics*. Cambridge, 1999.

[54] F. Abelès. *Ann. Physique (Paris)*, 5, 1950.

[55] L. Névot and P. Croce. *Rev. Phys. Appl.*, 15, 1980.

[56] Cowley R A and Ryan T W. *J. Phys. D: Appl. Phys.*, 20, 1987.

[57] C. Giacovazzo (ed.) International Union of Crystallography. *Fundamentals of Crystallography*. Oxford University Press, 1992.

[58] Ashcroft and N.D. Mermin. *Solid State Physics*. Saunders, 1976.

[59] Theo Hahn (ed.) International Union of Crystallography. *International Tables for Crystallography, Volume A: Space-group symmetry*. D. Reidel Publishing Company, Holland, 1987.

[60] N. F. M. Henry International Union of Crystallography and K. Lonsdale (eds.). *International Tables for X-Ray Crystallography, Volume I Symmetry Groups*. The Kynoch Press, Birmingham, UK, 1965.

[61] See the home page `http://www.crystallographica.co.uk/`.

[62] See the home page `http://www.ccp14.ac.uk/tutorial/powdcell`.

[63] J.I.L Langford and A.J.C. Wilson. *J. Appl. Cryst.*, 11:102, 1978.

[64] A. Kaestner et al. *Nuclear Instruments and Methods A*, 659:387–393, 2011.

[65] M. Strobl et al. *Journal of Physics D: Applied Physics*, 42:243001, 2009.

[66] I. S. Anderson, R. L. McGreevy, and H. Z. Bilheux. *Neutron imaging and applications*. Springer, 2009.

[67] A. S. Tremsin, W. Bruce Feller, and R. Gregory Downing. *Nuclear Instruments and Methods A*, 539:278–311, 2005.

[68] V. Litvin et al. *Bulletin of the Russian Academy of Sciences: Physics*, 73:219–221, 2009.

[69] C Kittel. *Introduction to Solid State Physics*. Wiley, 2004.

[70] M. Slaney and A. Kak. *Principles of computerized tomographic imaging*. SIAM, Philadelphia, 1988.

[71] J. Radon. *Classic papers in modern diagnostic radiology*, 5:00000–99999, 2005.

[72] J. Mishler et al. *Electrochimica Acta*, 75:1–10, 2012.

[73] R. Mukundan and R. Borup. *Fuel Cells*, 9:499–505, 20.

[74] A. Hilger, N. Kardjilov, M. Strobl, W. Treimer, and J. Banhart. *Physica B*, 385:1213–1215, 2006.

[75] I. Manke et al. *Appl. Phys. Lett.*, 92:244101, 2009.

[76] J. M. Warren et al. *Plant and soil*, 366:683–693, 2013.

[77] S. E. Oswald et al. *Vadose Zone Journal*, 7:1035–1047, 2008.

[78] U. Matsushima et al. *Visualisation of water flow in tomato seedlings using neutron imaging,* in *M. Arif and R. Downing, eds, 'Proc. 8th World conf. on Neutron Radiography (WCNR-8, Gaithersburg, USA)*. Lancaster, PA: DESTech Publ. Inc., 2006.

[79] D. Mannes et al. *Insight-Non-Destructive Testing and Condition Monitoring*, 56:137–141, 2014.

[80] G. Nilsson and G. Nelin. *Phys. Rev. B*, 3:364–369, 1971.

[81] S. Blundell. *Magnetism in Condensed Matter*. Oxford University Press, 2003.

[82] K. Yosida. *Theory of Magnetism*. Springer, 1996.

[83] J. Jensen and A.R. Mackintosh. *Rare-Earth Magnetism*. Oxford, 1991.

[84] C.G Shull W.A. Strauser and E.O. Wollan. *Phys Rev.*, 83:333, 1951.

[85] P.W. Anderson. *Phys. Rev.*, 86:694–701, 1952.

[86] M.F. Hansen *et al. Phys. Rev. Lett.*, 79:4910–4913, 1997.

[87] M.J. Cooper and R. Nathans. *Acta Cryst.*, 23:357, 1967.

[88] M. Popovici. *Acta Cryst. A*, 31:507, 1975.

[89] N. Metropolis. `http://library.lanl.gov/la-pubs/00326866.pdf`.

[90] See the home page of the Mersenne Twister Algorithm `http://www.math.sci.hiroshima-u.ac.jp/~m-mat/MT/emt.html`.

[91] D.P. Landau and K. Binder. *A Guide to Monte Carlo Simulations in Statistical Physics*. Cambridge, 2005.

[92] See the home page of the MCNSI part of NMI3 `www.mcnsi.risoe.dk`.

[93] See the NISP home page `www.paseeger.com`.

[94] See the IDEAS home page `http://www.ornl.gov/~xwl/publications/NeutronNews-2002.pdf`.

[95] See the McStas home page `www.mcstas.org`.

[96] See the VITESS home page `www.hmi.de/projects/ess/vitess`.

[97] See the RESTRAX home page `omega.ujf.cas.cz/restrax`.

[98] A. Vickery et al. *J. Jap. Phys. Soc. (in print)*, 2013.

[99] P.K. Willendrup *et al. Physica B*, 385-386:1032–1034, 2006.

[100] L. Udby *et al. Nucl. Instr. Meth. A*, 634:S138, 2011.

[101] P.L.W. Trigenna-Piggott. *J. Neutr. Res.*, 16:13, 2008.

[102] F. Mezei. The basic physics of neutron scattering experiments. In *Lecture Notes of the Introductory Course to the ECNS99*, pages 27–39. Report KFKI-1999-04/E.

[103] V.V. Nesvizhevsky *et al. Nature*, 415:297, 2002.

[104] R. Golub. *Rev. Mod. Phys.*, 68:329, 1996.

[105] Y. Hasegawa *et al. Nature*, 425:45, 2003.

[106] K. Kirch B. Lauss P. Schmidt-Wellenburg G. Zsigmond. *Nuclear Physics News*, 1:1, 2010.

[107] `http://xray.physics.ox.ac.uk/rescal/rescal.htm`.